



**HAL**  
open science

# Up-scaling of a pilot plant for the production of alternative fuels from waste plastics

Shawki Mazloun

► **To cite this version:**

Shawki Mazloun. Up-scaling of a pilot plant for the production of alternative fuels from waste plastics. Thermics [physics.class-ph]. Ecole nationale supérieure Mines-Télécom Atlantique, 2021. English. NNT : 2021IMTA0265 . tel-03917494

**HAL Id: tel-03917494**

**<https://theses.hal.science/tel-03917494v1>**

Submitted on 2 Jan 2023

**HAL** is a multi-disciplinary open access archive for the deposit and dissemination of scientific research documents, whether they are published or not. The documents may come from teaching and research institutions in France or abroad, or from public or private research centers.

L'archive ouverte pluridisciplinaire **HAL**, est destinée au dépôt et à la diffusion de documents scientifiques de niveau recherche, publiés ou non, émanant des établissements d'enseignement et de recherche français ou étrangers, des laboratoires publics ou privés.

# THESE DE DOCTORAT DE

L'ÉCOLE NATIONALE SUPERIEURE MINES-TELECOM  
ATLANTIQUE BRETAGNE PAYS DE LA LOIRE - IMT ATLANTIQUE

ECOLE DOCTORALE N° 602

*Sciences pour l'Ingénieur*

Spécialité : Energétique, Thermique et Combustion

Par

**Shawki MAZLOUM**

## **Extension et mise à niveau d'un pilote de production de carburants alternatifs à partir de déchets plastiques**

Thèse présentée et soutenue à Nantes, le 22/10/2021

Unité de recherche : GEPEA UMR CNRS 6144

Thèse N° : 2021IMTA0265

### **Composition du Jury :**

|                      |                              |  |
|----------------------|------------------------------|--|
| Président :          | <b>Agnès MONTILLET</b>       | Professeur, Université de Nantes                     |
| Rapporteur :         | <b>Frédéric MARIAS</b>       | Professeur, Université de Pau et des Pays de l'Adour |
| Rapporteur :         | <b>Laurent VAN DE STEENE</b> | Chargé de recherche (HDR), CIRAD                     |
| Examineur :          | <b>Karim ALLAF</b>           | Professeur, Université de La Rochelle                |
| Directeur de Thèse : | <b>Khaled LOUBAR</b>         | Maître-assistant (HDR), IMT Atlantique               |
| Co-encadrant :       | <b>Sary AWAD</b>             | Maître-assistant, IMT Atlantique                     |

### **Invité(s)**

|          |                     |                           |
|----------|---------------------|---------------------------|
| Invité : | <b>Nadine ALLAM</b> | Enseignant-chercheur, LIU |
|----------|---------------------|---------------------------|

## Articles Publiés

- S. MAZLOUM, Y. ABOU MSALLEM, S. AWAD, N. ALLAM, K. LOUBAR, **Modelling pyrolysis process for PP and HDPE inside thermogravimetric analyzer coupled with differential scanning calorimeter**, International Journal of Heat and Mass Transfer, (2021). <https://doi.org/10.1016/j.ijheatmasstransfer.2021.121468>
- S. MAZLOUM, S. AWAD, N. ALLAM, Y. ABOU MSALLEM, K. LOUBAR, M. TAZEROUT, **Modelling plastic heating and melting in a semi-batch pyrolysis reactor**, Applied Energy, (2020). <https://doi.org/10.1016/j.apenergy.2020.116375>
- S. MAZLOUM, S. AWAD, Y. ABOU MSALLEM, N. ALLAM, K. LOUBAR, M. TAZEROUT, **Modeling of a pyrolysis batch reactor using COMSOL Multiphysics**, CIFMA conference, (2018). [10.1051/mateconf/201926104003](https://doi.org/10.1051/mateconf/201926104003)

### Remerciement

This thesis, which took up a great challenge, was full of discoveries. For that I wish to thank all the people who have contributed to this work. My thanks go first to my thesis director Khaled LOUBAR, my co-supervisor Sary AWAD, my co-supervisor Youssef ABOU MSALLEM, and to Dr. Nadine ALLAM for their guidance and great effort to accomplish this work.

I extend my sincere thanks to Frédéric MARIAS, professor at the University of Pau and the Adour countries and Laurent VAN DE STEENE, researcher at CIRAD, for agreeing to be the reviewers of this PhD thesis. Also, I thank also all the examiners of the thesis, Agnès MONTILLET, Karim ALLAF, and Nadine ALLAM. Moreover, I also thank the Lebanese International University and all the colleagues and Doctors in LIU for their support, especially the mechanical engineering department.

Nevertheless, I thank the entire technical team in IMT-Atlantique, Eric CHEVREL, François-Xavier BLANCHET, Patrick BRION, and Katell CHAILLOU who helped me a lot during this thesis by solving the technical problems and realizing the experimental devices. As well as all the staff in the Energy Systems and Environment Department (DSEE) of IMT-Atlantique, especially, Professor Yves ANDRES, Mme Dominique BRIAND, and Mme Ludivine SAHRAOUI.

In addition, I thank all of my colleagues in IMT-Atlantique, especially Walid, Christelle, Sara, Rita, Nouha, Allaa, Loubna, Samim, Marwa, Gaetan, and Morgane; with whom I shared happy moments enriched with respect and friendship.

Finally, this success and this doctorate are dedicated to my astonishing wife Touka HABIB who supported me all over this long journey with its difficult and amusing moments; honesty I owe here everything. Nonetheless, I devote this work to my first child Fatima and to all of my coming children; I wish them all success in their life and career and I hope that they will surpass me at some point. Also, I thank all of my friends in Lebanon, especially Ali ASHOUR and Hadi FAWAZ whom they supported me and provided me with all means of help to achieve this success. I also dedicate this work to my lovely parents for their sacrifices and invaluable love.

### Résumé

Le plastique est l'un des matériaux les plus abondants présents dans notre monde en même temps que dans les activités de la vie quotidienne. Depuis le début, les matières plastiques ont été présentées comme un dispositif pour se substituer des éléments rares et non durables tels que l'écaille de tortue, l'ivoire et les ossements d'animaux. Depuis lors, les plastiques ont façonné le monde en apportant une sécurité, hygiène, consolation et prospérité à notre société. La production de plastique a commencé dans les années 1950 et a augmenté de plus en plus jusqu'à atteindre 360 millions de tonnes en 2018 en tant que production annuelle de plastique dans le monde, alors que la demande est toujours en augmentation (Plastics - the Facts, 2019). De plus, l'Europe contribue à environ 18 % de la production annuelle mondiale, soit environ 62 millions de tonnes en 2018, et environ 50 % sont produites par les pays asiatiques. La majeure partie de la production de l'industrie du plastique va aux emballages - 40 % de l'industrie du plastique - et aux secteurs du bâtiment et de la construction, où les polymères leaders sont la polyoléfine, le polyéthylène (PE) et le polypropylène (PP), dont ils constituent environ 60 % des toute la production de plastique en Europe (Plastics – the Facts, 2019). D'autre part, les plastiques ont une durée de vie variable ; elle varie d'une journée ou une seule utilisation, comme les matériaux d'emballage à plus de 50 ans comme les plastiques utilisés dans l'industrie automobile. Ainsi, en raison de la courte durée de vie de la majorité des matières plastiques et de l'augmentation annuelle de la production de plastique, la production de déchets plastiques a énormément augmenté pour atteindre 307 millions de tonnes (Mt) dans le monde en 2015 (Geyer et al., 2017). Par ailleurs, de 1950 à 2015, environ 6300 Mt de déchets plastiques ont été générés, dont environ 9 % ont été recyclés, 12 % ont été incinérés et 79 % ont été accumulés dans des décharges ou dispersés dans la nature. Par conséquent, si les tendances actuelles de production et de gestion des déchets se poursuivent, environ 12000 Mt de déchets plastiques se retrouveront dans des décharges ou dans l'environnement naturel d'ici 2050 (Geyer et al., 2017). Chaque année, environ 8 millions de tonnes de déchets plastiques se déversent dans les océans en provenance des pays côtiers et causent la mort de millions d'animaux, des oiseaux aux poissons en passant par d'autres organismes marins. De plus, des microplastiques ont été trouvés dans plus de 100 espèces aquatiques, destinées à nos assiettes ; dans la plupart des cas, cela peut être nocif pour la santé humaine. Par conséquent, la

pollution plastique est un problème grave auquel l'humanité est confrontée et qui doit être résolue et surmontée.

En revanche, concernant le traitement des déchets plastiques, il existe trois grandes catégories : le recyclage, la valorisation énergétique et la mise en décharge. En Europe, 29,1 millions de tonnes de déchets plastiques post-consommation ont été collectés et traités en 2018 ; 32,5 % sont recyclés, 42,6 % sont utilisés pour la valorisation énergétique et 24,9 % sont mis en décharge (Plastics – the Facts, 2019). La mise en décharge est le pire traitement parmi tous, en raison du fait que les plastiques sont des matériaux non biodégradables ; les plastiques resteront enfouis pendant des siècles et l'espace d'enfouissement diminuera de plus en plus en plus de la pollution des sols. Ainsi, afin de parvenir à une économie circulaire du plastique, le traitement de la mise en décharge devrait être réduit jusqu'à zéro, tandis que les processus de recyclage et de récupération doivent être davantage utilisés (Plastics - the Facts, 2019). D'un autre côté, le processus de recyclage a des limites ; tous les déchets plastiques ne peuvent pas être recyclés et il y a des difficultés dans le processus de tri, de plus il s'agit d'un processus à coût d'exploitation élevé et à forte intensité de main-d'œuvre. Par conséquent, le traitement de récupération d'énergie devient une solution pour combler le vide et diminuer au maximum l'utilisation du processus de mise en décharge (Plastics – the Facts, 2019).

Il existe trois procédés principaux pour le traitement de valorisation énergétique ; Incinération, pyrolyse et gazéification. Les procédés de pyrolyse et de gazéification seraient similaires et plus respectueux de l'environnement que le procédé d'incinération. Cependant, le processus de pyrolyse est un sous-processus de gazéification et nécessite moins d'énergie. La pyrolyse plastique est un processus de dégradation thermique des hydrocarbures à longue chaîne en plus petits en l'absence d'oxygène. Elle produit une large gamme d'hydrocarbures et de produits chimiques qui peuvent être traités davantage, par distillation et raffinage, pour devenir des combustibles fossiles. Par conséquent, le procédé de pyrolyse est une solution très pratique pour la pollution des déchets plastiques et pour l'épuisement des réserves de combustibles fossiles. Mais, malheureusement, les technologies de pyrolyse et de gazéification au cours des quarante dernières années se sont heurtées à de nombreux obstacles qui ont considérablement réduit la mise en œuvre et l'utilisation de ces procédés prometteurs. Les principales raisons de cette chute étaient l'inefficacité des usines ou des réacteurs de pyrolyse, l'absence d'attraction du marché en raison de la concurrence des

combustibles conventionnels et le manque d'infrastructures pour un approvisionnement en matières premières de qualité contrôlée. Le fondement des deux premières raisons est que le développement des technologies de pyrolyse/gazéification était basé sur une voie expérimentale de mise à l'échelle qui est constamment testée et évaluée au cours des dernières années, en plus du coût élevé de l'alimentation thermique. Néanmoins, les principes fondamentaux et la procédure scientifique du processus de mise à l'échelle sont toujours conçus et intégrés au sein des entreprises de fabrication et ne sont pas divulgués au public ou à la communauté scientifique. De plus, l'approche numérique et simulation de cet aspect est également encore rarement traitée comme cela sera montré dans l'étude bibliographique.

Partant de ces problématiques cette thèse vient tenter de combler cette lacune et de poser les bases d'un modèle numérique de procédé de pyrolyse plastique basé sur la méthode des éléments finis dans un souci de compréhension et de construction de réacteurs de pyrolyse plastique plus performants. Ce travail s'inscrit dans la continuité des efforts et travaux réalisés auparavant par nos collègues Radu Kungser (Radu Kungser, 2015) et Chantal Kassargy (Kassargy, 2018) au sein de l'IMT-Atlantique "Département des Systèmes Energétiques et Environnementaux (DSEE) du laboratoire GEPEA. Les travaux précédents se sont concentrés sur des études expérimentales pour les procédés pyrolytiques et non pyrolytiques PE et PP dans un réacteur semi-batch et sur la comparaison entre les sous-produits pétroliers et les combustibles fossiles selon la norme caractéristique internationale. En outre, un réacteur de pyrolyse continue à l'échelle du laboratoire chauffé par les gaz d'échappement d'un moteur diesel de 8 kW a été construit à des fins d'expérimentation, d'amélioration des processus et de réduction des coûts d'approvisionnement thermique en utilisant la chaleur perdue du moteur. Malheureusement, il y avait une limitation dans le transfert de chaleur et le réacteur était inefficace car la fondation numérique et l'optimisation n'ont pas été faites avant la construction du réacteur. De plus, Chantal a proposé une conception et une modification par les pairs pour le réacteur de pyrolyse continue, basée sur une étude analytique ; cette conception sera testée numériquement en utilisant la méthode des éléments finis et un logiciel numérique tel que COMSOL Multiphasic à la fin de ce travail. Par conséquent, ce travail se concentrera sur la modélisation du processus de pyrolyse plastique à l'aide de la méthode des éléments finis et la simulation à l'aide de logiciels conventionnels comme COMSOL Multiphysics. Le procédé de pyrolyse sera modélisé dans un réacteur semi-batch, existant au laboratoire. Ensuite, ce modèle sera utilisé pour vérifier le réacteur de pyrolyse plastique en continu

proposé par les travaux de Chantal Kassargy. De plus, la géométrie et les conditions opératoires du réacteur continu seront optimisées pour une meilleure efficacité. Enfin, ce modèle peut être un pilier pour la configuration d'expérimentation à l'échelle du laboratoire du continu et plus tard de la mise à l'échelle pour la réalisation industrielle.

Cette thèse se compose de cinq chapitres, où les principales conclusions et illustrations de ces chapitres sont les suivantes :

Le premier chapitre est une étude bibliographique sur le procédé de pyrolyse des plastiques. Dans ce chapitre, la pyrolyse plastique a été définie et les paramètres d'influence ont été largement discutés. D'autre part, la technologie de pyrolyse plastique au cours des 40 dernières années s'est avérée basée sur une mise à l'échelle expérimentale, où malheureusement le processus de pyrolyse est encore inefficace et nécessite davantage d'améliorations (Huisman, 2001; IEA Bioenergy, 2020). Par conséquent, l'importance d'effectuer une modélisation et une simulation numériques pour la pyrolyse plastique à l'aide de la méthode des éléments finis dans le but de développer un processus efficace a été explorée et soulignée.

De plus, sachant que la pyrolyse est un processus complexe où différentes physiques et le couplage entre elles jouent un rôle majeur, l'étude approfondie du sous-processus devient une nécessité. Le processus de fusion est un sous-processus de pyrolyse; des modèles pratiques pouvant modéliser la fusion du plastique ont été suggérés dans le premier chapitre (revue de la littérature), tels que la méthode de capacité thermique apparente AHCM (Madruga et al., 2018 ; Murray et Groulx, 2011 ; Samara et al., 2012). De plus, la méthodologie d'exécution de la cinétique de pyrolyse plastique à l'aide d'analyses thermogravimétriques et de méthodes isoconversionnelles telles que Freidman, Kissinger-Akahira-Sunose, Ozawa-Flynn-Wall et Starink a été largement démontrée (Akahira et Sunose, 1971 ; Flynn, 1983 ; Friedman, 1964).

De plus, une revue de la littérature a été effectuée concernant la modélisation et la simulation du processus de pyrolyse à l'échelle de la milli particule et dans des réacteurs à l'échelle du laboratoire ou de l'industrie. Cette littérature a révélé que de nombreuses études ont été réalisées pour modéliser la pyrolyse plastique à l'échelle des particules dans un analyseur thermogravimétrique, mais elle est rarement modélisée sur un matériau en vrac de grande taille (Burden et Faires, 2011 ; Ding et al., 2020 ; Navarro et al., 2012). En outre, certains modèles et équations tels que le modèle de volume de fraction (VOF) peut être utilisés pour modéliser le volume en vrac de la pyrolyse

plastique, à l'aide de la FEM et d'un logiciel conventionnel ; ceux-ci ont été présentés par certaines études traitant de la pyrolyse plastique dans un réacteur à couche mince ou dans la modélisation de processus similaires comme l'ébullition et la condensation (Jin et al., 2019 ; Yan et Che, 2010).

De ce fait, la modélisation de la pyrolyse plastique d'une masse de plastique est encore rarement évoquée dans la littérature. De plus, la modélisation et l'optimisation de réacteurs de pyrolyse plastique efficaces qui seraient appliqués et investis à l'échelle industrielle n'est pas encore terminée. De plus, l'installation expérimentale d'un réacteur de pyrolyse plastique en continu chauffé par un moteur diesel de 8 kW par un précédent travail réalisé à l'IMT-Atlantique (laboratoire GEPEA) n'était pas très performante. Par conséquent, l'objectif de cette thèse était de modéliser et de concevoir un réacteur de pyrolyse plastique continue efficace chauffé par les gaz d'échappement d'un moteur diesel de 8 kW pour les matières plastiques les plus abondantes ; PP et PEHD. Cependant, afin de parvenir à une conception globale du réacteur de pyrolyse en continu, il est recommandé de modéliser et de valider le processus de pyrolyse plastique à l'échelle des particules en utilisant TGA-DCS, puis, dans un réacteur semi-batch à l'échelle du laboratoire (chapitre trois et chapitre quatre). Après cela, les modèles, les équations et les connaissances validés sont utilisés pour modéliser le réacteur continu (chapitre cinq).

Mais avant d'avancer pour démontrer les résultats de cette thèse (Chapitre 3 – Chapitre 5), le deuxième chapitre « Matériaux et méthodes » sera affiché. Le chapitre 2 illustre abondamment la méthodologie et les procédures permettant d'atteindre les objectifs de la thèse ; appréhender et modéliser le procédé de pyrolyse plastique. De plus, les équations et modèles de gouvernance utilisés sont également considérablement expliqués pour faciliter la compréhension de la modélisation. Au début du chapitre, les matériaux utilisés dans cette étude tels que les granulés de PP et les flocons de HDPE sont présentés, où les propriétés thermiques et l'analyse finale des matériaux correspondants sont illustrées. De plus, les équipements utilisés tels que les appareils TGA-DSC et le réacteur semi-batch sont également présentés et la procédure expérimentale menée pour le PP et le HDPE à l'aide de ces instruments est décrite. De plus, le logiciel COMSOL Multiphysics est introduit, en plus des solveurs dynamiques appropriés utilisés dans cette étude tels que le solveur PARDISO pour les systèmes linéaires et la méthode de Newton pour le non-linéaire.

En ce qui concerne la procédure de modélisation et de simulation, tout d'abord, des modèles et des équations de fusion tels que la méthode de capacité thermique apparente AHCM sont présentés dans le but de modéliser le processus de fusion à l'échelle de la milli-particule à l'intérieur du TGA-DSC et à une échelle du réacteur discontinu(semi-batch) de laboratoire. Le modèle de fusion à l'intérieur du TGA-DCS est régi par l'équation de conduction thermique modifiée par la méthode AHCM, où la particule est traitée comme un fluide fixe. Cependant, la modélisation de la fusion à l'intérieur du réacteur semi-batch est réalisée par deux approches : la première, en supposant que le plastique fondu est un fluide stationnaire, en raison de sa viscosité élevée, donc l'équation de conduction thermique modifiée par la méthode AHCM est l'équation dominante. Deuxième approche, l'écoulement de fluide et le transfert de chaleur du plastique fondu sont modélisés en couplant les équations de continuité et de quantité de mouvement avec l'équation d'énergie (modifiée par la méthode AHCM). Par ailleurs, la résistance électrique du réacteur semi-batch est modélisée par deux moyens ; tout d'abord, la puissance enregistrée des éléments chauffants, fonction du temps, est implémentée comme domaine de source de chaleur dans la simulation selon l'effet Joule, c'est-à-dire que la puissance électrique résistive est convertie en puissance thermique. D'autre part, la deuxième façon consiste à imiter le chauffage et le contrôleur réels pour maintenir la température de la paroi du réacteur à une température souhaitée dans la simulation. Toutes les simulations précédentes sont dites validées lorsque l'erreur relative moyenne entre le résultat expérimental et simulé, la température et le bilan énergétique, n'excède pas 10 %.

Passant au processus de craquage, la procédure de détermination des paramètres cinétiques ( $f(x)$ ,  $E$  (J/mol) et  $A$  ( $s^{-1}$ )) et de la vitesse cinétique ( $dx/dt$  ( $s^{-1}$ )) pour le PP et le HDPE est largement illustré. Premièrement, la fonction de modèle cinétique  $f(x)$  est déterminée par la méthode de Criado, qui est une méthode d'ajustement de courbe qui compare les données expérimentales avec les modèles cinétiques théoriques les plus courants trouvés dans la littérature. Ensuite, l'énergie d'activation  $E$  et le facteur pré-exponentiel  $A$  sont trouvés selon les trois méthodes d'isoconversion les plus couramment utilisées ; Friedman (FR), Kissinger-Akahira-Sunose (KAS) et méthode Flynn-Wall-Ozawa (FWO). Enfin, la conversion théorique  $x$  est calculée en fonction du triplet cinétique déterminé et comparée aux données expérimentales dans un souci de validation ; la limite supérieure de l'erreur relative moyenne est fixée à 10 %. Ensuite, le modèle cinétique TGA validé est utilisé pour modéliser le processus de craquage du PP et du HDPE à l'échelle de la milli particule à l'intérieur de l'appareil TGA-DSC. L'équation de conduction thermique avec un terme

de dissipateur thermique est utilisée comme équation déterminante. Alors que la densité de la particule est prise en fonction de la conversion au niveau de chaque maille ou élément, dans le domaine simulé, pour modéliser la perte de masse à l'intérieur du creuset. De plus, l'absorption de chaleur expérimentale et simulée par l'échantillon pyrolysé, fonction du temps, est comparée comme un hommage pour valider le modèle.

De plus, en ce qui concerne la modélisation de la pyrolyse plastique à l'intérieur du réacteur semi-batch, la méthode du champ de phase est couplée aux équations de continuité, de quantité de mouvement et d'énergie pour modéliser l'ensemble du processus de pyrolyse. La méthode du champ de phase vise à modéliser l'écoulement diphasique, c'est-à-dire le plastique fondu et les sous-produits gazeux, et la transition de l'un à l'autre, avec une interface de suivi de surface pour suivre les deux fluides. Un facteur clé de ce modèle est le terme source de masse qui convertit le plastique fondu en sous-produits gazeux selon le modèle de pyrolyse cinétique déduit, qui est multiplié par l'enthalpie de craquage du PP et du HDPE pour modéliser la réaction endothermique à l'intérieur du réacteur. Par ailleurs, un autre terme source massique est utilisé pour modéliser les phénomènes de condensation des sous-produits à l'intérieur du réacteur. Les résultats de température à différents emplacements du réacteur et le taux de fissuration seront comparés aux données expérimentales pour valider le modèle.

Enfin, après validation du modèle de pyrolyse dans le réacteur semi-batch, il est utilisé pour modéliser la pyrolyse plastique dans un réacteur continu dans les mêmes conditions de température (500 °C) et de chauffage (inférieur à 10 °C/min). Le réacteur continu est conçu pour être un échangeur de chaleur multitubes à contre-courant chauffé par les gaz d'échappement, à 500 °C, d'un moteur diesel de 8 kW. Un travail antérieur, réalisé par (Kassargy, 2018) au GEPEA, visait à modéliser analytiquement ce réacteur continu en utilisant la méthode de différence de température moyenne logarithmique (LMTD). Cependant, dans cette étude, le travail se poursuit en modélisant numériquement le réacteur continu par la méthode des éléments finis et selon le modèle et les équations de pyrolyse validés précédents (à l'intérieur du réacteur semi-batch). Presque les mêmes équations directrices, utilisées dans la modélisation de la pyrolyse à l'intérieur du réacteur semi-batch, sont appliquées au côté plastique lors de la modélisation du réacteur continu, sauf que la viscosité dynamique est remplacée par la viscosité apparente selon le modèle Carreau. Néanmoins, le modèle k- $\epsilon$  standard couplé à l'équation d'énergie est appliqué du côté des gaz d'échappement

pour modéliser le transfert de masse et de chaleur lorsque l'écoulement est turbulent. De plus, le réacteur continu est encore optimisé en utilisant une étude de sensibilité pour la géométrie du réacteur (longueur du réacteur et nombre de tubes intérieurs) et le débit massique du plastique.

Dans l'ensemble, les trois prochains chapitres (chapitre 3 – chapitre 5) illustreront les résultats de tous les modèles et simulations proposés. Où le chapitre trois démontrera la simulation et les résultats expérimentaux de la modélisation du processus de fusion du PP et du HDPE à différentes échelles. De plus, le chapitre quatre discutera des résultats de la modélisation de l'ensemble du processus de pyrolyse à l'intérieur du TGA-DSC et du réacteur semi-batch. Enfin, le chapitre cinq illustrera les résultats de la modélisation et de l'optimisation de la conception proposée du réacteur de pyrolyse continue en utilisant le modèle de pyrolyse validé utilisé dans le réacteur semi-continu.

Dans le chapitre trois, une étude DSC est réalisée pour trouver les caractéristiques de fusion (plage de fusion, température de pointe et enthalpie de fusion) et les capacités calorifiques du PP et du HDPE à plusieurs vitesses de chauffage (4 à 10 °C/min). Ensuite, le processus de fusion à l'échelle de la milli-particule pour le PP et le HDPE à l'intérieur de la DSC est modélisé par la méthode de la capacité thermique apparente (AHCM) et l'équation de conduction thermique, en utilisant COMSOL-Multiphysics et la méthode des éléments finis. Les flux de chaleur simulés absorbés par les échantillons de plastique sont comparés et validés avec ceux expérimentaux ; l'erreur relative moyenne maximale parmi tous les résultats n'a pas dépassé 9 %.

Par la suite, l'AHCM est également utilisé pour modéliser le processus de fusion du polypropylène et du polyéthylène haute densité à l'intérieur d'un réacteur semi-batch. Les résultats ont révélé la capacité et la précision élevées de la méthode AHCM dans la modélisation et la simulation des phénomènes de fusion. De plus, le plastique fondu est modélisé comme une masse de fluide au repos et également comme un fluide dynamique, où les deux méthodes (fluide stationnaire et dynamique) montrent les mêmes résultats en raison de la viscosité élevée du plastique fondu à des taux de cisaillement très faibles. De plus, les processus de fusion/solidification et de chauffage/refroidissement du PP et du HDPE sont modélisés et validés à différents taux de chauffage avec 8 % et 4 % d'erreur relative moyenne maximale pour les températures et les bilans énergétiques, respectivement.

Ainsi, après avoir validé les modèles de chauffage et de fusion du PP et du HDPE à l'échelle de la milli particule et du réacteur semi-batch à l'échelle du laboratoire (qui est le chapitre 3), les modèles

sont utilisés comme prérequis pour simuler le processus de fissuration plastique à ces échelles. Cependant, afin de procéder à la modélisation du processus de pyrolyse (Chapitre quatre), une étude cinétique est obligatoire et intervient dans la première étape.

Par conséquent, au début du chapitre quatre, les résultats expérimentaux TGA-DCS pour la pyrolyse du PP et du HDPE à de faibles vitesses de chauffage (4, 6, 8 et 10 °C/min) sont effectués et démontrés. De plus, les caractéristiques de pyrolyse telles que les températures de début, les températures maximales et les enthalpies de craquage sont également déterminées. De plus, un phénomène de pré-fissuration est détecté, par les résultats TGA-DCS, avant le début de la perte de masse pour la pyrolyse du PP et du HDPE.

Ensuite, une étude approfondie de pyrolyse cinétique est réalisée pour déterminer les meilleurs paramètres cinétiques qui modélisent le processus de pyrolyse pour le PP et le HDPE à de faibles vitesses de chauffage (inférieures à 10 °C/min). Les résultats révèlent que les meilleurs paramètres cinétiques qui modélisent la pyrolyse du PP sont le modèle cinétique d'Avrami-Erofe'va (A2) avec une énergie d'activation de 220 (kJ/mol) et un coefficient pré-exponentiel  $A = 4,15 \times 10^{15}$  ( $\text{min}^{-1}$ ) déterminé par la méthode KAS ou FWO. Les valeurs déterminées de l'énergie d'activation pour la pyrolyse du PP se situent dans les plages trouvées dans la littérature, 190 à 230 kJ/mol, cependant, les résultats déterminés pour le coefficient pré-exponentiel sont supérieurs à ceux trouvés dans la littérature,  $1 \times 10^{10}$  à  $1 \times 10^{13}$  (1/min) (Ceamanos et al., 2002 ; Das et Tiwari, 2017 ; Gao et al., 2003). Alors que cela pourrait être causé par la différence entre les vitesses de chauffage appliquées dans cette étude (inférieures à 10 °C/min) et celles trouvées dans la littérature (de 10 à 50 °C/min). Néanmoins, l'erreur relative moyenne entre le modèle cinétique déduit et les résultats TGA expérimentaux n'excédait pas 5 %.

De la même manière, les meilleurs résultats cinétiques déduits pour la pyrolyse du HDPE à faibles vitesses de chauffe (4, 6, 8 et 10 °C/min) sont :  $E = 264$  (kJ/mol) (selon méthode KAS ou FWO), le modèle cinétique  $f(x)$  est également Avrami-Erofe'va (A2), et le facteur pré-exponentiel  $A = 8,3 \times 10^{17}$  (1/min). Alors que l'erreur relative moyenne entre les courbes de conversion théorique et expérimentale est inférieure à 6 %. De plus, la valeur déterminée de l'énergie d'activation du HDPE se situe dans la fourchette (230 à 270 kJ/mol) que l'on retrouve dans la littérature (Ceamanos et al., 2002 ; Das et Tiwari, 2017 ; Gao et al., 2003). Mais le modèle cinétique déduit (A2) est différent de celui trouvé dans la littérature (R2) en raison de la différence des vitesses de chauffe ;

vitesse de chauffage d'environ 10 à 50 °C/min trouvée dans la littérature. De plus, la valeur pré-exponentielle moyenne déduite,  $8,3 \times 10^{17}$  (1/min), diffère des valeurs trouvées dans la littérature, comprises entre  $10^8$  et  $3 \times 10^{17}$  (1/min), car les modèles cinétiques déduits  $f(x)$  sont différents (Ceamanos et al., 2002 ; Das et Tiwari, 2017 ; Gao et al., 2003).

Après cela, les paramètres cinétiques déduits sont implémentés avec les équations et les conditions aux limites appropriées dans le logiciel COMSOL-Multiphysics pour modéliser et simuler l'ensemble du processus de pyrolyse pour le PP et le HDPE à l'intérieur du TGA-DSC à l'échelle de la milli-particule. Le modèle de craquage (TGA) semble fonctionner très bien, comme prévu, avec une erreur relative moyenne parmi toutes les conversions simulées et expérimentales pour la pyrolyse du PP et du HDPE inférieure à 5 %. D'autre part, les résultats de la comparaison DSC, c'est-à-dire la comparaison des résultats de flux de chaleur simulés avec ceux expérimentaux, sont améliorés par la modélisation du phénomène de fissuration latente (pré-fissuration), qui se produit avant et parallèlement à la fissuration en masse. Ainsi, l'erreur relative moyenne passe de 20 % à moins de 8 % en modifiant la capacité calorifique pour le PP et le HDPE. Enfin, les résultats simulés sont en très bon accord avec les résultats expérimentaux pour la modélisation du PP et du HDPE à l'échelle de la milli-particule à l'intérieur d'un TGA-DSC ; l'erreur relative moyenne maximale ne dépassait pas 8 %.

Enfin et surtout, après la modélisation du processus de pyrolyse à l'échelle des milli particules, le processus de pyrolyse pour le PP et le HDPE est modélisé à l'échelle du laboratoire dans un réacteur semi-batch à la même plage de vitesse de chauffage (inférieure à 10 °C/min). Comme le montrent les résultats, le processus de pyrolyse à l'intérieur du réacteur semi-continu comporte deux étapes progressives différentes ; La première étape est l'état transitoire, où il existe un processus de condensation des sous-produits vapeur à l'intérieur du réacteur semi-continu car la partie supérieure du réacteur est encore froide et en cours de réchauffement. Dans cette étape, la condensation des vapeurs de sous-produits à l'intérieur du réacteur (surtout en partie haute) joue un grand rôle pour faire recirculer et recraquer (craquage secondaire) les sous-produits et les empêcher de sortir du réacteur. Par contre, la deuxième étape est le régime permanent où le processus de condensation à l'intérieur du réacteur est très faible en raison de l'élévation de la température de la partie supérieure du réacteur (plus de 130 °C).

Après avoir illustré et analysé brièvement les résultats expérimentaux, le processus de pyrolyse pour le PP et le HDPE est modélisé à l'intérieur du réacteur semi-batch en utilisant le modèle cinétique déduit (de la section 4.2) et un modèle d'écoulement à deux phases (modèle de champ de phase intégré dans COMSOL-Multiphysics) pour simuler l'écoulement fluide du plastique fondu et de ses vapeurs de sous-produits de pyrolyse. Dans un souci de simplicité et pour notifier l'influence du processus de condensation sur les résultats de simulation, deux approches de simulation sont réalisées. La première approche consiste à simuler le processus de pyrolyse sans prendre en compte le phénomène de condensation, tandis que la seconde modélise le processus de condensation avec celui de pyrolyse. Les résultats révèlent que le modèle est validé par les résultats expérimentaux (la perte de hauteur de lit à l'intérieur du réacteur) pour la première approche de simulation en phase stationnaire (c'est-à-dire sans condensation). Alors que la vitesse idéale (sans condensation) de la perte de lit du réacteur déterminée à partir de la simulation est presque la même que celle expérimentale à la phase d'équilibre pour le PP et le HDPE. De plus, l'erreur relative moyenne maximale parmi les résultats ne dépassait pas 9 %. Par conséquent, le processus de pyrolyse pour le PP et le HDPE à l'intérieur du réacteur semi-batch est modélisé et validé avec succès par les résultats expérimentaux pour l'étape d'état stationnaire du processus, c'est-à-dire sans présence de condensation.

D'autre part, les résultats de la perte de lit à la période d'état transitoire doivent être encore améliorés en modélisant le processus de condensation des vapeurs pyrolytiques à l'intérieur du réacteur. Ainsi, la condensation à l'intérieur du réacteur est modélisée par deux moyens ; La première est la voie naturelle, en attribuant plusieurs températures de condensation à la vapeur de sous-produit pour modéliser la condensation à différents niveaux de température. D'autre part, la deuxième méthode consiste à imposer un reflux de condensation forcé dans la simulation pour contrôler la chute de lit simulée à l'état transitoire pour qu'elle soit la même que celle expérimentale. Cependant, plusieurs difficultés empêchent le succès total pour aucune des méthodes. Mais sachant que, lors de la modélisation du réacteur continu final, le processus de condensation est considéré comme négligeable en raison du type de réacteur, réacteur à tubes de fumée à contre-courant, c'est-à-dire que le plastique monte strictement en température au fur et à mesure qu'il progresse à l'intérieur du réacteur (**Figure 2-17**). Ainsi, le modèle de pyrolyse validé pour le PP et le HDPE dans un réacteur semi-batch à l'échelle du laboratoire en phase stationnaire est suffisant et constitue un très bon prérequis pour la modélisation du réacteur continu.

Enfin, tous les modèles et connaissances validés précédents (Chapitre 2 – Chapitre 4) sont utilisés pour concevoir le réacteur de pyrolyse continue ayant une longueur maximale de 1,5 à 2 m et un diamètre extérieur ( $D$ ) inférieur à 60 cm ; Qui est le contenu du chapitre cinq. Premièrement, le modèle suggéré de travaux antérieurs (Kassargy, 2018) qui est un réacteur de pyrolyse continue multitubes à contre-courant (les gaz chauds passent à l'intérieur de ces tubes), est utilisé pour lancer les études paramétriques en régime permanent pour différents nombres de tubes variant de 4 à 200 Tubes, diamètre du tube  $d$  passant de 0,7 à 1,4 cm, et débit massique de plastique décroissant par rapport à la valeur maximale (19 kg/h). Par conséquent, après analyse des résultats et prise en considération des critères généraux de conception souhaités (longueur de 1,5 m et  $D$  extérieur minimum ou en d'autres termes nombre minimum de tubes ( $N$ )), en plus de la conversion de pyrolyse de sortie la plus élevée  $x_{out}$ , et à la plus haute puissance totale transférée  $Q_t$ , le meilleur modèle est déduit ( $N = 100$  tubes,  $d = 1,4$  cm,  $\dot{m}_p = 7$  kg/h,  $L = 1,5$  m et  $D = 35,6$  cm).

Par ailleurs, une étude transitoire a été réalisée sur le meilleur modèle déduit pour vérifier la faisabilité du réacteur en phase de démarrage. De ce fait, il est recommandé d'augmenter le débit massique plastique de 1 à 7 kg/h en deux heures pour le modèle proposé, ce qui est un délai pratique et raisonnable.

Enfin, et somme toute, l'objectif optimal de cette thèse est atteint avec succès en concevant et modélisant un réacteur de pyrolyse plastique continue efficace (pour PP et HDPE) chauffé par les gaz d'échappement de 8 kW diesel. Où ce réacteur peut être étudié plus avant et modélisé en tant que modèle 3D. De plus, ce réacteur peut être construit à des fins d'expérimentation (validation) et d'amélioration. De plus, le modèle peut être utilisé pour différents types de plastiques comme le PS et le PVC, après avoir établi les études cinétiques de ces types de plastiques. Néanmoins, le procédé d'alimentation et d'injection du plastique devrait être bien conçu à l'avenir, en plus de l'étude de son effet sur le coefficient de transfert thermique par convection. De plus, le coefficient de transfert de chaleur par convection lors de la phase de craquage doit être étudié plus avant. Enfin, ce modèle est une première étape dans la modélisation de la pyrolyse plastique dans un réacteur continu dans un souci de conception et d'application industrielles, qui nécessite une mise à niveau et une amélioration supplémentaires.

## Table of Contents

|  |    |
|--|----|
| <b>List of Figures</b> .....                                   | 20 |
| <b>List of Tables</b> .....                                    | 28 |
| <b>Nomenclature</b> .....                                      | 30 |
| <b>Introduction</b> .....                                      | 38 |
| <b>Chapter 1 Bibliography</b> .....                            | 42 |
| 1.1 Plastic wastes accumulation.....                           | 42 |
| 1.2 Plastic pyrolysis process .....                            | 43 |
| 1.3 Plastic pyrolysis application and technology .....         | 44 |
| 1.4 Feedstock and operating parameters.....                    | 49 |
| 1.4.1 Type of feedstock.....                                   | 50 |
| 1.4.2 Temperature of degradation.....                          | 51 |
| 1.4.3 Heating rate and residence time.....                     | 52 |
| 1.4.4 Catalyst .....   | 53 |
| 1.5 Type of the reactor .....                                  | 54 |
| 1.5.1 Batch and semi-batch reactors .....                      | 54 |
| 1.5.2 Fixed bed, fluidized bed, and rotary kiln reactors ..... | 55 |
| 1.6 Importance of simulation using Finite Element Method ..... | 58 |
| 1.7 Melting models and equations .....                         | 60 |
| 1.8 Newtonian and non-Newtonian fluids .....                   | 64 |
| 1.9 Plastic pyrolysis kinetics.....                            | 68 |
| 1.10 Plastic pyrolysis modelling using FEM .....               | 76 |
| 1.11 Conclusion .....  | 81 |
| <b>Chapter 2 Materials and Methods</b> .....                   | 83 |
| 2.1 Materials and equipment.....                               | 83 |

## Table of Contents

---

|  |            |
|--|------------|
| 2.1.1 Raw materials.....   | 83         |
| 2.1.2 Thermogravimetric analysis.....  | 85         |
| 2.1.3 Differential Scanning Calorimetry.....                                 | 88         |
| 2.2 Semi-batch reactor .....   | 89         |
| 2.2.1 Description of the semi-batch reactor .....                            | 89         |
| 2.2.2 Procedure of pyrolysis process in the semi-batch reactor.....          | 91         |
| 2.3 COMSOL Multiphysics software .....                                       | 93         |
| 2.4 Procedure of modelling melting process and sensible heat .....           | 94         |
| 2.4.1 Milli-particle scale modeling of melting process for PP and HDPE ..... | 94         |
| 2.4.2 Modeling sensible heat transfer in the semi-batch reactor.....         | 99         |
| 2.4.3 Modeling melting process in the semi-batch reactor .....               | 104        |
| 2.5 Procedure of modeling the cracking process .....                         | 105        |
| 2.5.1 Kinetic rate for PP and HDPE pyrolysis.....                            | 105        |
| 2.5.2 Milli-particle scale modeling of PP and HDPE pyrolysis .....           | 108        |
| 2.5.3 Modelling PP and HDPE pyrolysis in a semi-batch reactor .....          | 110        |
| 2.6 Modelling continuous pyrolysis reactor.....                              | 116        |
| 2.7 . Conclusions.....   | 120        |
| <b>Chapter 3 Modelling of melting process for PP and HDPE.....</b>           | <b>123</b> |
| 3.1 Experimental DSC results for PP and HDPE .....                           | 123        |
| 3.2 Modelling melting process for PP and HDPE at a milli-particle scale..... | 127        |
| 3.3 Modelling sensible heat transfer within the semi-batch reactor .....     | 131        |
| 3.3.1 Empty reactor.....   | 133        |
| 3.3.2 Loaded reactor .....   | 142        |
| 3.4 Melting process for PP and HDPE inside the semi-batch reactor .....      | 151        |
| 3.4.1 Ice melting .....  | 151        |

## Table of Contents

---

|   |            |
|---|------------|
| 3.4.2 PP melting .....  | 152        |
| 3.4.3 HDPE melting.....   | 158        |
| 3.4.4 Numerical results of melting in literature .....  | 159        |
| 3.5 Conclusions.....  | 161        |
| <b>Chapter 4 Modelling and validating pyrolysis process for PP and HDPE.....</b>                      | <b>163</b> |
| 4.1 TGA-DSC results for PP and HDPE pyrolysis.....  | 163        |
| 4.2 Pyrolysis kinetic study for PP and HDPE.....  | 169        |
| 4.2.1 PP kinetic results.....   | 169        |
| 4.2.2 HDPE kinetic results.....   | 176        |
| 4.3 Results of modelling plastic pyrolysis for PP and HDPE at milli-particle scale .....              | 177        |
| 4.3.1 HDPE simulation results: pyrolysis at milli-particle scale .....                                | 178        |
| 4.3.2 PP simulation results: pyrolysis at milli-particle scale .....                                  | 183        |
| 4.4 Results of modelling PP and HDPE pyrolysis inside a laboratory-scale semi-batch reactor .....     | 185        |
| 4.4.1 PP and HDPE experimental results: pyrolysis in semi-batch reactor .....                         | 186        |
| 4.4.2 PP and HDPE simulation results using COMSOL-Multiphysics: pyrolysis in semi-batch reactor ..... | 192        |
| 4.5 Conclusions.....  | 207        |
| <b>Chapter 5 Modelling continuous plastic pyrolysis reactor .....</b>                                 | <b>210</b> |
| 5.1 Description of the reactor and the objectives.....  | 210        |
| 5.2 The original continuous reactor installation .....  | 214        |
| 5.3 Checking the previous suggested geometry of the continuous reactor.....                           | 220        |
| 5.4 Optimization of the continuous plastic pyrolysis reactor .....                                    | 225        |
| 5.4.1 Parametric study for 2 m long reactor with maximum plastic flow rate .....                      | 225        |
| 5.4.2 Parametric study for the best selected models at 1.5 m length reactor .....                     | 235        |
| 5.5 Transient simulation results of the best models.....  | 237        |

## Table of Contents

---

|                                  |     |
|----------------------------------|-----|
| 5.6 Conclusions.....             | 225 |
| <b>General conclusions</b> ..... | 245 |
| <b>Perspectives</b> .....        | 250 |
| <b>References</b> .....          | 252 |
| <b>Appendix: A</b> .....         | 266 |

## List of Figures

|   |     |
|---|-----|
| <b>Figure 1-1:</b> Polymerization of ethylene monomer to form a polyethylene chain.....   | 42  |
| <b>Figure 1-2:</b> Schematic representation of fluidized bed reactor.....   | 56  |
| <b>Figure 1-3:</b> Conical spouted reactor (a), and screw kiln reactor (b).....   | 57  |
| <b>Figure 1-4:</b> Conversion function $f_1$ used in AHCM built-in COMSOL.....  | 64  |
| <b>Figure 1-5:</b> Shear stress versus rate of strain for time-independent non-Newtonian fluids. ....   | 65  |
| <b>Figure 1-6:</b> Variation of apparent viscosity with respect to strain rate according to Carreau model.<br>.....                                   | 68  |
| <b>Figure 2-1:</b> PP virgin granules.....  | 84  |
| <b>Figure 2-2:</b> Preparing HDPE flakes from plastic waste containers. ....  | 84  |
| <b>Figure 2-3:</b> SETSYS Thermogravimetric analyzer. ....  | 86  |
| <b>Figure 2-4:</b> TGA-DSC sample and reference crucibles.....  | 87  |
| <b>Figure 2-5:</b> (a) TG curve and (b) DTG curve for HDPE thermal pyrolysis at $10\text{ }^\circ\text{C}\cdot\text{min}^{-1}$ .....                  | 88  |
| <b>Figure 2-6:</b> Heat flow versus temperature, DSC curve for HDPE thermal pyrolysis at $\beta = 10\text{ }^\circ\text{C}\cdot\text{min}^{-1}$ ..... | 89  |
| <b>Figure 2-7:</b> (a) Schematic diagram, units are in cm, and (b) real image of the semi-batch reactor.<br>.....                                     | 90  |
| <b>Figure 2-8:</b> SV-10 vibration viscometer of the AND brand.....   | 92  |
| <b>Figure 2-9:</b> Heat flow versus temperature of HDPE melting and heating at $\beta = 10\text{ }^\circ\text{C}\cdot\text{min}^{-1}$ .....           | 95  |
| <b>Figure 2-10:</b> (a) Real crucible image of the DSC/TGA analyzer, (b) 2D-axisymmetric crucible<br>model.....                                       | 97  |
| <b>Figure 2-11:</b> Conversion function $f_l$ used in AHCM built-in COMSOL.....   | 98  |
| <b>Figure 2-12:</b> 2-D axisymmetric draw with Boundary conditions for the batch reactor.....   | 100 |
| <b>Figure 2-13:</b> Type of flow depending on Rayleigh number. ....   | 101 |

## List of Figures

---

|   |     |
|---|-----|
| <b>Figure 2-14:</b> 2D-axisymmetry model for the reactor filled with sand with the plugged temperature location.....                        | 103 |
| <b>Figure 2-15:</b> Density versus conversion $x$ for HDPE used to model the mass loss in simulation. ....                                  | 109 |
| <b>Figure 2-16:</b> Schematic diagram of the designed continuous pyrolysis reactor heated by exhaust gases of 8 kW diesel engine.....       | 116 |
| <b>Figure 2-17:</b> Geometry and boundary conditions results of the continuous pyrolysis reactor designed analytically by LMTD method. .... | 117 |
| <b>Figure 3-1 :</b> DSC experiments for PP ( $18 \pm 0.5$ mg) and different heating rates. ....   | 124 |
| <b>Figure 3-2 :</b> DSC experiments for HDPE ( $18 \pm 1$ mg) and different heating rates. ....   | 124 |
| <b>Figure 3-3 :</b> Deduced heat capacities, function of temperature, for PP and HDPE.....  | 126 |
| <b>Figure 3-4 :</b> (a) Mesh display, (b) 2D-axisymmetric crucible model. ....  | 128 |
| <b>Figure 3-5 :</b> Experimental and simulated results for PP melting and heating by $\beta = 4$ °C/min. ....                               | 129 |
| <b>Figure 3-6 :</b> Experimental and simulated results for PP melting and heating by $\beta = 10$ °C/min. ....                              | 129 |
| <b>Figure 3-7 :</b> Experimental and simulated results for HDPE melting and heating by $\beta = 4$ °C/min. ....                             | 130 |
| <b>Figure 3-8 :</b> Experimental and simulated results for HDPE melting and heating by $\beta = 10$ °C/min. ....                            | 130 |
| <b>Figure 3-9 :</b> Extremely fined mesh used in all of the simulations. ....   | 133 |
| <b>Figure 3-10 :</b> 2D-axisymmetry simulation for the empty reactor heated using 450 W load, at $t = 3000$ s.....                          | 134 |
| <b>Figure 3-11 :</b> Temperature comparison, T2_wall and T4_top, for empty reactor heated at 450 W load, T2 regulated at 490°C. ....        | 135 |
| <b>Figure 3-12 :</b> Temperature comparison, T3_bottom and T5_insulator for empty reactor heated at 450 W load, T2 regulated at 490°C. .... | 136 |

## List of Figures

---

|   |     |
|---|-----|
| <b>Figure 3-13</b> : Parity plot for T2_wall and T3_bottom for empty reactor experiment, heated using 450 W heating load. ....  | 137 |
| <b>Figure 3-14</b> : Parity plot for T4_top and T5_insulator for empty reactor experiment, heated using 450 W heating load. ....  | 137 |
| <b>Figure 3-15</b> : Temperature comparison, T2_wall and T4_top, for empty reactor heated at 450 W load with simulation heat controller, T2 regulated at 490°C. ....  | 139 |
| <b>Figure 3-16</b> : Temperature comparison, T3_bottom and T5_insulator for empty reactor heated at 450 W load with simulation heat controller, T2 regulated at 490°C. ....   | 140 |
| <b>Figure 3-17</b> : Experimental power and simulated power according to the two approaches (power implementation and controller simulation, respectively) for the same experiment (heating empty reactor till 490 °C by 450 W). .... | 141 |
| <b>Figure 3-18</b> : 2D-axisymmetry simulation for the reactor filled with sand with simulated heat controller, heated using 450 W load, at t = 6000 s. ....  | 144 |
| <b>Figure 3-19</b> : Temperature comparison, T1, T2, and T4, for reactor filled with sand, heated using 450 W load with simulated heat controller. ....   | 145 |
| <b>Figure 3-20</b> : Temperature comparison, T3_bottom and T5_insulator, for reactor filled with sand, heated using 450 W load with simulated heat controller. ....   | 145 |
| <b>Figure 3-21</b> : Surface velocity and temperature profiles for the reactor filled with oil, 450 W, at t = 350 s. ....   | 147 |
| <b>Figure 3-22</b> : Surface velocity and temperature profiles for the reactor filled with oil, 450 W, at t = 1700 s. ....  | 148 |
| <b>Figure 3-23</b> : Temperature comparison, T1_oil, T2_wall, and T4_top, for reactor filled with oil, heated using 450 W with simulated heat controller. ....  | 149 |
| <b>Figure 3-24</b> : 3-D simulation result for reactor filled with water and heated by 150 W load. ..   | 150 |
| <b>Figure 3-25</b> : Wall temperature T2 and water temperature T1 for a batch reactor filled with water and heated by 150 W load with simulated heat controller. ....   | 150 |

**Figure 3-26** : Temperature comparison, T1\_ice/water and T4\_top, ice melting inside the batch reactor without heating. .... 152

**Figure 3-27** : Temperature comparison, T1\_PP, T2\_wall, and T4\_top, for melting and cooling PP, heated using 300 W load by direct implementation of  $q_{exp}(t)$  , set point 190°C..... 153

**Figure 3-28** : Parity plot for T1\_PP, T2\_wall, for melting and cooling PP, heated using 300 W load by direct implementation of  $q_{exp}(t)$ , set point 190°C..... 154

**Figure 3-29** : Parity plot for T4\_top, for melting and cooling PP, heated using 300 W load by direct implementation of  $q_{exp}(t)$  , set point 190°C. .... 154

**Figure 3-30** : Surface conversion and temperature profiles for melting PP considering the fluid flow approach, 450 W, at t = 560 s. .... 156

**Figure 3-31** : (a) Surface velocity and (b) temperature profiles for melting PP considering the fluid flow approach, 450 W, at t = 560 s. .... 156

**Figure 3-32** : Temperature comparison, T1, T2, and T4, for PP melting and heating by 450 W with direct implementation of  $q_{exp}(t)$ . .... 157

**Figure 3-33** : Temperature comparison, T1, T2, and T4, for HDPE melting and heating by 600 W, with direct implementation of  $q_{exp}(t)$ . .... 159

**Figure 4-1** : Mass versus temperature for PP pyrolysis at different heating rates. .... 164

**Figure 4-2** : Absorbed heat flow (by the sample) versus temperature for PP pyrolysis (melting and cracking) at different heating rates. .... 165

**Figure 4-3** : Mass versus temperature for HDPE pyrolysis at different heating rates. .... 165

**Figure 4-4** : Absorbed heat flow (by the sample) versus temperature for HDPE pyrolysis (melting and cracking) at different heating rates..... 166

**Figure 4-5** : PP pyrolysis heat flow just before the cracking phase starts at different heating rates. .... 167

**Figure 4-6** : Pre-cracking phase for HDPE pyrolysis at different heating rates. .... 167

**Figure 4-7** : Theoretical master plots for different reaction models compared with the experimental data for PP pyrolysis at different heating rates. .... 170

**Figure 4-8** : Coefficient of determination R2 versus heating rates, for PP pyrolysis, for different reaction models. .... 171

**Figure 4-9** : Plotting  $\ln(dx/dt)$  w.r.t.  $1/T$  at each conversion for PP pyrolysis at heating rates (4, 6, 8, 10 °C/min) according to FR method. .... 172

**Figure 4-10** : Plotting  $\ln(\beta T^2)$  w.r.t.  $1/T$  at each conversion for PP pyrolysis at heating rates (4, 6, 8, 10 K/min) according to KAS method. .... 173

**Figure 4-11** : Plotting  $\ln(\beta)$  w.r.t.  $1/T$  at each conversion for PP pyrolysis at heating rates (4, 6, 8, 10 K/min) according to FWO method. .... 173

**Figure 4-12** : Theoretical and experimental conversions for PP pyrolysis, at heating rate 4 °C/min, according to the best chosen kinetic models (R3, and A2). .... 175

**Figure 4-13** : Theoretical and experimental conversions for PP pyrolysis for four heating rates (4, 6, 8, and 10 °C/min), according to the best deduced kinetic parameters ( $E = 220$  (kJ/mol),  $f(x)$  is A2, and  $A = 4.15E+15$  (1/min)). .... 176

**Figure 4-14** : Theoretical and experimental conversions for HDPE pyrolysis at four heating rates (4, 6, 8, and 10 °C/min), according to best deduced kinetic parameters ( $E = 264$  (kJ/mol),  $f(x)$  is A2, and  $A = 8.3E+17$  (1/min)). .... 177

**Figure 4-15** : Simulated and experimental conversion results for HDPE pyrolysis inside TGA-DSC, heating rate  $\beta_3 = 8$  °C/min. .... 179

**Figure 4-16** : Simulated and experimental heat flow results for HDPE pyrolysis inside TGA-DSC, heating rate  $\beta_3 = 8$  °C/min. .... 179

**Figure 4-17** : Heat flow for HDPE pyrolysis, at different heating rates, illustrating the latent cracking phenomena before the mass loss cracking. .... 180

**Figure 4-18** : Heat capacity w.r.t. temperature for HDPE used to model the latent cracking for HDPE pyrolysis at heating rates below 10 °C/min. .... 181

**Figure 4-19** : Heat flow comparison for HDPE pyrolysis at 8 °C/min inside TGA-DSC according to the new enhanced model, latent cracking modelling. .... 182

**Figure 4-20** : Simulated and experimental results for HDPE pyrolysis at heating rate  $\beta_1 = 4$  °C/min. .... 183

## List of Figures

---

|   |     |
|---|-----|
| <b>Figure 4-21</b> : Heat capacity w.r.t. temperature for PP used to model the latent cracking for PP pyrolysis at heating rates below 10 °C/min. ....  | 183 |
| <b>Figure 4-22</b> : Simulated and experimental results for PP pyrolysis at heating rate $\beta_1 = 4$ °C/min. ....   | 184 |
| <b>Figure 4-23</b> : Temperature results of 400 g PP pyrolysis inside the semi-batch reactor of 600 W average heating power. ....   | 187 |
| <b>Figure 4-24</b> : Heater power versus time for PP pyrolysis experiment (400 g) inside the semi-batch reactor heated by 600 W average heating power. ....   | 188 |
| <b>Figure 4-25</b> : Mass of the oil by-product (at the outlet) vs time of 400 g PP pyrolysis inside the semi-batch reactor of 600 W average heating power.....   | 189 |
| <b>Figure 4-26</b> : Temperature results of 400 g PP pyrolysis inside the semi-batch reactor of 750 W average heating power. ....   | 190 |
| <b>Figure 4-27</b> : Mass of the oil by-product (at the outlet) vs time of 400 g PP pyrolysis inside the semi-batch reactor of 750 W average heating power.....   | 191 |
| <b>Figure 4-28</b> : Simulated results, surface temperature and pyrolysis conversion for PP pyrolysis at 600 W heating power, without modelling the condensation process.....   | 194 |
| <b>Figure 4-29</b> : Simulated results, Temperature profiles ( $T_1$ , $T_2$ , and $T_4$ ), for PP pyrolysis at 600 W heating power, without modelling the condensation process. ....   | 196 |
| <b>Figure 4-30</b> : Bed loss comparison between the simulated and experimental results for PP pyrolysis at 600 W heating power, without modelling the condensation process. ....   | 197 |
| <b>Figure 4-31</b> : Bed loss comparison between the simulated and experimental results for PP pyrolysis at 750 W heating power, without modelling the condensation process. ....   | 198 |
| <b>Figure 4-32</b> : Bed loss comparison between the simulated and experimental results for PP pyrolysis at 600 W heating power, without condensation, with modelling the condensation process ( $T_{\text{cond}} = 300$ °C and $\Delta h_{\text{cond}} = 350$ kJ/kg), and with modelling the condensation (2) process ( $T_{\text{cond1}} = 100$ °C, $T_{\text{cond2}} = 200$ °C, and $T_{\text{cond3}} = 300$ °C and $\Delta h_{\text{cond}} = 350$ kJ/kg)..... | 200 |
| <b>Figure 4-33</b> : Mass source of cracking and condensation for PP pyrolysis at 600 W heating power, with condensation model of six temperatures ((100 °C, 50, 350 °C) and $\Delta h_{\text{cond}} = 350$ kJ/kg). .   | 201 |

## List of Figures

---

|   |     |
|---|-----|
| <b>Figure 4-34</b> : Surface temperature result for PP pyrolysis at 600 W heating power, with condensation model of six temperatures ((100 °C, 50, 350 °C) and $\Delta h_{\text{cond}} = 350$ kJ/kg).....   | 202 |
| <b>Figure 4-35</b> : Mass source of cracking and condensation for PP pyrolysis at 600 W heating power, with a forced condensation reflux.....   | 203 |
| <b>Figure 4-36</b> : Bed loss comparison between the simulated and experimental results for PP pyrolysis at 600 W heating power, with forced condensation reflux. ....  | 204 |
| <b>Figure 4-37</b> : Temperature results for PP pyrolysis at 600 W heating power, with forced condensation reflux.....  | 205 |
| <b>Figure 4-38</b> : Surface profile results (melting conversion and temperature) for PP pyrolysis at 600 W heating power, with forced condensation reflux.....   | 206 |
| <b>Figure 5-1</b> : Triangular (a) and rectangular (b) formations of the inner tubes.....   | 211 |
| <b>Figure 5-2</b> : A 3D preview of the continuous reactor according to the triangular formation....  | 212 |
| <b>Figure 5-3</b> : Representative system (isolated concentric tube) of the continuous reactor. ....  | 213 |
| <b>Figure 5-4</b> : 14.7 kW two-cylinder Lister Petter diesel engine with an electrical generator MECCALTE ET20F-200 type.....  | 214 |
| <b>Figure 5-5</b> : Screw kiln counter-flow concentric tube continuous plastic pyrolysis reactor, first installation.....   | 215 |
| <b>Figure 5-6</b> : 2D-axisymmetric scheme model of the original continuous plastic pyrolysis reactor with the boundary conditions.....   | 217 |
| <b>Figure 5-7</b> : Surface simulation results (melting , cracking and temperature) for the original configuration of the continuous reactor at steady state, with plastic mass flow rate of 200 g/h. 219   |     |
| <b>Figure 5-8</b> : 2D-axisymmetric scheme of the representative single concentric tube of the continuous plastic pyrolysis reactor, with the proposed geometry and boundary conditions as Kassargy suggested.....  | 222 |
| <b>Figure 5-9</b> : Simulation results (temperatures and conversions) for the continuous pyrolysis reactor according to Kassargy model and geometry (1 m length and 34 tubes of diameter 0.6 cm with pitch length of 1.8 cm, and $mp, \text{max} = 19$ kg/h)..... | 223 |

**Figure 5-10** : Maximum heating rate of plastic evaluated at the interface wall between hot exhaust gas and plastic, for PP continuous pyrolysis according to Kassary suggested dimensions..... 224

**Figure 5-11** : Steady state parametric study results (total heat transfer and outlet conversion), varying N from 30 to 200 tubes and d from 0.7 to 1.4 cm..... 231

**Figure 5-12** : Moody chart, friction coefficient in pipes versus the Reynold's number and the relative pipe roughness. .... 232

**Figure 5-13** : Steady state parametric study results (total heat transfer and outlet conversion), varying N from 4 to 45 tubes and d from 0.7 to 1.4 cm..... 233

**Figure 5-14** : Average simulation results (temperatures and conversions) for the best model of the continuous pyrolysis reactor (1.5 m length and 100 tubes, d = 1.4 cm, plastic (PP) mass flow rate 7 kg/h). .... 236

**Figure 5-15** : Average heating rate of plastic with respect to the length of the reactor, for the best model of the continuous pyrolysis reactor (1.5 m length and 100 tubes, d = 1.4 cm, plastic (PP) mass flow rate 7 kg/h)..... 237

**Figure 5-16** : Average Transient simulation results (plastic cracking and heating rate) over time at L = 148 cm, for the best deduced model (N = 100, d = 1.4 cm, and L = 1.5 m), simulation for fully loaded reactor (with plastic) with total mass flow rate of plastic (7 kg/h) and heated from ambient temperature (20 °C)..... 239

**Figure 5-17** : Simulated conversion and designing conversion comparison at L = 148 cm of the transient study for the best deduced model, fully loaded reactor (with plastic) with 7 kg/h mass flow rate and heated from ambient temperature (20 °C). .... 240

**Figure 5-18** : Average transient simulation results (temperatures, and plastic conversions) with respect to length of the reactor at t = 8100 s (i.e. at t = 2.25 hours), for the best deduced model (N =100, d = 1.4 cm, and L = 1.5 m) with fully loaded reactor and total plastic flow rate 7 kg/h, heated from ambient temperature 20 °C. .... 241

**Figure 5-19** : Average transient simulation (using the two phase flow model) results, temperatures, and plastic conversions, with respect to length of the reactor at t = 8100 s (i.e. at t = 2.25 hours), for the best deduced model (N = 100, d = 1.4 cm, and L = 1.5 m) with fully loaded reactor (with plastic) and total plastic flow rate 7 kg/h, heated from ambient temperature 20 °C..... 242

## List of Tables

|  |     |
|--|-----|
| <b>Table 1-1:</b> Selected plastic pyrolysis plants in Europe and in North-America.....  | 49  |
| <b>Table 1-2:</b> Proximate analysis for polyolefin, PP and PE.....  | 50  |
| <b>Table 1-3:</b> Typical values of power-law parameters for different molten polymers. ....   | 66  |
| <b>Table 1-4:</b> Reaction model for the most common reaction mechanism. ....  | 70  |
| <b>Table 1-5:</b> Kinetic parameters for LDPE, HDPE, and PP pyrolysis determined according to the conventional isoconversional methods at seven heating rates, 5, 10, 15, 20, 30, 40, 50 K/min...    | 74  |
| <b>Table 1-6:</b> Kinetic parameters reported in literature for LDPE, HDPE, and PP using various isoconversional methods.....  | 75  |
| <b>Table 2-1:</b> Thermophysical properties for PP and HDPE at temperature range 20 – 500 °C.....  | 85  |
| <b>Table 2-2:</b> Ultimate analysis and calorific values for PE and PP. ....   | 85  |
| <b>Table 2-3:</b> Thermophysical properties for the semi-batch reactor material with the range of 25-500°C. ....   | 90  |
| <b>Table 2-4:</b> Average thermophysical properties for sand and sunflower oil with the range of 25-500°C. ....  | 91  |
| <b>Table 2-5:</b> Dynamic viscosity of sunflower oil.....  | 92  |
| <b>Table 2-6:</b> Reaction model for the most common reaction mechanism (Aboulkas <i>et al.</i> , 2010). ....  | 106 |
| <b>Table 2-7:</b> Average thermophysical properties of the gaseous hydrocarbon byproducts C <sub>7</sub> till C <sub>24</sub> compared with air (Cheméo, 2021; PubChem, 2021; Vargaftik, 1975). .... | 112 |
| <b>Table 3-1 :</b> Melting characteristics for PP and HDPE at different heating rates. ....  | 127 |
| <b>Table 3-2 :</b> Temperature and energy relative errors for all of the heating and melting experiments using the batch reactor. ....   | 161 |
| <b>Table 4-1 :</b> Characteristic temperatures and specific cracking enthalpies of PP and HDPE pyrolysis.....  | 169 |

## List of Tables

---

|  |     |
|--|-----|
| <b>Table 4-2</b> : Average deduced kinetic parameters ( $f(x)$ , $E$ , and $A$ ) for PP pyrolysis at heating rates below $10\text{ }^{\circ}\text{C}/\text{min}$ . .....   | 174 |
| <b>Table 4-3</b> : Mass loss enthalpies and deduced latent cracking enthalpies. ....   | 185 |
| <b>Table 4-4</b> : Average thermo-physical properties of the pyrolytic vapor.....  | 193 |
| <b>Table 5-1</b> : Thermo-physical properties of air at average temperature $325\text{ }^{\circ}\text{C}$ . ....   | 211 |
| <b>Table 5-2</b> : Steady state parametric study for the counter-flow multi-tubes continuous plastic pyrolysis reactor, having 2 m length, inner tube diameter $d$ of 0.7 cm, and 19 kg/h mass flow rate of PP.....                                      | 228 |
| <b>Table 5-3</b> : Steady state parametric study for the counter-flow multi-tubes continuous plastic pyrolysis reactor, having 2 m length, inner tube diameter $d$ of 1 cm, and 19 kg/h mass flow rate of PP. ....                                       | 229 |
| <b>Table 5-4</b> : Steady state parametric study for the counter-flow multi-tubes continuous plastic pyrolysis reactor, having 2 m length, inner tube diameter $d$ of 1.4 cm, and 19 kg/h mass flow rate of PP.....                                      | 230 |
| <b>Table 5-5</b> : Steady state turbulent parametric study for the counter-flow multi-tubes continuous plastic pyrolysis reactor, having 2 m length, inner tube diameter $d$ , and 19 kg/h mass flow rate of PP. ....                                    | 234 |
| <b>Table 5-6</b> : Steady state parametric study for the counter-flow multi-tubes continuous plastic pyrolysis reactor, having 1.5 m length, tube diameter $d = 1.4\text{ cm}$ , and <i>mp, max</i> decreasing with 5 % increment for PP pyrolysis. .... | 235 |

## Nomenclature

### Variables

|                    |  |                      |
|--------------------|--|----------------------|
| $A$                | Pre-exponential factor                                   | $[s^{-1}]$           |
| $C$                | Mushy region constant                                    | $[N.s.m^{-4}]$       |
| $C_p$              | Specific heat capacity                                   | $[J.K^{-1}.kg^{-1}]$ |
| $C_{p,s}$          | Solid specific heat capacity                             | $[J.K^{-1}.kg^{-1}]$ |
| $C_{p,l}$          | Liquid specific heat capacity                            | $[J.K^{-1}.kg^{-1}]$ |
| $C_{p,g}$          | Gas specific heat capacity                               | $[J.K^{-1}.kg^{-1}]$ |
| $C_{p,f}$          | Specific heat capacity of a fluid mixture                | $[J.K^{-1}.kg^{-1}]$ |
| $C_{p,lg}$         | Liquid-gas mixture specific heat capacity                | $[J.K^{-1}.kg^{-1}]$ |
| $C_{p,steel}$      | Heat capacity for stainless steel 321                    | $[J.K^{-1}.kg^{-1}]$ |
| $C_{p,insulator}$  | Heat capacity for ceramic fiber insulator                | $[J.K^{-1}.kg^{-1}]$ |
| $D(T)$             | Gaussian distribution function                           | $[K^{-1}]$           |
| $d$                | Inner diameter of the multi-tubes                        | $[m]$                |
| $d_s$              | Shaft diameter   | $[m]$                |
| $D$                | Outer diameter of the continuous reactor                 | $[m]$                |
| $D_h$              | Hydraulic diameter                                       | $[m]$                |
| $D_{max}$          | Maximum outer diameter of the continuous reactor         | $[m]$                |
| $E$                | Activation energy  | $[J/mol]$            |
| $E_{sim}$          | Simulated Energy given by heater for a period of time    | $[J]$                |
| $E_{exp}$          | Experimental Energy given by heater for a period of time | $[J]$                |
| $err_{Temp}$       | Relative error between temperature                       | $[\%]$               |
| $err_{HF}$         | Relative error of absorbed heat flow                     | $[\%]$               |
| $err_{Energy}$     | Relative error between calculated energy                 | $[\%]$               |
| $err_{conv}$       | Relative error between conversion function               | $[\%]$               |
| $\vec{e}_y$        | Unit vector in the up-ward y-axis direction              | $[1]$                |
| $\vec{e}_z$        | Unit vector in the up-ward z-axis direction              | $[1]$                |
| $f$                | Inverse of relaxation time of fluid                      | $[s^{-1}]$           |
| $f_l$              | Liquid conversion function                               | $[1]$                |
| $f_t$              | Friction coefficient in pipes                            | $[1]$                |
| $f_{experimental}$ | Normalized experimental function of Criado's method      | $[1]$                |
| $f_{theoretical}$  | Normalized theoretical function of Criado's method       | $[1]$                |
| $f(x)$             | Kinetic model function                                   | $[1]$                |
| $\vec{F}_{st}$     | Surface tension body force                               | $[N.m^{-3}]$         |
| $G$                | Chemical potential parameter                             | $[J.m^{-3}]$         |
| $Gr_L$             | Grashof number   | $[1]$                |
| $g$                | Gravity constant   | $[m.s^{-2}]$         |

## Nomenclature

---

|                   |  |                                       |
|-------------------|--|---------------------------------------|
| $g(x)$            | Integral form of the kinetic model function          | [1]                                   |
| $g(y)$            | Numerical approximation of the integral of $g(x)$    | [1]                                   |
| $\vec{g}$         | Gravitational force                                  | [m.s <sup>-2</sup> ]                  |
| $h$               | Heat transfer convection coefficient                 | [W.m <sup>-2</sup> .K <sup>-1</sup> ] |
| HCV               | Higher Calorific Value                               | [J.kg <sup>-1</sup> ]                 |
| $H_R$             | Change of enthalpy due to pyrolysis                  | [J.kg <sup>-1</sup> ]                 |
| $H_r$             | Average enthalpy of mixed plastic pyrolysis          | [J.kg <sup>-1</sup> ]                 |
| $I(E, T)$         | Integral of $g(x)$                                   | [1]                                   |
| $K(T)$            | Kinetic constant of the pyrolysis kinetic reaction   | [s <sup>-1</sup> ]                    |
| $k$               | Thermal conductivity                                 | [W.m <sup>-1</sup> .K <sup>-1</sup> ] |
| $k_s$             | Solid thermal conductivity                           | [W.m <sup>-1</sup> .K <sup>-1</sup> ] |
| $k_l$             | Liquid thermal conductivity                          | [W.m <sup>-1</sup> .K <sup>-1</sup> ] |
| $k_g$             | Gas thermal conductivity                             | [W.m <sup>-1</sup> .K <sup>-1</sup> ] |
| $k_f$             | Thermal conductivity of a fluid mixture              | [W.m <sup>-1</sup> .K <sup>-1</sup> ] |
| $k_{lg}$          | Liquid-gas mixture thermal conductivity              | [W.m <sup>-1</sup> .K <sup>-1</sup> ] |
| $k_{steel}$       | Thermal conductivity for the stainless steel 321     | [W.m <sup>-1</sup> .K <sup>-1</sup> ] |
| $k_{insulator}$   | Thermal conductivity for the ceramic fiber insulator | [W.m <sup>-1</sup> .K <sup>-1</sup> ] |
| $k_T$             | Turbulent kinetic energy                             | [m <sup>2</sup> .s <sup>-2</sup> ]    |
| $L$               | Latent heat of fusion                                | [kJ.kg <sup>-1</sup> ]                |
| $L_r$             | Length of the continuous reactor                     | [m]                                   |
| LCV               | Lower Calorific Value                                | [kJ.kg <sup>-1</sup> ]                |
| $L_c$             | Characteristic length                                | [m]                                   |
| $M$               | Fluid consistency coefficient                        | [Pa.s <sup>n</sup> ]                  |
| $M_c$             | Characteristic mesh size length                      | [m]                                   |
| $n$               | Fluid flow behavior index                            | [1]                                   |
| $nc$              | Correlation integer index for tube distribution      | [1]                                   |
| $N_L$             | Best number of tubes of the laminar flow model       | [1]                                   |
| $N_T$             | Best number of tubes of the turbulent flow model     | [1]                                   |
| $N_{L,min}$       | Minimum number of tubes of the laminar flow model    | [1]                                   |
| $N_{L,max}$       | Maximum number of tubes of the laminar flow model    | [1]                                   |
| $N_{T,min}$       | Minimum number of tubes of the turbulent flow model  | [1]                                   |
| $N_{T,max}$       | Maximum number of tubes of the laminar flow model    | [1]                                   |
| $m$               | Mass   | [kg]                                  |
| $m_0$             | Initial mass   | [kg]                                  |
| $m_\infty$        | Mass at the end of the process, i.e. final mass      | [kg]                                  |
| $m_t$             | Mass at time (t), i.e. mass function of time         | [kg]                                  |
| $\dot{m}$         | Mass flow rate                                       | [kg.s <sup>-1</sup> ]                 |
| $\dot{m}_p$       | Plastic mass flow rate                               | [kg.s <sup>-1</sup> ]                 |
| $\dot{m}_{p,max}$ | Maximum plastic mass flow rate                       | [kg.s <sup>-1</sup> ]                 |

## Nomenclature

---

|                    |   |  |
|--------------------|---|--|
| $\dot{m}_{p,t}$    | Plastic mass flow rate in a single concentric tube system | [kg.s <sup>-1</sup> ]                  |
| $\dot{m}_a$        | Mass flow rate of hot exhaust gases                       | [kg.s <sup>-1</sup> ]                  |
| $\dot{m}_{a,t}$    | Air mass flow rate in a single concentric tube system     | [kg.s <sup>-1</sup> ]                  |
| $N$                | Number of tubes   | [1]                                    |
| $n$                | Power Law index power                                     | [1]                                    |
| $Pr$               | Prandtl Number  | [1]                                    |
| $P_k$              | Turbulent production term                                 | [kg.m <sup>-1</sup> .s <sup>-3</sup> ] |
| $p$                | Thermodynamic static pressure                             | [Pa]                                   |
| $pitch$            | Pitch length of the tubes                                 | [m]                                    |
| $p(y)$             | Approximate solution function                             | [K]                                    |
| $Q$                | Volumetric heat source or heat sink                       | [W.m <sup>-3</sup> ]                   |
| $Q_{hs}$           | Domain heat source due to heater                          | [W.m <sup>-3</sup> ]                   |
| $Q_{sink}$         | Domain heat sink due to pyrolysis reaction                | [W.m <sup>-3</sup> ]                   |
| $Q_{cond}$         | Domain heat source due to condensation of byproducts      | [W.m <sup>-3</sup> ]                   |
| $Q_c$              | Heat sink for plastic cracking                            | [J.K <sup>-1</sup> .kg <sup>-1</sup> ] |
| $Q_t$              | Total heat power transferred                              | [W]                                    |
| $Q_{max}$          | Maximum heat power transferred                            | [W]                                    |
| $\dot{Q}_a$        | Absorbed heat flow  | [W]                                    |
| $\dot{Q}_{a,exp}$  | Experimental absorbed heat flow                           | [W]                                    |
| $\dot{Q}_{a,sim}$  | Simulated absorbed heat flow                              | [W]                                    |
| $q$                | Heat power transferred in a single tube                   | [W]                                    |
| $q_{conv}$         | Convection heat flux                                      | [W.m <sup>-2</sup> ]                   |
| $q_{rad}$          | Radiative heat flux                                       | [W.m <sup>-2</sup> ]                   |
| $\dot{q}_{exp}(t)$ | Experimental power delivered by the heaters               | [W]                                    |
| $R$                | Universal gas constant                                    | [J/mol/K]                              |
| $Re$               | Reynold's number  | [1]                                    |
| $Re_p$             | Plastic Reynold's number                                  | [1]                                    |
| $Re_a$             | Hot exhaust gas Reynold's number                          | [1]                                    |
| $Re_L$             | Laminar flow Reynold's number                             | [1]                                    |
| $R^2$              | Coefficient of determination                              | [1]                                    |
| $Ra_L$             | Rayleigh number   | [1]                                    |
| $R_p$              | Radius of spherical particle                              | [m]                                    |
| $r$                | Radius  | [m]                                    |
| $S_g$              | Mass source term from liquid to gas                       | [kg.m <sup>-3</sup> .s <sup>-1</sup> ] |
| $S_l$              | Mass source term from gas to liquid                       | [kg.m <sup>-3</sup> .s <sup>-1</sup> ] |
| $sp$               | Spacing length between the tubes                          | [m]                                    |
| $sf$               | Safety factor   | [1]                                    |
| $T$                | Temperature   | [°C]                                   |
| $T_0$              | Initial temperature                                       | [°C]                                   |

## Nomenclature

---

|                |  |      |
|----------------|--|------|
| $T_1$          | Temperature located inside the semi-batch reactor          | [°C] |
| $T_2$          | Temperature located at the wall of the semi-batch reactor  | [°C] |
| $T_3$          | Bottom temperature of the semi-batch reactor               | [°C] |
| $T_4$          | Top temperature of the semi-batch reactor                  | [°C] |
| $T_5$          | Temperature of the outer surface of the semi-batch reactor | [°C] |
| $T_{start}$    | Start temperature  | [°C] |
| $T_{end}$      | End temperature  | [°C] |
| $T_{start,c}$  | Pyrolysis start temperature                                | [°C] |
| $T_{onset,c}$  | Pyrolysis onset temperature                                | [°C] |
| $T_{offset,c}$ | Pyrolysis offset temperature                               | [°C] |
| $T_{end,c}$    | Cracking end temperature                                   | [°C] |
| $T_{start,lc}$ | Start latent cracking temperature                          | [°C] |
| $T_{start,mc}$ | Start mass cracking temperature                            | [°C] |
| $T_{onset,m}$  | Melting onset temperature                                  | [°C] |
| $T_{offset,m}$ | Melting offset temperature                                 | [°C] |
| $T_m$          | Peak melting temperature                                   | [°C] |
| $T_{c,max}$    | Maximum cracking temperature                               | [°C] |
| $T_g$          | Glass transition temperature                               | [°C] |
| $T_{crys}$     | Crystallization temperature                                | [°C] |
| $T_{sur}$      | Surface temperature  | [°C] |
| $T_{amb}$      | Ambient temperature  | [°C] |
| $T_{wall}$     | Wall temperature   | [°C] |
| $T_{exp}$      | Experimental temperature                                   | [°C] |
| $T_{sim}$      | Simulated temperature                                      | [°C] |
| $T_{ref}$      | Reference temperature                                      | [°C] |
| $T_{exp}(t)$   | Linear experimental temperature                            | [°C] |
| $T_{boil}$     | Boiling temperature  | [°C] |
| $T_{p,in}$     | Inlet plastic temperature                                  | [°C] |
| $T_{g,in}$     | Inlet temperature of hot exhaust gases                     | [°C] |
| $T_{a,inlet}$  | Inlet temperature of hot exhaust gases                     | [°C] |
| $T_{a,outlet}$ | Outlet temperature of hot exhaust gases                    | [°C] |
| $T_{p,outlet}$ | Outlet plastic temperature                                 | [°C] |
| $T_{a,out}$    | Average outlet temperature of hot exhaust gases            | [°C] |
| $T_{p,out}$    | Average outlet plastic temperature                         | [°C] |
| $T_{sat}$      | Vapor saturation temperature                               | [°C] |
| $T_s$          | Solid temperature  | [°C] |
| $T_l$          | Liquid temperature   | [°C] |
| $T_x$          | Temperature at conversion x                                | [°C] |
| $T_{0.5}$      | Temperature at conversion x = 0.5                          | [°C] |
| $T_i(t_x)$     | Arbitrary temperature at constant conversion x             | [°C] |

## Nomenclature

---

|               |   |                                       |
|---------------|---|---------------------------------------|
| $t$           | Time  | [s]                                   |
| $th$          | Pipe thickness  | [m]                                   |
| $t_x$         | Time at conversion $x$                                      | [s]                                   |
| $t_{start,c}$ | Start latent cracking time                                  | [s]                                   |
| $T_{end,c}$   | Time for end of cracking                                    | [s]                                   |
| $test(\psi)$  | Quadratic Lagrange Shape function                           | [1]                                   |
| $U_{max}$     | Magnitude of maximum velocity                               | [m.s <sup>-1</sup> ]                  |
| $U_p$         | Average velocity of plastic entering the continuous reactor | [m.s <sup>-1</sup> ]                  |
| $U_a$         | Average inlet velocity of hot exhaust gases                 | [m.s <sup>-1</sup> ]                  |
| $U_t$         | Overall heat transfer coefficient                           | [W.K <sup>-1</sup> .m <sup>-2</sup> ] |
| $u$           | X component of the velocity vector                          | [m.s <sup>-1</sup> ]                  |
| $\vec{u}$     | Velocity vector   | [m.s <sup>-1</sup> ]                  |
| $V_{f,l}$     | Phase field liquid volume fraction domain function          | [1]                                   |
| $V_{f,g}$     | Phase field gas volume fraction domain function             | [1]                                   |
| $v$           | Y component of the velocity vector                          | [m.s <sup>-1</sup> ]                  |
| $w$           | Z component of the velocity vector                          | [m.s <sup>-1</sup> ]                  |
| $X_l$         | Mass liquid fraction  | [1]                                   |
| $X_g$         | Mass gas fraction   | [1]                                   |
| $x$           | Pyrolysis conversion function                               | [1]                                   |
| $x_{exp}$     | Experimental pyrolysis conversion function                  | [1]                                   |
| $x_{sim}$     | Simulated pyrolysis conversion function                     | [1]                                   |
| $x_{out}$     | Average outlet pyrolysis conversion of plastic              | [1]                                   |
| $z(x)$        | Multiple of $f(x)$ and $g(x)$                               | [kg]                                  |

## Greek letters

|                     |  |                                    |
|---------------------|--|------------------------------------|
| $\alpha$            | Thermal expansion coefficient          | [K <sup>-1</sup> ]                 |
| $\alpha_l$          | Liquid volume fraction domain function | [1]                                |
| $\alpha_g$          | Gas volume fraction domain function    | [1]                                |
| $\beta$             | Heating rate                           | [°C.s <sup>-1</sup> ]              |
| $\gamma$            | Ratio of specific heats                | [1]                                |
| $\dot{\gamma}$      | Shear strain rate                      | [s <sup>-1</sup> ]                 |
| $\dot{\gamma}_{ij}$ | Shear strain rate tensor               | [s <sup>-1</sup> ]                 |
| $\varepsilon$       | Surface emissivity                     | [1]                                |
| $\varepsilon_T$     | Turbulent dissipation rate             | [m <sup>2</sup> .s <sup>-3</sup> ] |
| $\epsilon$          | Very small meaningless constant ~ zero | [1]                                |
| $\zeta$             | Mixing energy density                  | [N]                                |
| $\xi$               | Surface roughness                      | [m]                                |
| $\xi_r$             | Relative surface roughness             | [1]                                |

## Nomenclature

---

|                    |  |                                       |
|--------------------|--|---------------------------------------|
| $\zeta$            | Thermal effectiveness                                    | [1]                                   |
| $\eta$             | Apparent viscosity                                       | [Pa.s]                                |
| $\eta_0$           | Apparent viscosity at very low shear rate, zero          | [Pa.s]                                |
| $\eta_\infty$      | Apparent viscosity at very high shear rate, infinity     | [Pa.s]                                |
| $\vartheta$        | Interface thickness parameter                            | [m]                                   |
| $\kappa$           | Surface interface curvature                              | [m <sup>-1</sup> ]                    |
| $\lambda$          | Relaxation time of fluid                                 | [s]                                   |
| $\mu$              | Dynamic viscosity  | [Pa.s]                                |
| $\mu_l$            | Liquid dynamic viscosity                                 | [Pa.s]                                |
| $\mu_g$            | Gas dynamic viscosity                                    | [Pa.s]                                |
| $\mu_f$            | Viscosity of a fluid mixture                             | [Pa.s]                                |
| $\mu_T$            | Turbulent dynamic viscosity                              | [Pa.s]                                |
| $\nu$              | Kinematic viscosity                                      | [m <sup>2</sup> .s <sup>-1</sup> ]    |
| $\rho$             | Density  | [kg.m <sup>-3</sup> ]                 |
| $\rho_0$           | Initial density  | [kg.m <sup>-3</sup> ]                 |
| $\rho_\infty$      | Final density  | [kg.m <sup>-3</sup> ]                 |
| $\rho_g$           | Gas density  | [kg.m <sup>-3</sup> ]                 |
| $\rho_l$           | Liquid density   | [kg.m <sup>-3</sup> ]                 |
| $\rho_f$           | Density of a fluid mixture                               | [kg.m <sup>-3</sup> ]                 |
| $\rho_p$           | Density of plastic                                       | [kg.m <sup>-3</sup> ]                 |
| $\rho_a$           | Hot exhaust gas density                                  | [kg.m <sup>-3</sup> ]                 |
| $\sigma$           | Surface tension coefficient                              | [N.m <sup>-1</sup> ]                  |
| $\tau_0$           | Minimum yield shear stress                               | [Pa]                                  |
| $\vec{\tau}$       | Shear stress   | [Pa]                                  |
| $\vec{\tau}_{ij}$  | Shear stress tensor                                      | [Pa]                                  |
| $\varphi$          | Stefan-Boltzmann constant                                | [W.K <sup>-4</sup> .m <sup>-2</sup> ] |
| $\phi$             | Thermal diffusivity                                      | [m <sup>2</sup> .s <sup>-1</sup> ]    |
| $\Phi$             | Phase field variable                                     | [1]                                   |
| $\psi$             | Phase field help variable                                | [1]                                   |
| $\omega$           | Mobility coefficient                                     | [m <sup>3</sup> .s.kg <sup>-1</sup> ] |
| $\Delta T_m$       | Melting range temperature                                | [W]                                   |
| $\Delta h_m$       | Specific melting enthalpy                                | [kJ.kg <sup>-1</sup> ]                |
| $\Delta h_c$       | Specific cracking enthalpy                               | [kJ.kg <sup>-1</sup> ]                |
| $\Delta h_{evap}$  | Specific evaporation enthalpy                            | [kJ.kg <sup>-1</sup> ]                |
| $\Delta H_p$       | Specific total plastic pyrolysis enthalpy                | [kJ.kg <sup>-1</sup> ]                |
| $\Delta p_{max}$   | Maximum back pressure at the outlet of the diesel engine | [Pa]                                  |
| $\Delta p_f$       | Pressure loss due to friction in pipes                   | [Pa]                                  |
| $\Delta p_{f,max}$ | Maximum pressure loss due to friction in pipes           | [Pa]                                  |
| $\vec{\nabla}$     | Spatial gradient operator                                | [m <sup>-1</sup> ]                    |

### Abbreviations

|         |  |
|---------|--|
| ABS     | Acrylonitrile Butadiene Styrene                        |
| AIC     | Advanced IsoConversional method                        |
| AHCM    | Apparent Heat Capacity Method                          |
| BMG     | BioMass Gasification process                           |
| CFD     | Computational Fluid Dynamics                           |
| CSBR    | Conical Spouted Bed Reactor                            |
| DCM     | Direct Computer Mapping                                |
| DSC     | Differential Scanning Calorimetry                      |
| DTG     | Derivative ThermoGravimetry                            |
| FEM     | Finite Element Method                                  |
| FR      | FRiedman isoconversional method                        |
| FWO     | Flynn Wall Ozawa isoconversional method                |
| HDPE    | High Density PolyEthylene                              |
| IDE     | Integrated Development Environment                     |
| IEA     | International Energy Agency                            |
| KAS     | Kissinger-Akahira-Sunose isoconversional method        |
| LDPE    | Low Density PolyEthylene                               |
| MUMPS   | MULTifrontal Massively Parallel sparse direct Solver   |
| MSW     | Municipal Solid Waste                                  |
| OFW     | Ozawa-Flynn-Wall isoconversional method                |
| PARDISO | PARAllel DIrect Solver                                 |
| PCM     | Phase Change Material                                  |
| PDE     | Partial Differential Equation                          |
| PE      | PolyEthylene   |
| PET     | PolyEthylene Terephthalate                             |
| PID     | Proportional Integral Derivative                       |
| PIMPLE  | Pressure Implicit Method for Pressure-Linked Equations |
| PP      | PolyPropylene  |
| PS      | PolyStyrene  |
| PVC     | PolyVinyl Chloride                                     |
| SOR     | Successive Over-Relaxation method                      |
| SPOOLES | Sparse Object-Oriented Linear Equations Solver         |
| SPR     | Sapporo Plastic Recycling facility                     |
| SST     | Shear Stress Transport turbulent model                 |
| TG      | ThermoGravimetry                                       |
| TGA     | ThermoGravimetric Analysis                             |
| TPD     | Ton Per Day  |

## Nomenclature

---

|     |                            |
|-----|----------------------------|
| TRL | Technology Readiness Level |
| VOF | Volume Of Fraction method  |

# Introduction

Plastic is one of the most abundant materials present in our world and daily life activities. Since the beginning, plastic materials were presented as an arrangement to substitute the rare and non-sustainable assets such as tortoiseshell, ivory and animal bones. Since at that point, plastics have shaped the world bringing security, hygiene, consolation and prosperity to our society. Plastic production started in 1950s and it grew bigger and bigger till it reached 360 million tons in 2018 as the world's annual plastic production, whereas the demand is still in increase (Plastics – the Facts, 2019). Moreover, Europe contributes to around 18 % of the world annual production, about 62 million tons in 2018, and about 50 % are produced by Asian countries. The major production in the industry of plastic goes for packaging – 40 % of the plastic industry- and Building and construction sectors, where the leading polymers are the polyolefin, Polyethylene (PE) and Polypropylene (PP), which they constitute around 60 % of the whole plastic production in Europe (Plastics – the Facts, 2019). On the other hand, plastics have a variable service life span; it varies from a one day or a single use, like packaging materials to more than 50 years like plastics used in the automotive industry. Thus, due to the short life service of the majority of plastic materials and the yearly increase in plastic production, the plastic wastes production increased enormously to reach 307 million tons (Mt) worldwide in 2015 (Geyer et al., 2017). Moreover, from 1950 to 2015, approximately 6300 Mt of plastic waste had been generated, around 9 % of which had been recycled, 12 % was incinerated, and 79 % was accumulated in landfills or dispersed in nature. Therefore, if the current production and waste management trends continue, roughly 12,000 Mt of plastic waste will be in landfills or in the natural environment by 2050 (Geyer et al., 2017). Every year, about 8 million tons of plastic waste are flowing into the oceans from coastal countries and cause death for millions of animals, from birds to fish to other marine organisms. In addition, Micro plastics have been found in more than 100 aquatic species, destined for our dinner plates; in most cases this can be harmful for the human health. Consequently, plastic pollution is a serious issue facing humanity that needs to solve and overcome.

On the other hand, regarding plastic wastes treatment, there exist three main categories: recycling, energy recovery, and landfilling. In Europe, 29.1 million tons of plastic post-consumer wastes were collected and treated in 2018; 32.5 % are recycled, 42.6 % are used for energy recovery and 24.9 % are landfilled (Plastics – the Facts, 2019). Landfilling is worse treatment among all, due to

the fact that plastics are non-biodegradable material; plastics will stay buried for centuries and the landfill space will decrease more and more in addition to soil pollution. Thus, in order to achieve plastic circular economy, landfilling treatment should be decreased till null, whereas recycling and recovery processes must be more used (Plastics – the Facts, 2019). On the other side, recycling process has limitations; not all plastic wastes can be recycled and there are difficulties in the sorting process, moreover it is high operation cost and labor intensive process. Therefore, the energy recovery treatment becomes a solution to fill the gap and to decrease the usage of the landfilling process to the maximum (Plastics – the Facts, 2019).

There exist three main processes for the energy recovery treatment; Incineration, pyrolysis, and gasification. Pyrolysis and gasification processes are said to be similar and more environmentally friendly than the incineration process. However, pyrolysis process is a sub-process of gasification and require less energy. Plastic pyrolysis is a thermal degradation process of long chain hydrocarbons into smaller ones in absence of oxygen. It produces a wide range of hydrocarbons and chemicals that can be treated further, by distillation and refinement, to be fossil-like fuels. Consequently, pyrolysis process is a very convenient solution for plastic waste pollution and for the depletion of fossil fuel reserves. But, unfortunately, pyrolysis and gasification technologies all over the past forty years, faced many obstacles that diminished dramatically the implementation and the usage of such promising processes. The main reasons behind this fall out were the inefficiency of the pyrolysis plants or reactors, the absence of market pull due to competition from conventional fuels, and the lack of infrastructure for quality controlled feedstock supply. The foundation of the first two reasons is that the pyrolysis/gasification technologies development were based on experimental up-scaling path that is tested and evaluated constantly over the past years, in addition to the high cost of the thermal supply. Nevertheless, the fundamentals and the scientific procedure for the up-scaling process is still conceived and embedded within the manufacturing companies and not released to the public or the scientific community. Moreover, the numerical and simulation approach for this aspect is also still rarely treated as it will be shown in the bibliographic study.

Starting from these issues this thesis comes to try to fulfill this gap and to set the assists of a numerical model for plastic pyrolysis process based on finite element method for the sake of comprehension and building more efficient plastic pyrolysis reactors. This work is a continuation

for the efforts and works done before by our colleagues Radu Kungser (Radu Kungser, 2015) and Chantal Kassargy (Kassargy, 2018) in the IMT-Atlantique “Department of Energy and Environmental Systems (DSEE) in the GEPEA laboratory. The previous work focused on experimental studies for PE and PP pyrolytic and non-pyrolytic processes in a semi-batch reactor and making comparison between the oil byproducts and fossil fuels according to the international characteristic norm. In addition, a lab scale continuous pyrolysis reactor heated by the exhaust gas of 8 kW diesel engine was built for the sake of experimentation, process enhancement and reducing cost of thermal supply by using the heat wasted from the engine. Unfortunately, there was a limitation in heat transfer and the reactor was inefficient since numerical foundation and optimization was not done before building the reactor. Moreover, Chantal proposed a peer design and modification for the continuous pyrolysis reactor, based on analytical study; this design will be tested numerically using finite element method and numerical software such as COMSOL Multiphasic at the end of this work. Therefore, this work will focus on modeling the plastic pyrolysis process using finite element method and simulating using conventional software like COMSOL Multiphysics. Pyrolysis process will be modelled in a semi-batch reactor, exist in the laboratory. Then, this model will be used to verify the continuous plastic pyrolysis reactor suggested by Chantal Kassargy’s work. Moreover, the geometry and the operating conditions of the continuous reactor will be optimized for better efficiency. Finally, this model can be a pillar for lab-scale experimentation setup of the continuous and later the up-scaling for the industrial realization.

The work will follow a chronological order as it is explained in the following chapters:

Chapter One is a bibliographic study about plastics pyrolysis process. Moreover, the chapter will include a brief review about the pyrolysis technologies applied for the past 40 years and important and main retained conclusions. The effecting parameters in the plastic pyrolysis process, the plastic pyrolysis kinetics, plastic viscosity, phase change and plastic melting models and equations will be presented in this chapter. Furthermore, it includes a literature review concerning numerical modelling and simulating plastic pyrolysis process using conventional software like ANSYS or COMSOL Multiphysics. Finally, a brief illustration of the importance of employing numerical simulation using finite element method and brief comparison between the conventional software COMSOL Multiphysics and ANSYS will be demonstrated.

## Introduction

---

The second chapter “Materials and Methods” will first list and describe the used materials, reactors, and the equipment utilized in this study. Then, it will illustrate the procedure of performing experiments and producing results. Finally, all models and equations used in modelling and simulating process will be presented with their sequential flow of work to conduct the anticipated results.

The third chapter will develop the modelling and show results for Polypropylene (PP) and high density polyethylene (HDPE) melting and heating processes at a particle scale using differential scanning calorimetry (DSC) apparatus and as a buffer lab-scale in a semi-batch reactor. Moreover, the results will be discussed and a comparison between simulated and experimental results will be demonstrated. In addition, sensible heat transfer will be conducted and validated for the semi-batch reactor (loaded and empty) Also a sensitivity study concerning the reactor’s thermal properties will be demonstrated.

The fourth chapter will continue to display the results for PP and HDPE as the cracking phase in the pyrolysis process. Thus, pyrolytic experimental studies for PP and HDPE are conducted using thermogravimetric analyzer (TGA). Then, the chosen pyrolysis kinetics methodology will be used to determine analytically the pyrolysis kinetic parameters for PP and HDPE. Furthermore, the analytical solution of the model will be compared with the experimental TGA. After that, the entire pyrolysis process inside the TGA will be modeled, simulated using COMSOL-Multiphysics and compared with the DSC results. Then, the validated pyrolysis kinetic model will be used to model pyrolysis process for PP and HDPE inside the semi-batch reactor; the experimental and the simulated results will be compared for further confirmation. Moreover, the validated plastic pyrolysis process model in the semi-batch reactor will used later on in modelling the continuous reactor.

Finally, chapter five will deal with the implementation of the validated kinetic model, and the validated pyrolysis model in the semi-batch reactor into a model for a continuous pyrolysis reactor heated by exhaust gas of 8 kW diesel engine. Then, after interpreting and comparing the results, a parametric study for the geometry (length and number of tubes) and the operating conditions (plastic mass flow rate) will be conducted in order to enhance the proposed analytical model and to design an efficient continuous plastic pyrolysis reactor.

## Chapter 1 Bibliography

This chapter will provide a bibliographic study about plastics, plastic pyrolysis process and operating parameters. Moreover, this chapter will state a brief review about the pyrolysis technologies applied in Europe and worldwide for the past 40 years and the important conclusions that were retained. In addition, plastic viscosity, phase change and plastic melting models will be discussed in this chapter. Furthermore, plastic pyrolysis kinetics terminology using isoconversional methods will be also illustrated. Then, a state of the art concerning numerical modelling and simulating plastic pyrolysis process using conventional software, like ANSYS or COMSOL Multiphysics, will be addressed; the importance of using numerical simulation using finite element method with a brief comparison between the two well-known commercial numerical software COMSOL Multiphysics and ANSYS will be presented.

### 1.1 Plastic wastes accumulation

Plastic is a high molecular weight material that was invented by Alexander Parkes in 1862 (Gilbert, 2017). Plastics are also called polymers whose term means a molecule formed by the repetition of a single unit called the monomer. For example, **Figure 1-1** shows the structure of polyethylene that is formed from the ethylene monomer ( $\text{CH}_2=\text{CH}_2$ ).

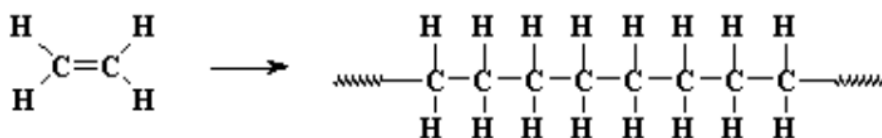


**Figure 1-1:** Polymerization of ethylene monomer to form a polyethylene chain.

Polymers are divided into two distinct classes, thermoplastics and thermosets which are differentiated according to their behavior in the presence of heat. The main physical difference is that thermoplastics can be re-melted and reshaped while thermosets always stay in their solid state permanently, once they are synthesized (Swallowe, 1999). Moreover, about 82.6 % of the polymers produced in the world are thermoplastics and mainly made of polyolefin materials, polypropylene (PP) and polyethylene (PE), which represent more than 60 % of the global demand of plastics (PlasticEurope, 2019).

Plastic plays a vital role in enhancing the standard lives of human being for more than 50 years. It is a key of innovation of many products in various sectors such as construction, healthcare, electronics, automotive, packaging and others. The demand of commodity plastics has been increased due to the rapid growth of the world population. The global production of plastic has reached about 360 million tons in 2018 and the rate is still in increase. Where, Asia alone contributes to 50 % of the global production in the world and around 18 % are produced in Europe (PlasticEurope, 2019). The continuous rising of plastic demand led to the growing in waste accumulation every year, which reached 307 million tons (Mt) worldwide in 2015 (Geyer *et al.*, 2017).

### 1.2 Plastic pyrolysis process

Three main processes are employed now a day to resolve the plastic waste accumulation dilemma; recycling, energy recovery, and landfilling. However, about 79 % of the global plastic wastes are accumulated in landfills and it is estimated that, roughly, 12,000 Mt of plastic waste will be in landfills by 2050, if the current production rate and waste management trends continue (Geyer *et al.*, 2017). But, due to the fact that plastic is non-biodegradable material, landfilling treatment is a soil pollution threat that should be diminished, whereas recycling and energy recovery processes should be more invested. On the other hand, because of the constrains and high cost of sorting process, recycling treatment is less preferable and less efficient. Therefore, energy recovery treatments are the most preferable, which constitute of three different processes: incineration, pyrolysis, and gasification. Whereas, one of the most environmental and efficient process is the pyrolysis process, which it doesn't cause water contamination and it reduces the greenhouse effect.

Plastic pyrolysis is thermal degradation of long chain hydrocarbons into smaller one with high temperatures and in an inert atmosphere. Three main products are produced during this process: oil, gas and char residue. The process produces wide range of hydrocarbons and chemicals that can be treated further, by refinement and purification processes, to be a fossil-like fuels. Moreover, it is able to produce high amounts of oil yield, above 80 wt% at moderate temperatures, around 500 °C. In addition, the yield and the distribution of the byproducts can vary because the process is affected directly by the operating parameters such as type of the feedstock, temperature, heating rate, type of reactor, usage of catalyst, residence time and pressure (Chen *et al.*, 2014).

### 1.3 Plastic pyrolysis application and technology

Nowadays, plastic pyrolysis technology is employed and spread all over the world either by commercial companies or by governmental strategies. A large scale governmental collaboration program called IEA Bioenergy is one of the most important programs enrolled nowadays. The IEA Bioenergy is an organization set up in 1978 by the International Energy Agency (IEA) with the aim of improving cooperation and information exchange between countries that have national programs in bioenergy research, development and deployment. Twenty-five countries, including China, India, USA, Japan, Canada, Brazil, and Australia, plus the European Union participate in IEA Bioenergy program. This program facilitates the co-operation among IEA member and non-member countries to develop new and improved energy technologies and introduce them into the market. Moreover, the IEA Bioenergy program constitute of, about 20 tasks or projects, seven of them are completed whereas the 13 tasks are still ongoing. Task 33, Gasification of Biomass and Waste, is one of the largest and most important tasks that are still ongoing, knowing that the pyrolysis process is a sub-process of the gasification process. Task 33 is a working group of international experts with the aim to promote the commercialization of efficient, economical and environmentally preferable thermal biomass gasification processes. Moreover, annual reports and publications are frequently published for the sake of progress and achievements (IEA Bioenergy, 2020).

In year 2000, a report was published under the title of “Acceptance test for large biomass gasifiers” emphasize that almost all of the gasification/pyrolysis industrial technologies, worldwide, was achieved by experimental up-scaling without the theoretical bases. Additionally, it is reported that after developing and building number of different technologies such as, pilot plants and some commercial demonstration plants, they are still under evaluation till the current day (2000). Moreover, the summary of the report illustrated that there is still a long road ahead for further development and optimization of the gasification/pyrolysis technology to be more reliable and efficient (Huisman, 2001).

Furthermore, in 2005 another publication was released, by the part of task 33, having a title of “Observations on the Current Status of Biomass Gasification” (Babu, 2005). It is stated that during the last 25 years, a significant research and technology development and demonstration effort has been launched both in Europe and North America. However, all of these developments were based

## Bibliography

---

on selected scale-up efforts, which are broadly representative of the current status of biomass gasification (BMG). As a conclusion, it stated that despite the widely acknowledged benefits, the commercialization of BMG was fallen short of expectations due to the fact that the process was still inefficient and uneconomically deployed (Babu, 2005).

In addition, in 2011, a publication under the title of “Reaction kinetics and producer gas compositions of steam gasification of coal and biomass blend chars, part 2: Mathematical modelling and model validation” was published (Jafri, 2020), by the part of task 33, to investigate a mathematical model that describes the gasification process for char particles inside a gasifier (Xu *et al.*, 2011). Nonetheless, in 2018 a general gasification guide was released under the title of “Final Guideline for Safe and Eco-friendly Biomass Gasification”. This guideline was based on an accepted methodology, science, common sense, and measurable parameters from the existing biomass gasification plants and those under development or construction (Vos *et al.*, 2017). Finally, a report was published by IEA group (Task 33: gasification technology) in 2020 of title “Emerging Gasification Technologies for Waste & Biomass” aimed to settle a methodological approach to evaluate the emerging gasification technologies in different countries (Jafri, 2020). This approach designates discrete technology readiness level (TRL) scores, from 1 to 9, to the essential sub-processes common to all gasification technologies, namely, feedstock handling, gasification reactor with heat supply, product gas separation and integrated operation. Mainly, the report shows that the gasifier reactor is still not totally commercialized and has an average TRL score of 5 (Jafri, 2020).

As a conclusion, the huge effort on the gasification/pyrolysis technology, by task 33, was mainly focused on experimental up-scaling that is tested and evaluated in order to enhance and overcome the popped up issues and problems. Nevertheless, the process is not much efficient and it requires more enhancing and optimization to be efficiently well employed. On the other hand, there exist another promising and efficient procedure that can optimize and resolve many occurring problems in the gasifiers or pyrolysis processes at a very low cost. Where it is by using numerical software according to the Finite Element Method to simulate and animate the whole pyrolysis/gasification process for the sake of gaining better knowledge and optimizing the processes for better efficiency. Moreover, the empirical studies or formulas that are adapted for gasification/pyrolysis systems can't be used in other geometries or systems. In contrast, numerical modelling by Finite Element

## Bibliography

---

Method and spatial simulation for pyrolysis and gasification processes represent a great tool in understating and developing such phenomena. Moreover, the fundamentals and the scientific procedure for the up-scaling process is still conceived and embedded within the manufacturing companies and not released to the public and to the scientific community. Therefore, spatial modelling and simulating such processes, using Finite Element Method and conventional software, opens the door for a cumulative knowledge to grow and describe accurately these complex phenomena in order to increase its efficiency and utility.

On the other hand, regarding private companies and industry, many pilot and commercial plastic pyrolysis plants are built today by variant technologies and with different capacities for fuel production. Several companies build and operate these factories starting from Klean Industries in 2000 till most recent Vadxx technology in 2016.

Klean Industries, established in Japan in year 2000, is an environmentally conscious industrial company that focuses on recovering clean energy and resources from waste. The company operates globally and it has three large operating plastic waste pyrolysis facilities: Sapporo Plastic Recycling (SPR) in Japan, KleanFuels Canada, and GreenFuels Germany. Moreover, SPR Japan is the world's largest plant for oil production from plastic waste pyrolysis. In addition, the plant works with a capacity of 50 tons per day (TPD) of mixed plastic waste (PE, PP, polystyrene (PS), polyvinyl chloride (PVC), polyethylene terephthalate (PET), etc...), where the fuel oil yield is 70 % and the total byproducts yield is 90 %. Thus, about 950 liters of fuel oil is recovered from each ton of mixed plastic waste. The oil yield undergoes an advanced thermal process to produce light oil that is used as a chemical feedstock for the production of new plastics, a medium fuel oil equivalent to diesel, and heavy oil that is used to generate electricity. Moreover, the SPR technology has a patented dechlorination process that removes the hydrochloric gas produced by the thermal decomposition of PVC and uses water to convert the gas into hydrochloric acid leaving only 100 ppm of chlorine in the oil products. This installation is capable of producing 4 MW of electricity, 8.75 million liters of liquid fuel and 4 MW of thermal energy and 3000 tons per year of solid residues (char) and 150 tons per year of hydrochloric acid (Klean Industries, 2020).

In addition, ETIA is a French engineering group specialized in innovation, equipment, and processes for continuous thermal treatments. They invented the Spirajoule technology to perform continuous pyrolysis for municipal and industrial waste, plastics, and rubber (powder or shredded

## Bibliography

---

pieces). The reactor is made up of a hollow shaft with an electrical screw conveyor heated by a low voltage current and can reach temperatures up to 850 °C. This technology is simple and robust, and industrially proven since 1999 (ETIA, 2019).

Moreover, Agilyx company was founded in Oregon in the United states in 2004. The company has a commercialized dual screw reactor which converts waste polystyrene (PS) to styrene oil plastic with capacity of 10 tons per day and about 70 % gallon of fuel oil yield (about 9050 liters per day). That oil would later be refined into styrene monomer and re-polymerized into plastic (Greenwood, 2018).

Recycling Technologies is a British company founded in UK in 2011 and aims for chemical recycling of plastic waste. They developed a fluidized bed reactor called RT7000, which converts mixed plastic waste, complex or even contaminated plastic (e.g. food trays), by thermal degradation into liquid hydrocarbon with low sulfur content called Plaxx. Plaxx is a valuable chemical feedstock which, after refinement, can be used in the manufacturing of new virgin quality plastic and it is not intended to be used as fuel. The system is able to process up to 7,000 tons of mixed plastic waste per year with 75 % of oil yield. Furthermore, RT7000 is a compact and modular pyrolysis reactor that allows an easy transportation and installation, this overcomes the problem of unnecessary transportation of plastic waste and associated carbon emissions. The company has built a demonstration plant in a testing facility based at Swindon Borough Council's recycling facility, where it has been operating since 2018. This facility is running trials on different types of input materials to test the technological upgrades for the first commercial-scale unit RT7000, which will be installed at Binn Eco Park in Perth, Scotland (Recycling Technologies, 2018).

Unlike the Recycling Technologies company, Plastic Energy is the only commercial scale company in Europe. The company is first founded in 2009 in Spain, then it progressed to construct two plastic pyrolysis pilot plants in 2015 and 2017 (in Spain) running continuously and becoming commercial. These two plants are now processing 30 tons per day of end-of-life plastics, where the waste plastics are mixed domestic plastic waste, contaminated, multi-layered, as well as plastics that can no longer be mechanically recycled. First, a pre-process is conducted to remove non-desirable materials from the feedstock such as metals, textiles, paper, leftover PET and PVC. Then, thermal pyrolysis process transforms plastic waste into variety of hydrocarbon oils or known

as TACOIL, where every ton of processed plastic waste produces approximately 860 L of TACOIL. Finally, the TACOIL is subjected to additional purification and polishing steps before the final storage, these are mainly composed of naphtha and diesel. In addition, the company is now scaling up new plants to process 20,000-25,000 tons per year of plastic waste with a cost of 35 million euros for each. They are aiming to build 20 of these new-generation plants by 2023, ten plants in Europe and ten in Asia, with an overall budget of 800 million euros and total capacity of 500,000 tons per year (IChemE, 2019). Moreover, Plastic Energy is collaborating with ExxonMobil company to build an advanced recycling plant of capacity of 25,000 tons/year in Notre-Dame-de-Gravenchon, France, that will convert post-consumer plastic waste into raw materials due to pyrolysis for manufacturing virgin-quality polymers later on (Plastic Energy, 2021).

Vadxx technology company has built a plastic pyrolysis plant in Akron, Ohio state in the United States in 2015, whereas now its name is changed to Alterra Energy. The 20 million dollars facility is located approximately 300 m from the nearest domestic household. Moreover, the pyrolysis plant consumes up to 25,000 tons per year of plastics, thus about 60 tons per day, where non-hazardous mixed plastic waste (PE, PP, PS, etc...) are converted into four main byproducts called EcoFuels (Vadxx energy, 2016):

- **EcoFuel-I:** A diesel stock to be used as a blending agent to improve the overall quality of Ultra Low Sulfur Diesel and other distillate fuels blended with diesel for on-road use.
- **EcoFuel-II:** A Naphtha that can be used as a gasoline additive to increase octane.
- **EcoFuel-SNG:** A synthetic natural gas.
- **EcoFuel-S:** A carbon powder that can be used as a low grade fuel source.

Furthermore, **Table 1-1** below list some of the pilot and commercial scale plastic pyrolysis plants in Europe and in North-America with the used technology (Qureshi *et al.*, 2020).

**Table 1-1:** Selected plastic pyrolysis plants in Europe and in North-America.

| <b>Technology provider</b>    | <b>Capacity tons per day</b> | <b>Products</b>   | <b>Technology utilized</b> | <b>Location</b> |
|-------------------------------|------------------------------|---|----------------------------|-----------------|
| <b>VadXX</b>                  | 60                           | Syncrude, diesel  | Rotary kiln                | US              |
| <b>Nexus</b>                  | 50                           | Light crude, diesel, gasoline, kerosene blend-stocks, wax | Melting Vessel             | US              |
| <b>Agilyx</b>                 | 10 – 50                      | Light synthetic crude oil                                 | Dual screw reactor         | US              |
| <b>Recycling Technologies</b> | 20                           | Low Sulphur hydrocarbon<br>Plaxx – wax                    | Fluidized Bed              | UK              |
| <b>Plastic Energy</b>         | 20 – 30                      | Raw diesel, light oil, synthetic gas components           | Stirred-Tank Reactor       | Spain           |
| <b>Susteen Technologies</b>   | 12                           | Green Crude, Diesel, Gasoline and Jet fuel                | Screw with recirculation   | Germany         |
| <b>PHJK</b>                   | 12 – 14                      | Light crude oil, diesel                                   | Rotary kiln                | Finland         |

The majority of these industrial units are relatively far from urban areas and occupy a big space. Therefore, this increases the cost of transporting plastic waste to these units as well as the investment cost which is high. Moreover, almost all of these technologies is still under development and at the present time only a few demonstration or pilot plants are in operation globally, including Agilyx in the US and Recycling Technologies in the UK. However, only two plants or technologies have been in operation at the commercial scale for over a decade, which are Klean Industries in Japan and Plastic Energy company in Spain. Moreover, the technology that is used by the industrial companies is kept away from the scientific public and it is founded on trials and experimentation and later on up-scaling the system as has been illustrated.

### 1.4 Feedstock and operating parameters

In plastic pyrolysis, the key process parameters may influence the production of end products such as liquid oil, gases and char. Those important parameters may be summarized as the type of feedstock, temperature, heating rate, residence time, reactors type, and catalysts; the desired product can be achieved by setting these parameters. These operating parameters are reviewed and their effects are discussed in the following subsections.

### 1.4.1 Type of feedstock

Fundamentally, pyrolysis products are directly related to the chemical composition and chemical structure of the plastics (feedstock). Each type of plastics has its specific composition. This composition is normally reported in terms of the proximate analysis: a technique used to measure the chemical properties of plastic based on four particular elements which are moisture content, fixed carbon, volatile matter and ash content. Volatile matter and ash content are the major factors that influence the liquid and gas yields in pyrolysis process. High volatile matter enhance the liquid and non-condensable gases production while high ash content effects it oppositely (Goswami, 2004). Based on **Table 1-2**, polyolefin materials, PP and PE, have a very high volatile content, above 97 %, which makes them suitable for pyrolysis process (Anuar Sharuddin *et al.*, 2016).

High density polyethylene (HDPE) is a long linear polymer chain with high degree of crystallinity and low branching which leads to high strength properties. Due to that, HDPE is widely used in manufacturing of milk bottles, detergent bottles, oil containers, toys and more. These various applications contribute to about 18 % of plastic waste; HDPE is the third largest plastic type found in municipal solid waste (MSW) (Antelava *et al.*, 2019).

**Table 1-2:** Proximate analysis for polyolefin, PP and PE.

| Types of plastics                       | Moisture<br>(wt %) | Fixed carbon<br>(wt %) | Volatile<br>(wt %) | Ash<br>(wt %) |
|---|--------------------|------------------------|--------------------|---------------|
| <b>High-density polyethylene (HDPE)</b> | 0.00               | 0.03                   | 98.57              | 1.4           |
| <b>Low-density polyethylene (LDPE)</b>  | 0.00               | 0.00                   | 99.60              | 0.40          |
| <b>Polypropylene (PP)</b>               | 0.18               | 0.16                   | 97.85              | 1.99          |

In contrast to HDPE, low density polyethylene (LDPE) has more branching resulting in weaker intermolecular force, thus lower tensile strength and hardness. However, LDPE has better ductility than HDPE since the side branching causes the structure to be less crystalline and easy to be molded. It has an excellent resistance to water, so it is widely applied as plastic bags, wrapping foils for packaging, trash bags and much more. LDPE waste is known as the second largest plastic waste, 18 %, in MSW, after PP (Antelava *et al.*, 2019).

Polypropylene (PP) is a saturated polymer with linear hydrocarbon chain that has a good chemical and heat resistance. Unlike HDPE and LDPE, PP does not melt at a temperature below 160 °C. It has a lower density than HDPE but has higher hardness and rigidity that make it preferable in plastic industry. The diverse applications include flowerpot, office folders, car bumpers, pails, carpets, furniture, storage boxes and more. PP contributes to about 24 % in plastic wastes, this forms the largest amount of plastics found in MSW (Antelava *et al.*, 2019). Therefore, this study will focus on polyolefin, PP and PE, due to their high abundance, about 60 % of plastic wastes production, and their high volatile content, which gives them a great potential to be used in pyrolysis process.

### 1.4.2 Temperature of degradation

Temperature is one of the most significant operating parameters affecting pyrolysis since it controls the main cracking behavior of the polymers. Molecules are bounded together by Van der Waals force, whereas as temperature increases the molecules vibration also increases and it tends to evaporate as the vibration is great enough. However, the carbon chain will be broken if the energy induced by van der Waals force along the polymer chains is greater than the enthalpy of the C-C bond in the chain. This is the reason why high molecular weight polymer decomposes rather than boiling when it is heated in absence of oxygen (Sobko, 2008). Moreover, temperature has an important influence on the pyrolysis byproducts. Long chain hydrocarbons are produced at low temperatures, whereas short chain compounds are produced at elevated temperatures (above 500 °C).

Elordi *et al.* studied the influence of temperature on the distribution of the byproducts (Elordi *et al.*, 2011). They found that at 460 °C, a large proportion of viscous liquids with high content of long chain carbons are produced, while at 600 °C, a small proportion of light liquids with high aromatic contents are obtained. Meanwhile, Marcilla *et al.* (Marcilla *et al.*, 2009) studied the effect of temperature on the thermal pyrolysis process for HDPE and PP. They stated that the main degradation phase occurs within the range of 400 – 500 °C based on the thermogravimetric analysis (TGA) curves; however, the weight loss for PP pyrolysis started to occur below 400 °C. Moreover, they concluded that a further increase in temperature to 600 °C reduces only the oil yielding and increases the gaseous products. Moreover, in another study (Marcilla *et al.*, 2005), they found that

the maximum degradation rate for PP pyrolysis occurred at 447 °C, whereas HDPE pyrolysis occurred at 467 °C.

### 1.4.3 Heating rate and residence time

Heating rate also plays an important role in the pyrolysis process and influences the distribution of the byproducts. Pyrolysis process could be broadly classified as slow and fast depending on the heating rate. Slow pyrolysis heats up the material at low heating rates, approximately from 5 to 60 °C/min, up to a moderate temperature within the range of 400 – 600 °C (Basu, 2013). For example, the thermal degradation of the HDPE, at different heating rates in the range of 10 – 50 °C/min, starts at 378 – 404 °C and is almost completed at 517 – 539 °C based on the thermogravimetric analysis (TGA) results (Chin *et al.*, 2014). Moreover, slow pyrolysis promotes the formation of all of the three byproducts (oil, gas, and char) depending on the chemical composition of the pyrolyzed material, in other words depending on the proximate analysis. In addition, this process leads for secondary cracking reactions that ultimately lead to the increase of the light oil fraction in the byproducts.

On the other hand, fast pyrolysis is characterized by very high heating rates that can reach 1000 °C/s, consequently the residence time of the byproducts is in seconds. The primary goal of fast pyrolysis is to maximize the production of the oil yield, but the peak temperature should be below 650 °C, otherwise gas byproduct will be the dominant (Basu, 2013).

The definition of residence time varies according to the type of pyrolysis; for fast pyrolysis, like in some continuous reactors, the residence time represents the contact time of the plastic with the hot surface of the reactor. Mastral *et al.* (Mastral *et al.*, 2002) studied the effect of temperature and residence time on the composition of the byproducts of thermal cracking for HDPE in a fluidized bed reactor; the temperatures range was between 650 and 850 °C, whereas the residence time range was from 0.64 to 2.6 s. It was found that higher liquid yields were obtained at a longer residence time (2.6 s) for temperatures below 685°C, but above this temperature the residence time had less influence on the oil and gas yields.

On the other hand, in slow pyrolysis such as in batch and semi-batch reactors, the residence time is defined as the duration of time that plastic spends inside the reactor from the beginning till the end of the process. In this type of reactors, longer residence time increases the conversion of

primary products, thus more thermal stable byproducts are yielded such as light molecular weight hydrocarbons and non-condensable gases (Hernández *et al.*, 2006).

### 1.4.4 Catalyst

Catalysts are very important as they are used to optimize and enhance plastic pyrolysis process. Catalyst speeds up the pyrolysis reaction by shortening the long carbon chain molecules, thus it decreases the optimum pyrolysis temperature and increases the byproducts selectivity; surely, the overall pyrolysis process becomes more efficient. Generally, using catalyst increases the byproducts selectivity, oil or gaseous yields, by promoting the production of a restricted distribution of compounds (Elordi *et al.*, 2011). In addition, in some cases, the use of a catalyst increases the production of gas and in return decreases the oil yield but improves its quality. Ratnasari *et al.* (Ratnasari *et al.*, 2017) illustrated in their study that the catalytic plastic pyrolysis showed a higher conversion rate than the non-catalytic one (thermal pyrolysis) and improved the quality of oil byproduct at lower cracking temperatures. Also, the catalyst usage affects and enhances the physical properties of the oil byproducts such as viscosity, density, flash point, boiling range and heat calorific value (Miandad *et al.*, 2016). For these reasons, catalytic pyrolysis is an interesting process for obtaining byproducts compatible with the commercial interest and demand, such as light olefins ( $C_2 - C_4$ ), gasoline and diesel (Elordi *et al.*, 2009).

There are two types of catalysts, homogeneous and heterogeneous catalysts. The classical Lewis acid such as  $AlCl_3$  is a homogeneous catalyst mostly used for polyolefin pyrolysis (PE and PP) (Stelmachowski, 2010). On the other side, heterogeneous catalysts are the most commonly used since they can be easily separated from the fluid byproduct mixture. In addition, knowing that most catalysts are quite costly, it is economically preferable to use a heterogeneous catalyst since it can be recovered and reused again. Heterogeneous catalysts are classified as Nano-crystalline zeolites, conventional acid solid, mesostructured catalyst, metal supported on carbon, and basic oxides, each one has its own influence on the byproduct distribution (Stelmachowski, 2010).

For example, using zeolite catalysts decreases the heavy fractions present in the oil byproduct and increases the gasoline fraction ( $C_5 - C_{12}$ ), thus reducing the need for further improvement (Seo *et al.*, 2003). Moreover, Miskolczi *et al.* (Miskolczi *et al.*, 2009) reported that the use of ZSM-5 zeolite produced gases containing mainly  $C_3$  from PP, while  $C_2$  and  $C_4$  were produced from PE.

Therefore, zeolites increase the formation of branched and aromatic hydrocarbons and decrease the formation of linear paraffin and olefins. However, the catalyst/polymer ratio cannot exceed 20 wt% to avoid the domination of coke and gaseous products (Miskolczi *et al.*, 2009). Finally, knowing that aromatic hydrocarbons and light oil products are desired byproducts to be obtained, thus the usage of zeolite catalysts is more preferable.

### 1.5 Type of the reactor

Type of reactor has an important impact on residence time, on mixing the catalyst with the pyrolyzed material, and in enhancing heat transfer for more efficient process. Pyrolysis reactors can be classified as batch, semi-batch, and continuous. Moreover, there exist different types of pyrolysis continuous reactors such as, fixed bed, fluidized bed, screw kiln and rotary kiln, where each type has its advantages and disadvantages.

#### 1.5.1 Batch and semi-batch reactors

Batch reactor is basically a closed system with no inflow of reactants and no outflow of products while the reaction is being carried out. High conversion of matter can be achieved by leaving the reactants in the batch reactor for an extended time, which is an advantage. On the other hand, semi-batch reactor is more flexible since it allows the addition of the reactants or the removal of the byproducts continuously over time, which is an additional advantage. However, the drawbacks of batch and semi-batch reactors are the high labor costs per batch, the variability of the byproducts, and the difficulty of large-scale production. Moreover, there exist some issues when using catalyst because of the high tendency of coke formation on the surface of catalyst, which reduces the catalyst efficiency over time and causes high residue in the byproducts. Besides that, it is also a challenge to separate the catalyst from the char residue at the end of the experiment (Kassargy, 2018). Furthermore, according to literature, batch and semi-batch reactors have been widely adopted as small-scale plastic pyrolysis reactors due to their simple design, high conversion, and feasibility of controlling operating parameters (Kassargy, 2018).

Van Grieken *et al.* (Van Grieken *et al.*, 2001) studied catalytic and non-catalytic pyrolysis of PE (HDPE and LDPE) using a batch reactor, equipped with a stirrer, at three temperatures (380, 400 and 420 °C) and different residence times (0 – 360 min). Moreover, Abbas-Abadi *et al.* and Lee carried out other studies on PE pyrolysis using a semi-batch reactor with a stirrer (Abbas-Abadi *et*

*al.*, 2013; Lee, 2008). They concluded that the usage of an agitator increased the efficiency of the process by enhancing the mixing process between catalysts and plastics, and improving the heat transfer inside the reactor.

### 1.5.2 Fixed bed, fluidized bed, and rotary kiln reactors

Continuous reactor is an open control volume that allows reactants inflow and products outflow over time in a steady state process. This type of reactors, with complex design, is suitable for large industrial production. There exist different types of pyrolysis continuous reactors such as fixed bed, fluidized bed, and rotary kiln, where each type has its advantages and disadvantages.

In fixed-bed reactor, pyrolysis occurs on a stationary bed, where the catalyst is usually in a palletized form and packed in the static bed. It is easy to design and operate such reactor, but there are some constraints such as the irregular particle size and shape of plastics feedstock that would cause a problem during feeding process. Moreover, a high temperature gradient will exist due to the low thermal conductivity of plastics and the stacked bed. In addition, the area of the catalyst available at the reaction is also limited. Vasile et al (Vasile *et al.*, 2001) studied catalytic pyrolysis of PE and PP using PZSM-5 and HZSM-5 zeolites using a fixed bed reactor. The results of using the two catalysts influenced the oil yield and increased the gaseous yield to 65 % for PE and 57 % for PP, in addition to the increase of the aromatic hydrocarbons fraction in the byproducts. Moreover, using this type of reactor solves some problems such as the difficulty of recovering the catalyst at the end of the process and it overcomes the rapid deactivation of the catalyst when contacted with molten plastic. Therefore, in certain conditions, fixed bed reactors are simply used as a secondary pyrolysis reactor in order to crack the heavy oil fractions resulting from primary pyrolysis. But on the other hand, this configuration is still inefficient to be applied on a large scale because it is not profitable in terms of cost and results, since the obtained results are quite comparing to those of a one step process (Anuar Sharuddin *et al.*, 2016).

In contrast to fixed-bed reactor, the catalyst particles (about the size of grain of sand) in fluidized bed reactor are situated on a distributor plate, where the fluidizing gas, most often nitrogen gas, passes through it and carries the catalyst particles in a form of fluid state as illustrated in **Figure 1-2**. Several advantages can be reached like higher heat and mass transfer rates, negligible temperature gradient due to the good mixing, shorter residence time, and better access to the

catalyst area, since the catalyst is well-mixed with the fluid. Moreover, fluidized bed reactors overcome several problems that occur in fixed-bed reactors, in addition they are used to achieve fast pyrolysis. Several studies concerning plastic pyrolysis have been carried out using a fluidized bed reactor such as (Aida *et al.*, 2015; Del Remedio Hernández *et al.*, 2007).

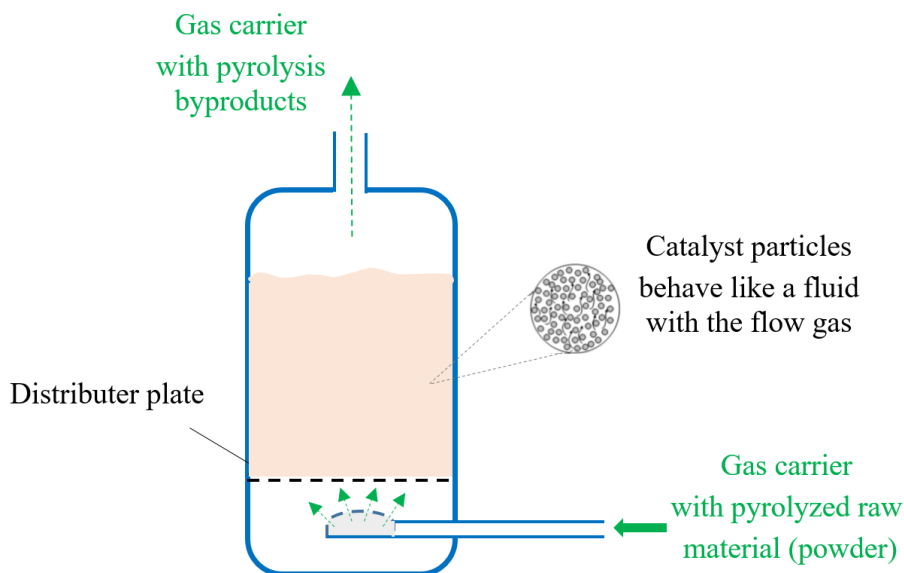


**Figure 1-2:** Schematic representation of fluidized bed reactor.

However, the industrial application of fluidized bed reactors is not suitable for plastic pyrolysis depending on different aspects. First, de-fluidization of the bed should be avoided, since molten plastic rapidly sticks to the fluidized bed and then it is hard to remove (Predel and Kaminsky, 2000). Secondly, raw materials (plastics) should be very fine in size, about 100  $\mu\text{m}$ , so that it can float in the fluid. Finally, there is a serious problem in separating the char residue from the bed material, as well as the external heating system and its recirculation, is much complicated. Consequently, this type of reactor is rarely used for plastic pyrolysis process in a large scale installation (Chen *et al.*, 2014).

Conical spouted bed reactor (CSBR), shown in **Figure 1-3(a)**, provides good mixing and heat transfer rate. Besides, it solves the problem of de-fluidization that occurs in fluidized bed reactors (Aguado *et al.*, 2005). Although, once plastic wastes are introduced to the reactor they melt and form a coating around the sand particles due to their cyclical movement. Furthermore, it is important to sustain a desired residence time, around 20 ms, to avoid side reactions (that promotes the char formation) from occurring (Wong *et al.*, 2015). For this reason, CSBR has complex design

that requires the utilization of several pumps, this leads to high operating cost (Anuar Sharuddin *et al.*, 2016). Then, there are varieties of technical challenges that are encountered during the operation such as the catalyst feeding and the collection of the byproducts (oil and char), so as a result the usage of such reactor becomes less favorable.

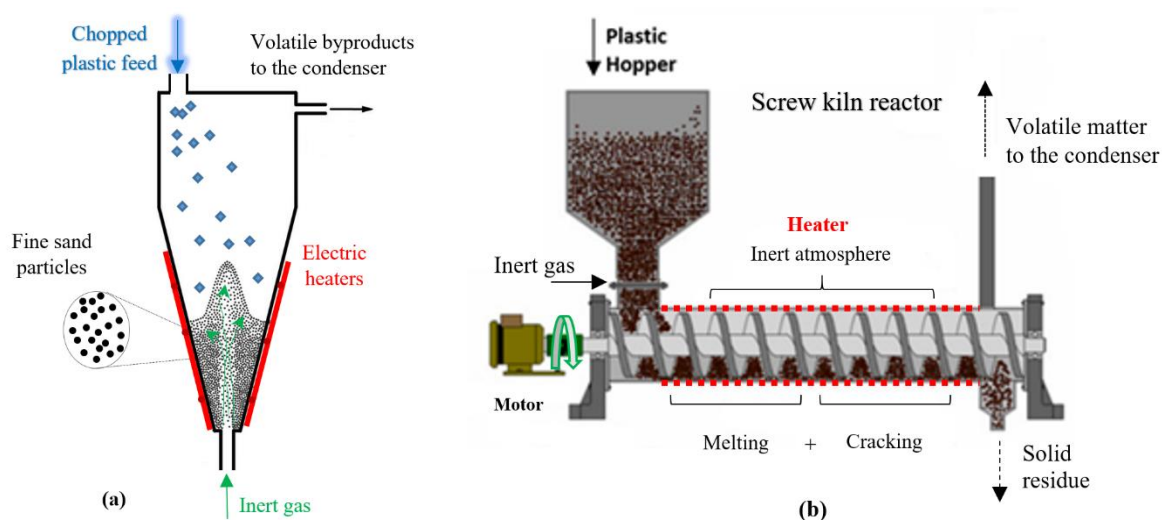


**Figure 1-3:** Conical spouted reactor (a), and screw kiln reactor (b).

A screw kiln reactor consists of a tubular reactor and a screw conveyor as shown in **Figure 1-3(b)**. Molten plastic or even plastic particles are fed to the reactor by the extruder this ensures good mixing and enhance heat distribution, as well, it permits controlling the pyrolysis temperature and heat transfer (Vasile *et al.*, 2001). Also different advantages can be listed like the flexibility and the feasibility of handling of the plastic pyrolysis continuously (Czajczyńska *et al.*, 2017; Wallis *et al.*, 2008). The feeding rate can be controlled by adjusting the rotational speed of the extruder, this leads to controlling the residence time inside the reactor. Unlike the other reactors, the screw kiln reactor overcomes easily a main problem which is the high viscosities of molten plastics, comparatively this is a significant advantage over conventional bed reactors. More and more, compared to a batch reactor, the screw kiln reactor reduces the secondary cracking phenomena and limits more the formation of gaseous products. As a result, almost all hydrocarbon fractions exhibit the same residence time inside the reactor, and so, this leads to a uniform distribution of the byproducts (Scheirs and Kaminsky, 2006). Finally, the screw kiln reactor is widely applied in the industrial scale and commercial plants due to its advantages and lower operating cost.

### 1.6 Importance of simulation using Finite Element Method

Finite element method (FEM) is a numerical technique used to solve and approximate the solution for physical phenomena and complex engineering problems. Moreover, over the last few decades finite element method was written and developed using computers to solve partial differential equations (PDEs) that describe and quantify most of the physical phenomena. Thus over the years, the potential of the method to solve different types of applied science and engineering problems such as structural mechanics, fluid behavior, heat transfer, aerodynamics, chemical engineering, electromagnetism and many other domains was verified. Nowadays, it is considered one of the best methods to solve a wide variety of practical problems efficiently (Rao, 2017). Furthermore, one of the most exciting prospects is its application to solve coupled problems such as fluid-thermo-structure interaction, thermomechanical, thermo-chemo-mechanical problems, etc....

Consequently, with FEM simulations, many design iterations and optimization are no longer dependent upon experimental prototyping and manufacturing; each new design can be virtually tested in hours, instead of waiting weeks or months for experimental building and testing and spending high amounts of money and budget. Conducting a design analysis in this way can extremely reduce the amount of physical testing and prototyping before the marketing. In addition, FEM allows easier modeling of complex geometrical and irregular shapes because the designer is allowed to model an entire system (interior and exterior), which is a great advantage for the product development. Furthermore, engineers can easily spot any vulnerability in design using FEM and also can determine the critical factors and parameters that are affecting or causing failure or success of a design. Hence, it is very efficient and necessary to model and simulate any process or design using FEM before building any prototype for the sake of experimentation (IEEE, 2019).

There are many well-known commercial software, based on FEM, performing computer simulation such as ANSYS, COMSOL Multiphysics, SimScale, Nastran, Abaqus, etc. Despite the reliability and the accuracy of all these software each one has its own specifications and characteristics and its advantages and disadvantages. So, it is necessary to choose which software to use based on the physical domain and the objective of the simulation. For this sake, a brief comparison will be illustrated below between two of the most popular and used software nowadays, which are ANSYS and COMSOL Multiphysics.

ANSYS is an American company founded in 1970 that develops and markets engineering simulation software for product design, testing and operation. It is a general-purpose software that could be used to model and simulate different engineering domains such as fluid flow, heat transfer, solid mechanics etc..., where the most famous software suite is the Fluent used for computational fluid dynamics (CFD) and heat transfer and other physics. Similarly, COMSOL Multiphysics is a cross-platform finite element analysis solver, founded in 1986 as COMSOL AB in Stockholm, Sweden. COMSOL provides an integrated development environment (IDE) and unified workflow for electrical, mechanical, fluid, heat transfer, and chemical applications. However, the main differences between the two software can be stated as follow (COMSOL, 2017; Mostafa and Farhoud, 2013):

1. COMSOL is oriented more towards the academia and research work, while ANSYS is more industry oriented.
2. COMSOL permits an easy access to the underlying equations for the modelled physics, whereas it is restricted in ANSYS.
3. COMSOL is more flexible to use comparing to ANSYS, where all of the model building blocks such as geometry, mesh, solvers and post processing are all in one window, this is not the case in ANSYS.
4. COMSOL is more user friendly comparing to ANSYS since it provides easier tools to be used. For example, in COMSOL the user-defined functions and equations are easier to be generated than ANSYS where it takes a lot of time and coding effort.
5. COMSOL provides the ability to define and solve (PDEs) in a weak form whereas in ANSYS it is very difficult to solve or even define a mathematical problem as (PDEs).
6. ANSYS could be more robust and stronger than COMSOL in solving some physics such as CFD.
7. COMSOL has an interesting feature that ANSYS doesn't have, which is the application builder tool that permits to build a friendly graphical user interface application that permits other users that don't know modelling to perform sensitivity studies and analysis.

As illustrated previously, numerical modeling and simulation using finite element method describe the scientific fundamentals beneath the real life processes and experiments, this provides better understanding of the physics behind. In addition, the use of simulation reduces the enormous loss

in time, cost, and labor that the experimental plastic pyrolysis up-scaling requires. As a consequence, understanding and simulating plastic pyrolysis process as a pure fundamental process is a first step in the path of optimizing and enhancing such processes. From here comes the importance of a lab-scale experimental studies to model and understand well the phenomena by validating the simulated results with the experimental ones and then designing efficient reactors or systems depending on the validated model. Moreover, the spatial modelling and simulating of such processes using finite element method and conventional software open the door for a cumulative knowledge that grows and describes accurately these complex phenomena in order to increase efficiency and utility of the process.

### 1.7 Melting models and equations

After illustrating the need in **section 1.3** (pyrolysis technology) and the importance in **section 1.6** of modelling and simulating plastic pyrolysis process, the main objective of this work is to apprehend and numerically model plastic pyrolysis process. But, knowing the fact that pyrolysis process passes through different sub-processes such as heating and melting, before undergoing thermal cracking, it is necessary to model the melting process as a first step then modelling the cracking part.

Modelling and simulating a buffer solution of plastic melting using FEM and commercial simulation software is rarely reported in literature. On the other hand, many researchers investigated melting process and heat convection for other relatively similar materials, which can help in modelling the plastic melting process. Madruga et al. (Madruga *et al.*, 2018) made experimental investigation and numerical simulation on melting tetracosane paraffin within a cubic enclosure. The initial temperature of tetracosane was set at 40 °C and the cube is heated from the bottom, the temperature was held at 80 °C; the thermal diffusivity was low and the tetracosane was heated and melted slowly. Also, they implemented several K-type thermocouples at different layers in the cube to measure and record the temperature of tetracosane, as it undergoes melting and heating. To model the phenomena, Madruga et al. carried out their simulations by coupling the Navier-Stokes equation, represented in **Eq. 1-1**, with the energy equation showed in **Eq. 1-3**, with an additional sink term in the energy equation; that accounts for the latent heat absorption during the melting process, and also additional terms in the Navier-Stokes equation to model the buoyancy flow of the molten paraffin. **Eq. 1-1** below shows the vectorial form of the modified

Navier-Stokes equations that was used, considering two-dimensional laminar and incompressible flow.

$$\begin{aligned} \rho \left[ \frac{\partial \vec{u}}{\partial t} + (\vec{u} \cdot \vec{\nabla}) \vec{u} \right] \\ = -\vec{\nabla} p + \vec{\nabla} \cdot \left( \mu \left( \vec{\nabla} \vec{u} + (\vec{\nabla} \vec{u})^T \right) \right) - \rho g [1 - \alpha(T - T_{ref})] \vec{e}_z \\ - \frac{C(1 - f_l)^2}{\epsilon + f_l^3} \vec{u} \end{aligned} \quad \text{Eq. 1-1}$$

where  $\vec{u} = u\vec{i} + v\vec{j} + w\vec{k}$  is the velocity vector (m/s),  $\vec{\nabla} = \frac{\partial}{\partial x}\vec{i} + \frac{\partial}{\partial y}\vec{j} + \frac{\partial}{\partial z}\vec{k}$  is the spatial gradient operator,  $\rho$  is the density ( $\text{kg.m}^{-3}$ ),  $p$  is the static pressure (Pa), and  $\mu$  is the dynamic viscosity (Pa.s). The third term in the right side of the equation contributes for the buoyancy force according to the Boussinesq approximation to model the natural convection flow due the density variance,  $T$  is the average temperature of the finite element control volume.  $g$  is the magnitude of gravity acceleration ( $\text{m.s}^{-2}$ ),  $\vec{e}_z$  is a unit vector pointing in the vertical direction upwards,  $T_{ref}$  is the reference temperature, based on it the physical properties are given i.e. melting temperature  $T_m$  (50 °C), and  $\alpha$  is the thermal expansion coefficient ( $9.4 \times 10^{-4} \text{ K}^{-1}$ ).  $f_l$  is a linear liquid fraction function depending on temperature as defined by **Eq. 1-2**, this is the master variable responsible for the phase change process (Madruga *et al.*, 2018).

$$f_l = \begin{cases} 0, & T \leq T_s \\ 1, & T \geq T_l \\ (T - T_s)/(T_l - T_s), & T_s < T < T_l \end{cases} \quad \text{Eq. 1-2}$$

where  $T_s$  (°C) and  $T_l$  (°C) are respectively the solid and liquid temperatures of tetracosane. The last term in the momentum equation, **Eq. 1-1**, provides an empirical proportionality relationship, due to Darcy law, between the pressure gradient in a porous medium and the fluid velocity within it and act as damping term between the solid and liquid phase. In this term,  $\epsilon \ll 1$  is a very small constant without physical meaning just to avoid diving by zero, whereas  $C$  ( $\text{N.s.m}^{-4}$ ) is a constant for the mushy region that depends on the media. When the control volume is completely liquid ( $f_l = 1$ ) the Darcy term is null, like in a single phase fluid, however when it is completely solid ( $f_l = 0$ ) the Darcy term diverges and the velocity of the liquid becomes null, therefore the control volume acts as a solid. Moreover, for the intermediary values of  $f_l$ , the phase change material (PCM) is in

the mushy state. The thermal energy of the system comes from the contribution of the usual sensible heat, due to changes of temperature in the solid and liquid phases of the PCM, and from the latent heat content. On the other hand, the last term in the energy equation, **Eq. 1-3**, below is the sink term due to the phase change from solid to liquid phase (Madruga *et al.*, 2018).

$$\rho((1 - f_l)C_{p,s} + f_l C_{p,l}) \left( \frac{\partial T}{\partial t} + \vec{u} \cdot \vec{\nabla} T \right) = \vec{\nabla} \cdot ((1 - f_l)k_s + f_l k_l) \vec{\nabla} T - \rho L \frac{\partial f_l}{\partial t} \quad \text{Eq. 1-3}$$

where  $L$  (J.kg<sup>-1</sup>) is the latent heat of fusion (melting),  $C_{p,s}$  and  $C_{p,l}$  (J.K<sup>-1</sup>.kg<sup>-1</sup>) are respectively the solid and liquid heat capacities, and  $k_s$  and  $k_l$  (W.K<sup>-1</sup>.m<sup>-1</sup>) are respectively the solid and liquid thermal conductivities. Madruga *et al.* used the open source software OpenFOAM based on the finite element approach to simulate the time evolution of the model, then they compared the experimental and simulated results. In addition, they used the PIMPLE (Pressure Implicit Method for Pressure-Linked Equations) algorithm to solve the coupled momentum and energy equations. Finally, they stated the model implementation was very successful and typical for phase change problems in rectangular and circular geometries, with low Prandtl numbers for liquid metals and high Prandtl numbers for paraffin and other similar materials. In addition, they reported that the numerical and experimental results were in a good agreement.

On the other side, Samara *et al.* and Murray used a similar approach in modelling melting process for phase change material (RT25) and octadecane respectively (Murray and Groulx, 2011; Samara *et al.*, 2012). Again they used almost the same conversion function  $f_l$ , damping term (Darcy), and buoyancy term in the momentum equation, **Eq. 1-1**, but the latent heat ( $L$ ) was not added directly as a heat sink in the energy equation, **Eq. 1-3**. However, they attributed the latent heat effect to the heat capacity property of the material, where this method is called apparent heat capacity method (AHCM). Moreover, they used a Gaussian function shown by **Eq. 1-4**,  $D(T)$ , to account for the normal distribution of the latent heat over an interval of melting temperature. This function has a value of zero everywhere except the interval  $(T_m - \Delta T_m/2)$  to  $(T_m + \Delta T_m/2)$ , centered at  $T_m$ , where  $\Delta T_m = T_l - T_s$ . However, its integral is equal to 1, thus  $D(T)$  is multiplied by the latent heat of fusion ( $L$ ) and added to the heat capacity as shown in **Eq. 1-5**, which closes the energy balance in the energy equation.

$$D(T) = \frac{4 \exp(-8(T - T_{pc})^2 / (\Delta T_m)^2)}{\Delta T_m \sqrt{2\pi}} \quad \text{Eq. 1-4}$$

$$\rho((1 - f_l)C_{p,s} + f_l C_{p,l} + L D(T)) \left( \frac{\partial T}{\partial t} + \vec{u} \cdot \vec{\nabla} T \right) = \vec{\nabla} \cdot ((1 - f_l)k_s + f_l k_l) \vec{\nabla} T \quad \text{Eq. 1-5}$$

This apparent heat capacity method (AHCM) was used also by Salvi et al. to model the phase change (boiling) for a carboxymethyl cellulose solution heated by microwave induction (Salvi *et al.*, 2011). They used the normal distribution Gaussian function  $D(T)$  to model the latent heat during phase change, this term is added to the heat capacity. COMSOL Multiphysics was used to develop and simulate the numerical model, where the simulated results were validated against experimental temperature profiles.

This apparent heat capacity method (AHCM) was used frequently in different research studies to incorporate the phase change phenomenon (Curet *et al.*, 2006; Pryor, 2007; Vallejos and Duston, 2005), due to its major advantage; it provides a convenient way to use the momentum equation in the whole domain and to model the phase change when fluid motion is present without the complication of tracking the solid/liquid or liquid/gas interfaces. Furthermore, the apparent heat capacity method (AHCM), is a built-in feature in COMSOL Multiphysics, where the method is modified and enhanced as shown in **Eq. 1-6**. The conversion function  $f_l$  is smoothed at the corners which prevents simulation divergence and sudden change in properties, as shown in **Figure 1-4**. In addition, the conversion function is differentiated with respect to temperature and multiplied by the latent heat ( $L$ ) then added to the heat capacity. Moreover, the integration of  $\partial f_l / \partial T$  over  $\Delta T_m$  is set equal to 1 to ensure exact latent heat absorbed or released in each cell or element. Finally, the major advantage of this method is that the location of the phase interface does not need to be known ahead of time (COMSOL, 2017).

$$\rho \left( (1 - f_l)C_{p,s} + f_l C_{p,l} + L \frac{\partial f_l}{\partial T} \right) \left( \frac{\partial T}{\partial t} + \vec{u} \cdot \vec{\nabla} T \right) = \vec{\nabla} \cdot ((1 - f_l)k_s + f_l k_l) \vec{\nabla} T \quad \text{Eq. 1-6}$$

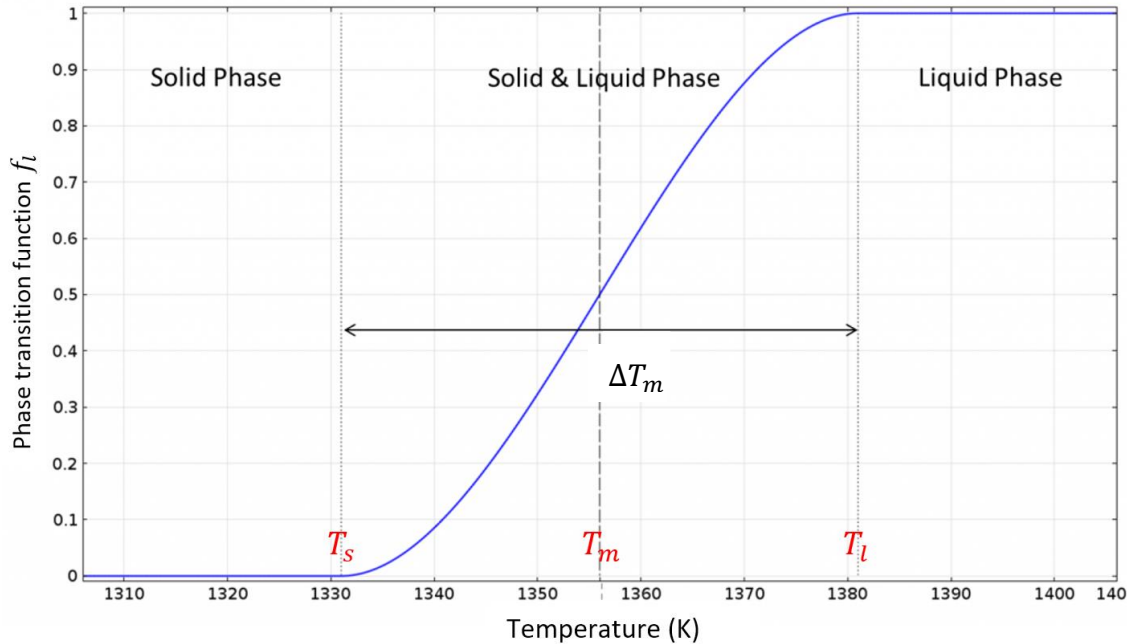


**Figure 1-4:** Conversion function  $f_i$  used in AHCM built-in COMSOL.

## 1.8 Newtonian and non-Newtonian fluids

Polymers are known to be very viscous material in the molten state or liquid state and they said to be non-Newtonian fluids. Therefore, it is necessary to know the viscosity of molten plastic and how it act in the system.

First fluids can be classified into two general types: Newtonian and non-Newtonian fluids. Newtonian fluids are mainly described by the constant proportionality between shear stress  $\vec{\tau}$  (Pa) and shear strain rate  $\dot{\gamma}$  ( $s^{-1}$ ), as shown in **Figure 1-5**. This constant proportionality is called the dynamic viscosity  $\mu = \mu(T, p)$  which may vary with temperature and pressure, but temperature has the major effect, as illustrated by Eq. (7). On the other hand, non-Newtonian fluids don't have such proportionality, however they have an apparent viscosity  $\eta$  (Pa.s) function of the shear strain rate tensor  $\dot{\gamma}_{ij}$ ,  $\eta = f(\dot{\gamma}_{ij})$ . Therefore, a nonlinear relation between shear stress and shear strain rate exist (Ionescu *et al.*, 2020).

Moreover, non-Newtonian fluids can be either time-independent or time-dependent. Time-independent fluids, for example polymers, are the fluids where their apparent viscosity  $\eta$  is independent of the duration of shearing, i.e. the shearing time doesn't affect the viscosity. On the other hand, time-dependent non-Newtonian fluid viscosity depends on both shear strain rate and

shear time, such as many industrial materials as well as some common food materials. The most common example is honey: when it is sheared at a constant rate (i.e. constant shear stress), following a period of rest, its apparent viscosity gradually decreases as its internal ‘structure’ breaks down progressively. Moreover, time-independent non-Newtonian fluids can be divided into three categories, shear-thinning or pseudoplastic, shear-thickening or dilatant, and viscoelastic, as shown in **Figure 1-5** (Gan, 2012).

A fluid is said to be pseudoplastic or shear-thinning when its apparent viscosity  $\eta$  decreases with the increase of the shear strain rate  $\dot{\gamma}_{ij}$ . This behavior is one of the polymer’s (molten plastic) characteristics, which is the concern of this work. Alternately, the apparent viscosity of the dilatant or shear-thickening fluid increases with the increase of the shear strain rate. However, the third type, viscoelastic, is characterized by a minimal yield stress  $\tau_0$  that must be exceeded before the flow occurs, such as cosmetic creams, toothpaste, tomato paste, mayonnaise (Ionescu *et al.*, 2020).

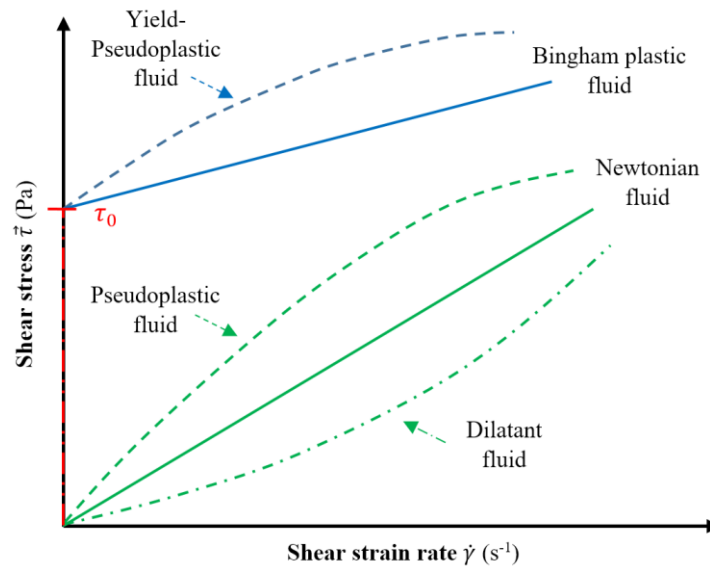


**Figure 1-5:** Shear stress versus rate of strain for time-independent non-Newtonian fluids.

As said before that the shear stress tensor is related to the shear strain rate tensor by the viscosity term, thus **Eq. 1-7** it represents the general formula for incompressible Newtonian fluids (White, 2007).

$$\vec{\tau}_{ij} = 2\mu\dot{\gamma}_{ij} \quad \text{Eq. 1-7}$$

On the other hand, for non-Newtonian fluids especially pseudoplastic fluid, the dynamic viscosity term,  $\mu$ , is replaced with the apparent viscosity as shown in **Eq. 1-8** below., This latter,  $\eta$ , is modeled by different models found in literature.

$$\vec{\tau}_{ij} = 2\eta\dot{\gamma}_{ij} \quad \text{Eq. 1-8}$$

The first simple and famous model is the Power Law model or also known as the Ostwald–De Waele model, which defines the apparent viscosity for pseudoplastic fluid as the following (Gan, 2012).

$$\eta = M(\dot{\gamma}_{ij})^{n-1} \quad \text{Eq. 1-9}$$

where  $M$  and  $n$  are two empirical curve-fitting parameters known as the fluid consistency coefficient ( $\text{Pa}\cdot\text{s}^n$ ) and the flow behavior index (1), respectively. **Table 1-3** provides some results of the power-law constants ( $M$  and  $n$ ) for a variety of polymer melts. For a shear-thinning fluid, the index may have any value between 0 and 1. However, smaller values of  $n$  refer to the greater degree of shear-thinning. Moreover, the equation becomes constitutive to describe Newtonian fluid when the index value equals one,  $n = 1$  (Gan, 2012).

**Table 1-3:** Typical values of power-law parameters for different molten polymers.

| Molten polymers                         | Temperature (°C) | $n$        | $M$ ( $\text{Pa}\cdot\text{s}^n$ ) $\times 10^3$ |
|---|------------------|------------|--|
| <i>High density polyethylene (HDPE)</i> | 180 – 220        | 0.6        | 3.75 – 6.2                                       |
| <i>High impact polystyrene</i>          | 170 – 210        | 0.2        | 35 – 75  |
| <i>Polystyrene</i>                      | 190 – 225        | 0.25       | 15 – 45  |
| <i>Polypropylene</i>                    | 180 – 200        | 0.4        | 4.5 – 7  |
| <i>Low density polyethylene (LDPE)</i>  | 160 – 200        | 0.45       | 4.3 – 9.4  |
| <i>Nylon</i>                            | 220 – 235        | 0.65       | 1.8 – 2.6  |
| <i>Polymethylmethacrylate (PMMA)</i>    | 220 – 260        | 0.25       | 25 – 90  |
| <i>Polycarbonate</i>                    | 280 – 320        | 0.65 – 0.8 | 1 – 8.5  |

Although the power-law model offers the simplest representation of shear-thinning behavior, it does have some limitations. Generally, it is applied over the intermediate range of shear strain rates and it does not predict the zero and infinite shear viscosities,  $\eta_0$  and  $\eta_\infty$  respectively. Despite these

limitations, the Power Law model is the most widely used in literature dealing with different process engineering applications.

On the other hand, other models like Cross and Carreau models describe the pseudoplastic apparent viscosity behavior over a wider range of shear strain rate. The Cross model is shown in **Eq. 1-10** below.

$$\frac{\eta - \eta_{\infty}}{\eta_0 - \eta_{\infty}} = \frac{1}{1 + (\lambda\dot{\gamma}_{ij})^n} \quad \text{Eq. 1-10}$$

where  $n$  (-) and  $\lambda$  (s) are two fitting parameters and  $\eta_0$  and  $\eta_{\infty}$  are the limiting values of the apparent viscosity at low and high shear rates, respectively. An initial suggestion for the Cross model is taking a constant value of  $n=2/3$ , which is adequate to approximate the viscosity data for a wide variety of pseudoplastic media. However, it is now better to treat the index,  $n$ , as an adjustable parameter which offers a considerable improvement over the use of the constant value of  $n$  (Barnes *et al.*, 1989).

On the other hand, when there are significant deviations from the power-law model at very high and very low shear rates, it is necessary to use the Carreau (1972) model which takes account of the limiting values of viscosities  $\eta_0$  and  $\eta_{\infty}$ . The Carreau model is represented by **Eq. 1-11**.

$$\frac{\eta - \eta_{\infty}}{\eta_0 - \eta_{\infty}} = \left(1 + (\lambda\dot{\gamma}_{ij})^2\right)^{\frac{n-1}{2}} \quad \text{Eq. 1-11}$$

where  $\lambda$  (s) and  $n$  are also two curve-fitting parameters that represent the relaxation time of the fluid and the power index of the flow, respectively. In addition, the Carreau model shows a Newtonian behavior at very low and very high shear strain rates having apparent viscosities  $\eta_0$  and  $\eta_{\infty}$  respectively as shown in **Figure 1-6**. However, at moderate shear strain rates it acts following a Power Law model. The relaxation time  $\lambda$  (s) is equal to the inverse of the strain rate value at which the fluid changes from Newtonian to Power Law behavior. This model can describe shear thinning-behavior, i.e. molten plastic, over wide ranges of shear strain rates, in addition it is more convenient than the Cross model in modelling the transition between Newtonian and Power law behavior for some polymers (Aho, 2011).

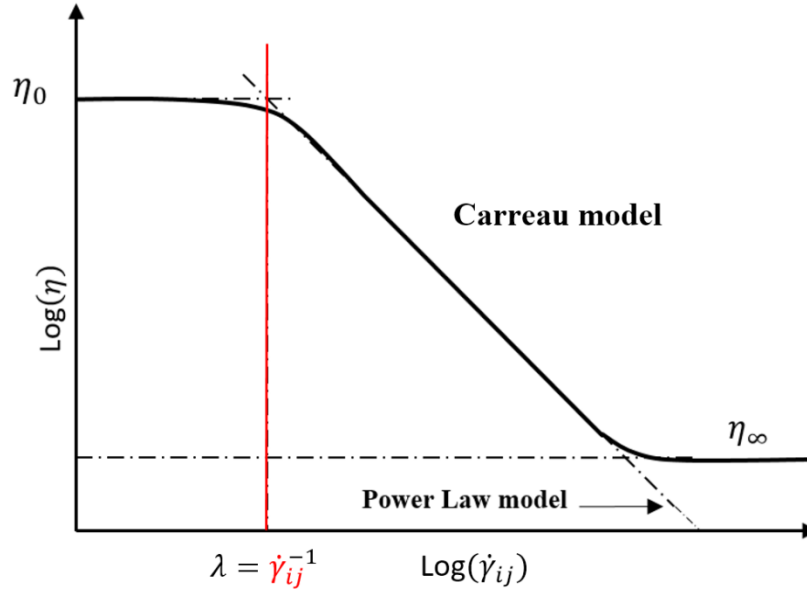


**Figure 1-6:** Variation of apparent viscosity with respect to strain rate according to Carreau model.

Thomas and David, (Bress and Dowling, 2011) stated, in their study about viscosity of molten plastic (Styron 615APR), that the best-fitting Carreau parameters for molten plastic, at 245 °C, resulted as following,  $\eta_0 = 295$  Pa.s,  $\lambda = 0.019$  s, and  $n = 0.42$ . Moreover, they stated that at intermediate shear strain rates, the Carreau model reduces to the simpler Power Law model, with  $n = 0.42$  and  $M = 2900$  Pa.s<sup>n</sup>.

Therefore, when modeling molten plastic flow, the dynamic viscosity is replaced by the apparent viscosity  $\eta$  based on one of the three preceding models. Whereas, the Power Law model can be used to model molten plastic flow at moderate flow rates, whereas, Cross and Carreau models can be used for the whole range, from low and high flow rates up to  $10^{10}$  s<sup>-1</sup> shear strain rate.

## 1.9 Plastic pyrolysis kinetics

After illustrating the models that can describe plastic melting process, which is sub-process of pyrolysis, and in order to proceed to plastic pyrolysis modelling (cracking phase), plastic pyrolysis kinetics must be studied and well understood at the first place. Studying plastic pyrolysis kinetics is done mainly by applying and using the isoconversional methods to interpret the thermogravimetric analysis (TGA) results of plastic pyrolysis, done by a thermogravimetric analyzer. These methods are different mathematical models applied to the TGA results in order to

find the activation energy  $E$  (J/mol) and pre-exponential factor  $A$ (s<sup>-1</sup>) characteristic of plastic pyrolysis reaction.

Thermogravimetric analysis is a thermal treatment protocol applied to plastics to perform thermal analysis for undergoing pyrolysis process. The thermogravimetric analyzer continuously measures mass and temperature of a sample (particle scale) over time at different desired heating rates. In addition, it provides different beneficial data results such as the weight loss of the sample and its derivative over time or temperature, which is essential to understand and model pyrolysis process (Coats and Redfern, 1963).

Moreover, to proceed with studying plastic pyrolysis kinetics, the equation that describes the kinetic or the rate of a certain chemical reaction should be introduced first. **Eq. 1-12** below is known as the kinetic equation, or sometimes called Friedman equation, it describes the rate of conversion,  $dx/dt$  (s<sup>-1</sup>), of plastic that undergoes pyrolysis reaction. Where,  $K(T)$  (s<sup>-1</sup>) represents the kinetic constant of the reaction and  $f(x)$  presents the reaction model of pyrolysis (Friedman, 1964).

$$\frac{dx}{dt} = K(T) f(x) \quad \text{Eq. 1-12}$$

where  $x$  is the conversion function ( $0 < x < 1$ ) which is defined by the following equation

$$x = \frac{m_0 - m_t}{m_0 - m_\infty} \quad \text{Eq. 1-13}$$

where  $m_0$  (mg) is the initial mass,  $m_t$  is the residual mass (mg) at time  $t$  (s), and  $m_\infty$  is the residual mass (mg) at the end of the process. Furthermore,  $K(T)$  is a function depending on temperature, and is also represented by the Arrhenius equation, **Eq. 1-14**, where  $E$  (J/mol) is the activation energy,  $A$  is the pre-exponential factor also called the frequency factor, and  $R$  is the universal gas constant (8.314 J/mol.K).

$$K(T) = A \exp\left(\frac{-E}{RT}\right) \quad \text{Eq. 1-14}$$

The reaction model  $f(x)$  can be one of the most common reaction mechanisms listed in **Table 1-4** (Aboulkas *et al.*, 2010), where  $g(x)$  is the integrated form of the reciprocal of the reaction model  $f(x)$ , with respect to the conversion  $dx$ , **Eq. 1-15**:

$$g(x) = \int_0^x \frac{dx}{f(x)} \quad \text{Eq. 1-15}$$

As a result, the aim of the kinetic study is to find and determine the kinetic triplet:  $E$ ,  $A$ , and  $f(x)$  that best describe the plastic pyrolysis process.

First of all, the reaction model  $f(x)$  is determined by the Criado's method, **Eq. 1-16**, which is a graphical curve-fitting method that compares and fits the experimental TGA results with all the theoretical reaction models  $f(x)$  found in literature, listed in **Table 1-4**.

$$\frac{z(x)}{z(0.5)} = \frac{f(x)g(x)}{f(0.5)g(0.5)} = \left( \frac{T_x^2}{T_{0.5}^2} \right) \frac{(dx/dt)_x}{(dx/dt)_{0.5}} \quad \text{Eq. 1-16}$$

**Table 1-4:** Reaction model for the most common reaction mechanism.

| <i>Mechanism</i>                        | <i>f(x)</i>                             | <i>g(x)</i>                  |
|---|---|------------------------------|
| <b>First-order (F1)</b>                 | $(1 - x)$                               | $-\ln(1 - x)$                |
| <b>Second-order (F2)</b>                | $(1 - x)^2$                             | $(1 - x)^{-1} - 1$           |
| <b>Third-order (F3)</b>                 | $(1 - x)^3$                             | $[(1 - x)^{-2} - 1]/2$       |
| <b>Power law (P2)</b>                   | $2x^{1/2}$                              | $x^{1/2}$                    |
| <b>Power law (P3)</b>                   | $3x^{2/3}$                              | $x^{1/3}$                    |
| <b>Power law (P4)</b>                   | $4x^{3/4}$                              | $x^{1/4}$                    |
| <b>One-dimensional diffusion (D1)</b>   | $1/2(x)$                                | $x^2$                        |
| <b>Two-dimensional diffusion (D2)</b>   | $[-\ln(1 - x)]^{-1}$                    | $[(1 - x)\ln(1 - x)] + x$    |
| <b>Three-dimensional diffusion (D3)</b> | $3(1 - x)^{2/3}/[2(1 - (1 - x)^{1/3})]$ | $[1 - (1 - x)^{1/3}]^2$      |
| <b>Ginstling-Brounshtein (D4)</b>       | $3/2[(1 - x)^{-1/3} - 1]$               | $1 - (2x/3) - (1 - x)^{2/3}$ |
| <b>Contracting cylinder (R2)</b>        | $2(1 - x)^{1/2}$                        | $[1 - (1 - x)^{1/2}]$        |
| <b>Contracting sphere (R3)</b>          | $3(1 - x)^{2/3}$                        | $[1 - (1 - x)^{1/3}]$        |
| <b>Avrami-Erofe'va (A2)</b>             | $2(1 - x)[- \ln(1 - x)]^{1/2}$          | $[- \ln(1 - x)]^{1/2}$       |

|                               |                            |                      |
|-------------------------------|----------------------------|----------------------|
| <b>Avarami-Erofe' ve (A3)</b> | $3(1-x)[- \ln(1-x)]^{2/3}$ | $[- \ln(1-x)]^{1/3}$ |
| <b>Avarami-Erofe' ve (A4)</b> | $4(1-x)[- \ln(1-x)]^{3/4}$ | $[- \ln(1-x)]^{1/4}$ |

After that, the normalized experimental and theoretical data, expressed by **Eq. 1-17** and **Eq. 1-18**, are plotted and compared at each heating rate (Criado, 1978).

$$f_{\text{experimental}} = \left( \frac{T_x^2}{T_{0.5}^2} \right) \frac{(dx/dt)_x}{(dx/dt)_{0.5}} \quad \text{Eq. 1-17}$$

$$f_{\text{theoretical}} = \frac{f(x)g(x)}{f(0.5)g(0.5)} \quad \text{Eq. 1-18}$$

where  $T_{0.5}$  and  $(dx/dt)_{0.5}$  represent the temperature and conversion rate at conversion  $x = 0.5$  respectively. Note that the purpose of dividing by 50 % condition is to normalize the function  $z(x)$ . Then, the coefficient of determination ( $R^2$ ) is calculated between the experimental curves and the theoretical curves for each heating rate ( $\beta$ ). However, the models that have the highest regression coefficient ( $R^2$ ) are said to be the best fitting reaction models that describe the pyrolysis reaction (Das and Tiwari, 2017).

The second step in plastic pyrolysis kinetic study is to find the activation energy  $E$  (J/mol), thus the isoconversional method concept must be introduced. The kinetic equation or so-called Friedman equation (FR), **Eq. 1-12**, is manipulated by applying the logarithmic function on both sides and differentiating by  $1/T$  at a constant conversion  $x$  to give **Eq. 1-19** (Vyazovkin *et al.*, 2011).

$$\left[ \frac{\partial \ln(dx/dt)}{\partial(T^{-1})} \right]_x = -\frac{E}{R} \quad \text{Eq. 1-19}$$

Thus, from interpreting Eq. (19) the isoconversional concept is illustrated, where it states that the rate of conversion ( $dx/dt$ ) at a constant conversion ( $x$ ) is only function of temperature. Therefore, the activation energy  $E$  (J/mol) is the same at each constant conversion  $x$  for different temperatures at different heating rates. Different isoconversional methods are invented to calculate the activation energy at every conversion  $x$  using the TGA experimental results ( $x$ ,  $dx/dt$ ,  $1/T$ , and  $\beta$ ). The Friedman method, expressed by **Eq. 1-20**, is the first differential isoconversional method, where the activation energy is determined from the slope ( $-E/R$ ) of the linear fitting straight lines from

plotting  $\ln(dx/dt)$  with respect to  $1/T$  for different heating rates at each constant conversion  $x$ ; then the coefficient of determination ( $R^2$ ) is calculated between the linear fitting straight lines and the experimental data or points to be compared later on with the results of the other isoconversional methods (Snegirev *et al.*, 2013).

$$\ln\left(\frac{dx}{dt}\right) = \ln[A f(x)] - \frac{E}{RT} \quad \text{Eq. 1-20}$$

Now After introducing the isoconversional concept, the kinetic equation, **Eq. 1-12**, can be written as

$$\frac{dx}{dT} = \frac{A}{\beta} \cdot \exp\left(\frac{-E}{RT}\right) \cdot f(x) \quad \text{Eq. 1-21}$$

where  $\beta$  ( $^{\circ}\text{C}/\text{min}$ ) is the constant linear heating rate,  $\beta = dT/dt$ , so by splitting variables and integrating both sides we obtain

$$g(x) = \int_0^x \frac{dx}{f(x)} = \frac{A}{\beta} \int_{T_0}^T \exp\left(\frac{-E}{RT}\right) dT = \frac{A}{\beta} I(E, T) \quad \text{Eq. 1-22}$$

However, since there is no analytical solution for the integral  $I(E, T)$ , the aforementioned integral can be written in another numerical form,  $g(y)$  having an approximate function  $p(y)$ , such as

$$g(x) \cong g(y) = \frac{AE}{R\beta} \left[ \frac{\exp(-y)}{y} - \int_y^{\infty} \left( \frac{\exp(-y)}{y} \right) dy \right] = \frac{AE}{R\beta} p(y) \quad \text{Eq. 1-23}$$

where  $y = E/RT$  is the reduced activation energy at the temperature  $T$ . Moreover, the approximate integral,  $p(y)$ , can be replaced by a number of useful approximations. From here came the integral isoconversional methods. Akahira and Sunose (Akahira and Sunose, 1971) used  $p(y) \cong e^{-y}/y^2$  as an approximation function then they linearized and rearranged both sides of the previous equation, **Eq. 1-23**, to get the known Kissinger-Akahira-Sunose equation (KAS), **Eq. 1-24**.

$$\ln\left(\frac{\beta}{T^2}\right) = -\frac{E}{RT} + \ln\left(\frac{AR}{Eg(x)}\right) \quad \text{Eq. 1-24}$$

This equation is used in the same manner as the FR equation; it was used to calculate activation Energy  $E$  i.e. from the slope of the fitting lines of  $\ln(\beta/T^2)$  vs  $1/T$  at all the heating rates, under the isoconversional principle at each constant conversion. KAS method is categorized as an

integral method since it uses an approximation function to solve the integral of  $g(x)$ , however FR method is a differential method.

Similarly to KAS method, other two integral methods are derived using different approximation of the numerical integral function  $p(y)$  such as Ozawa-Flynn-Wall method (OFW) (Flynn, 1983; Flynn and Wall, 1966) and Starink method (Starink, 2003), **Eq. 1-25** and **Eq. 1-26** respectively. These methods are applied in the same manner as the FR and KAS methods to evaluate the activation energy  $E$  using the experimental TGA results.

$$\ln \beta = -1.052 \frac{E}{R T} + \ln \left[ \frac{A E}{R g(x)} \right] - 5.331 \quad \text{Eq. 1-25}$$

$$\ln \left( \frac{\beta}{T^{1.92}} \right) = -1.0008 \frac{E}{R T} + \ln \left[ \frac{A E}{R g(x)} \right] + \ln \left( \frac{R}{E} \right)^{1.92} - 0.312 \quad \text{Eq. 1-26}$$

On the other side, there exist another method which performs a numerical integration for the kinetic integral,  $I(E, T)$ , instead of using approximation function such as  $p(y)$ . One such method is called the advanced isoconversional method (AIC) developed by Vyazovkin et al. (Vyazovkin *et al.*, 2011). AIC method can be applied for any arbitrary temperature programs  $T_i(t_x)$  including cooling processes (negative heating rate). The value of  $E$  at each conversion is determined by minimizing the following function presented in **Eq. 1-27** (Vyazovkin and Wight, 1997, 1998).

$$\Phi(E) = \sum_{i=1}^n \sum_{j \neq i}^n \frac{J[E, T_i(t_x)]}{J[E, T_j(t_x)]} = 0 \quad \text{Eq. 1-27}$$

Where, the temperature integral:

$$J[E, T_i(t_x)] \equiv \int_{t_{(x-\Delta x)}}^{t_x} \exp \left[ \frac{-E}{R T_i(t_x)} \right] dt \quad \text{Eq. 1-28}$$

is solved numerically, i.e. by the Trapezoidal rule. Minimization is repeated for every conversion  $x$  to obtain the relative dependency between  $E$  and  $x$ .

Finally, the third kinetic parameter  $A$  (1/s) is determined from each isoconversional equation, **Eq. 1-20**, **Eq. 1-24** and **Eq. 1-26**, by calculating the intercept values for the fitting straight lines at each conversion  $x$  and by using the deduced previous kinetic parameters  $E$  and  $f(x)$ . Then the theoretical

## Bibliography

conversion is determined according to the deduced kinetic triplet for all of the preceding isoconversional methods for the sake of comparison and finding the best fitting kinetic parameters.

A kinetic pyrolysis study done by Pallab and Pankaj (Das and Tiwari, 2017) for LDPE, HDPE, and PP at seven different heating rates (5, 10, 15, 20, 30, 40, 50 K/min) and by using five isoconversional methods with temperature range of 303 – 973 K. The study showed the calculated range values of the kinetic triplet of the three materials depending on the usage of the five isoconversional methods, where the results are listed in **Table 1-5** below.

**Table 1-5:** Kinetic parameters for LDPE, HDPE, and PP pyrolysis determined according to the conventional isoconversional methods at seven heating rates, 5, 10, 15, 20, 30, 40, 50 K/min.

| Material | Isoconversional methods | $E$ (kJ/mol) | $A$ ( $\text{min}^{-1}$ )                   | $f(x)$ |
|----------|-------------------------|--------------|---|--------|
| LDPE     | Friedman                | 178 – 256    | $2.79 \times 10^{11} - 1.64 \times 10^{17}$ | R2     |
|          | OFW                     | 165 – 242    | $5.77 \times 10^{10} - 1.78 \times 10^{16}$ |        |
|          | KAS                     | 162 – 242    | $3.67 \times 10^{10} - 1.72 \times 10^{16}$ |        |
|          | Starink                 | 148 – 222    | $4.07 \times 10^9 - 8.44 \times 10^{14}$    |        |
|          | AIC                     | 170 – 231    | $9.19 \times 10^{10} - 3.59 \times 10^{15}$ |        |
| HDPE     | Friedman                | 134 – 258    | $1.89 \times 10^8 - 2.34 \times 10^{17}$    | R2     |
|          | OFW                     | 146 – 242    | $1.26 \times 10^9 - 1.57 \times 10^{16}$    |        |
|          | KAS                     | 146 – 241    | $1.18 \times 10^9 - 1.52 \times 10^{16}$    |        |
|          | Starink                 | 146 – 240    | $1.06 \times 10^9 - 1.23 \times 10^{16}$    |        |
|          | AIC                     | 143 – 233    | $8.06 \times 10^8 - 4.29 \times 10^{15}$    |        |
| PP       | Friedman                | 124 – 187    | $4.74 \times 10^7 - 4.98 \times 10^{12}$    | R3     |
|          | OFW                     | 140 – 176    | $5.77 \times 10^8 - 9.65 \times 10^{11}$    |        |
|          | KAS                     | 136 – 173    | $3.22 \times 10^8 - 5.91 \times 10^{11}$    |        |
|          | Starink                 | 136 – 173    | $2.92 \times 10^8 - 5.16 \times 10^{11}$    |        |
|          | AIC                     | 133 – 233    | $1.82 \times 10^8 - 5.48 \times 10^{11}$    |        |

Moreover, **Table 1-6** illustrates a comparable values of kinetic parameters achieved by previous studies using various methods in literature (Das and Tiwari, 2017).

**Table 1-6:** Kinetic parameters reported in literature for LDPE, HDPE, and PP using various isoconversional methods.

| <b>Material</b> | <b>Isoconversional methods</b> | $E$ (kJ/mol) | $A$ ( $\text{min}^{-1}$ ) | $f(x)$                            |
|-----------------|--------------------------------|--------------|---------------------------|-----------------------------------|
| <b>LDPE</b>     | DTG <sup>†</sup> curve fitting | 222          | –                         | $n^{\text{th}}$ order; $n = 0.7$  |
|                 | FR                             | $221 \pm 3$  | –                         | R2                                |
|                 | KAS                            | $215 \pm 8$  | –                         | R2                                |
|                 | OFW                            | $218 \pm 7$  | –                         | R2                                |
|                 | AIC                            | 150 – 240    | –                         | –                                 |
|                 | Direct integration             | 100 – 220    | –                         | –                                 |
| <b>HDPE</b>     | DTG curve fitting              | 240          | $3.4 \times 10^{16}$      | $n^{\text{th}}$ order; $n = 0.56$ |
|                 | FR                             | $247 \pm 5$  | –                         | R2                                |
|                 | KAS                            | $238 \pm 11$ | –                         | R2                                |
|                 | OFW                            | $243 \pm 11$ | –                         | R2                                |
| <b>PP</b>       | DTG curve fitting              | 126          | –                         | $n^{\text{th}}$ order; $n = 0.5$  |
|                 | FR                             | 53 – 194     | –                         | –                                 |
|                 | FR                             | $188 \pm 6$  | –                         | R3                                |
|                 | KAS                            | $179 \pm 8$  | –                         | R3                                |
|                 | OFW                            | $183 \pm 8$  | –                         | R3                                |
|                 | AIC                            | 150 – 250    | –                         | –                                 |
|                 | FR                             | $215 \pm 9$  | –                         | –                                 |
|                 | Starink                        | $203 \pm 6$  | –                         | –                                 |
|                 | OFW                            | $204 \pm 6$  | –                         | –                                 |
| KAS             | $203 \pm 5$                    | –            | –                         |                                   |

<sup>†</sup> DTG is the derivative thermogravimetry (DTG) data, which is the derivative of the thermogravimetry (TG) data resulted from the thermogravimetric analysis (TGA).

## 1.10 Plastic pyrolysis modelling using FEM

As illustrated previously, plastic pyrolysis process is widely implemented and studied experimentally in lab-scale reactors by different researchers. Moreover, in the industrial sector, pyrolysis technology is studied and up-scaled experimentally, but not of all information are accessible to the scientific audience, and yet the process is inefficient and has its limitations. On the other hand, there are great advantages and capabilities for numerical modelling and simulation in upgrading and designing efficient processes and reactors with low cost in a short time. Nevertheless, numerical modelling and optimizing of the plastic pyrolysis process, using FEM and conventional software, for the sake of developing and efficiently implementing at the industrial scale are rare and seldom reported in literature.

(Bockhorn *et al.*, 1999) modelled plastic pyrolysis at a milli-particle scale, 50 mg spherical polystyrene (PS) sample with radius  $R_p = 2.3$  mm, in a thermogravimetric analyzer. The objective of their work was to model heat transfer within the sample as it undergoes pyrolysis, thus to find the temperature gradient of the pyrolyzed sample. They assumed that the volume of the sample to be constant, whereas the evolution of volatiles is modelled by changing the particle bulk density linearly from  $\rho_0 = 1$  g.cm<sup>-3</sup> to  $\rho_\infty = 0.001$  g.cm<sup>-3</sup> depending on the conversion  $x$  of the sample. Moreover, they stated that the basis for the heat transfer model is given by the energy balance equation below, **Eq. 1-29**.

$$\rho C_p \frac{\partial T}{\partial t} = \frac{\partial}{\partial r} \left( k \frac{\partial T}{\partial r} \right) + (\rho_0 - \rho_\infty) H_R \frac{dx}{dt} \quad \text{Eq. 1-29}$$

where  $H_R = 300$  J.g<sup>-1</sup> is the change of enthalpy due to pyrolysis reaction and  $dx/dt$  (s<sup>-1</sup>) is the rate of the reaction

$$\frac{dx}{dt} = A \exp \left( \frac{-E}{RT} \right) (1 - x)^{0.9} \quad \text{Eq. 1-30}$$

where  $A = 10^{16}$  min<sup>-1</sup>, and  $E = 200$  kJ.mol<sup>-1</sup> are the kinetic parameters for polystyrene pyrolysis with a heating rate of 10 K.min<sup>-1</sup>.

They applied FEM to transform the partial differential equation, **Eq. 1-29**, into a system of ordinary differential equations, which are solved using a modified Runge–Kutta algorithm (Press *et al.*,

1989). The model converged successfully and the simulation results, temperature profile and degree of conversion, were validated by the experimental results of TGA for polystyrene pyrolysis.

Navarro et al. (Navarro *et al.*, 2012) used the same energy equation, **Eq. 1-29**, to model pyrolysis process for plastic, tire, coal and biomass also at particle scale inside a thermogravimetric analyzer. The samples were pyrolyzed with a moderate nitrogen flow rate, about 200 mL/min with 20 mm internal diameter of the TGA tube, at two different heating rates (5 and 10 °C/min) and with temperatures ranging from 150 to 950 °C. They used heat convection coefficient,  $h$  ( $\text{W}\cdot\text{K}^{-1}\cdot\text{m}^{-2}$ ) as shown by Eq. (31), at the outer surface of the samples to model the forced heat convection due to the flow of nitrogen gas.

$$k \left( \frac{\partial T}{\partial r} \right)_{r=R_p} = h(T_b - T_{sur}) \quad \text{Eq. 1-31}$$

where  $R_p$  (mm) is the radius of the spherical particle,  $T_b$  and  $T_{sur}$  (°C) are the bulk and surface temperatures of the sample particle, respectively. Moreover, they stated that the typical values of the global heat transfer coefficient,  $h$ , depending on the type of the reactor are:  $100 \text{ W}\cdot\text{m}^{-2}\cdot\text{K}^{-1}$  to  $1000 \text{ W}\cdot\text{m}^{-2}\cdot\text{K}^{-1}$  for fluidized-bed reactors, while a value of  $10 \text{ W}\cdot\text{m}^{-2}\cdot\text{K}^{-1}$  for fixed bed reactors. The model was resolved by the finite difference approximation method which is a type of FEM, however the successive over-relaxation (SOR) method has been used for solving the linear equations of the system (Burden and Faires, 2011). As a result, the used algorithm was successfully implemented together with the heat transfer model to predict the temperature profiles in the pyrolyzed particles.

Also (Ding *et al.*, 2020) modelled pyrolysis process for plastic particles inside a fluidized bed reactor using one-step model and the same previous approach; the results were compatible and validated with the experimental data. In addition, there exist in literature several different studies that modelled and simulated pyrolysis process for plastic and other materials at milli-particle scale (Alves and Figueiredo, 1989; Miller and Bellan, 1997; Peters, 2011). These models and equations were coupled with reaction schemes ranging from single one-step reaction, i.e. one rate of reaction equation such as **Eq. 1-12**, to multiple reaction system. However, most of the studies nominated the one-step model to describe plastic pyrolysis (Ding *et al.*, 2020; Encinar and González, 2008).

On the other hand, regarding simulations of pyrolysis in lab-scale reactors, Csukas et al. (Csukas *et al.*, 2013) modelled plastic pyrolysis in a continuous tubular reactor using Direct Computer Mapping (DCM) algorithm i.e. C++ algorithm with a graphical user interface, but without using FEM or any conventional software and without mentioning the global heat transfer coefficient used.

Moreover, (Jin *et al.*, 2019) modelled and simulated pyrolysis process for a thin film flow, about 2 mm thickness, for polyethylene (PE), polypropylene (PP), polystyrene (PS) and mixture of all, inside a vertical falling film reactor. They used FEM method and a conventional software (ANSYS) to model the process. Furthermore, they used the volume of fraction (VOF) method to model the interface between the molten plastic and the gaseous byproducts phase, in addition to the continuity, momentum, and energy equations. The VOF model is a method that successfully tracks the liquid surface of a liquid–gas flow or any two-phase flow by solving the volume fraction equation, **Eq. 1-32** (Yan and Che, 2010).

$$\frac{\partial \alpha_g}{\partial t} + \nabla \cdot \alpha_g \vec{u} = \frac{S_g}{\rho_g} \quad \text{Eq. 1-32}$$

where  $\rho_g$  and  $\alpha_g$  (1) are the gas density and the gas volume of fraction respectively,  $\vec{u}$  is the velocity vector of the fluid, and  $S_g$  ( $\text{kg}\cdot\text{m}^{-3}\cdot\text{s}^{-1}$ ) is the mass source transfer term from molten plastic to pyrolysis byproducts (gas) modeled as one-step kinetic model given by **Eq. 1-33**.

$$S_g = A \exp\left(\frac{-E}{RT}\right) \rho_l \alpha_l \quad \text{Eq. 1-33}$$

where  $A = 1.54 \times 10^{18}$  ( $\text{s}^{-1}$ ) and  $E = 314$  ( $\text{kJ}\cdot\text{mol}^{-1}$ ) are the kinetic parameters describing mixed plastic pyrolysis (PE, PP, and PS),  $\rho_l$  and  $\alpha_l = 1 - \alpha_g$  are the liquid density and the liquid volume of fraction respectively. In addition, it is good to mention that the kinetic model function  $f(x)$  is taken as a first order  $f(x) = (1 - x)$  (Jin *et al.*, 2019).

Moreover, the utilized continuity and momentum equations are given by the following equations, **Eq. 1-34** and **Eq. 1-35**.

$$\frac{\partial \rho_f}{\partial t} + \vec{\nabla} \cdot (\rho_f \vec{u}) = 0 \quad \text{Eq. 1-34}$$

$$\rho_f \left[ \frac{\partial \vec{u}}{\partial t} + (\vec{u} \cdot \vec{\nabla}) \vec{u} \right] = -\vec{\nabla} p + \vec{\nabla} \cdot \left( \mu_f \left( \vec{\nabla} \vec{u} + (\vec{\nabla} \vec{u})^T \right) \right) - \rho_f g \vec{e}_y - \frac{2\sigma \rho_f \kappa \vec{\nabla} \alpha_g}{\rho_l + \rho_g} \quad \text{Eq. 1-35}$$

where  $\rho_f = \alpha_l \rho_l + \alpha_g \rho_g$  is the density of the mixture fluid,  $\alpha_l$  and  $\alpha_g$  are, respectively, the volume of fraction functions for liquid and gaseous phases which are active in the whole fluid domain.  $\mu_f = \alpha_l \mu_l + \alpha_g \mu_g$  is the dynamic viscosity for the mixture fluid (Pa.s),  $\vec{e}_y$  is a unit vector of the y-axis pointing upwards. In addition, the last term in the momentum equation, **Eq. 1-35**, allocates for the surface tension (body force) between liquid and gas, where  $\sigma$  (N.m<sup>-1</sup>) is the surface tension coefficient, and  $\kappa$  (m<sup>-1</sup>) is the surface interface curvature illustrated by **Eq. 1-36**.

$$\kappa = -\vec{\nabla} \cdot (\vec{\nabla} \alpha_g / |\vec{\nabla} \alpha_g|) \quad \text{Eq. 1-36}$$

where  $|\vec{\nabla} \alpha_g|$  is the magnitude of the vector  $\vec{\nabla} \alpha_g$ . Finally, the last term in the energy equation, **Eq. 1-37**, represents the heat sink term due to the occurring plastic pyrolysis reaction.

$$\rho_f C_{p,f} \left( \frac{\partial T}{\partial t} + \vec{u} \cdot \vec{\nabla} T \right) = \vec{\nabla} \cdot k_f \vec{\nabla} T - S_g H_r \quad \text{Eq. 1-37}$$

where  $C_{p,f} = \alpha_l C_{p,l} + \alpha_g C_{p,g}$  and  $k_f = \alpha_l k_l + \alpha_g k_g$  are, respectively, the heat capacity and the thermal conductivity for the fluid mixture, and  $H_r = 541$  (kJ.kg<sup>-1</sup>) is the average enthalpy of the pyrolysis reaction for mixed plastic (PE, PP, and PS). However regarding the simulation results, they stated that the model functioned well and the results were compatible with the experimental results. Moreover, they deduced that the apparent convection heat transfer coefficient for pyrolyzed plastic in the falling film reactor is greater than that in the rotary kiln reactor; 4000 vs 1000 W.m<sup>-2</sup>.K<sup>-1</sup> (Jin *et al.*, 2019).

Nonetheless, the same approach (VOF method) is employed to model and simulate similar processes such as boiling and condensation phenomena. Where the mass source term in boiling and condensation processes can be modelled according to **Eq. 1-38** and **Eq. 1-39** respectively (**ANSYS, 2009**).

$$S_g = f \rho_l \alpha_l \left( \frac{T - T_{sat}}{T_{sat}} \right) \quad \text{Eq. 1-38}$$

$$S_l = f \rho_g \alpha_g \left( \frac{T - T_{sat}}{T_{sat}} \right) \quad \text{Eq. 1-39}$$

## Bibliography

---

where  $f$  ( $s^{-1}$ ) is a boiling or condensation relative coefficient that reflects the inverse of the relaxation time of a fluid,  $T_{sat}$  is the vapor saturation temperature, and  $S_l$  ( $kg.m^{-3}.s^{-1}$ ) is the source of mass transfer from the vapor state to the liquid phase.

Guo et al. (Guo *et al.*, 2009) established the falling film model of the gas–liquid two-phase flow in an evaporative condenser and analyzed the effect of wall heating flux on the temperature of the liquid film using the VOF method. In addition, Liu (Jin *et al.*, 2019) simulated the evaporation process of water in a filler-type saturator, using the VOF method, and discussed the influences of inlet velocity and feeding rate on the heating and mass transfer coefficients.

Furthermore, it is good to emphasise that acquiring the knowledge of Computational Fluid Dynamics (CFD) represents a vital aspect in accurately modelling and simulating such complex processes. CFD is said to be the science that predicts fluid flow using computational methods and algorithms (module) to solve the mathematical equations that govern the fluid flow. Therefore, understanding the current fluid motion and choosing the appropriate mathematical models and parameters are the first steps in modelling any fluid flow problem. Fluid flow regimes may be represented by single-phase or multiphase flows, laminar or turbulent flows, free or porous media flows, and compressible or incompressible flows. For example, VOF equation along with the continuity and momentum equations, **Eq. 1-32 – Eq. 1-35**, are used to model the two-phase flow of plastic pyrolysis process. Moreover, within each type of flow there exist further different complex models and details that expand to apprehend the nature of the existing fluid flow, like for example, various closure models for turbulent flows such as  $k-\epsilon$  model,  $k-\omega$  model, SST (Shear Stress Transport) model, algebraic  $yPlus$  model, etc... In addition, CFD module can be coupled with heat transfer and chemical reaction modules to model more complex real life processes as illustrated in the previous equations; coupling between the continuity, momentum, and VOF equations, with the energy equation, **Eq. 1-32 – Eq. 1-37** (Dabiri Atashbeyk *et al.*, 2018; Moradi *et al.*, 2014).

All in all, VOF model had been used to simulate gas–liquid two-phase flow mainly based on water or aqueous solutions, but its application in the simulation of highly viscous molten fluids is seldom reported in literature. Nevertheless, modelling and simulating plastic pyrolysis process using FEM and conventional commercial software such as COMSOL Multiphysics and ANSYS for a bulk of scale is still rarely found in literature.

### 1.11 Conclusion

After illustrating the importance of plastic pyrolysis process in facing the crisis of plastic pollution and the depletion of fossil fuels, plastic pyrolysis was defined and the influence parameters were discussed extensively. On the other hand, plastic pyrolysis technology over the past 40 years is found to be based on experimental up-scaling, where unfortunately pyrolysis process is still inefficient and needs more improvements. In addition, almost all the experimental industrial studies and norms used semi-empirical models and overall heat transfer coefficients to model the process. However, the flaw of semi-empirical approaches is that they are dependant of operating conditions and experimental set-ups and are rarely extendible to more general cases. consequently, the importance of performing numerical modelling and simulation for plastic pyrolysis using finite element method for the sake of developing efficient process was explored and emphasized. So the finite element method (FEM) was defined and the advantages of using this method were listed and a brief comparison between two well-known computational software (COMSOL Multiphysics and ANSYS) was presented.

In addition, knowing that the pyrolysis is a complex process where different physics and the coupling between them plays a major role, the deep study of the sub-process becomes a need. The melting process is a sub-process of pyrolysis; convenient models that can model plastic melting were suggested, such as the apparent heat capacity method (AHCM). Furthermore, the models that predicts the flow of molten plastic and its viscosity such as Power Law, Cross, and Carreau models were also illustrated. Moreover, the methodology of performing plastic pyrolysis kinetics using thermogravimetric analysis and isoconversional methods such as, Freidman, Kissinger-Akahira-Sunose, Ozawa-Flynn-Wall, and Starink wer demonstrated extensively. In addition, the Criado's method, which is a curve fitting method, is suggested to be used to find the best reaction model  $f(x)$  that represents the plastic pyrolysis process, from the most commonly used reaction models found in literature.

Finally, a literature review was done concerning modelling and simulating pyrolysis process as a particle size scale and in lab-scale or industrial-scale reactors. This literature revealed that many studies were done to model plastic pyrolysis at a particle scale in a thermogravimetric analyser, however it is rarely modelled as a large bulk material. In addition, some models and equations such as volume of fraction model (VOF) can be used to model bulk volume of plastic pyrolysis,

using FEM and conventional software; these were presented by some studies dealing with plastic pyrolysis in a thin film reactor or in modelling similar processes like boiling and condensation. VOF model can easily track the liquid surface interface of a liquid–gas flow or any two-phase flow by solving the volume fraction equation. However, the knowledge in Computational Fluid Dynamics (CFD) represents a vital aspect in accurate modelling and simulating such complex processes especially when designing and modelling continuous reactors.

As a result, modelling plastic pyrolysis for a bulk material of plastic is still rarely mentioned in the literature. Furthermore, modelling and optimizing efficient plastic pyrolysis reactors that would be applied and invested at the industrial scale is not done yet. Therefore, in order to achieve an overall design and conception of an industrial plastic pyrolysis reactor, pyrolysis process is recommended to be modelled and validated at a lab-scale as a first step, due to the complexity of such procedure. Then this model is upgraded and numerically optimized (geometry, process, boundary and operating conditions, etc.) to be later on built and checked experimentally.

# Chapter 2 Materials and Methods

In this chapter, the methodology and the modelling equations used to achieve the objectives of this thesis; apprehending and modelling plastic pyrolysis process, will be displayed extensively. First, materials and equipment that are used in this study are defined. Then, knowing that pyrolysis process can be divided into two sub-processes; melting and cracking, the procedure of modeling melting and cracking processes for PP and HDPE at a milli-particle scale (using TGA-DSC apparatus) and in a fixed bed semi-batch reactor will be illustrated. Finally, the equations used to model and simulate plastic pyrolysis process in a continuous reactor, heated by the exhaust gases of a diesel engine, are demonstrated.

## 2.1 Materials and equipment

The type of plastic used in our study and its thermo-physical properties are defined in this section. In addition, utilized equipment, experimental procedure, and type of reactor are discussed below. Finally, the employed numerical software in modelling and its characteristics are explained.

### 2.1.1 Raw materials

As mentioned in Chapter One (**section 1.4.1**), polyolefin (PE and PP) contribute to 60 % of the global plastic waste production. For this reason, plastic feedstock materials used in this study are composed of polyolefin, especially PP and HDPE.

Polypropylene virgin granules of a variable diameter between 2 and 4 mm (**Figure 2-1**) will be pyrolyzed using a thermogravimetric analyzer and in a lab-scale semi-batch reactor in this study.



**Figure 2-1:** PP virgin granules.

On the other hand, since low density polyethylene (LDPE) and high density polyethylene (HDPE) have the same properties with a very slight difference, thus there is no difference in modelling pyrolysis for one of them. Therefore, HDPE post-consumer materials, containers and bottles, are collected from the municipal waste facilities and finely chopped, using a fine chopper machine, into small flakes as shown in **Figure 2-2**. Whereas, the obtained HDPE flakes, having a length range from 3 to 6 mm and a thickness of about 1 mm, will be also pyrolyzed in the same semi-batch pyrolysis reactor after conducting thermogravimetric analysis (TGA).



**Figure 2-2:** Preparing HDPE flakes from plastic waste containers.

**Table 2-1** illustrates the thermophysical properties of PP and HDPE found in literature (INEOS, 2014a, 2014b).

**Table 2-1:** Thermophysical properties for PP and HDPE at temperature range 20 – 500 °C.

| Materials   | Thermal conductivity k<br>(W/K/m) | Specific heat capacity $C_p$<br>(J/kg/K) | Density $\rho$<br>(kg/m <sup>3</sup> ) | Ref            |
|-------------|-----------------------------------|--|--|----------------|
| Solid PP    | 0.15 – 0.16                       | 1900 – 2000                              | 900                                    | (INEOS, 2014a) |
| Molten PP   | 0.17 – 0.18                       | 2300 – 2500                              | 890                                    | (INEOS, 2014a) |
| Solid HDPE  | 0.4 – 0.42                        | 1800 – 2000                              | 940 – 950                              | (INEOS, 2014b) |
| Molten HDPE | 0.45                              | 2200 – 2400                              | 930 – 940                              | (INEOS, 2014b) |

In addition, a previous work done by (Kassargy, 2018) to determine the ultimate analysis and the calorific values (high and low, HCV and LCV) for PP and HDPE, is illustrated in **Table 2-2**.

**Table 2-2:** Ultimate analysis and calorific values for PE and PP.

|             | Ultimate analysis |            |      |      |      | HCV (MJ/kg) | LCV (MJ/kg) |
|-------------|-------------------|------------|------|------|------|-------------|-------------|
|             | C (%)             | H(%)       | N(%) | O(%) | S(%) |             |             |
| <b>HDPE</b> | 86.2 ± 0.8        | 14.4 ± 0.8 | -    | -    | -    | 46.4        | 43.5        |
| <b>PP</b>   | 86.4 ± 0.8        | 14.4 ± 0.8 | -    | -    | -    | 46.4        | 43.5        |

### 2.1.2 Thermogravimetric analysis

Thermogravimetric analyzer is an apparatus that measures, continuously, the change of mass and the temperature of a sample, during thermal degradation, in a controlled atmosphere. It allows user to set the heating profile of the sample, the vector gas and its flowrate.

In this study, the SETSYS Evolution 1750 device developed by SETARAM (**Figure 2-3**) is used to perform the thermogravimetric analysis. It is made up of an integrated structure such as controller, oven, cooling system, gas circuits system and other safety elements. The device is a coupling between TGA and differential scanning calorimetry (DSC) elements, thus it measures the heat flow absorbed/released by the material as it undergoes thermochemical phenomena (melting, cracking, and combusting). Moreover, Setsoft software is used to set up a programmed heating rate in addition to the flow rate of the purging gases (Nitrogen, Oxygen, Aragon, etc...) and other

## Materials and Methods

---

parameters. The software acquires and saves thermogravimetry (TG), DSC, TG-DSC and derivative thermogravimetry (DTG) signals.



**Figure 2-3:** SETSYS Thermogravimetric analyzer.

This instrument is used to conduct simultaneous TG-DSC analysis for PP and HDPE pyrolysis at different heating rates. Two twin aluminum crucibles (100  $\mu$ L capacity) are suspended from a microbalance and situated in a heating chamber; one is empty and set as a reference while the other one holds the sample as shown in **Figure 2-4**. An electrical graphite furnace is used to control the heating rate and the temperature of the sample under an inert atmosphere, which can reach 1750  $^{\circ}$ C. In addition, an electric microbalance measures the mass loss of the sample over time ( $\pm 1$   $\mu$ g deviation). However, the mass of the analyzed sample should not exceed 20 mg.

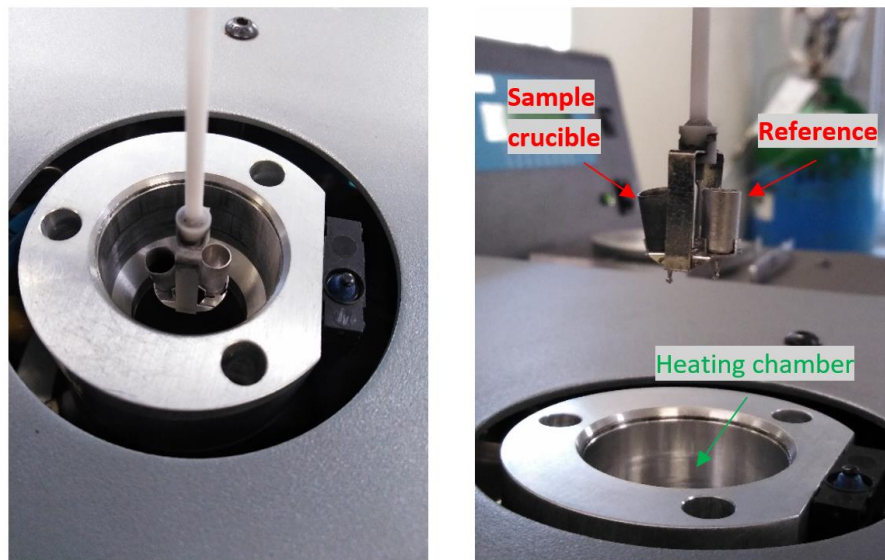


**Figure 2-4:** TGA-DSC sample and reference crucibles.

Different experiments are carried out at different heating rates (4, 6, 8, and 10 °C/min), and each experiment is replicated for validation. In this study, the pyrolyzed samples have a mass of  $18 \pm 2$  mg. In addition, Nitrogen gas ( $N_2$ ) with a flow rate of 20 mL/min, is used to purge the system, i.e. to carry out the gaseous by-products and to maintain an inert atmosphere during the process. The control of the pyrolysis temperature is achieved by two steps; first, the sample is sustained at an isothermal state (25 °C) for 20 min to eliminate any disturbances at the start of heating, then temperature rises from 25 to 500 °C using a constant heating rate  $\beta$  (4, 6, 8, and 10 °C/min). Furthermore, the sample temperature (°C), the mass (mg), and the heat flow absorbed by the sample material  $\dot{Q}_a$  (mW) are recorded during the whole experiment.

**Figure 2-5** shows the TG and DTG curves of HDPE thermal pyrolysis at 10 °C/min heating rate. Using these curves, the temperature at which maximum degradation occurs ( $T_{c,max}$ ) is measured at the crest of the DTG curve as shown in **Figure 2-5(b)**. However, the Onset and Offset temperatures ( $T_{onset,c}$  and  $T_{offset,c}$ ) shown in the curves are respectively the initial and the final temperature of the major and the fast part of the pyrolysis process.  $T_{onset,c}$  and  $T_{offset,c}$  are found respectively from the intersection of the tangent of the TG curve at  $T_{c,max}$  with the initial and final asymptotes as shown in **Figure 2-5(a)**.

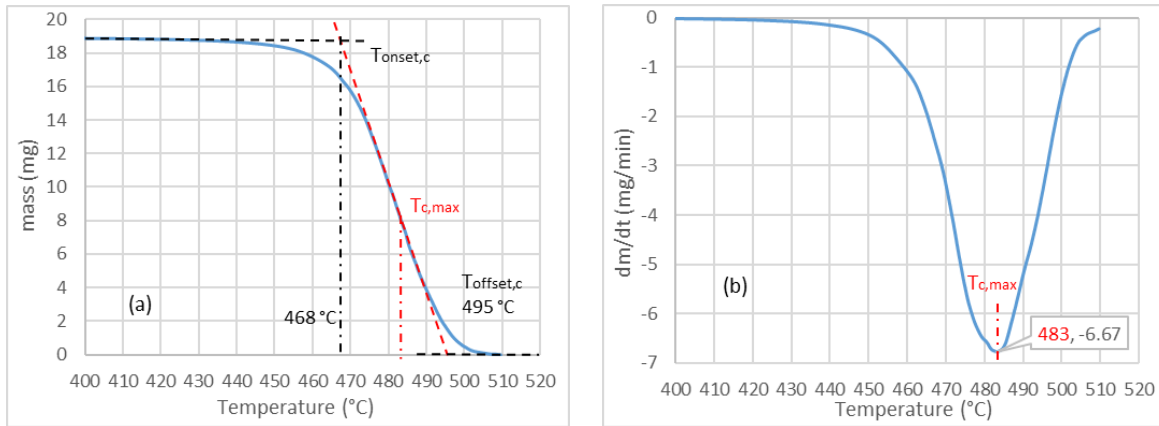


**Figure 2-5:** (a) TG curve and (b) DTG curve for HDPE thermal pyrolysis at 10 °C.min<sup>-1</sup>.

### 2.1.3 Differential Scanning Calorimetry

In order to perform the energy analysis (thermal), SETSYS Evolution apparatus coupled to the DSC analysis system is used. DSC is mainly measuring the difference of heat flow between the sample crucible containing polymer and the reference one (empty) during the evolution of the furnace temperature, as shown previously in **Figure 2-4**. As a result, the thermal power absorbed by the sample is given with respect to time or temperature, which is so-called the DSC results or data.

For example, **Figure 2-6** shows the DSC results of HDPE pyrolysis at  $\beta = 10$  °C/min, where the measured absorbed heat flow  $\dot{Q}_a$  (mW) varies with respect to temperature. As shown in the figure, the first convex curve is due to melting whereas the second one is related to pyrolysis reaction, knowing that the two processes are endothermic.

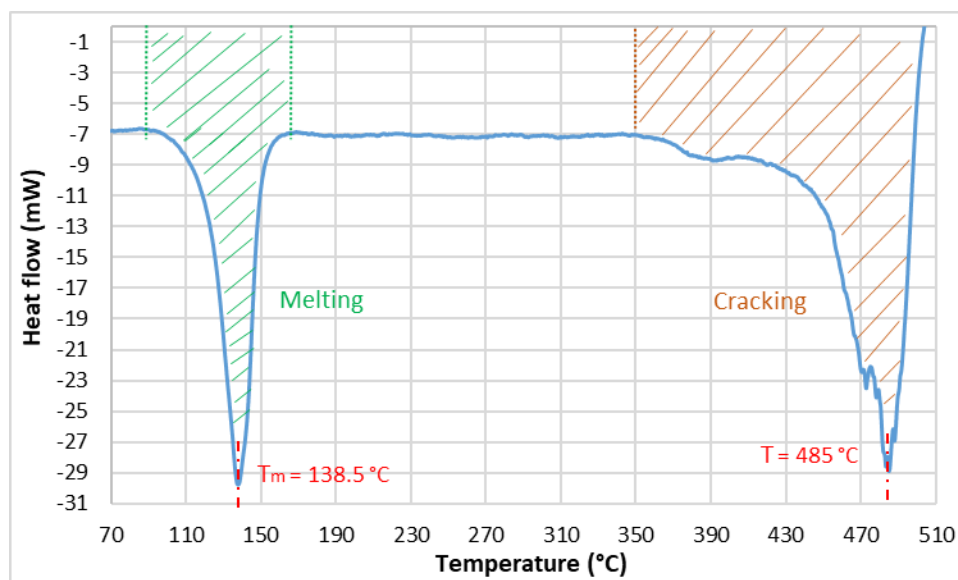


**Figure 2-6:** Heat flow versus temperature, DSC curve for HDPE thermal pyrolysis at  $\beta = 10 \text{ }^\circ\text{C}\cdot\text{min}^{-1}$ .

Furthermore, DSC results are normally used to calculate the thermal characteristics of a specific material such as; specific heat capacity ( $C_p$ ), melting and cracking temperatures ( $T_m$  and  $T_{c,\text{max}}$ ), specific melting and cracking enthalpies ( $\Delta h_m$  and  $\Delta h_c$ , respectively), and other properties, out of the scope of this study, like glass transition ( $T_g$ ) and crystallization ( $T_{\text{crys}}$ ) temperatures of polymers.

## 2.2 Semi-batch reactor

### 2.2.1 Description of the semi-batch reactor

The pyrolysis experiments are carried out in a laboratory-scale semi-batch reactor, developed by Pyrum Innovations. The reactor is shown in **Figure 2-7** below, where (1) is the stainless steel hollow cylinder reactor of 200 mm height, 80 mm inner diameter, and 4 mm thickness. An electrical resistive coil (heater) of 1500 W rated power (3) is used to heat up the reactor. The heater is coupled to a programmable controller that regulates the power and the final temperature of the resistance, using a PID (proportional integral derivative) regulation system. In addition, the power consumed by the electrical heater is measured and recorded.

The reactor is covered by a ceramic fibre jacket for thermal insulation. Additionally, five K-type thermocouples (diameter: 0.1 mm, uncertainty:  $\pm 0.1 \text{ K}$ ) are installed in the reactor to measure the temperature at different locations; the reactor temperature is controlled via wall temperature  $T_2$ .

## Materials and Methods

Thermocouple  $T_1$  is plunged inside the reactor to monitor the feedstock temperature, which is a main recorded temperature. On the other hand, other thermocouples such as  $T_3$  and  $T_4$  are plugged at the bottom and the top of the reactor, as shown in **Figure 2-7(a)**, to acknowledge more the heat dissipation inside the reactor. Also a thermocouple  $T_5$  is fixed at the external surface of the insulator to measure the temperature and heat at the outer boundary of the reactor.

Moreover, a spiral water cooling condenser (4) connected to the outlet of the reactor; condensate gases are collected in a container (5) for further analysis. Whereas, non-condensable gases are evacuated using the laboratory air handling unit (6).

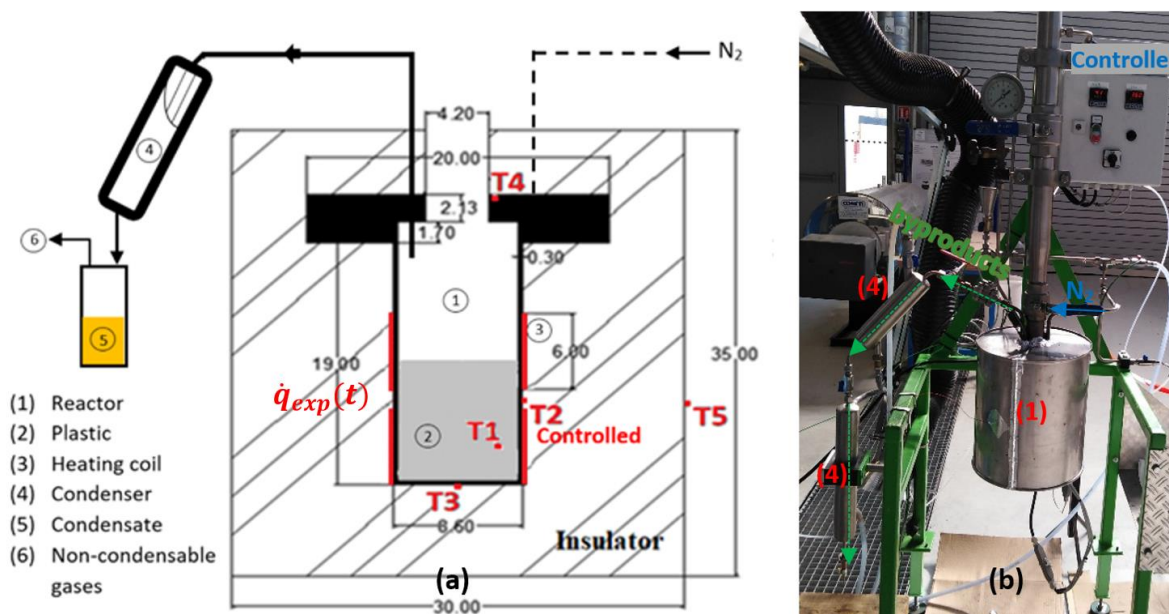


**Figure 2-7:** (a) Schematic diagram, units are in cm, and (b) real image of the semi-batch reactor.

**Table 2-3** below illustrates the thermophysical properties of the semi-batch reactor material; ceramic fiber insulator and the stainless steel metal (Hall, 2010; Harvey, 1982).

**Table 2-3:** Thermophysical properties for the semi-batch reactor material with the range of 25-500°C.

| Materials           | Thermal conductivity $k$ (W/K/m) | Specific heat capacity $C_p$ (J/kg/K) | Density $\rho$ (kg/m <sup>3</sup> ) | Ref            |
|---------------------|----------------------------------|---------------------------------------|-------------------------------------|----------------|
| Stainless steel 321 | 15 – 22                          | 490 – 530                             | 8000                                | (Harvey, 1982) |
| Ceramic fiber       | 0.08 – 0.16                      | 900 – 1100                            | 150                                 | (Hall, 2010)   |

**2.2.2 Procedure of pyrolysis process in the semi-batch reactor**

Since this study is dealing with slow pyrolysis, the selected heating rates are below 10 °C/min. Therefore, all of the proceeding experiments are realized at different heater powers below 50 % of the heater full load (1500 W), and each experiment is replicated for confirmation. In addition, in each experiment, temperatures at different positions are recorded to be compared later to the simulated results. But, before going directly to the pyrolysis experiments of PP and HDPE in the semi-batch reactor, different series of experiments are realized first as a prerequisite, such as modelling empty and loaded reactor (solid or fluid), and modelling plastic melting experiments.

The first three series of experiments are realized to apprehend and model the sensible heat transfer within empty and loaded reactor (solid or fluid). While, the first series of experiments are heating the empty reactor to 490 °C at different heating rates then cooling it. The second series of experiments are heating the reactor filled with sand to 570 °C at different heating rates. As for the third, the reactor is filled with sunflower oil (light viscous fluid) and heated at different heating rates to reach 180 °C. **Table 2-4** shows the thermophysical properties of sand and sunflower oil as found in literature (Hamdhan and Clarke, 2010; Rojas *et al.*, 2013).

**Table 2-4:** Average thermophysical properties for sand and sunflower oil with the range of 25-500°C.

| Materials     | Thermal conductivity $k$ (W/K/m) | Specific heat capacity $C_p$ (J/kg/K) | Density $\rho$ (kg/m <sup>3</sup> ) | Ref                          |
|---------------|----------------------------------|---------------------------------------|-------------------------------------|------------------------------|
| Fine dry Sand | 0.2                              | 800                                   | 1600                                | (Hamdhan and Clarke, 2010)   |
| Sunflower oil | 0.165                            | 2400                                  | 915                                 | (Rojas <i>et al.</i> , 2013) |

Moreover, the viscosity of the sunflower oil is measured at different temperatures using a type SV-10 vibration viscometer of the AND brand, shown in **Figure 2-8**.

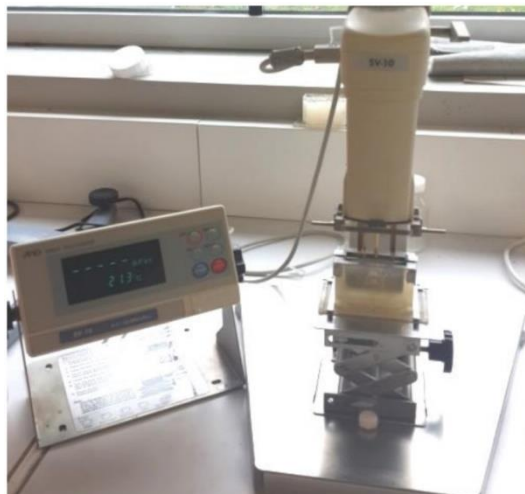


**Figure 2-8:** SV-10 vibration viscometer of the AND brand.

The viscosity drops logarithmically from 51 mPa.s at ambient temperature (25 °C) to 3.3 mPa.s at 180 °C, as shown in **Table 2-5**, i.e. the viscosity at ambient temperature is 15 times greater than that at 180 °C. This large drop and difference affects drastically the natural flow of oil inside the reactor, which affects the heat transfer. Therefore, temperature-dependent oil viscosity is taken into consideration and implemented in the simulation when modelling heating sunflower oil inside the reactor.

**Table 2-5:** Dynamic viscosity of sunflower oil.

| Temperature (°C)  | 25 | 30 | 40   | 50   | 60   | 70   | 80  | 90  | 110 | 120 | 140 | 160 | 180 |
|-------------------|----|----|------|------|------|------|-----|-----|-----|-----|-----|-----|-----|
| Viscosity (mPa.s) | 51 | 42 | 29.2 | 21.1 | 15.9 | 12.2 | 9.6 | 7.7 | 6.3 | 5.7 | 4.7 | 3.9 | 3.3 |

The fourth series of experiments are the phase change experiments: melting process of plastics (PP and HDPE), which is a sub-process of pyrolysis. The used samples are granular virgin polypropylene and chopped flakes of HDPE with particle size of, approximately, 2 – 5 mm. But in order to avoid porosity issues inside the reactor, the loaded PP and HDPE particles are melted first then cooled to ambient temperature, before each experiment, to have a bulk of solid plastic inside the reactor. Then, plastic is heated from ambient temperature to 300 °C at different heating rates.

Finally, regarding the pyrolysis experiments of PP and HDPE, for each experiment, the reactor is filled with 400 g of plastic (PP or HDPE) and the system is purged for 15 minutes with nitrogen

gas at room temperature to ensure an inert atmosphere. Then, the plastic is heated from ambient temperature to 500 °C at different heating rates (below 50 % of the full power load of the heater, 1500 W). As the pyrolysis byproduct gases pass through the stainless steel condenser to be cooled with tap water at 15 °C, the condensate is collected in a graduated container and the volume of the oil byproduct is recorded over time. The byproducts are classified into three groups: liquid products, non-condensed gases and residues. Whereas, the non-condensed gases are discharged through a discharge ventilation pipe and the possible remaining residues at the bottom of the reactor are collected at the end of the reaction.

### 2.3 COMSOL Multiphysics software

COMSOL Multiphysics permits an easy editing of the underlying equations of the physical models, and, a coupling of different physics such as solid mechanics, heat transfer, fluid flow, chemical reaction, mass transfer, and other physics. In addition, it is flexible and has a compatible graphic user interface with many options and models capabilities oriented towards the research domain, such as sensitivity and sweep studies, optimizations models, application model builder, live link to MATLAB and Excel, and many other features (COMSOL, 2017). Thus, COMSOL Multiphysics software is chosen to perform all numerical studies and modelling in this work.

Regarding the general study settings in all of the future conducted simulations, the absolute tolerance is taken as 0.0001 and set as the termination criteria for simulation. In addition, mesh refinement methodology is employed in all of the numerical studies to achieve mesh convergence or known as solution convergence.

Meanwhile, coupled physics, such as heat transfer, fluid flow, and chemical reaction models, are treated in two approaches in COMSOL Multiphysics. First approach is the “Fully Coupled” approach which forms a single large system of linear equations that includes all the dependent variables such as temperature  $T$ , velocity vector  $\vec{u}$ , and conversion  $x$ , which are solved at the same time within a single iteration. Where this approach often converges robustly i.e. doesn't have divergence issues, however, each iteration will require relatively more memory and time to be solved. On the other hand, the “Segregated” approach is used sometimes instead of the fully-coupled one, to provide less memory and time requirement, but on the expense of convergence robustness. The “Segregated” approach subdivides the problem up into two or more segregated

steps, where each step can represent a single physics, then these segregated steps are solved sequentially within a single iteration.

Regardless of the fully-coupled or segregated approach, there exists two classes of algorithms that can be used to solve the linearized system of equations within each iteration, which are direct and iterative solvers. Direct solvers have the advantage of being the most robust and general, but they require relatively a lot of memory and time, especially for large size problems (number of mesh elements above 1 million). In contrast, iterative solvers require less memory and time, which scale more slowly with increasing model size. However, iterative solvers are less robust, less converging and so-called ill-conditioned problems. Moreover, it requires appropriate and manual adjustments of the solver settings to solve a particular problem, thus it is less preferable.

Direct solvers such as PARDISO (PARAllel DIrect SOLver), MUMPS (MULTifrontal Massively Parallel sparse direct Solver), and SPOOLES (Sparse Object-Oriented Linear Equations Solver), are available in COMSOL Multiphysics. However, PARDISO and MUMPS are likely to be the fastest, whereas SPOOLES is the least memory demanding, but all of the solvers almost converge to the same solution. Therefore, either PARDISO or MUMPS solver will be used in this study because of their robustness and time efficiency. Furthermore, the Newton's Method (Newton-Raphson Method), with automatic damping factor, is used to calculate the solution at each time step taken by the solver. Consequently, the time stepping method follows the BDF algorithm (Backward Differentiation Formula), which is an implicit solver that uses backward differentiation formulas with order of accuracy varying from one (also known as the backward Euler method) to five (COMSOL, 2017).

### **2.4 Procedure of modelling melting process and sensible heat**

First, melting process for PP and HDPE is modelled at a milli-particle scale using DSC results. Then, before proceeding to model plastic melting process in the semi batch-reactor, sensible heat transfer for the empty and loaded reactor is modeled.

#### **2.4.1 Milli-particle scale modeling of melting process for PP and HDPE**

In order to obtain the melting characteristics for PP and HDPE, several experiments, at different constant heating rates (4, 6, 8, and 10 °C/min) are carried out using DSC analysis, by SETSYS

Evolution apparatus. Granules of PP and thin flakes of HPDE, of 2 – 6 mm length, are used as the experimental samples with a total mass of  $18 \pm 2$  mg for each sample (PP or HDPE). The heat flow  $\dot{Q}_a$  (mW) consumed by the plastic and the temperature of the material are recorded with respect to time.

Using the DSC data, peak melting temperature  $T_m$  is obtained as the temperature at the crest of the melting curve, and  $\Delta T_m$  is determined as the melting range temperature between melting onset and offset temperatures, as shown in **Figure 2-9**. Nevertheless, melting onset and offset temperatures ( $T_{onset,m}$  and  $T_{offset,m}$ ) that are respectively the initial and the final temperatures of the major and fast part of the melting process are determined. It is good to mention that this major part (between  $T_{onset,m}$  and  $T_{offset,m}$ ) that contributes to more than 90 % of the melting process will be modelled. However, the softening slow part of melting, from the beginning of melting till the onset temperature, will be ignored for the sake of simplicity and to sustain a symmetrical shape of melting curve.

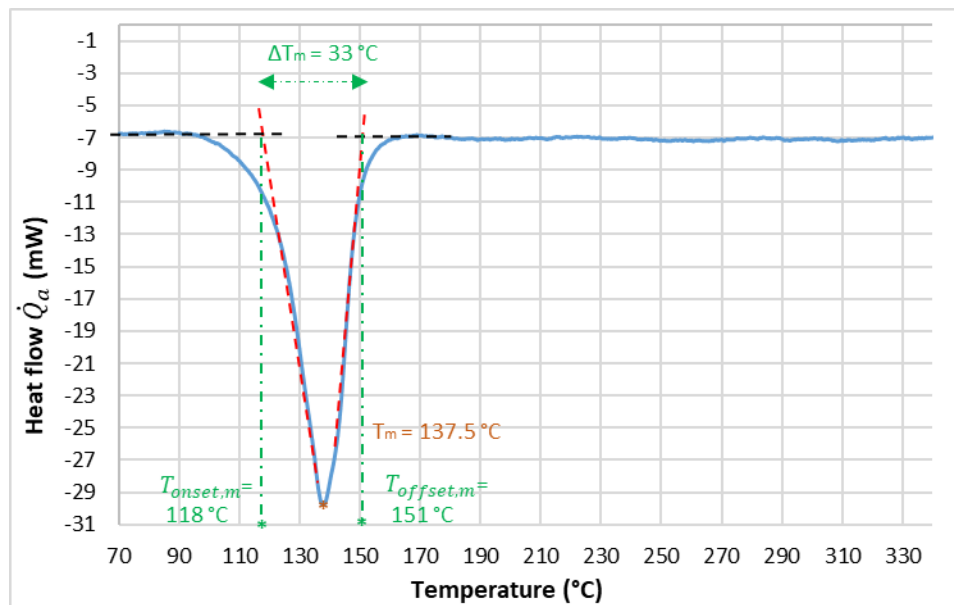


**Figure 2-9:** Heat flow versus temperature of HDPE melting and heating at  $\beta = 10^\circ\text{C}\cdot\text{min}^{-1}$ .

In addition, specific heat capacities for PP and HDPE are determined before and after the melting process (at the solid and molten state, respectively) by **Eq. 2-1**, which is supposed to be constant during the phase change process (melting).

$$C_p = \frac{1}{m} \frac{dH}{dT} = \frac{1}{m} \frac{dH}{dt} \frac{dt}{dT} = \frac{1}{m} \frac{\dot{Q}_a}{\beta} \quad \text{Eq. 2-1}$$

where  $H$  (J) is the enthalpy thermodynamic property,  $m$  (kg) is the mass of the specimen,  $\dot{Q}_a$  (W) is the recorded heat flow absorbed by the material, and  $\beta$  ( $^{\circ}\text{C}\cdot\text{s}^{-1}$ ) is the constant heating rate set by the TGA-DSC.

Moreover, the specific melting enthalpy  $\Delta h_m$  (J/kg) is determined from the DSC data by **Eq. 2-2** below.

$$\Delta h_m = \int_{t_{onset,m}}^{t_{offset,m}} \dot{Q}_a dt - m C_{p,s} \Delta T_m \quad \text{Eq. 2-2}$$

where  $t_{onset,m}$  and  $t_{offset,m}$  (s) are respectively the time relative to the melting onset and offset temperatures,  $\dot{Q}_a$  (W) is the recorded heat flow absorbed by the material,  $m$  (kg) is the mass of the specimen,  $C_{p,s}$  (J/K/kg) is the solid specific heat capacity of plastic just before melting, and  $\Delta T_m$  ( $^{\circ}\text{C}$ ) is the melting range temperature between melting onset and offset temperatures.

The second step is to draw the geometry of the DSC environment and to set the initial and boundary conditions of the system using COMSOL Multiphysics. The DSC analyzer includes two twin aluminum crucibles; one contains the sample material (plastic), and the other one is empty (reference crucible). These two crucibles are heated from the sides via radiation by, a hollow cylindrical shape, programmable electrical furnace. The crucible that contains plastic material (100  $\mu\text{L}$  volume and 4 mm diameter) is drawn as 2D-axisymmetric with the exact dimensions as measured from the instrument, shown in **Figure 2-10**. Therefore, a linear temperature,  $T_{\text{exp}}(t)$ , depending on the experimental constant heating rate  $\beta$  ( $^{\circ}\text{C}/\text{min}$ ) is set as the heat boundary condition on the side wall of the sample crucible, as shown in **Figure 2-10(b)**. Hence, the fluid flow effect for molten plastic inside the crucible is neglect due to the small size and high viscosity of the plastic particle.

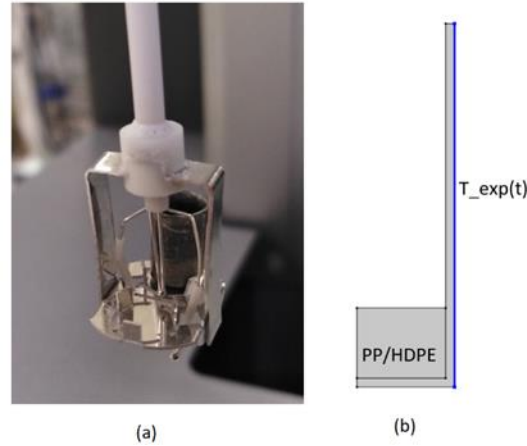


**Figure 2-10:** (a) Real crucible image of the DSC/TGA analyzer, (b) 2D-axisymmetric crucible model.

The heat conduction equation combined with the modified apparent heat capacity method (AHCM), described by **Eq. 2-3**, is used as a governing equation to model plastic melting process inside the TGA-DSC crucible.

$$\rho \left( (1 - f_l) C_{p,s} + f_l C_{p,l} + L \frac{\partial f_l}{\partial T} \right) \frac{\partial T}{\partial t} = \vec{\nabla} \cdot ((1 - f_l) k_s + f_l k_l) \vec{\nabla} T \quad \text{Eq. 2-3}$$

where,  $\rho$  is the constant density taken for solid and molten plastic,  $\vec{\nabla} = \frac{\partial}{\partial x} \vec{i} + \frac{\partial}{\partial y} \vec{j} + \frac{\partial}{\partial z} \vec{k}$  is the spatial gradient operator,  $L = \Delta h_m$  (J.kg<sup>-1</sup>) is the latent heat of fusion (melting) obtained from the DSC results,  $C_{p,s}$  and  $C_{p,l}$  (J.K<sup>-1</sup>.kg<sup>-1</sup>) are respectively the solid and liquid heat capacities that are also determined from the DSC results, and  $k_s$  and  $k_l$  (W.K<sup>-1</sup>.m<sup>-1</sup>) are respectively the solid and liquid thermal conductivities. Additionally,  $f_l$  is a smoothed Heaviside conversion function defined by the AHCM over the deduced melting interval ( $\Delta T_m = T_{offset,m} - T_{onset,m}$ ), determined by the DSC analysis. This function is linear and symmetrical, where it is centered at the peak melting temperature  $T_m$  as shown in **Figure 2-11**. Moreover, the integration of  $\partial f_l / \partial T$  over  $\Delta T_m$  is equal to 1 and it is multiplied by the fusion energy  $L$ , as shown in **Eq. 2-3**, to ensure the exact latent heat absorbed in each cell during melting.

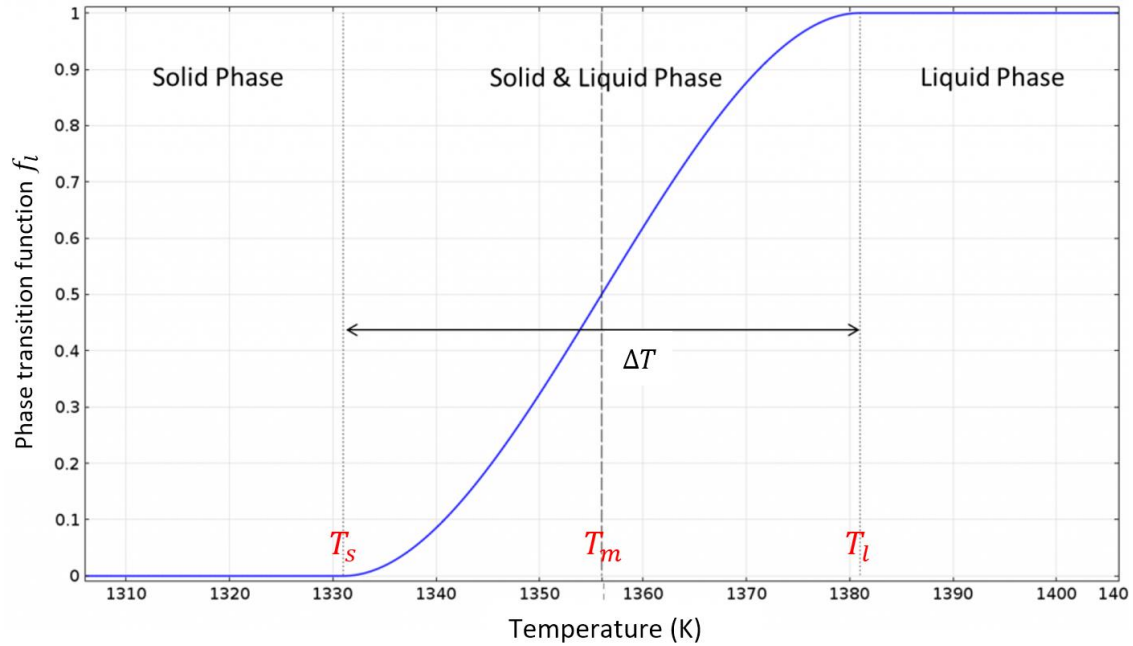


**Figure 2-11:** Conversion function  $f_l$  used in AHCM built-in COMSOL.

After adjusting the equations in COMSOL and setting the initial temperature, the domain is finely meshed and the time dependent (dynamic) solver is set up to solve the problem with respect to time. In addition, further mesh refinement is done to achieve simulation conversion. Then, the simulated results, heat absorption  $\dot{Q}_{a,sim}$  by HDPE or PP, are determined and compared with the experimental heat flow  $\dot{Q}_{a,exp}$  recorded by the DSC apparatus with respect to time. Finally, a relative error between experimental and simulated results is determined by **Eq. 2-4**.

$$err_{HF} = \frac{\dot{Q}_{a,exp} - \dot{Q}_{a,sim}}{\dot{Q}_{a,exp}} * 100 \quad \text{Eq. 2-4}$$

The model is said to be validated as long as the computed average relative error between the experimental and simulated results, for all experiments (at four different heating rates 4, 6, 8, and 10 °C/min), is less than 10 %. The 10 % value is taken as the maximum margin of average error in this study to assure the accuracy and the validity of the numerical solution, because it is found that in literature there is no standard value of an acceptable error between the experimental and simulated results.

## 2.4.2 Modeling sensible heat transfer in the semi-batch reactor

In this section, the procedure of modelling sensible heat transfer within the empty and loaded (sand, and sunflower oil) reactor will be illustrated.

### 2.4.2.1 Modelling empty semi-batch reactor

The first step is to model heat transfer in an empty reactor in order to validate and verify the material properties of the reactor. Therefore, the reactor is heated empty till 500 °C for long periods of time (about 2 or 3 hours) at different heating rates, 20 to 50 % of the heater full load (1500 W). Five temperatures at different spots of the reactor are recorded with respect to time, in addition to the experimental power supply,  $\dot{q}_{exp}(t)$ , i.e. power delivered by the heater, as shown in **Figure 2-7**.

The reactor is modelled as 2D-axisymmetric. The heat conduction equation presented in **Eq. 2-5** is used to model heat transfer within the empty reactor.

$$\rho C_p \frac{\partial T}{\partial t} = Q + \vec{\nabla} \cdot k \vec{\nabla} T \quad \text{Eq. 2-5}$$

where  $\rho$ ,  $C_p$ , and  $k$  are the temperature-dependent thermophysical properties of the reactor's material displayed previously by **Table 2-3**, and  $Q$  ( $\text{W}/\text{m}^3$ ) is a volumetric heat source generation due to the heaters, which is equal to  $\dot{q}_{exp}(t)$  divided by the volume of the heater.

On the other hand, regarding the boundary conditions, heat loss fluxes due to natural convection  $q_{conv}$  ( $\text{W}/\text{m}^2$ ), **Eq. 2-6**, and radiation  $q_{rad}$  ( $\text{W}/\text{m}^2$ ), **Eq. 2-7**, are applied at the external surface of the insulator as shown in **Figure 2-12**. In addition, surface to surface radiation is added between the bottom of the reactor and the insulator to model the heat loss due to the air gap at the bottom of the reactor.

$$q_{conv} = h(T_{sur} - T_{amb}) \quad \text{Eq. 2-6}$$

$$q_{rad} = \varepsilon \varphi (T_{sur}^4 - T_{amb}^4) \quad \text{Eq. 2-7}$$

$h$  is the convection heat transfer coefficient ( $\text{W}/(\text{K} \cdot \text{m}^2)$ ),  $T_{sur}$  ( $^{\circ}\text{K}$ ) is the temperature of the insulator external surface,  $T_{amb}$  ( $\text{K}$ ) is the ambient temperature,  $\varepsilon$  is the surface emissivity, and  $\varphi$  ( $\text{W}/(\text{K}^4 \cdot \text{m}^2)$ ) is the Stefan-Boltzmann constant.

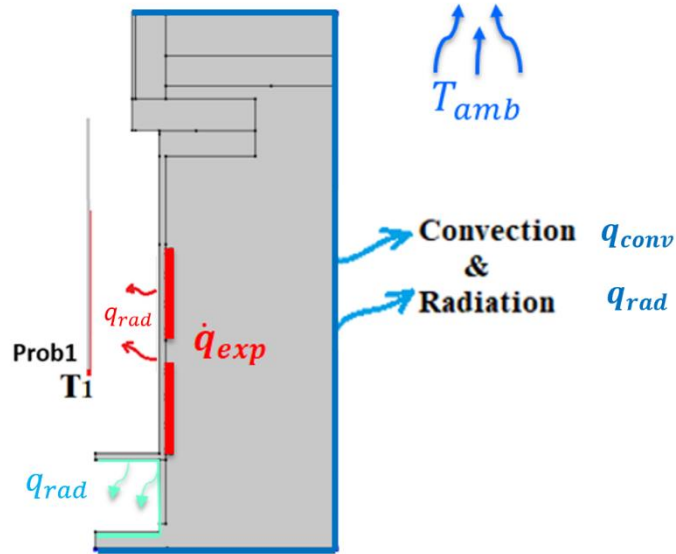


**Figure 2-12:** 2-D axisymmetric draw with Boundary conditions for the batch reactor.

The surface emissivity values of stainless steel used for the reactor walls and insulator's cover are set to  $\varepsilon = 0.7$  and,  $\varepsilon = 0.4$ , respectively (Harvey, 1982). Whereas, the free convection heat transfer coefficient  $h$  at the outer wall of the insulator is determined by a built-in empirical correlation for the vertical and horizontal plates (Incropera *et al.*, 2007). This correlation depends on the Rayleigh Number  $Ra_L$  value, as represented in **Eq. 2-8** – **Eq. 2-10** and **Figure 2-13**.

$$Ra_L = Gr_L \cdot Pr = \frac{g\alpha (T_{wall} - T_{amb})L_c^3}{\nu \cdot \phi} \quad \text{Eq. 2-8}$$

where  $Gr_L$  is the Grashof Number,  $Pr = \nu/\phi$  is Prandtl Number,  $\nu = \mu/\rho$  (m<sup>2</sup>/s) is the kinematic viscosity (momentum diffusivity),  $\phi = k/\rho C_p$  (m<sup>2</sup>/s) is the thermal diffusivity,  $\alpha$  (K<sup>-1</sup>) is the thermal expansion coefficient, and  $L_c$  (m) is the characteristic length.

If  $Ra_L \leq 10^9$ :

$$h = \frac{k}{L_c} \left( 0.68 + \frac{0.67Ra_L^{1/4}}{\left( 1 + \left( \frac{0.492k}{\mu C_p} \right)^{9/16} \right)^{4/9}} \right) \quad \text{Eq. 2-9}$$

else if  $Ra_L > 10^9$ :

$$h = \frac{k}{L_c} \left( 0.825 + \frac{0.387 Ra_L^{1/6}}{\left( 1 + \left( \frac{0.492k}{\mu C_p} \right)^{9/16} \right)^{8/27}} \right)^2 \quad \text{Eq. 2-10}$$

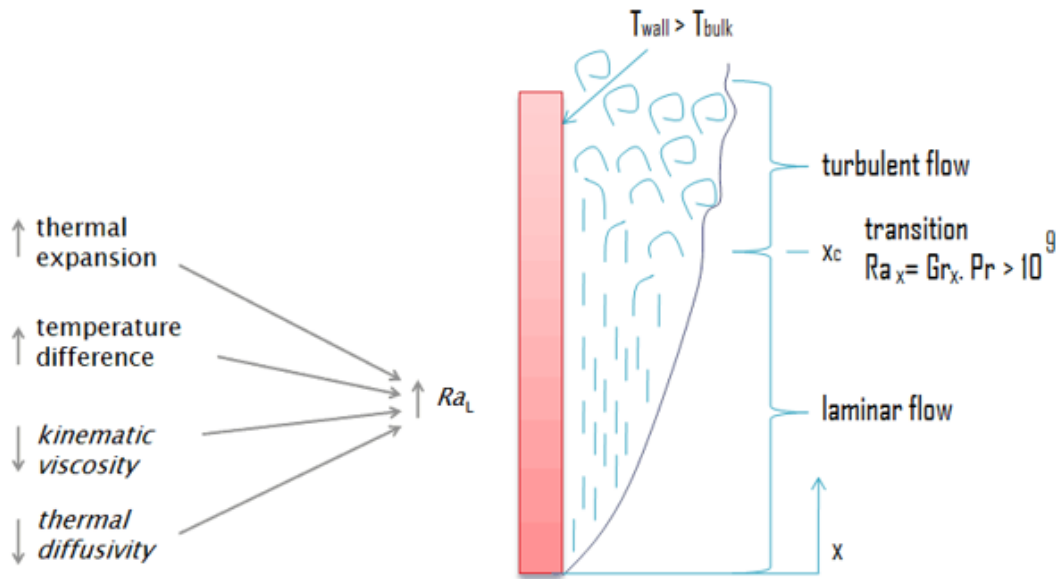


Figure 2-13: Type of flow depending on Rayleigh number.

Finally, after setting up a fine mesh to all simulated domains and adjusting the time dependent solver settings, the dynamic simulations are launched. Then, the experimental and simulated results (temperatures) are compared and the relative error is determined by Eq. 2-11. The validation criteria is the same in this study to all of the simulations i.e. the desired average relative error shouldn't exceeds 10 % among all of the experimental and simulated results.

$$err_{Temp} = \frac{T_{exp} - T_{sim}}{T_{exp} - T_0} \times 100 \quad \text{Eq. 2-11}$$

where  $T_0$  is the initial temperature,  $T_{exp}$  is the recorded experimental temperature at a specific position of the reactor and  $T_{sim}$  is the simulated temperature corresponding to the same position.

After validating the model, the next step is conducting a sensitivity study on the thermophysical properties of the reactor's material (stainless steel and ceramic fiber insulator) to notify the influence of varying the thermal properties on the results and to detect the sensitive parameters.

Hence, an average values of the reactor's thermal properties are used instead of properties function of temperature, and the simulation results are compared with the experimental ones.

Furthermore, after performing the sensitivity study and validating the reactor's thermal properties, another approach of modelling the heat source in the semi-batch reactor is checked and simulated. Recalling the first approach which is done by direct implementation of the experimental recorded power  $\dot{q}_{exp}(t)$  to COMSOL as a heat source. Whereas, the second one is to imitate the operation of the experimental controlled heater by modelling heater's controller. A heat source, in the simulation, is set to provide the same maximum experimental power (1500 W) and it is controlled by the simulated wall temperature ( $T_2$ ), to regulate and stabilize  $T_2$  at 500 °C by alternate ON and OFF cycles. Thus, when  $T_2$  is below the desired temperature the simulated heat source provides 1500 W else it gives zero, same as the real regulator does.

Besides validating the temperature results by **Eq. 2-11**, an additional validation index is determined when using the second approach (i.e. modelling a simulated heater and controller instead of using  $\dot{q}_{exp}(t)$ ), for further validation. The experimental and simulated energy provided by the heaters are compared and calculated by **Eq. 2-12**, where the desired average relative error shouldn't exceed 10 % for this study.

$$err_{Energy} = \frac{E_{exp} - E_{sim}}{E_{exp}} \times 100 \quad \text{Eq. 2-12}$$

where  $E_{exp}$  (J) is the total energy delivered by the electrical heater over time and  $E_{sim}$  (J) is the calculated energy released by the simulated heat source, i.e. heater, over the same period of time.

### **2.4.2.2 Modelling loaded semi-batch reactor**

After modelling the empty semi-batch reactor and before starting by the plastic (highly viscous material), several further experiments and simulations are conducted to assure the validation of heat transfer model inside the loaded reactor, loaded with solid (sand) and light viscous liquid (sunflower oil). So, modelling heat transfer within the loaded reactor is a further validation to the used models, equations and to the semi-batch reactor properties, especially that heat transfer differs between loaded and empty reactor. Also, it favors in reducing the potential errors as much possible before modelling plastic melting and cracking inside the reactor.

First, the reactor filled with sand, 0.3 mm particle size, is heated to reach a temperature of about 570 °C, where the temperature is stabilized. Heat transfer for solid material is also modelled by the heat conduction equation, **Eq. 2-5**, used to model heating of the empty reactor. **Figure 2-14** shows the modelled semi-batch reactor filled with sand with the five temperatures to be validated. Then, the simulated results (all temperatures and energy) are validated by the experimental results using **Eq. 2-11** and **Eq. 2-12**.

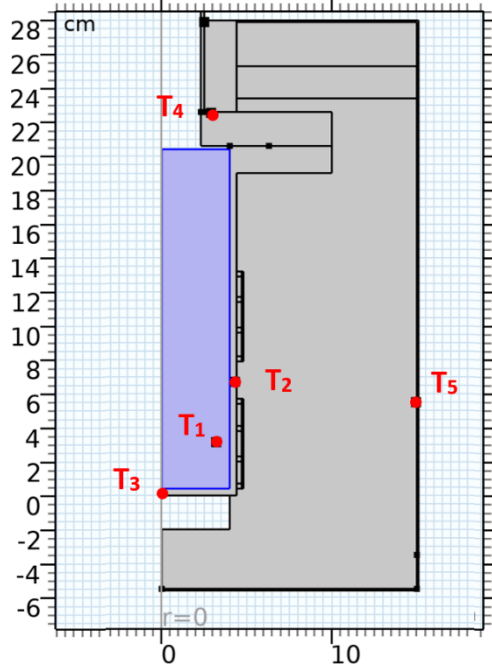


**Figure 2-14:** 2D-axisymmetry model for the reactor filled with sand with the plugged temperature location.

However, concerning modelling natural fluid flow and heat transfer for sunflower oil inside the semi-batch reactor, the continuity, momentum, and energy equations, **Eq. 2-13** – **Eq. 2-15**, are coupled together and utilized to model this phenomenon. The reactor is filled with sunflower oil and heated to a maximum temperature of 180 °C at different heating rates to prevent oil boiling.

$$\nabla \cdot \vec{u} = 0 \quad \text{Eq. 2-13}$$

$$\rho \left[ \frac{\partial \vec{u}}{\partial t} + (\vec{u} \cdot \nabla) \vec{u} \right] = -\vec{\nabla} p + \vec{\nabla} \cdot \left( \mu (\vec{\nabla} \vec{u} + (\vec{\nabla} \vec{u})^T) \right) - \rho g [1 - \alpha(T - T_{ref})] \vec{e}_z \quad \text{Eq. 2-14}$$

$$\rho C_p \left( \frac{\partial T}{\partial t} + \vec{u} \cdot \nabla T \right) = Q + \vec{\nabla} \cdot k \vec{\nabla} T \quad \text{Eq. 2-15}$$

where  $\vec{u} = u\vec{i} + v\vec{j} + w\vec{k}$  is the velocity vector (m/s) of the fluid,  $\vec{\nabla} = \frac{\partial}{\partial x}\vec{i} + \frac{\partial}{\partial y}\vec{j} + \frac{\partial}{\partial z}\vec{k}$  is the spatial gradient operator,  $\rho$  is the constant density (kg.m<sup>-3</sup>) of the sunflower oil,  $p$  is the static pressure (Pa), and  $\mu$  is the determined dynamic viscosity (Pa.s) of sunflower oil with respect to temperature, illustrated by **Table 2-5**. Whereas, the last term of **Eq. 2-14** contributes to the buoyancy force that models the natural flow for oil due the density variance i.e. due to temperature difference, which is given according to the Boussinesq approximation (**COMSOL, 2017**).  $g$  is the magnitude of gravitational acceleration (m.s<sup>-2</sup>),  $\vec{e}_z$  is a unit vector pointing upwards in the z-axis,  $T_{ref}$  is the reference temperature where the physical properties are given i.e. the average bulk temperature, and  $\alpha$  is the thermal expansion coefficient of the sunflower oil (K<sup>-1</sup>).

Furthermore, simulated results are also compared and validated by the experimental ones using **Eq. 2-11** and **Eq. 2-12**, under the same criteria (average relative error should be below 10 %). Therefore, after modelling sensible heat transfer within the loaded semi-batch reactor (solid and fluid), the next step is to model phase change process inside the semi-batch reactor, especially plastic melting process.

### 2.4.3 Modeling melting process in the semi-batch reactor

Before modelling plastic melting, the AHCM model is validated for ice melting inside the reactor as a bulk size. Thus, the reactor is filled and well packed with ice flakes, then, it is let to melt at ambient temperature ( $T_{amb}=19$  °C) without heating. The heat conduction equation with the AHCM model, **Eq. 2-3**, is used alone as a governing equation since fluid motion is negligible due to the very slow rate of ice melting (heaters are turned off). The experimental and simulated temperatures are compared and the relative error is illustrated by **Eq. 2-11**.

After the validation of the AHCM method for melting (using ice), this method is used to simulate plastic melting for PP and HDPE inside the semi-batch reactor. The bulk solid plastic inside the reactor is melted and heated till high temperatures, about 350 °C, at different heating rates. Then, the energy equation with AHCM method, continuity and momentum equations are coupled and used to model plastic melting process (**Eq. 2-16 - Eq. 2-18**).

$$\nabla \cdot \vec{u} = 0 \quad \text{Eq. 2-16}$$

$$\rho \left[ \frac{\partial \vec{u}}{\partial t} + (\vec{u} \cdot \vec{\nabla}) \vec{u} \right] = -\vec{\nabla} p + \vec{\nabla} \cdot \left( \mu (\vec{\nabla} \vec{u} + (\vec{\nabla} \vec{u})^T) \right) - \rho g [1 - \alpha(T - T_{ref})] \vec{e}_z \quad \text{Eq. 2-17}$$

$$\rho \left( (1 - f_l) C_{p,s} + f_l C_{p,l} + L \frac{\partial f_l}{\partial T} \right) \left( \frac{\partial T}{\partial t} + \vec{u} \cdot \vec{\nabla} T \right) = Q + \vec{\nabla} \cdot ((1 - f_l) k_s + f_l k_l) \vec{\nabla} T \quad \text{Eq. 2-18}$$

where  $\mu$  is the viscosity of plastic taken as a linear function that decreases from the solids viscosity (more than 10000 Pa.s) to the molten viscosity (about 1000 Pa.s) over the plastic melting temperature range  $\Delta T_m$ , as plastic changes phase and melts (Agassant *et al.*, 2019). The dynamic viscosity  $\mu$  is said to be Newtonian because of the very low shear rate of the natural fluid motion of molten plastic inside the batch reactor. In addition, another approach of simulation is used, where the molten plastic is treated as a solid because of its high viscosity. Therefore, plastic melting process is modeled only with the energy equation coupled with AHCM as described by **Eq. 2-19**. Moreover, the results of the two approaches will be compared. Finally, after mesh conversion, simulated and experimental results are compared and the relative error is calculated among the results, **Eq. 2-11** and **Eq. 2-12**.

$$\rho \left( (1 - f_l) C_{p,s} + f_l C_{p,l} + L \frac{\partial f_l}{\partial T} \right) \frac{\partial T}{\partial t} = Q + \vec{\nabla} \cdot ((1 - f_l) k_s + f_l k_l) \vec{\nabla} T \quad \text{Eq. 2-19}$$

Thus after modeling melting process for PP and HDPE, the next step is to model the cracking process (pyrolysis) at milli-particle and semi-batch reactor scale.

## 2.5 Procedure of modeling the cracking process

Modeling plastic pyrolysis (cracking phase) starts first by finding the kinetic parameters; reaction or kinetic model  $f(x)$ , activation energy  $E$  (J/mol), and pre-exponential factor  $A$  ( $s^{-1}$ ) or so-called frequency factor, that describes the reaction by the kinetic rate,  $dx/dt$  ( $s^{-1}$ ). Then this kinetic model is implemented in COMSOL Multiphysics with a two-phase model in order to model plastic pyrolysis in a lab-scale semi-batch reactor.

### 2.5.1 Kinetic rate for PP and HDPE pyrolysis

After establishing the specific TGA experiments for PP and HDPE pyrolysis at low heating rates (4 – 10 °C/min), the kinetic parameters can be determined. First, the kinetic model function  $f(x)$  is determined by the Criado's method, **Eq. 2-20**, which is a graphical curve-fitting method that

compares and fits the experimental TGA results with all the theoretical reaction models  $f(x)$  found in literature, listed in **Table 2-6** (Aboulkas *et al.*, 2010). The theoretical and the experimental functions according to the **Eq. 2-20** (left and right side, respectively) are evaluated and plotted for the sake of comparison. However, the models that have the highest coefficient of determination ( $R^2$ ) with respect to the experimental data, are selected to be the best fitting reaction models that describe the pyrolysis reaction for PP and HDPE (Criado, 1978; Das and Tiwari, 2017).

$$\frac{f(x)g(x)}{f(0.5)g(0.5)} = \left( \frac{T_x^2}{T_{0.5}^2} \right) \frac{(dx/dt)_x}{(dx/dt)_{0.5}} \quad \text{Eq. 2-20}$$

where  $T_{0.5}$  and  $(dx/dt)_{0.5}$  represent the temperature and conversion rate at a conversion of 0.5. The purpose of dividing by 50 % condition is for normalization.

**Table 2-6:** Reaction model for the most common reaction mechanism (Aboulkas *et al.*, 2010).

| <i>Mechanism</i>                        | $f(x)$                                  | $g(x)$                       |
|---|---|------------------------------|
| <b>First-order (F1)</b>                 | $(1 - x)$                               | $-\ln(1 - x)$                |
| <b>Second-order (F2)</b>                | $(1 - x)^2$                             | $(1 - x)^{-1} - 1$           |
| <b>Third-order (F3)</b>                 | $(1 - x)^3$                             | $[(1 - x)^{-2} - 1]/2$       |
| <b>Power law (P2)</b>                   | $2x^{1/2}$                              | $x^{1/2}$                    |
| <b>Power law (P3)</b>                   | $3x^{2/3}$                              | $x^{1/3}$                    |
| <b>Power law (P4)</b>                   | $4x^{3/4}$                              | $x^{1/4}$                    |
| <b>One-dimensional diffusion (D1)</b>   | $1/2(x)$                                | $x^2$                        |
| <b>Two-dimensional diffusion (D2)</b>   | $[-\ln(1 - x)]^{-1}$                    | $[(1 - x)\ln(1 - x)] + x$    |
| <b>Three-dimensional diffusion (D3)</b> | $3(1 - x)^{2/3}/[2(1 - (1 - x)^{1/3})]$ | $[1 - (1 - x)^{1/3}]^2$      |
| <b>Ginstling-Brounshtein (D4)</b>       | $3/2 [(1 - x)^{-1/3} - 1]$              | $1 - (2x/3) - (1 - x)^{2/3}$ |
| <b>Contracting cylinder (R2)</b>        | $2(1 - x)^{1/2}$                        | $[1 - (1 - x)^{1/2}]$        |
| <b>Contracting sphere (R3)</b>          | $3(1 - x)^{2/3}$                        | $[1 - (1 - x)^{1/3}]$        |
| <b>Avrami-Erofe'Ve (A2)</b>             | $2(1 - x)[- \ln(1 - x)]^{1/2}$          | $[- \ln(1 - x)]^{1/2}$       |

|                              |                            |                      |
|------------------------------|----------------------------|----------------------|
| <b>Avarami-Erofe'ye (A3)</b> | $3(1-x)[- \ln(1-x)]^{2/3}$ | $[- \ln(1-x)]^{1/3}$ |
| <b>Avarami-Erofe'ye (A4)</b> | $4(1-x)[- \ln(1-x)]^{3/4}$ | $[- \ln(1-x)]^{1/4}$ |

Furthermore, the activation energy  $E$ , function of conversion  $x$ , can be calculated for PP and HDPE pyrolysis according to the most three commonly used isoconversional methods given by **Eq. 2-21** – **Eq. 2-23**.

### 1. Friedman Method (FR)

$$\ln\left(\frac{dx}{dt}\right) = \ln[A f(x)] - \frac{E}{RT} \quad \text{Eq. 2-21}$$

Using FR method, the activation energy is determined from the slope ( $-E/R$ ) of the linear fitting straight lines from plotting  $\ln(dx/dt)$  with respect to  $1/T$  for different heating rates (i.e. different temperatures) at each constant conversion  $x$  (Snegirev *et al.*, 2013; Vyazovkin *et al.*, 2011).

### 2. Kissinger-Akahira-Sunose Method (KAS)

$$\ln\left(\frac{\beta}{T^2}\right) = -\frac{E}{RT} + \ln\left(\frac{AR}{Eg(x)}\right) \quad \text{Eq. 2-22}$$

For KAS method, the activation energy ( $E$ ) is calculated from the slope of the fitting lines of plotting  $\ln(\beta/T^2)$  vs  $1/T$  at all the heating rates, under the isoconversional principle at each constant conversion (Akahira and Sunose, 1971).

### 3. Flynn-Wall-Ozawa Method (FWO)

$$\ln \beta = -1.052 \frac{E}{RT} + \ln\left[\frac{AE}{Rg(x)}\right] - 5.331 \quad \text{Eq. 2-23}$$

Using FWO method, the activation energy is determined from the slope ( $-1.052 E/R$ ) of the straight lines of plotting  $\ln \beta$  with respect to  $1/T$  for different heating rates (i.e. different temperatures) at each constant conversion  $x$  (Flynn, 1983).

Therefore, the coefficient of determination ( $R^2$ ) is calculated between the linear fitting straight lines and the experimental data for all of the preceding methods, where the methods that have the best fitting ( $R^2$ ) are chosen.

Finally, the third kinetic parameter  $A$  (1/s) is determined from each isoconversional equation, **Eq. 2-21 – Eq. 2-23**, by calculating the intercept values for the fitting straight lines and by using the deduced previous kinetic parameters  $E$  and  $f(x)$ .

The final step, after finding several combinations of the kinetic triplet for PP and HDPE pyrolysis process ( $f(x)$ ,  $E$  and  $A$ ), is to calculate the theoretical conversion using the kinetic equation **Eq. 2-24** and to compare the results with the experimental conversion for further validation.

$$\frac{dx}{dt} = A \exp\left(\frac{-E}{RT}\right) f(x) \quad \text{Eq. 2-24}$$

The relative error is determined between the theoretical and experimental conversion by **Eq. 2-25**, where the best fitting results are selected to be the kinetic parameters that describe the most PP and HDPE pyrolysis.

$$err_{conv} = \frac{x_{exp} - x_{sim}}{x_{exp}} \times 100 \quad \text{Eq. 2-25}$$

Finally, after finding the best kinetic rate that describes pyrolysis process for PP and HDPE at moderated temperatures and low heating rates, the next step is to implement this model into COMSOL Multiphysics and simulate the pyrolysis process at a milli-particle a semi-batch reactor scales, respectively.

### 2.5.2 Milli-particle scale modeling of PP and HDPE pyrolysis

First, it is more convenient to model pyrolysis process in a thermogravimetric analyzer before doing this in a lab-scale semi-batch reactor, since the temperature gradient is negligible and the experimental results are more accurate. Therefore, the best validated kinetic rate and parameters are used to model pyrolysis process for PP and HDPE, at a milli-particle size, inside TG-DSC analyzer. The DSC feature is coupled with TGA in the SETSYS Evolution apparatus, where the heat flow,  $\dot{Q}_a$  (mW), consumed by the plastic material and the mass of the material are recorded function of time and temperature.

COMSOL Multiphysics is used to model and simulate the processes. The aluminum sample crucible (100  $\mu$ L volume and 4 mm diameter), shown previously in **Figure 2-10**, is drawn (2D-axisymmetric) using the exact dimensions. The applied boundary and initial conditions are the same that are used in **section 2.4.1** to model the melting process. The profile temperature  $T_{exp}(t)$ ,

corresponding to the experimental constant heating rate for each experiment (4 to 10 °C/min), is taken as a boundary condition at the side wall of the crucible as shown in **Figure 2-10(b)**. Therefore, the plastic material and the crucible are heated linearly by a constant heating rate from the ambient temperature (25 °C) to 500 °C.

Because of the very small volume of the tested particle, fluid flow effect can be neglected in modelling. Therefore, the heat conduction equation is used to model the heat transfer within the pyrolyzed material, where a heat sink term,  $Q_{sink} = \rho_0 \Delta h_c dx/dt$ , is added to **Eq. 2-26** to model the latent heat absorption due to the pyrolysis reaction. In addition, the rate of cracking  $dx/dt$  ( $s^{-1}$ ) is solved for each element in the domain by adjusting a domain ordinary differential equation solver that solves the kinetic equation, **Eq. 2-24**, depending on the deduced kinetic parameters ( $f(x)$ ,  $E$  (J/mol), and  $A$  ( $s^{-1}$ )). So, each finite element will undergo pyrolysis conversion in the domain.

$$\rho C_p \frac{\partial T}{\partial t} = \rho_0 \Delta h_c dx/dt + \vec{\nabla} \cdot k \vec{\nabla} T \quad \text{Eq. 2-26}$$

where  $\rho_0$  is the initial density of plastic and  $\Delta h_c$  (J/kg) is the specific cracking enthalpy deduced from the experimental DSC results. However, in this model, the density  $\rho$  decreases with respect to the conversion  $x$  in order to model the mass loss phenomena as shown in **Figure 2-15**, since the domain of simulation has a fixed volume.

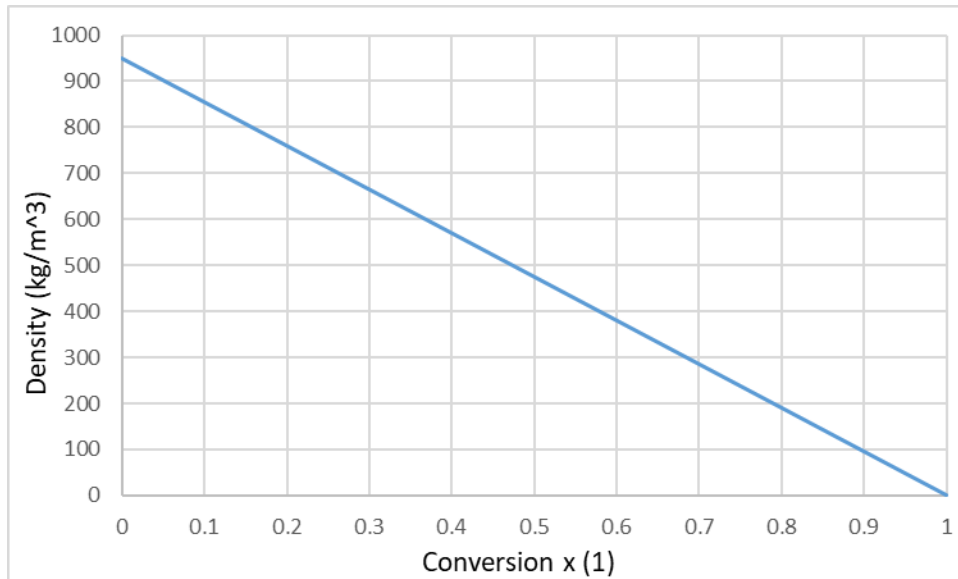


**Figure 2-15:** Density versus conversion  $x$  for HDPE used to model the mass loss in simulation.

Finally, after performing the mesh conversion, the simulated heat absorption  $\dot{Q}_{a,sim}$  due to HDPE or PP pyrolysis is determined with respect to time and compared to the experimental heat flow  $\dot{Q}_{a,exp}$  for further validation; **Eq. 2-4** is used to calculate the relative error. Moreover, the overall simulated and experimental conversions are also compared and the relative error is conducted using **Eq. 2-25**.

### 2.5.3 Modelling PP and HDPE pyrolysis in a semi-batch reactor

After determining the kinetic model and modeling pyrolysis process for PP and HDPE inside a TGA-DSC analyzer at milli-particle scale, the next step is to model this process at the same moderate temperatures and low heating rates in the lab-scale semi-batch reactor.

Regarding the experimental set up, the prepared plastic bulk of PP or HDPE of about 400 g, is heated from ambient temperature till 500 °C at different constant heating rates (30, 40, and 50 % of the total heater power 1500 W). The gas byproducts from pyrolysis process rises up and leaves the reactor naturally, then it enters the condenser and exits as oil byproducts and non-condensable gases. The volume and mass of the collected oil byproducts are recorded experimentally with respect to time for further analysis and validation.

Regarding the modelling approach using COMSOL Multiphysics, two approaches of simulation are used. First approach is the simple one, where it states that the same model used in modelling pyrolysis in TGA-DSC is employed in the semi-batch reactor. Where, molten plastic is considered as a static liquid, i.e. solid, because it has very high viscosity (above 1000 Pa.s). Thus, the same heat conduction equation with the deduced kinetic rate and density function, **Eq. 2-24** and **Eq. 2-26**, are used to model plastic pyrolysis.

On the other hand, the second approach aims to model two-phase flow; molten plastic and gas byproducts, with a surface tracking interface which results in changing the volume of the two phases. “Phase Field” or “Level Set” methods are almost two similar methods built in COMSOL Multiphysics that depend on the volume of fraction method (VOF) concept discussed in the last part of the bibliography (Chapter One: **section 1.10**). The Phase Field method is coupled with the continuity, momentum and energy equations (that includes the AHCM method to model melting), **Eq. 2-27 – Eq. 2-29**, to model the cracking phase inside a lab-scale semi-batch reactor. The AHCM

is coupled with the energy equation to model melting in the solid regions, since the three phases (solid, liquid, and gas) exist at the same time.

$$\vec{\nabla} \cdot \vec{u} = 0 \quad \text{Eq. 2-27}$$

$$\rho \left[ \frac{\partial \vec{u}}{\partial t} + (\vec{u} \cdot \vec{\nabla}) \vec{u} \right] = -\vec{\nabla} p + \vec{\nabla} \cdot \left( \mu \left( \vec{\nabla} \vec{u} + (\vec{\nabla} \vec{u})^T \right) \right) + \rho \vec{g} + \vec{F}_{st} \quad \text{Eq. 2-28}$$

$$\begin{aligned} \rho \left( (1 - f_l) C_{p,s} + f_l C_{p,l} + L \frac{\partial f_l}{\partial T} \right) \left( \frac{\partial T}{\partial t} + \vec{u} \cdot \vec{\nabla} T \right) \\ = Q_{hs} + Q_{sink} + Q_{cond} + \vec{\nabla} \cdot ((1 - f_l) k_s + f_l k_l) \vec{\nabla} T \end{aligned} \quad \text{Eq. 2-29}$$

where  $\rho \vec{g}$  (N/m<sup>3</sup>) stands for the body gravitational force to model the natural fluid motion due to the density variation and  $\vec{F}_{st}$  (N/m<sup>3</sup>) is the surface tension force acting at the liquid/gas interface. On the other hand, in the energy equation **Eq. 2-29**,  $Q_{hs} = \dot{q}_{exp}$  is the heat source due to the electrical heaters,  $Q_{sink}$  (W/m<sup>3</sup>) is the domain (molten plastic) heat sink term due to pyrolysis reaction, and  $Q_{cond}$  (W/m<sup>3</sup>) is the heat source due to the condensation process for the gaseous byproducts in the semi-batch reactor.

However, the Phase Field method is governed by the Cahn-Hilliard equations, **Eq. 2-30** and **Eq. 2-31**. The equations track a diffuse interface separating the immiscible phases. The diffuse interface is defined as the region where the dimensionless phase field variable  $\Phi$  goes from -1 to 1.

$$\frac{\partial \Phi}{\partial t} + \vec{u} \cdot \vec{\nabla} \Phi = \vec{\nabla} \cdot \frac{\omega \zeta}{\vartheta^2} \vec{\nabla} \psi + \frac{S_g + S_l}{\rho_g} \quad \text{Eq. 2-30}$$

$$\psi = -\vec{\nabla} \cdot \vartheta^2 \vec{\nabla} \Phi + \Phi(\Phi^2 - 1) \quad \text{Eq. 2-31}$$

where  $\vec{u}$  is the fluid velocity (m/s),  $\omega$  is the mobility (m<sup>3</sup>·s/kg),  $\zeta$  is the mixing energy density (N),  $\vartheta$  is the interface thickness parameter (m),  $\psi$  (-) is called the phase field help variable,  $S_g$  is the source of mass transfer from molten plastic to pyrolysis byproducts (gas) due to cracking reaction (kg·m<sup>-3</sup>·s<sup>-1</sup>),  $S_l$  is the source of mass transfer from gaseous to liquid state of the pyrolysis byproducts due to condensation (kg·m<sup>-3</sup>·s<sup>-1</sup>), and  $\rho_g$  is the gas density.

Furthermore, a condensation process for various hydrocarbon byproducts may exist inside the semi-batch reactor, since the top part of the reactor is relatively colder and has a high thermal

## Materials and Methods

inertia (high mass). Therefore,  $S_l$  is used to model the source of mass transfer from gaseous byproducts to liquid due to condensation. So, thermal properties, evaporation enthalpies, and boiling temperatures for the most common hydrocarbon byproducts, range from C<sub>7</sub> till C<sub>24</sub>, are investigated and used to model the condensation process inside the reactor, as shown in **Table 2-7** (Cheméo, 2021; PubChem, 2021; Vargaftik, 1975).

**Table 2-7:** Average thermophysical properties of the gaseous hydrocarbon byproducts C<sub>7</sub> till C<sub>24</sub> compared with air (Cheméo, 2021; PubChem, 2021; Vargaftik, 1975).

| Properties                       | C <sub>7</sub> – C <sub>9</sub> | C <sub>10</sub> – C <sub>15</sub> | C <sub>16</sub> – C <sub>24</sub> | Air (100 – 400 °C)         |
|----------------------------------|---------------------------------|-----------------------------------|-----------------------------------|----------------------------|
| $T_{\text{boil}}$ (°C)           | 100 – 130                       | 170 – 270                         | 300 – 390                         | –                          |
| $\Delta h_{\text{evap}}$ (kJ/kg) | 340 – 350                       | 350 – 360                         | 360 – 370                         | –                          |
| $\rho_g$ (kg/m <sup>3</sup> )    | 3.5 – 4.4                       | 4.4 – 6.5                         | 7 – 9.7                           | 0.95 – 0.5                 |
| $C_{p,g}$ (kJ/kg/K)              | 2.2                             | 2.2 – 2.35                        | 2.5 – 3.2                         | 1 – 1.07                   |
| $\mu_g$ (Pa.s)                   | $1.2 – 1.4 \times 10^{-5}$      | $1.3 – 1.6 \times 10^{-5}$        | $1.7 – 2.1 \times 10^{-5}$        | $2.1 – 3.2 \times 10^{-5}$ |
| $k_g$ (W/K/m)                    | 0.02 – 0.05                     | 0.05 – 0.07                       | 0.07 – 0.09                       | 0.03 – 0.05                |

Moreover, the mixing energy density  $\zeta$  and the interface thickness  $\vartheta$  are related to the surface tension by the following equation:

$$\sigma = \frac{2\sqrt{2}}{3} \frac{\zeta}{\vartheta} \quad \text{Eq. 2-32}$$

where  $\sigma$  (N.m<sup>-1</sup>) is the surface tension. Typically the interface thickness parameter  $\vartheta$  is set to be  $\vartheta = M_c / 2$ , where  $M_c$  is the characteristic mesh size in the region passed by the interface. In addition, the mobility parameter  $\omega$  determines the time scale of the Cahn-Hilliard diffusion and must be chosen judiciously; it must be large enough to retain a constant interfacial thickness but small enough so that the convective terms are not overly damped. Consequently the default value of  $\omega = \vartheta^2$ , which is usually a good initial guess (COMSOL, 2017).

Moreover, the surface tension force  $\vec{F}_{st}$  used in the momentum equation, **Eq. 2-28**, is described by **Eq. 2-33** below.

$$\vec{F}_{st} = G\nabla\Phi \quad \text{Eq. 2-33}$$

where  $G$  ( $\text{J}/\text{m}^3$ ) is the chemical potential parameter defined by

$$G = \zeta \left[ -\nabla^2\Phi + \frac{\Phi(\Phi^2 - 1)}{\vartheta^2} \right] = \frac{\zeta}{\vartheta^2}\psi \quad \text{Eq. 2-34}$$

As seen in the **Eq. 2-33** and **Eq. 2-34**, the phase field surface tension is computed as a distributed force over the interface using only  $\psi$  and the gradient of the phase field variable  $\Phi$ . This computation avoids the use of the surface normal and the surface curvature that are troublesome to be represented numerically. Furthermore, the phase field variable  $\Phi$  is divided into two domain volume fraction variables representing the liquid and the gas, as illustrated by **Eq. 2-35** and **Eq. 2-36** below (COMSOL, 2017).

$$V_{f,l} = \frac{1 - \Phi}{2} \quad \text{Eq. 2-35}$$

$$V_{f,g} = \frac{1 + \Phi}{2} \quad \text{Eq. 2-36}$$

where  $V_{f,l}$  is the liquid volume fraction which is equal to 1 for liquid and 0 for gas, in contrast,  $V_{f,g}$  is the gas volume fraction which is equal to 1 for gas fluid and zero for liquid domain. In addition, the two volume fraction variables are domain functions varying from 0 to 1, exactly same as  $\alpha_l$  and  $\alpha_g$  variables that are used in the VOF method discussed in last section of the bibliography (Chapter One: **section 1.10**). The density and dynamic viscosity terms presented in the previous equations, **Eq. 2-28** and **Eq. 2-29**, are written as function of these variables as shown in the **Eq. 2-37** and **Eq. 2-38**, respectively.

$$\rho = \rho_l V_{f,l} + \rho_g V_{f,g} \quad \text{Eq. 2-37}$$

$$\mu = \mu_l V_{f,l} + \mu_g V_{f,g} \quad \text{Eq. 2-38}$$

Where  $\rho_l$  and  $\mu_l$  are the density and viscosity for molten plastic, while  $\rho_g$  and  $\mu_g$  are the properties for the pyrolysis byproduct gas.

In addition, because melting and cracking processes don't superpose, the thermal properties presented in the energy equation, **Eq. 2-29**, are modified to take in consideration the change of properties when the molten plastic cracks and transforms into gaseous byproducts and vice versa.

Therefore,  $C_{p,l}$  and  $k_l$ , in **Eq. 2-29**, are replaced by  $C_{p,lg}$  and  $k_{lg}$  as follow:

$$X_l = V_{f,l} \rho_l / \rho \quad \text{Eq. 2-39}$$

$$X_g = 1 - X_l = V_{f,g} \rho_g / \rho \quad \text{Eq. 2-40}$$

$$C_{p,lg} = X_l C_{p,l} + X_g C_{p,g} \quad \text{Eq. 2-41}$$

$$k_{lg} = k_l V_{f,l} + k_g V_{f,g} \quad \text{Eq. 2-42}$$

where  $X_l$  and  $X_g$  are liquid and gas mass fractions, respectively,  $C_{p,lg}$  and  $k_{lg}$  are, respectively, the mixture (molten plastic and gas byproducts) specific heat capacity and thermal conductivity, whereas,  $C_{p,g}$  and  $k_g$  are the specific heat capacity and thermal conductivity for the gas byproducts, respectively.

Finally, the last term of the phase field equation, **Eq. 2-30**, is one of the most important terms, where the two sources are defined as follow:

$$S_g = V_{f,l} \rho_l A \exp\left(\frac{-E}{R T}\right) f(x) \rho_{ratio} \quad \text{Eq. 2-43}$$

$$S_l = V_{f,g} \rho_g f \cdot \left(\frac{T - T_{sat}}{T_{sat}}\right) \rho_{ratio} \quad \text{Eq. 2-44}$$

$S_g$  ( $\text{kg.m}^{-3}.\text{s}^{-1}$ ) is the source of mass transfer from molten plastic to pyrolysis byproducts (gas) due to cracking reaction, elsewhere,  $S_l$  ( $\text{kg.m}^{-3}.\text{s}^{-1}$ ) is the source of mass transfer from gaseous to liquid state of the pyrolysis byproducts due to condensation, where the deduced kinetic parameters are implemented in **Eq. 2-43** to solve the kinetic rate  $dx/dt$  ( $\text{s}^{-1}$ ) for PP and HDPE pyrolysis.

In this model, the pyrolysis byproduct condensate will evaporate using the same cracking law in **Eq. 2-43**, since the used model is limited to model two phases flow only. In addition, this assumption is accepted due to the fact that the cracking process is the major and the dominant process whereas the evaporation process of the heavy liquid hydrocarbon process is the minor one. Furthermore, the heat of evaporation of the condensate, displayed previously by **Table 2-7**, is found to be approximately equal to the cracking enthalpy of PP and HDPE, as will be illustrated in Chapter Four (**section 4.1**).

## Materials and Methods

---

Moreover,  $\rho_{ratio} = \rho_l/\rho_g$  is the density ratio added to ensure the mass conservation in the system, since the total volume (liquid + gas) of the system is fixed,  $f$  ( $s^{-1}$ ) is the condensation relative coefficient that reflects the inverse of the relaxation time of a fluid, which needs to be fine-tuned where the default value is chosen to be  $0.1 s^{-1}$ , and  $T_{sat}$  is the vapor saturation temperature. Therefore, the heat sink term due to pyrolysis process and the heat source term due to the condensation of the gaseous byproducts assigned in the energy equation, **Eq. 2-29**, are defined, respectively, as follow:

$$Q_{sink} = \Delta h_c S_g \quad \text{Eq. 2-45}$$

$$Q_{cond} = \Delta h_{evap} S_l \quad \text{Eq. 2-46}$$

where  $\Delta h_c$  (J/kg) is the cracking enthalpy due to pyrolysis reaction deduced from the TGA-DSC experimental results for PP and HDPE, and  $\Delta h_{evap}$  (J/kg) is the average value of the latent heat of evaporation for the most common hydrocarbon byproducts given in **Table 2-7**.

Finally, it is important to mention that the last term in the “Phase Field” equation, **Eq. 2-30**, which is the source term is not found in the initial built-in equation in COMSOL, thus it is added to the equation as a domain weak formulation such as:

$$2 \text{ test}(\psi) \frac{S_g + S_l}{\rho_g} = 0 \quad \text{Eq. 2-47}$$

where  $\text{test}(\psi)$  is a Quadratic Lagrange shape function or test function. Note that the test function is an arbitrary function used in finite element method to write the weak formulation equation (Rao, 2017).

After performing mesh convergence and setting up the dynamic solver properties, simulated and experimental results are compared for further validation, where the relative error is computed between the results. Whereas, plastic temperature  $T_1$  is compared to the simulated results, in addition to other temperatures ( $T_2$ ,  $T_3$ , and  $T_4$ ) located at different positions in the reactor as shown in **Figure 2-7**. Furthermore, during pyrolysis experiments the oil yield volume is recorded over time, this leads to know the amount of cracked material that left the reactor. This experimental output yield is compared to the simulated output yield using two approaches of simulation; with and without condensation.

## 2.6 Modelling continuous pyrolysis reactor

After modelling plastic pyrolysis inside a lab-scale semi-batch reactor at moderate temperatures (500 °C) and low heating rates (about 10 °C/min), the next step is to apply all the previous validated models in a continuous pyrolysis reactor. The continuous plastic pyrolysis reactor is designed to be heated by the exhaust gases of an 8 kW diesel engine as shown in **Figure 2-16**. The designed reactor is suggested to be a counter flow multi-concentric tube reactor. The temperature of the exhaust gases entering the reactor is 500 °C with a mass flow rate of about 82 kg/h. Hot exhaust gases pass through the inner tubes to heat up and crack plastic, where shredded plastic enters the reactor at ambient temperature from the opposite side with average velocity  $U_p$  (m/s). Then pyrolysis byproducts pass through a condenser to separate the condensate oil yield from the non-condensable gases. Moreover, the main part to be modelled is the counter flow multi-concentric tube reactor marked by number (1), as shown in **Figure 2-16**.

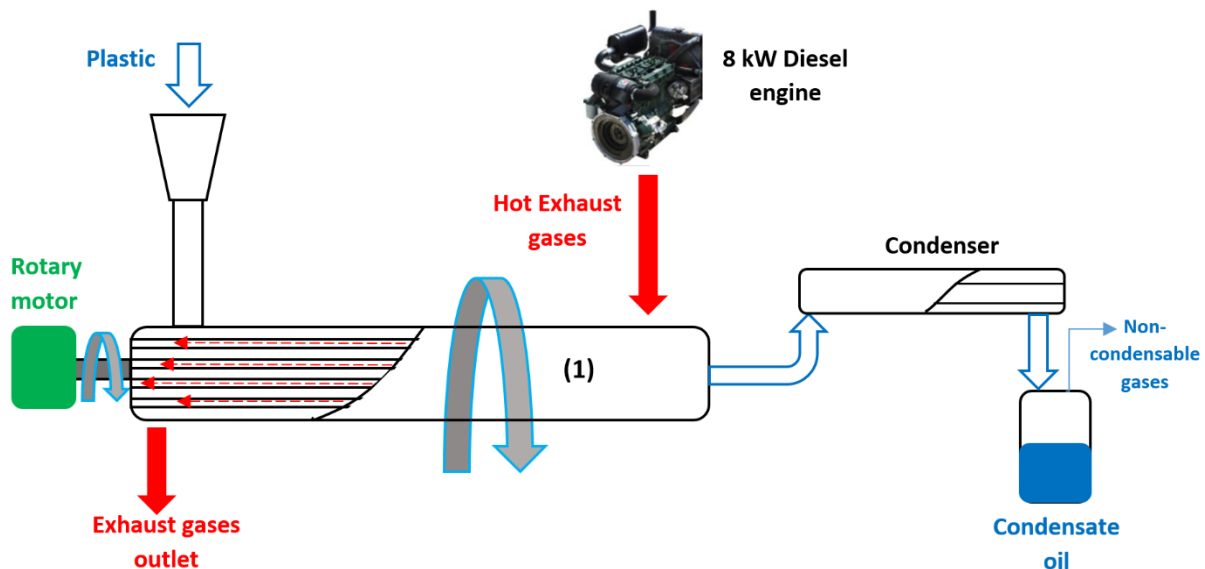


**Figure 2-16:** Schematic diagram of the designed continuous pyrolysis reactor heated by exhaust gases of 8 kW diesel engine.

A previous work done in GEPEA lab, DSEE department, to model this continuous reactor (Kassargy, 2018), where the logarithmic mean temperature difference (LMTD) method was used to model the continuous reactor analytically. The proposed design reactor has a 1 m length and 30 cm diameter cylindrical rotary kiln reactor with 34 inner tubes of 0.6 cm diameter with 1.8 cm pitch length as shown in **Figure 2-17**. Shredded plastic (PP or HDPE) enters with a mass flow rate

## Materials and Methods

of 35 kg/h at ambient temperature 20 °C, whereas, from the counter side, hot exhaust gases enter through the inner tubes at a temperature of 500 °C and a mass flow rate of 82 kg/m<sup>3</sup> and leave the reactor with a temperature of 150 °C.

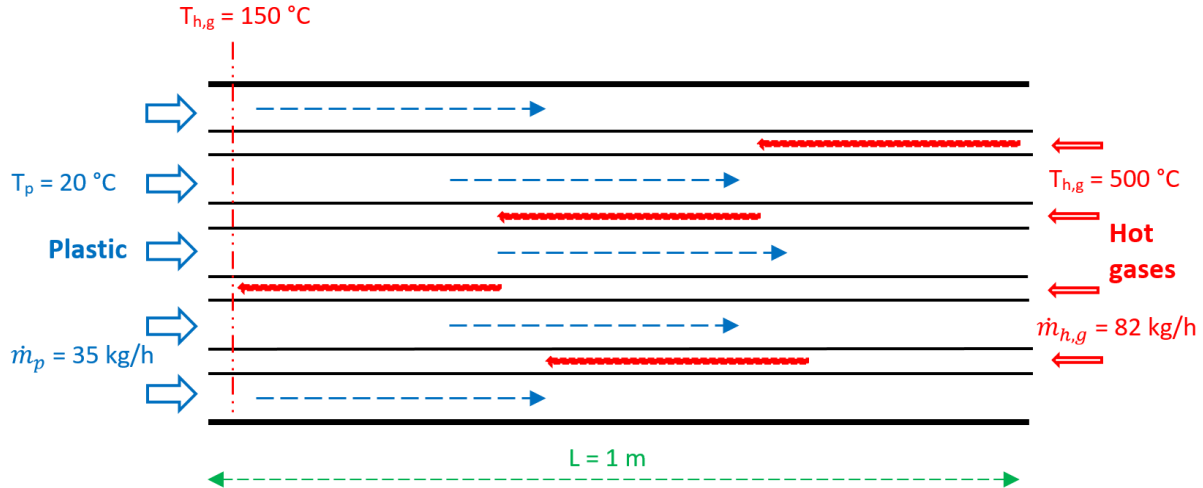


**Figure 2-17:** Geometry and boundary conditions results of the continuous pyrolysis reactor designed analytically by LMTD method.

This analytical model (geometry and plastic flow rate) will be checked and improved by modelling numerically the continuous reactor using COMSOL-Multiphysics. The previous validated pyrolysis model (melting and cracking models) will be used aside with the viscosity Carreau model, described by **Eq. 2-48**, to model plastic flow and pyrolysis inside the continuous reactor.

$$\frac{\eta - \eta_{\infty}}{\eta_0 - \eta_{\infty}} = \left(1 + (\lambda \dot{\gamma}_{ij})^2\right)^{\frac{n-1}{2}} \quad \text{Eq. 2-48}$$

where  $\eta$  (Pa.s) is the apparent viscosity, whereas  $\eta_0$  and  $\eta_{\infty}$  are the limiting values of the apparent viscosity at low and high shear rates, respectively, and  $\dot{\gamma}_{ij}$  (s<sup>-1</sup>) is the shear strain rate. In addition,  $\lambda$  (s) and  $n$  are two curve-fitting parameters that represent the relaxation time of the fluid and the index power of the flow, respectively.

Moreover, knowing that the outlet temperature of the byproducts exceeds the pyrolysis onset temperature and it is designed to be close as much as possible to the inlet exhaust gas temperature (500 °C) for better efficiency, thus the condensation phenomena will not appear inside the

continuous reactor. Therefore, continuity, momentum, energy, and phase field equations that model pyrolysis process inside the continuous reactor are, respectively, written as follow:

$$\vec{\nabla} \cdot \vec{u} = 0 \quad \text{Eq. 2-49}$$

$$\rho \left[ \frac{\partial \vec{u}}{\partial t} + (\vec{u} \cdot \vec{\nabla}) \vec{u} \right] = -\vec{\nabla} p + \vec{\nabla} \cdot \left( \eta \left( \vec{\nabla} \vec{u} + (\vec{\nabla} \vec{u})^T \right) \right) + \rho \vec{g} + \vec{F}_{st} \quad \text{Eq. 2-50}$$

$$\begin{aligned} \rho \left( (1 - f_l) C_{p,s} + f_l C_{p,l} + L \frac{\partial f_l}{\partial T} \right) \left( \frac{\partial T}{\partial t} + \vec{u} \cdot \vec{\nabla} T \right) \\ = Q_{sink} + \vec{\nabla} \cdot ((1 - f_l) k_s + f_l k_l) \vec{\nabla} T \end{aligned} \quad \text{Eq. 2-51}$$

$$\frac{\partial \Phi}{\partial t} + \vec{u} \cdot \vec{\nabla} \Phi = \vec{\nabla} \cdot \frac{\omega \zeta}{\vartheta^2} \vec{\nabla} \psi + \frac{S_g}{\rho_g} \quad \text{Eq. 2-52}$$

$$\psi = -\vec{\nabla} \cdot \vartheta^2 \vec{\nabla} \Phi + \Phi(\Phi^2 - 1) \quad \text{Eq. 2-53}$$

where the dynamic viscosity  $\mu$  is replaced by apparent viscosity  $\eta$ , and  $Q_{hs}$ ,  $Q_{cond}$  and  $S_l$  terms are removed from the energy and phase field equations, **Eq. 2-51** and **Eq. 2-52**, since there is no electric heater and due to the absence of condensation of the byproducts inside the reactor once it reaches the steady state.

On the other hand, inside the inner tubes, heat transfer for the hot exhaust gas is modelled using **Eq. 2-54**.

$$\rho C_p \left( \frac{\partial T}{\partial t} + \vec{u} \cdot \vec{\nabla} T \right) = \vec{\nabla} \cdot k \vec{\nabla} T \quad \text{Eq. 2-54}$$

where  $\rho$ ,  $C_p$  and  $k$  are the density, specific heat capacity, and the thermal conductivity of the hot exhaust gases, respectively. However, the fluid flow is modelled by the following two sets of equations depending on the Reynold's number given by **Eq. 2-55**, i.e. according to the type of flow:

$$\text{Re} = \frac{4\dot{m}}{N\pi d\mu} \quad \text{Eq. 2-55}$$

where  $\dot{m}$  (kg/s) is the mass flow rate of exhaust gases,  $N$  is the number of the inner tubes,  $d$  (m) is the inner diameter of the inner tubes, and  $\mu$  is the viscosity of the hot gases at the average temperature (325 °C).

If  $Re \leq 2300$ , i.e. laminar flow:

$$\frac{\partial \rho}{\partial t} + \vec{\nabla} \cdot (\rho \vec{u}) = 0 \quad \text{Eq. 2-56}$$

$$\rho \left[ \frac{\partial \vec{u}}{\partial t} + (\vec{u} \cdot \vec{\nabla}) \vec{u} \right] = -\vec{\nabla} p + \vec{\nabla} \cdot \left[ \mu (\vec{\nabla} \vec{u} + (\vec{\nabla} \vec{u})^T) - \frac{2}{3} \mu (\vec{\nabla} \cdot \vec{u}) \vec{I} \right] \quad \text{Eq. 2-57}$$

where  $\vec{I}$  is a  $3 \times 3$  identity matrix,  $\rho$  and  $\mu$  are the density and the dynamic viscosity of the hot exhaust gases.

Else if  $Re > 2300$ , i.e. turbulent flow, thus the turbulent flow of exhaust gas is modelled according to k- $\epsilon$  model:

$$\frac{\partial \rho}{\partial t} + \vec{\nabla} \cdot (\rho \vec{u}) = 0 \quad \text{Eq. 2-58}$$

$$\begin{aligned} \rho \left[ \frac{\partial \vec{u}}{\partial t} + (\vec{u} \cdot \vec{\nabla}) \vec{u} \right] &= -\vec{\nabla} p \\ &+ \vec{\nabla} \cdot \left[ (\mu + \mu_T) (\vec{\nabla} \vec{u} + (\vec{\nabla} \vec{u})^T) - \frac{2}{3} (\mu + \mu_T) (\vec{\nabla} \cdot \vec{u}) \vec{I} - \frac{2}{3} \rho k_T \vec{I} \right] \end{aligned} \quad \text{Eq. 2-59}$$

$$\rho \left( \frac{\partial k_T}{\partial t} + \vec{u} \cdot \vec{\nabla} k_T \right) = \vec{\nabla} \cdot (\mu + \mu_T) \vec{\nabla} k_T + P_k - \rho \epsilon_T \quad \text{Eq. 2-60}$$

$$\rho \left( \frac{\partial \epsilon_T}{\partial t} + \vec{u} \cdot \vec{\nabla} \epsilon_T \right) = \vec{\nabla} \cdot \left( \mu + \frac{\mu_T}{1.3} \right) \vec{\nabla} \epsilon_T + 1.44 \frac{\epsilon_T}{k_T} P_k - 1.92 \rho \frac{\epsilon_T^2}{k_T} \quad \text{Eq. 2-61}$$

The model introduces to the continuity and momentum equations, **Eq. 2-58** and **Eq. 2-59**, two additional transport equations (**Eq. 2-60** and **Eq. 2-61**) and two dependent variables: the turbulent kinetic energy  $k_T$  ( $m^2/s^2$ ), and the turbulent dissipation rate,  $\epsilon_T$  ( $m^2/s^3$ ).

In addition, the turbulent viscosity  $\mu_T$  (Pa.s) and the production term  $P_k$  ( $kg \cdot m^{-1} \cdot s^{-3}$ ) are described respectively in the following equations:

$$\mu_T = 0.09 \rho \frac{k_T^2}{\epsilon_T} \quad \text{Eq. 2-62}$$

$$P_k = \mu_T \left[ \vec{\nabla} \vec{u} : (\vec{\nabla} \vec{u} + (\vec{\nabla} \vec{u})^T) - \frac{2}{3} (\vec{\nabla} \cdot \vec{u})^2 \right] - \frac{2}{3} \rho k_T \vec{\nabla} \cdot \vec{u} \quad \text{Eq. 2-63}$$

In addition, this standard k- $\epsilon$  model is one of the most used turbulence models for industrial applications (COMSOL, 2017).

Finally, after setting up all of the simulation settings and respecting mesh convergence, the previous analytical results, illustrated by **Figure 2-17**, are checked and the modelled continuous reactor is further optimized by employing a sensitivity study for the reactor's geometry (length of the reactor and number of the inner tubes) and plastic mass flow rate.

### 2.7 . Conclusions

In this chapter, methodology and procedures are illustrated extensively in order to achieve the objectives of the thesis; apprehending and modelling plastic pyrolysis process. In addition, utilized governing equations and models are also considerably explained to facilitate the grasp of modelling.

At the beginning of the chapter, the materials that are used in this study such as PP granules and HDPE flakes are introduced, where the thermal properties and the ultimate analysis of the corresponding materials are illustrated. Moreover, the used equipment such as TGA-DSC apparatus and the semi-batch reactor are also presented and the experimental procedure conducted for PP and HDPE using these instruments are described. Furthermore, COMSOL Multiphysics software is introduced, in addition to the suitable dynamic solvers used in this study such as the PARDISO solver for linear systems and the Newton's method for the nonlinear one.

Regarding the procedure of modelling and simulation, first, melting models and equations such as the apparent heat capacity method AHCM are presented for the sake of modelling the melting process at a milli-particle scale inside the TGA-DSC and at a lab-scale semi-batch reactor scale. Melting model inside the TGA-DCS is governed by the heat conduction equation modified by the AHCM method, where the particle is treated as a fixed fluid. However, modelling melting inside the semi-batch reactor is achieved by two approaches: First one, assuming molten plastic as a stationary fluid, due to its high viscosity, thus the heat conduction equation modified by the AHCM method is the governing equation. Second approach, fluid flow and heat transfer of molten plastic are modelled by coupling continuity and momentum equations with the energy equation (modified by the AHCM method). Moreover, the electric heater of the semi-batch reactor is modelled by two means; first, the recorded power of the heaters, function of time, is implemented as a heat source

domain in the simulation according to the Joule's effect, i.e. electric resistive power is converted into thermal power. On the other hand, the second way is by imitating the real heater and controller to maintain the reactor's wall temperature at a desired temperature in the simulation. All of the preceding simulations are said to be validated when the average relative error among the experimental and simulated result, temperature and energy balance, doesn't exceeds 10 %.

Moving on to the cracking process, the procedure of determining kinetic parameters ( $f(x)$ ,  $E$  (J/mol), and  $A$  ( $s^{-1}$ )) and the kinetic rate ( $dx/dt$  ( $s^{-1}$ )) for PP and HDPE is broadly illustrated. First, the kinetic model function  $f(x)$  is determined by the Criado's method, which is a curve fitting method that compares the experimental data with the most common theoretical kinetic models found in literature. Then the activation energy  $E$  and the pre-exponential factor  $A$  are found according to the most three commonly used isoconversional methods; Friedman (FR), Kissinger-Akahira-Sunose (KAS), and Flynn-Wall-Ozawa Method (FWO). Finally, the theoretical conversion  $x$  is computed according to the determined kinetic triplet and compared with the experimental data for the sake of validation; the upper limit of the average relative error is set to be 10 %. Then the validated TGA kinetic model is employed to model the cracking process of PP and HDPE at milli-particle scale inside the TGA-DSC apparatus. The heat conduction equation with a heat sink term is used as a governing equation. Whereas, the density of the particle is taken to be function of conversion at each mesh or element, in the simulated domain, to model mass loss inside the crucible. In addition, experimental and simulated heat absorption by the pyrolyzed sample, function of time, is compared as a tribute to validate the model.

Furthermore, regarding modelling plastic pyrolysis inside the semi-batch reactor, Phase Field method is coupled with the continuity, momentum and energy equations to model the whole pyrolysis process. Phase Field method aims to model the two-phase flow, i.e. molten plastic and gas byproducts, and the transition from one to another, with a surface tracking interface to track the two fluids. A key factor in this model is the mass source term that converts molten plastic into gas byproducts according to the deduced kinetic pyrolysis model, which is multiplied by the cracking enthalpy of PP and HDPE to model the endothermic reaction inside the reactor. Moreover, another mass source term is used to model the condensation phenomena of the byproducts inside the reactor. Temperature results at different location of the reactor and the rate of cracking will be compared with the experimental data to validate the model.

Finally, after the pyrolysis model is validated in the semi-batch reactor it is used to model plastic pyrolysis in a continuous reactor under the same temperature (500 °C) and heating conditions (below 10 °C/min). The continuous reactor is designed to be a counter flow multi-tube heat exchanger heated by the exhaust gas, 500 °C, of 8 kW diesel engine. A previous work, realized by (Kassargy, 2018) at the GEPEA, aimed to model this continuous reactor analytically using logarithmic mean temperature difference (LMTD) method. However, in this study, the work is continued by modelling the continuous reactor numerically using finite element method and according to the preceding validated pyrolysis model and equations (inside the semi-batch reactor). Almost the same governing equations, used in modelling pyrolysis inside the semi-batch reactor, are applied to the plastic side when modelling the continuous reactor, except that the dynamic viscosity is replaced by the apparent viscosity according to Carreau model. Nonetheless, standard k- $\epsilon$  model coupled with the energy equation is applied to the exhaust gases side to model mass and heat transfer as the flow is turbulent. Additionally, the continuous reactor is further optimized by employing a sensitivity study for the reactor's geometry (length of the reactor and number of the inner tubes) and plastic mass flow rate.

All in all, the next three chapters will illustrate the results of all of the suggested models and simulations. Where the next chapter will demonstrate the simulation and experimental results of modelling melting process for PP and HDPE at different scales. Moreover, Chapter Four will discuss the results of modelling whole pyrolysis process inside TGA-DSC and the semi-batch reactor. Finally, Chapter Five will illustrate the results of modelling and optimizing the proposed design of the continuous pyrolysis reactor by utilizing the validated pyrolysis model used in the semi-batch reactor.

## Chapter 3 Modelling of melting process for PP and HDPE

Recalling the desired work of this thesis, modelling plastic pyrolysis at low heating rates, below 10 °C/min, and knowing the fact that plastic pyrolysis is divided into two consecutive sub-processes i.e. melting and chemical cracking. Thus, the melting process will be modelled prior to the latter one (cracking process); where the results will be illustrated in this chapter. First, DSC experimental results for melting PP and HDPE according to the following heating rates (4, 6, 8, and 10 °C/min) will be illustrated. Then, the simulation results of modelling melting process for PP and HDPE, at a milli-particle scale, using AHCM method are presented. After that, the melting process is modelled in a laboratory scale fixed bed semi-batch reactor. However prior to modelling melting inside the semi-batch reactor, a sensitivity study for the thermal properties of the reactor is accomplished first and the sensible heat transfer within the loaded reactor (loaded by solid or fluid) is also modelled.

### 3.1 Experimental DSC results for PP and HDPE

In order to evaluate the melting characteristics (melting range, peak temperature, and the latent heat of fusion) for the PP and HDPE, DSC experiments of a mass sample, about  $18 \pm 1$  mg, are performed at different heating rates (4, 6, 8, and 10 °C/min). **Figure 3-1** and **Figure 3-2** illustrate the experimental results for PP and HDPE, respectively, where the heat absorbed by the sample (heat flow,  $\dot{Q}_a$  (mW)) is drawn with respect to the sample's temperature.

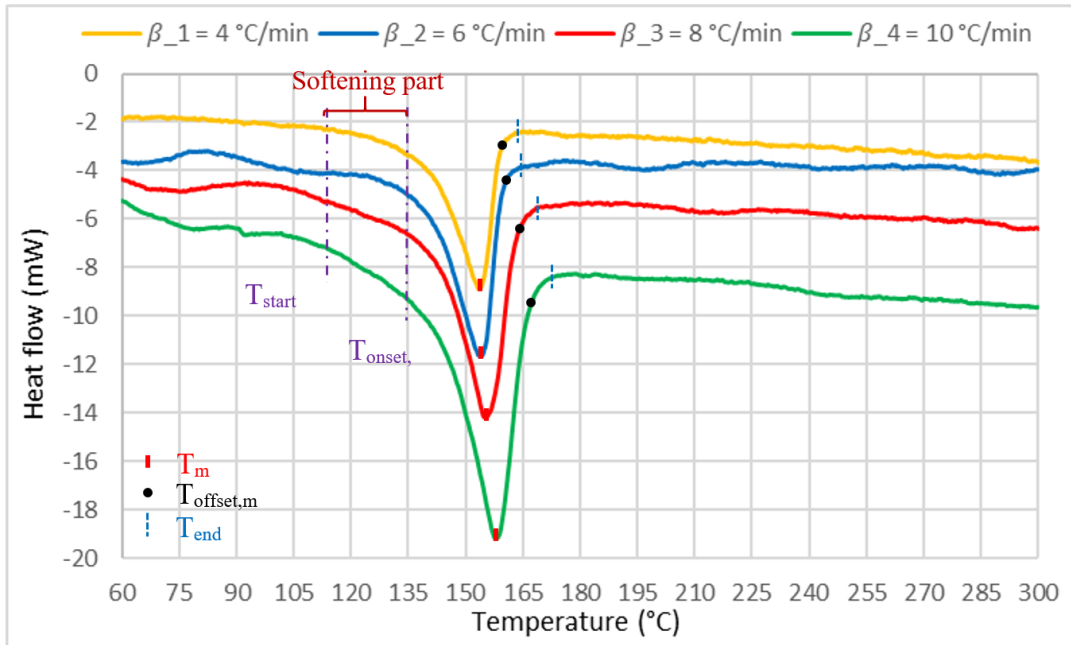


Figure 3-1 : DSC experiments for PP ( $18 \pm 0.5$  mg) and different heating rates.

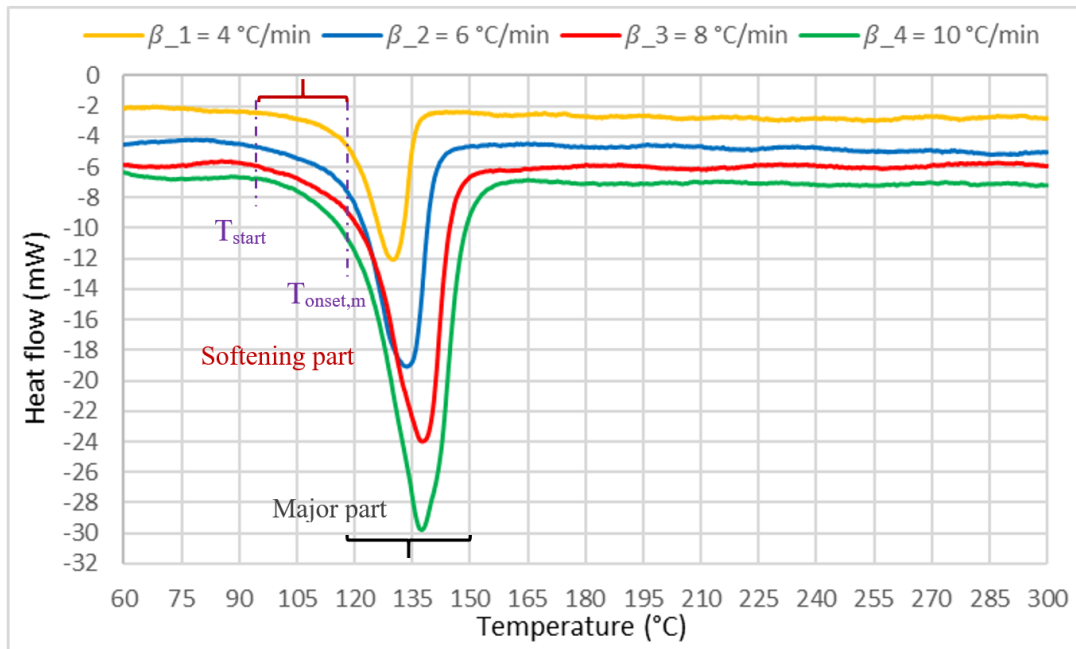


Figure 3-2 : DSC experiments for HDPE ( $18 \pm 1$  mg) and different heating rates.

First of all, heat flow has a negative sign because of the heating and melting processes are endothermal. In addition, the absorbed heat is said to be directly proportional to the heating rate,

i.e. when the heating rate increases the rate of heat absorbed by the samples also increases and vice versa.

On the other hand, regarding the melting temperatures  $T_m$ , it is defined as the peak melting temperature located at the troughs of the melting curves, which is said to increase or shifts to the right as the heating rate increases. Moreover, in the same manner to  $T_m$ ,  $T_{end}$  or  $T_{offset,m}$  shifts to the right as the heating rate increases (**Figure 3-1**).  $T_{end}$  and  $T_{offset,m}$  are two approximately equal temperatures that indicate the end of the melting process and they are located just before the heat flow curves starts to flatten after the convex melting curve, as shown in **Figure 3-1**.

Additionally, melting range temperature  $\Delta T_m$  for PP and HDPE varies from 50 to 60 °C, whereas melting undergoes two stages. First stage is the softening part which is a weak and slow phase, and it begins from the start melting temperature till the onset temperature (at which the second major and fast phase starts) as shown in **Figure 3-2**. However, the second stage is the major part of melting process that starts at the onset temperature and ends at the offset one. Therefore, melting starts very slow, at the beginning, at the start temperatures (116 °C for PP and 95 °C for HDPE) then it increases after the temperature passes the onset temperatures (about 135 °C for PP and 118 °C for HDPE), where the major melting phenomena clearly appears.

This major part is faster than the softening phase and contributes to more than 90 % of the whole melting process and energy absorption. Furthermore, melting curves are not symmetrical at the peak melting temperature, and  $T_m$  is more close to the end temperature rather than the start one. In contrast, if the major part is taken alone, the convex melting curve is said to be symmetrical at  $T_m$  as **Figure 3-2** shows.

After defining and determining the corresponding melting temperatures ( $\Delta T_m$ ,  $T_m$ ,  $T_{start}$ , etc...), the heat capacities function of temperature for PP and HDPE are determined from the DSC curves and by using **Eq. 3-1**.

$$C_p = \frac{1}{m} \frac{\dot{Q}_a}{\beta} \quad \text{Eq. 3-1}$$

where  $\dot{Q}_a$  (mW) is the heat flow consumed by the material, given by the DCS, and  $\beta$  (°C.s<sup>-1</sup>) is the programmed heating rate by the DSC apparatus. For PP, the heat flow curves tend to decrease linearly after the melting process ends (**Figure 3-1**), thus its heat capacity is assumed to increase

## Modelling of melting process for PP and HDPE

linearly from 2190 J/K/kg at 170 °C to 2500 J/K/kg at 250 °C then it stabilizes at this value. In contrast, HDPE heat capacity increases from 2190 J/K/kg at 150 °C to 2500 J/K/kg at 200 °C then it remains constant after 200 °C, since the heat flow  $\dot{Q}_a$  is almost constant as **Figure 3-2** shows. **Figure 3-3** shows the deduced average heat capacities for PP and HDPE with respect to temperature. As it is noticed from **Figure 3-3**, the magnitude of the heat capacity for PP and HDPE at the solid state equals to 1800 J/K/kg, then it increases till a constant value about 2190 J/K/kg at the onsets temperatures (95 °C for HDPE and 116 °C for PP) as the melting process occurs. After that, melting process ends and the heat capacities increase to 2500 J/K/kg and stabilize at this value at 250 °C for PP and at 200 °C for HDPE.

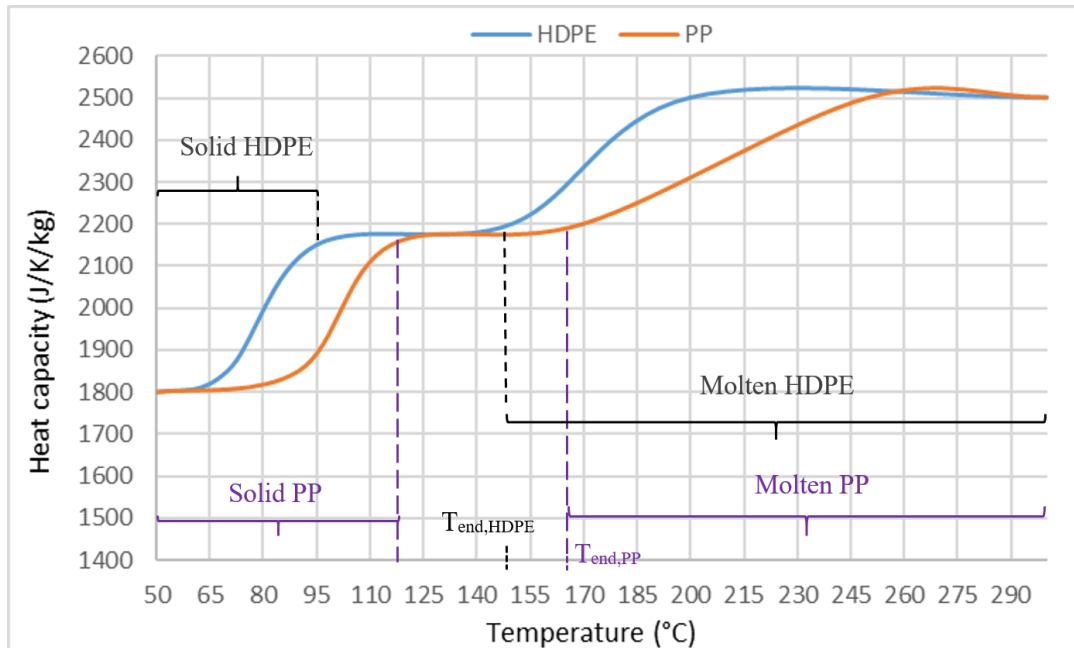


**Figure 3-3** : Deduced heat capacities, function of temperature, for PP and HDPE.

Nonetheless, for each heating rate the fusion enthalpies for PP and HDPE are evaluated by integrating the melting curves with respect to time between the start and the end temperatures, and dividing the obtained values by the mass of the samples. Therefore, **Table 3-1** demonstrates the melting characteristics (with the heat of fusion included) for PP and HDPE at different heating rates. The heat capacity results and the deduced melting characteristics for PP and HDPE are found to be in a good agreement with results illustrated in literature (INEOS, 2014a, 2014b; Li *et al.*, 2019; Shafigullin *et al.*, 2018).

**Table 3-1** : Melting characteristics for PP and HDPE at different heating rates.

| Melting Characteristics  |                            |      |                        |       |                          |      |                            |       |
|--------------------------|----------------------------|------|------------------------|-------|--------------------------|------|----------------------------|-------|
| Heating rate<br>(°C/min) | T <sub>start</sub><br>(°C) |      | T <sub>m</sub><br>(°C) |       | T <sub>end</sub><br>(°C) |      | Fusion enthalpy<br>(kJ/kg) |       |
|                          | PP                         | HDPE | PP                     | HDPE  | PP                       | HDPE | PP                         | HDPE  |
| <b>4</b>                 | 116                        | 95   | 153.5                  | 130   | 163                      | 141  | 58.5                       | 108.5 |
| <b>6</b>                 | 116                        | 95   | 154                    | 133.5 | 166                      | 148  | 58                         | 117   |
| <b>8</b>                 | 117                        | 98   | 155.5                  | 137.5 | 169                      | 153  | 57.5                       | 121   |
| <b>10</b>                | 125                        | 98   | 158                    | 137.5 | 174                      | 158  | 56.5                       | 124.5 |

### 3.2 Modelling melting process for PP and HDPE at a milli-particle scale

After presenting the DCS results, the melting phenomena inside the DSC apparatus is modelled by the apparent heat capacity method (AHCM) using COMSOL-Multiphysics, where the sample crucible is modelled as 2D-axisymmetric as shown in **Figure 3-4(b)**.

The experimental melting characteristics and heat capacities for PP and HDPE, are implemented in the simulation along with the heat conduction equation and the AHCM (**Eq. 2-3**) presented in Chapter Two **section 2.4.1**. However, only the major part of the melting process is modelled due to the fact that the used conversion function in the AHCM is symmetrical and centered at the peak melting temperature ( $T_m$ ), as presented by **Figure 2-9** in **section 2.4.1**. Moreover, a melting range of 30 °C from the onset temperatures (135 °C for PP and 118 °C for HDPE) till the end temperatures is employed. Moreover, the density values for PP and HDPE are assumed to be constant, 900 and 950 kg/m<sup>3</sup> respectively. In addition, molten plastic is assumed to be a stationary fluid because of the small volume of the crucible (2 mm radius and 2 mm height) and the high viscosity (more than 1000 Pa.s) of the molten plastic, especially at low shear rates (*Agassant et al., 2019*).

After setting the model properly, all the numerical simulations (at different heating rates) are converged using an extremely fine mesh of an element size that doesn't exceed 0.09 mm. Note

that further decrease in the element size didn't change the solution (**Figure 3-4(a)**). Regarding the skewness and the condition number mesh characteristics, the values of the minimum and average element qualities are 0.6 and 0.9, respectively, for 2000 triangular element. In addition, the PARDISO algorithm is used to solve the linearized system at each iteration step set by the Newton's method algorithm for solving the non-linear systems (dynamic system).

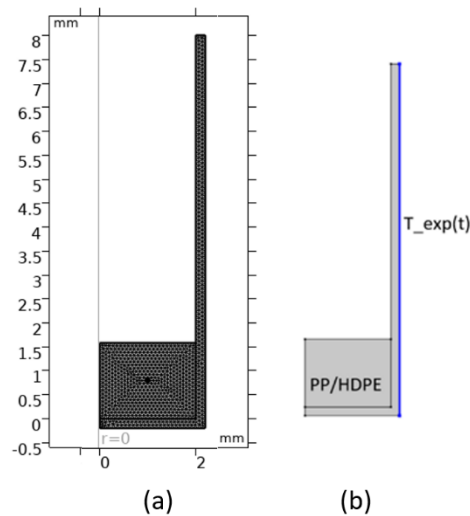


**Figure 3-4 :** (a) Mesh display, (b) 2D-axisymmetric crucible model.

**Figure 3-5** and **Figure 3-6** show the simulated and experimental heat flow consumed during the melting process of PP at two heating rates respectively (the lowest and the highest), 4 and 10 °C/min. On the other hand, **Figure 3-7** and **Figure 3-8** show the results for HDPE at 4 and 10 °C/min as heating rates. For the PP and HDPE, the average relative error between the experimental and simulated results of the heat flow didn't exceed 9 % and the simulation results are in well agreement with the experimental ones.

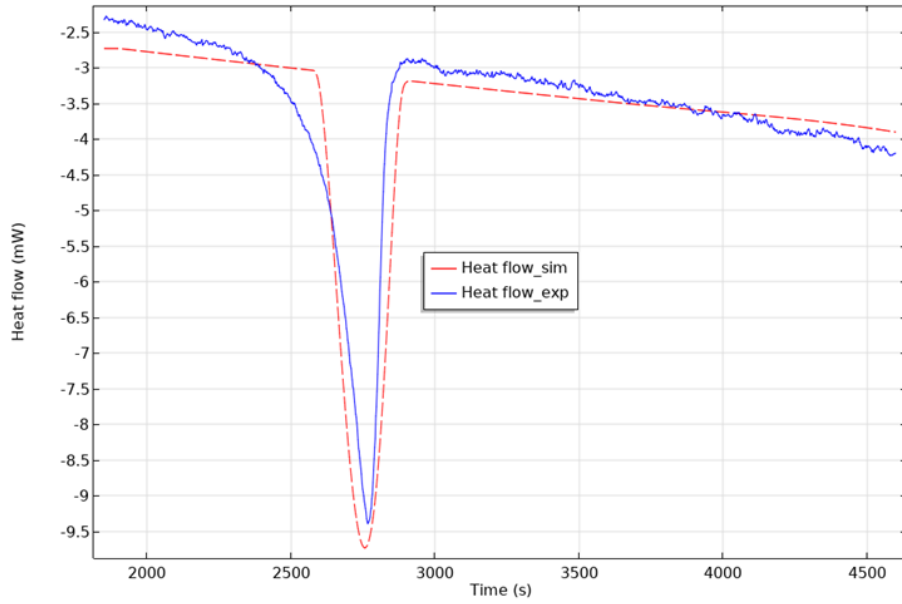


Figure 3-5 : Experimental and simulated results for PP melting and heating by  $\beta = 4 \text{ }^\circ\text{C/min}$ .

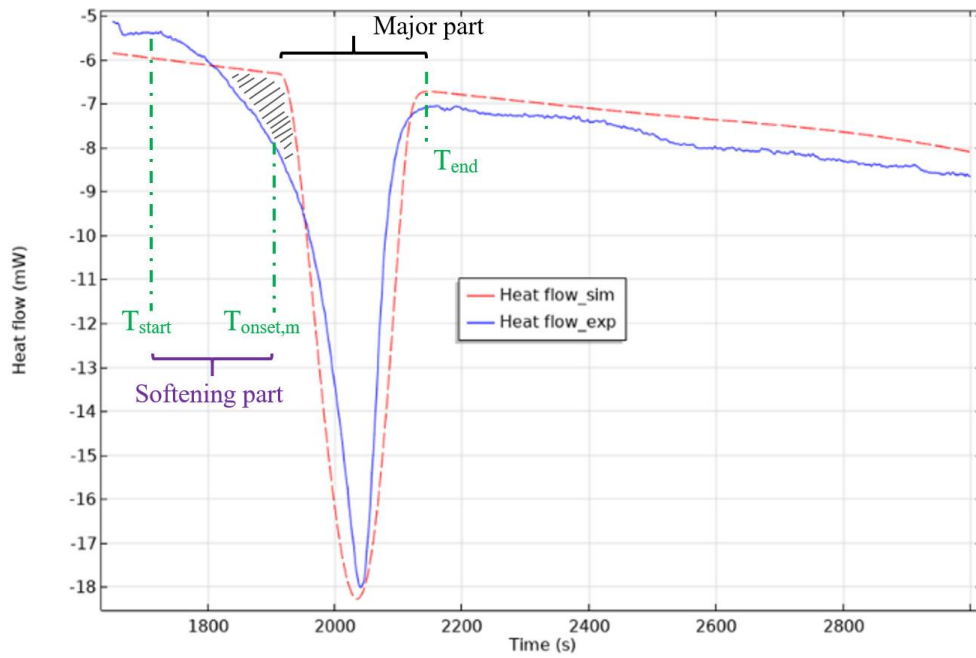
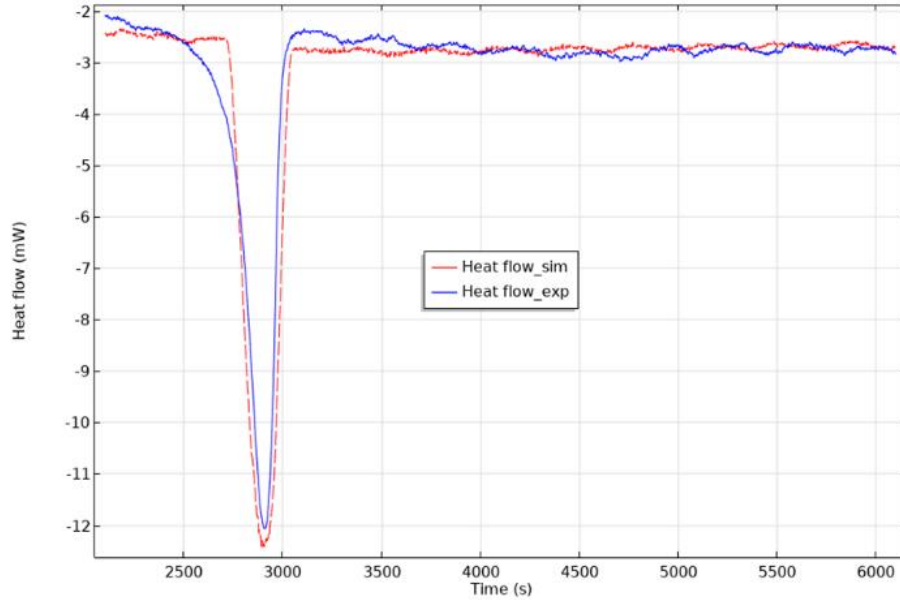
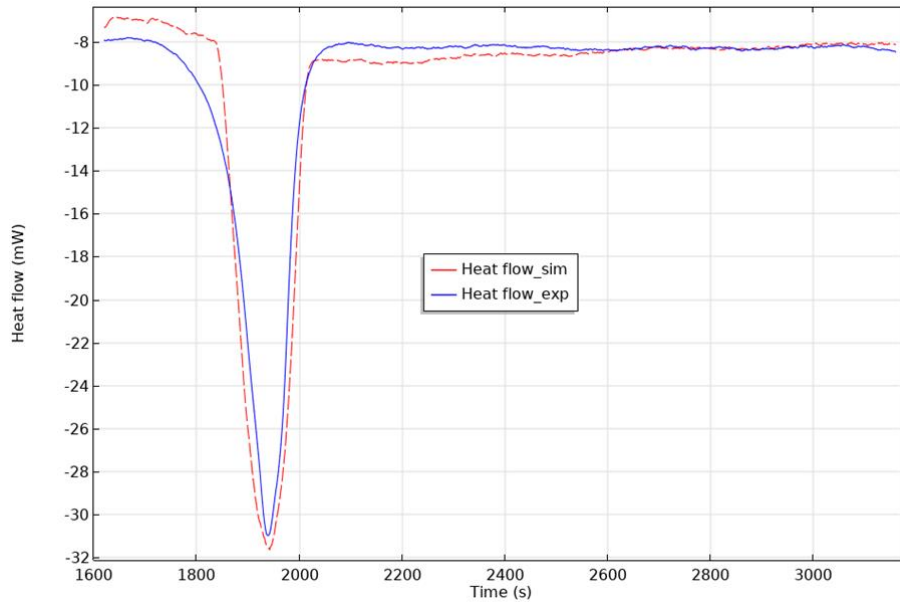


Figure 3-6 : Experimental and simulated results for PP melting and heating by  $\beta = 10 \text{ }^\circ\text{C/min}$ .



**Figure 3-7 :** Experimental and simulated results for HDPE melting and heating by  $\beta = 4 \text{ }^\circ\text{C/min}$ .



**Figure 3-8 :** Experimental and simulated results for HDPE melting and heating by  $\beta = 10 \text{ }^\circ\text{C/min}$ .

As shown from the results, the softening part (from the start temperature till the onset one as shown in **Figure 3-6**) of the melting process is not modelled. Thus, the simulated heat absorption in this region is increasing slowly and linearly for HDPE and PP due to the increase of the heat capacity as mentioned earlier in **Figure 3-3**. In contrast, the experimental heat flow starts to increase faster and nonlinearly (softening phase) at the starting temperatures of the melting phenomenon. Therefore, a small gap (shaded part) appears between the simulated and experimental results at the

beginning of the process as shown in **Figure 3-6**. However after the softening phase ends, this gap starts to decrease till the results are said to be matched for the major and main part of melting, which contributes to more than 90 % of the process. Nevertheless, the experimental and simulated results in this part are in a very good agreement with a relative error less than 5 %.

Yet, a further improvement can be done to model this softening part, like by using AHCM to model this part or by using an exponential conversion function according to the Arrhenius law instead of the linear symmetrical conversion function used in this study.

Furthermore, regarding the heating part after the melting process, i.e. after  $T_{\text{end}}$ , the heat flow seems to remain constant for HDPE (after 200 °C) due to its constant heat capacity, about 2500 J/K/kg. Whereas, PP's heat flow decreases linearly due the increase of the heat capacity from 2190 J/K/kg at 170 °C to 2500 J/K/kg at 250 °C, as shown previously in **Figure 3-3**. The relative error for this part is less than 5 % for PP and HDPE. Moreover, the remaining simulation results for PP and HDPE at the other heating rates (6 and 8 °C/min) are shown in the **Appendix: A (Figure 3-1A and Figure 3-2A)**, where the average relative error didn't exceed 9 %.

To conclude, the results comparison and error calculations prove that the AHCM successfully models the melting process for PP and HDPE at a milli-particle scale inside a DSC apparatus with a maximum average relative error of 9 % among all of the simulated and experimental results.

### 3.3 Modelling sensible heat transfer within the semi-batch reactor

For the sake of simplicity and error reduction, modelling plastic melting process inside the semi-batch reactor is not achieved directly. Otherwise, the thermal properties of the reactor's material are checked and verified by modelling the empty reactor as a first step. Where the results of modelling sensible heat transfer within the empty semi-batch reactor are illustrated in this section. Afterwards, the reactor is loaded with solid and fluid materials and modelled to check the validity of heat transfer model within the loaded material and the reactor. In addition, the purpose of this step is to reduce the margin of the possible rising errors and to prevent the confusion of the source of error later on when modelling the melting process. Hence, the results of modelling sensible heat transfer of the loaded reactor with solid and fluid such as sand, sunflower oil, and water will be also presented.

The common simulation guide lines and the used mesh analysis to obtain all of the proceeding simulation results in this section and in the next section (**section 3.4**) are as follow:

- 1- The semi-batch reactor is modelled as 2D-axisymmetric, in order to reduce the computational time.
- 2- All of the numerical studies are carried out using COMSOL-Multiphysics software and converged using an absolute tolerance of 0.0001.
- 3- A fully coupled approach is used for the numerical calculation instead of the segregated approach, where all of the dependent variables, such as T, and  $\mathbf{u}$ , are evaluated at the same time and not subsequently.
- 4- The PARDISO (Parallel Direct Solver) algorithm, which is based on the lower-upper decomposition method for matrices, is used to solve the linearized system at each iteration step defined by the Newton's Method (Newton-Raphson Method), with an automatic damping factor to calculate the solution at each time step taken by the solver.
- 5- A mesh sensitivity study is conducted for each simulation result in order to ensure the solution convergence. First, a coarse triangular mesh of 5 mm element size is used, where the relative solution is stored. Then the mesh is gradually refined as the new solution still differs from the previous one. Finally, at 0.5 mm element size the solution is converged and the results didn't change as the mesh element size is further decreased. Whereas, the corresponding skewness and condition number mesh characteristics have a minimum element quality above 0.6 and an average element quality of 0.9 for approximately 40000 triangular elements. **Figure 3-9** shows the final mesh used in all of the simulations, where the solutions are converged.

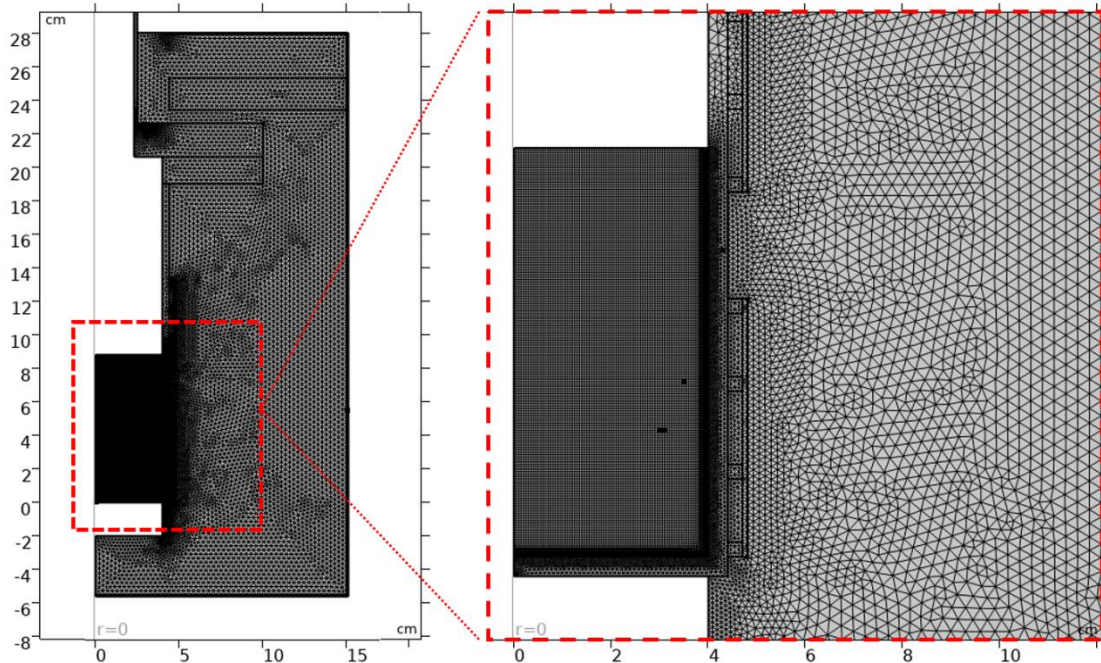


**Figure 3-9 :** Extremely fined mesh used in all of the simulations.

6- Finally, all of the coming simulations are done in two ways; the first way is by direct implementation of the experimental recorded power  $\dot{q}_{exp}(t)$  as a heat source into COMSOL, and, the second way is by modelling a controller at the wall temperature ( $T_2$ ) to imitate the operation of the real heater and controller, as described in Chapter Two **section 2.4.2.1**.

### 3.3.1 Empty reactor

The empty semi-batch reactor is modelled using the heat conduction equation (**Eq. 2-5**) with the appropriate boundary conditions (illustrated in Chapter Two **section 2.4.2.1** and displayed by **Figure 2-12**). In addition, regarding the other boundary and initial conditions, the reactor is heated by electrical heater from ambient temperature 18 °C to 490 °C then cooled down after stabilizing at this temperature for a period of time. Thus, a heat source  $Q$  (in **Eq. 2-5**) function of time and equals to the experimental power of the electrical heater  $\dot{q}_{exp}(t)$  is used as the heating boundary condition in the simulation (refer to Chapter Two **section 2.4.2.1**). However, concerning the thermal properties of the reactor, temperature-dependent properties (range of 25 – 500 °C) illustrated previously in **Table 2-3** are implemented into the simulation.

Different experiments are done at different heating rates (10, 20 and 30 % of the heater full load 1500 W) to assure that the model is working well at the desired heating rates (below 10 °C/min).

**Figure 3-10** shows the simulated results, surface profile temperature at a specific time, for one of the experiments (heating load 30 % i.e. 450 W). The figure shows the diffusion of temperature and the distribution of the thermocouples that are measured and compared with the experimental one. As seen, the main part of the interior wall of the reactor (where  $T_2$  is located) reached temperature about 500 °C, however, the outer wall of the reactor (insulator) didn't exceeds 50 °C. More detailed results are presented by **Figure 3-11** and **Figure 3-12**.

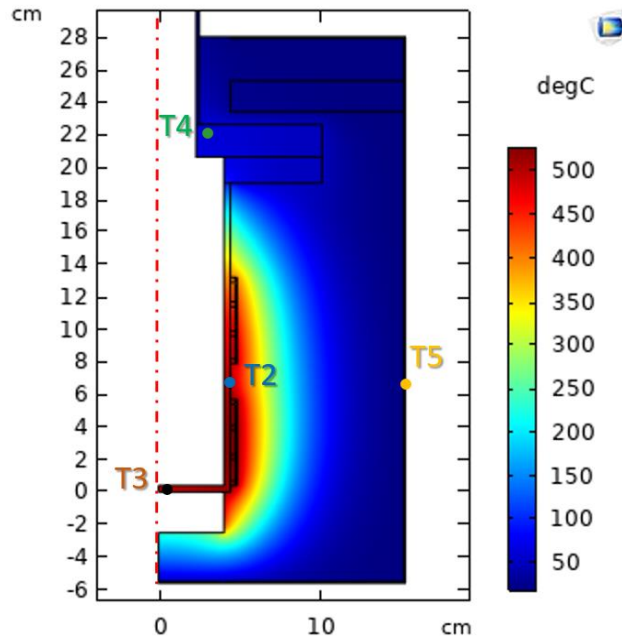


**Figure 3-10** : 2D-axisymmetry simulation for the empty reactor heated using 450 W load, at  $t = 3000$  s.

**Figure 3-11** and **Figure 3-12** illustrate the evolution of the experimental and simulated temperatures with respect to time. It is noticed that  $T_2$  (wall) and  $T_3$  have almost the same profile temperature due to the high thermal conductivity of stainless steel. In addition, as  $T_2$  (temperature of the wall) reaches the given controlled temperature 490 °C the regulator undertakes temperature stabilization which leads to a periodic fluctuation due to the heater's on and off cycles.

Also it is noticed that when the heating process ended and the cooling process started at  $t = 6000$  s, the top temperature ( $T_{4\_exp}$ ) remained increasing for a short period of time (from 6000 to 7500 s), in contrast to the simulated temperature  $T_{4\_sim}$ , which started directly decreasing in a slow cooling rate. Still, after this period (7500 s), the cooling rate of  $T_{4\_exp}$ , 0.6 °C/min, is almost equal to that of the simulated temperature  $T_{4\_sim}$ , 0.57 °C. Also as revealed from the results, **Figure 3-12**,

T5\_sim (insulator temperature) is in a good agreement with the experimental one, thus the heat dissipation inside the reactor and the heat loss to the surrounding is well modelled.

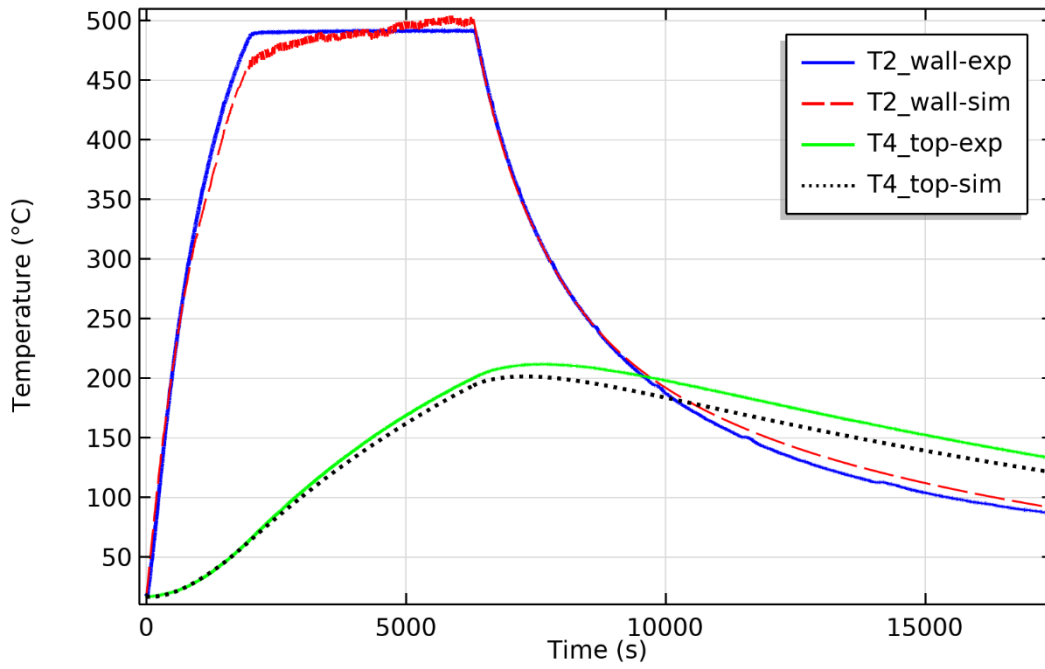


**Figure 3-11 :** Temperature comparison, T2\_wall and T4\_top, for empty reactor heated at 450 W load, T2 regulated at 490°C.

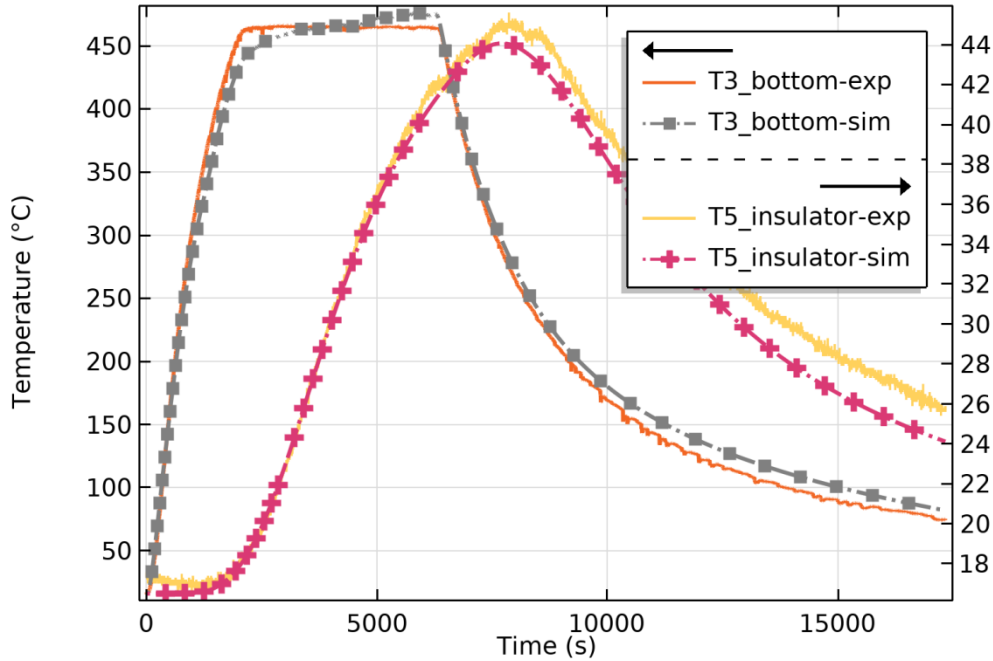


**Figure 3-12** : Temperature comparison, T3\_bottom and T5\_insulator for empty reactor heated at 450 W load, T2 regulated at 490°C.

The average relative errors (all over the heating and cooling periods) for all temperatures are calculated, they are lower than 6 % and this lead to validate the used thermal properties of the reactor (displayed in Chapter Two **Table 2-3**) and the model for heating an empty reactor. Furthermore, **Figure 3-13** and **Figure 3-14** show the parity plots for the simulated results and the experimental data for further validation, where the maximum relative error didn't exceed 10 %, as **Figure 3-14** illustrates. Finally, the empty reactor is modelled and the thermal properties are validated along with the boundary conditions and the used governing equations.

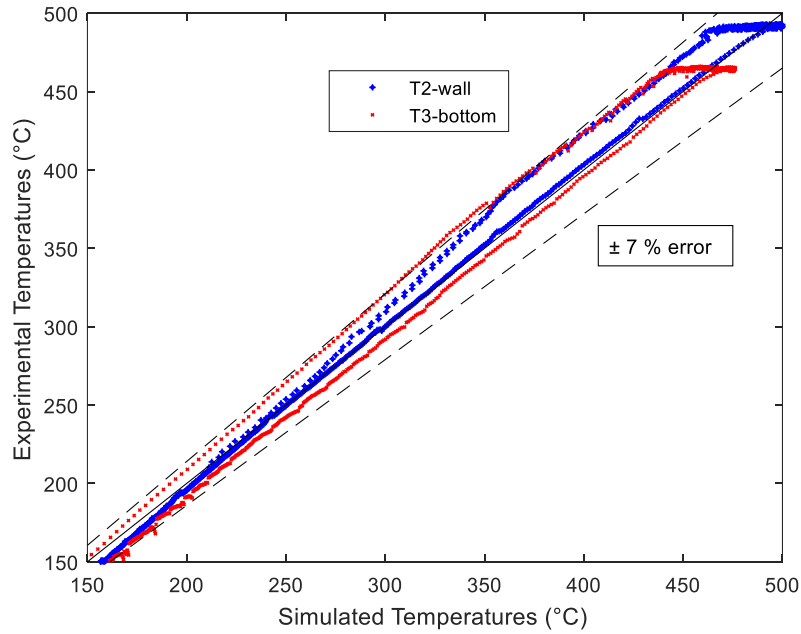


Figure 3-13 : Parity plot for T2\_wall and T3\_bottom for empty reactor experiment, heated using 450 W heating load.

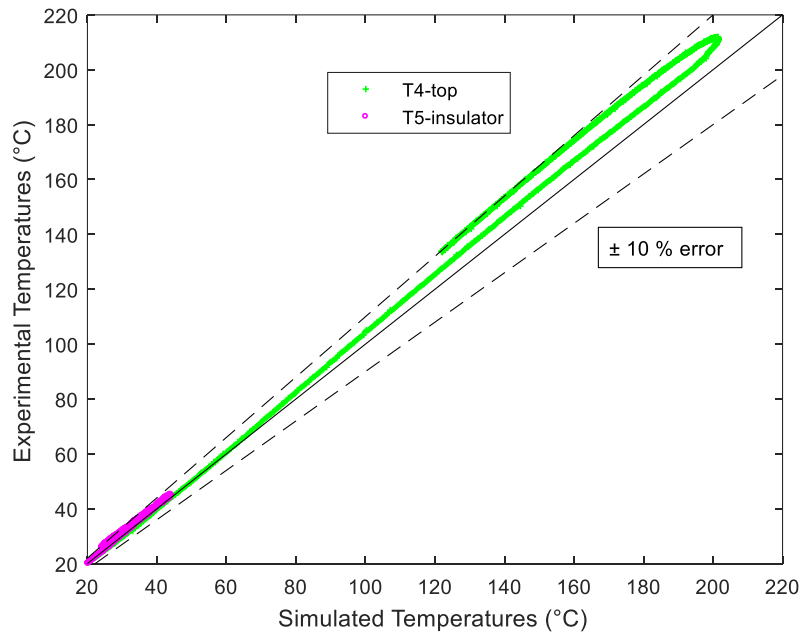


Figure 3-14 : Parity plot for T4\_top and T5\_insulator for empty reactor experiment, heated using 450 W heating load.

### 3.3.1.1 Sensitivity study

After the empty reactor is modelled, a sensitivity study is done to notify the influence of varying the thermal properties on the results and to detect the sensitive parameters. Hence, average values of the reactor's thermal properties are used instead of temperature-dependent properties, and the simulation results are compared with the experimental ones. As a result, by using the average values of properties the overall average relative error increased by 3 % to become 9 % between the experimental and simulated results, however, it didn't affect the simulation time or model complexity. The main parameter that influenced this increase is the insulator thermal conductivity (average value of  $k_{ins}$ ), which increased the error by 3 %. On the other hand, all of the other parameters alerted the resulted by less than 1 % error, which is a negligible effect. This is logic because their values don't change notably with temperature like the insulator's thermal conductivity that doubles as temperature increases from 25 to 500 °C, as **Table 2-3** illustrates.

Besides that, natural air flow inside the reactor is taken into consideration to enhance the results. However, this is due to the weak air flow inside the reactor and at the bottom gap and also because of the low thermal conductivity and heat capacity of air. Therefore, surface to surface radiation is preferred to be the only mode of heat transfer inside the empty reactor and at the bottom gap to reduce the high computational costs required by the fluid flow simulation in these regions.

### 3.3.1.2 Controller simulation

After the empty reactor is modelled by implementing the experimental power  $\dot{q}_{exp}(t)$  directly into simulation, another approach of simulation is used to mimic the role of the heater. This approach provides an independent numerical model of the semi-batch reactor that can be used later on for simulation studies without performing experimental studies, i.e. without the need of the experimental power.

Therefore, a heat source is implemented in the simulation and it is set to provide the same experimental power of the heaters to control the simulated wall temperature ( $T_2$ ). Where,  $T_2$  is stabilized at the desired temperature by switching ON and OFF the implemented heat source, same as the real regulator does.

Figure 3-15 and Figure 3-16 show the simulation results for the empty reactor heated by 450 W load with a simulated controller to mimic the function of the heaters. First thing to notice is that the temperature profiles are almost the same as they are obtained by the first method, displayed by Figure 3-11 and Figure 3-12. Whereas, the relative error difference between the two methods (power implementation and controller simulation) didn't exceed 2 %, i.e. the relative error among all simulated and experimental temperatures according to the second approach is below 8 %. However, unlike  $T_2$  in Figure 3-11, the simulated wall temperature  $T_2$  rises till the desired and controlled temperature 490 °C to stabilize then at this temperature, as Figure 3-15 shows, which is due to the effect of the simulated controller. Recalling other temperatures ( $T_3$ ,  $T_4$ , and  $T_5$ ) the temperature profiles are almost the same as obtained in Figure 3-11 and Figure 3-12, however,  $T_3$  (Figure 3-16) reached the stabilized temperature (460 °C) faster than it did in the first approach (Figure 3-12). Where this is due to the effect of  $T_2$ , since  $T_3$  is said to follow the pattern of the wall temperature as it is observed from the results.

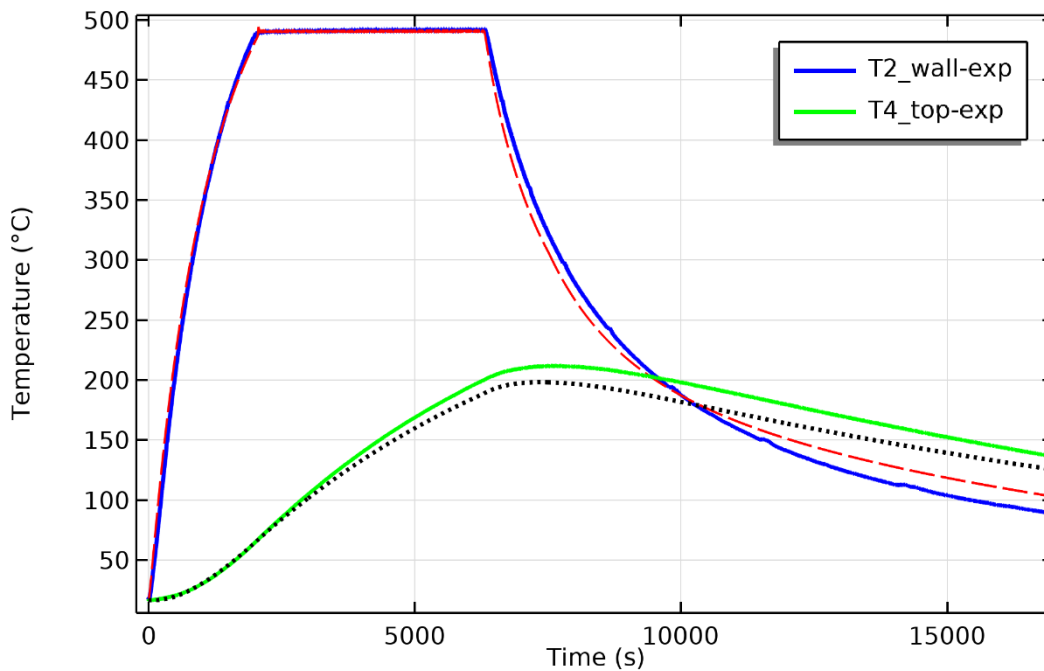
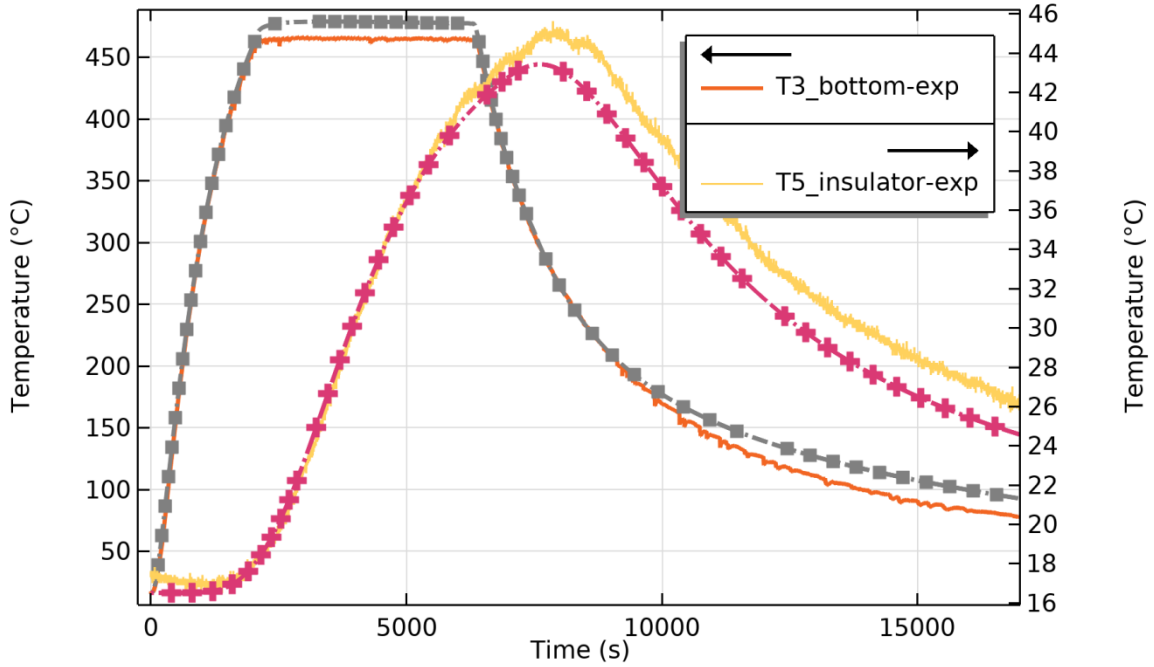
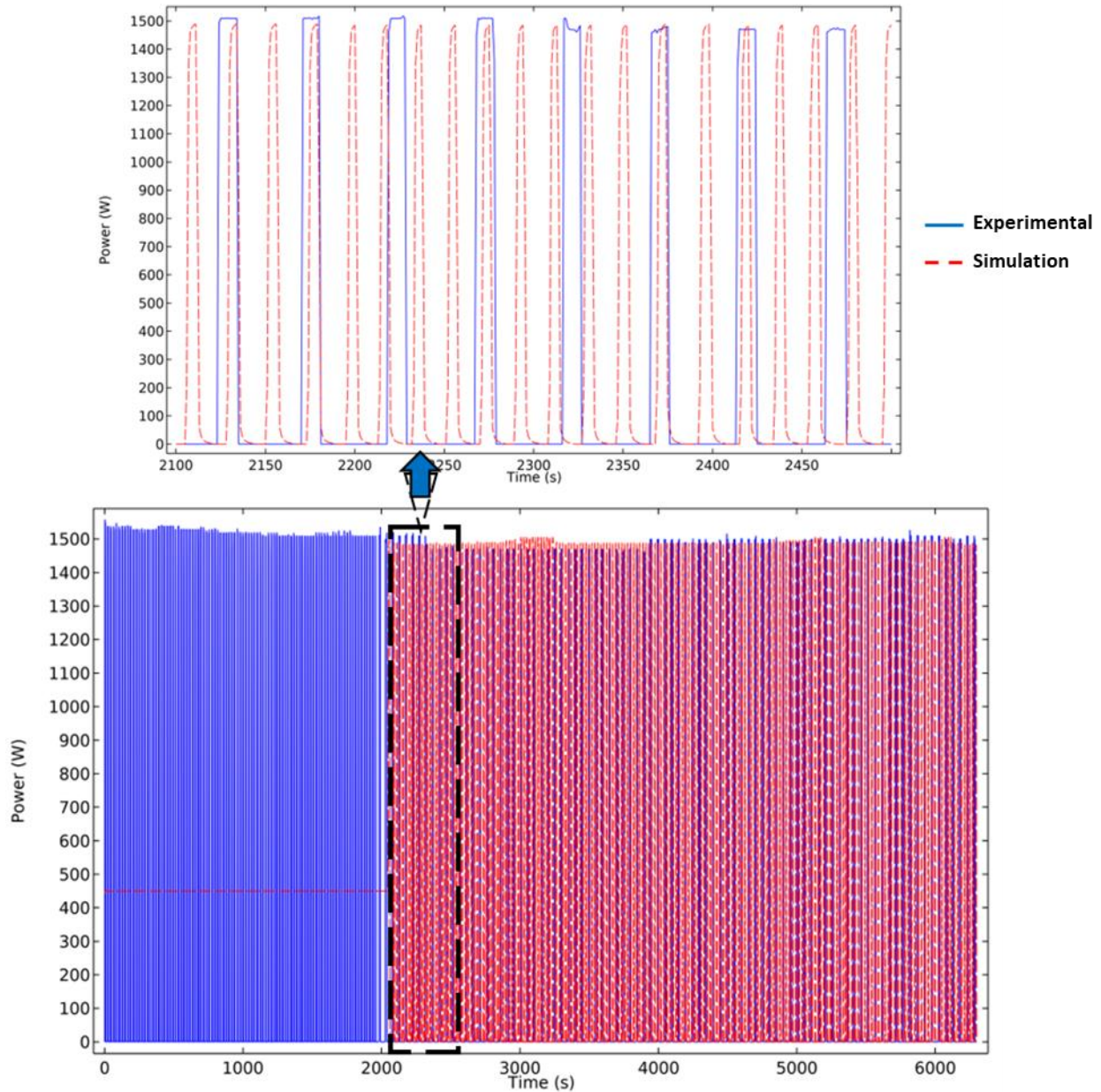


Figure 3-15 : Temperature comparison,  $T_2$ \_wall and  $T_4$ \_top, for empty reactor heated at 450 W load with simulation heat controller,  $T_2$  regulated at 490°C.



**Figure 3-16 :** Temperature comparison, T3\_bottom and T5\_insulator for empty reactor heated at 450 W load with simulation heat controller, T2 regulated at 490°C.

In addition, using this method, the simulated power of the heater is obtained and compared with the experimental power as shown in **Figure 3-17**.



**Figure 3-17** : Experimental power and simulated power according to the two approaches (power implementation and controller simulation, respectively) for the same experiment (heating empty reactor till 490 °C by 450 W).

As shown in **Figure 3-17**, the simulation power is set be 450 W (30 % of the full load 1500 W) at the beginning of heating until the wall temperature  $T_2$  reaches 490 °C (at time  $\approx$  2100 s), then the power starts to fluctuate to the stabilize  $T_2$ . On the other hand, the experimental power starts to fluctuate from the beginning till 2050 s to provide the same average power 450 W, then after  $T_2$  reaches the desired temperature reaches 490 °C (at  $\approx$  2050 s) it starts to oscillate in a different pattern to control the reactor's wall temperature. The reason that the experimental power fluctuate

from the begging of the process is the fact that the electric heater always functions at its maximum power (1500 W), so it turns ON and OFF in a specific cycle (6 s ON and 14 s OFF) to provide the set power (450 W). In addition, by observing the zoomed figure, it is noticed that the frequency of the simulated power is two times greater than that of the experimental one, but the period of time for each peak is less than that for the experimental power and also it has a different shape (triangular shape). However, the provided energy by the simulated heater and the experimental heater are computed and the relative error is determined to be lower than 1.5 % using (Eq. 2-12) in Chapter Two.

Thus, the method of modelling a simulated heater and controller revealed a great accuracy as inserting the real experimental power as a heat source, where the results of both methods are validated by the experimental data as preceded. Moreover, since the second method is validated, the semi-batch reactor can be even used to perform theoretical studies (heating, melting, cracking etc...) without the need to run out relative experiments. However, this is valid under one condition which is the correct setting and modelling of the phenomena inside the reactor. Therefore, the two methods will be done for all of the coming simulations to compare the error between them and to assure the use of the second method in more advanced models such as plastic melting. But only the second method will be presented to prevent result repetition. Finally, sensible heat transfer within the empty semi-batch reactor is validated, thus, the next step is to model and validate heating for different materials (solid and fluid) inside the reactor to upgrade the model.

### 3.3.2 Loaded reactor

After validating the governing equations, boundary conditions, geometry, simulation settings (mesh size, tolerance, solver, and time step) and the material properties of the reactor, the next step is to check this model for a loaded reactor.

Knowing that the heat diffusion and temperature distribution differ drastically when the reactor is loaded from the empty reactor. This is due to that the loaded material absorbs a great part of resistances energy. Thus, the main reason behind modelling the loaded reactor before the melting process is to assure that the heat transfer model works well before introducing plastic inside the reactor and to decrease the margin of error as possible. Fine sand material is chosen to be the

loaded solid material because it withstands high temperature (500 °C and above) and can be easily loaded and discharged.

However, regarding heating fluid material inside the reactor, its main purpose is to check the natural fluid flow model for viscous (sunflower oil) and light liquids (water) before using it later on to model the natural flow of molten plastic inside the reactor.

### *3.3.2.1 Heating sand inside the reactor*

First, the reactor is filled with fine dry sand particles, and heated until it reaches temperature of 570 °C, then it is stabilized at this temperature to achieve a steady state. The loaded sand is modelled as a bulk solid with a measured apparent density of 1484 kg/m<sup>3</sup>.

Same as the previous experiments, simulations are done by the two methods. Both methods gave almost the same promising results about 3 % as a maximum average relative error among all temperatures with and 4.5 % as an average error in energy balance when using the second approach (controller simulation). But to prevent repetition and to keep the model fully simulated and independent from the experiment input (i.e. the heater power), only the second method results are presented.

**Figure 3-18 – Figure 3-20** show the results of heating sand inside the semi-batch reactor by 450 W heating power. **Figure 3-18** demonstrates the surface temperature profile of the reactor filled with sand at time = 6000 s. It is obvious from the results that the insulator temperature is below 50 °C same as the previous result when heated empty (**Figure 3-10**). In addition, it is clear that the bottom part of the reactor is hotter than the upper part, where this is due to the high mass inertia of the top of the reactor. This affects the sand temperature  $T_1$  (580 °C) to overcome the wall temperature (570 °C) as it is displayed in **Figure 3-19**. In addition, the thermocouple  $T_1$  is facing the direct heat flux released by the heaters whereas  $T_2$  is located between the two heaters, as shown previously in **Figure 3-18**. Yet the average relative error between the simulated and the experimental results for  $T_1$  is about 1 %. Moreover, **Figure 3-19** presents the simulated and experimental temperatures for the other two thermocouples  $T_2$ , and  $T_4$ , where  $T_2$  is the controlled temperature that fluctuates when it reaches the desired temperature of 570 °C. This temperature is then aligned with the experimental one under the regulator's effect, the same as in **Figure 3-15**. In addition, the temperature of the top side of the reactor ( $T_4$ ), increases slowly with time due to its large mass

(high inertia) and its relatively far position from the heaters. It reaches almost 280 °C at steady state with an average error of 4 % with respect to experimental results.

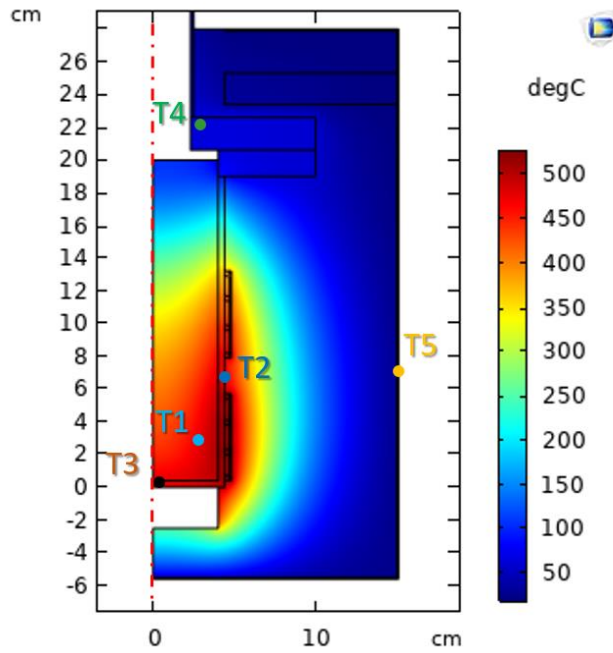


**Figure 3-18** : 2D-axisymmetry simulation for the reactor filled with sand with simulated heat controller, heated using 450 W load, at  $t = 6000$  s.

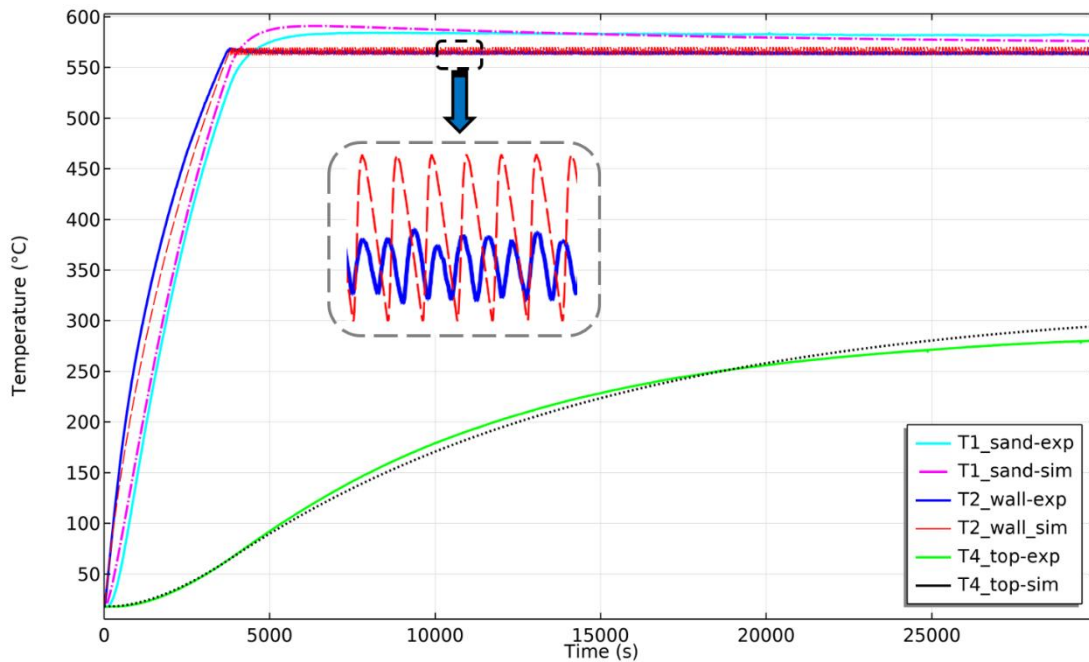


**Figure 3-19 :** Temperature comparison, T1, T2, and T4, for reactor filled with sand, heated using 450 W load with simulated heat controller.

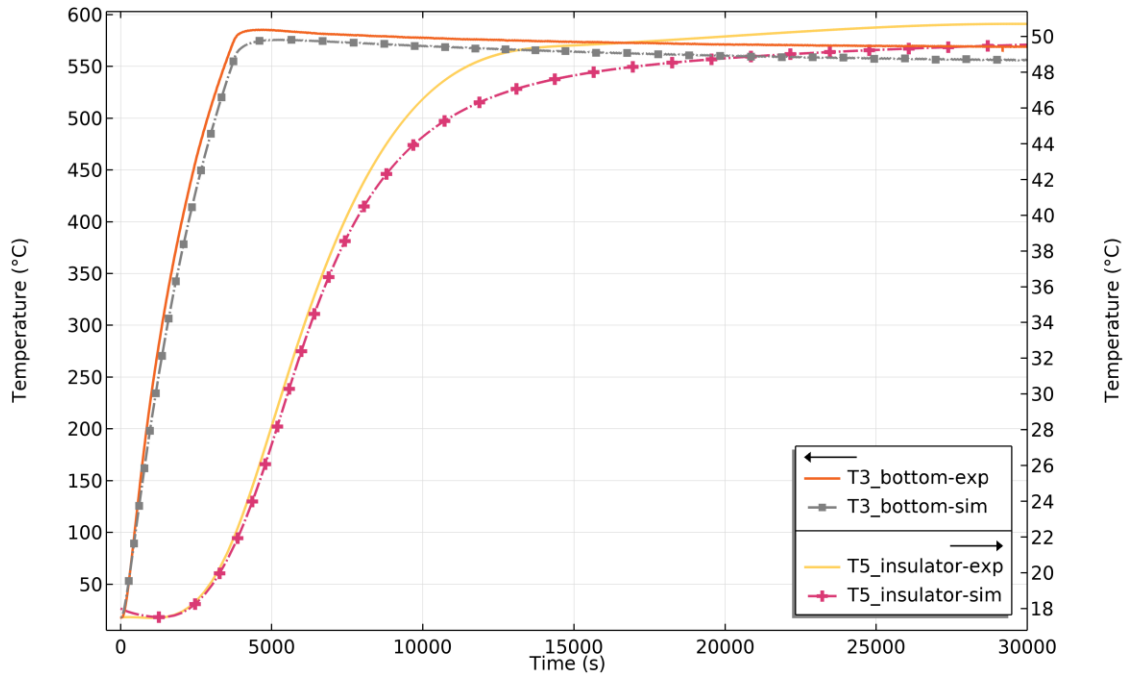


**Figure 3-20 :** Temperature comparison, T3\_bottom and T5\_insulator, for reactor filled with sand, heated using 450 W load with simulated heat controller.

Regarding the bottom temperature ( $T_3$ ) and the insulator temperature  $T_5$ , **Figure 3-20** shows that the experimental and simulated results have almost the same profile with average relative errors of 5 % and 5.2 % respectively, where  $T_3$  reached 460 °C and  $T_5$  reached 50 °C.

Furthermore, supplementary experiment and simulation conducted at lower heating rate (150 W heater power) gave the same accuracy with an average error of 5 % for the temperatures and the energy balance (**Appendix: A, Figure 3-3A**). Therefore, the model of the loaded reactor is successfully validated as heating solid materials at different temperatures and heating rates. So far, the model can predict the heat distribution with respect to time for any solid material heated inside the reactor with imposed heating power and set point temperature, if the thermal properties of this material are well defined. The next step is to upgrade the model to heat fluid materials by validating the heating process for a viscous fluid inside the reactor.

### 3.3.2.2 Heating viscous and light fluids inside the reactor

The third stage of modelling and validating sensible heat transfer, is heating the reactor with relatively viscous (sunflower oil) and light (water) fluids inside to validate the natural fluid flow model that will be used later on to model natural flow of molten plastic. For this sake, the reactor is filled with sunflower oil or water, and heated at different heating rates.

#### a) Heating sunflower oil

In the following experiments, the loaded reactor is heated by 450 W to reach 180 °C and kept at this temperature for more than one hour. Heat transfer in fluid is modelled by coupling the energy and momentum equations, **Eq. 2-13 – Eq. 2-15** with the buoyancy force term to conduct the natural fluid flow, as presented in the Chapter Two **section 2.4.2.2**. Normally, a fluid at atmospheric pressure having a temperature gradient will also demonstrate density gradient within. This slight change in density results in moving downwards the denser fluid that replaces the lighter one. Moreover, this fluid motion enhances heat transfer from the heat source to the fluid's bulk, where this phenomenon is called natural heat convection of the fluid.

In the present model, a body force termed the buoyancy force is used to model this phenomena according to the Boussinesq's approximation (refer to Chapter Two **section 2.4.2.2, Eq. 2-14**). The buoyancy force is proportional to the difference between the local temperature (element temperature) and the fluid's bulk mean temperature, which is multiplied by the thermal expansion property of the material,  $\alpha$  ( $K^{-1}$ ). Therefore, at the beginning of the experiment and as the fluid near the wall starts to heat up, a body force is activated to move the thin film upwards along the wall and consequently to descend again, which forms an anticlockwise weak fluid vortex in the reactor shown in **Figure 3-21**. However, the regions that are far away from the wall have almost zero body force (buoyancy force) magnitude, due to low temperature gradient.

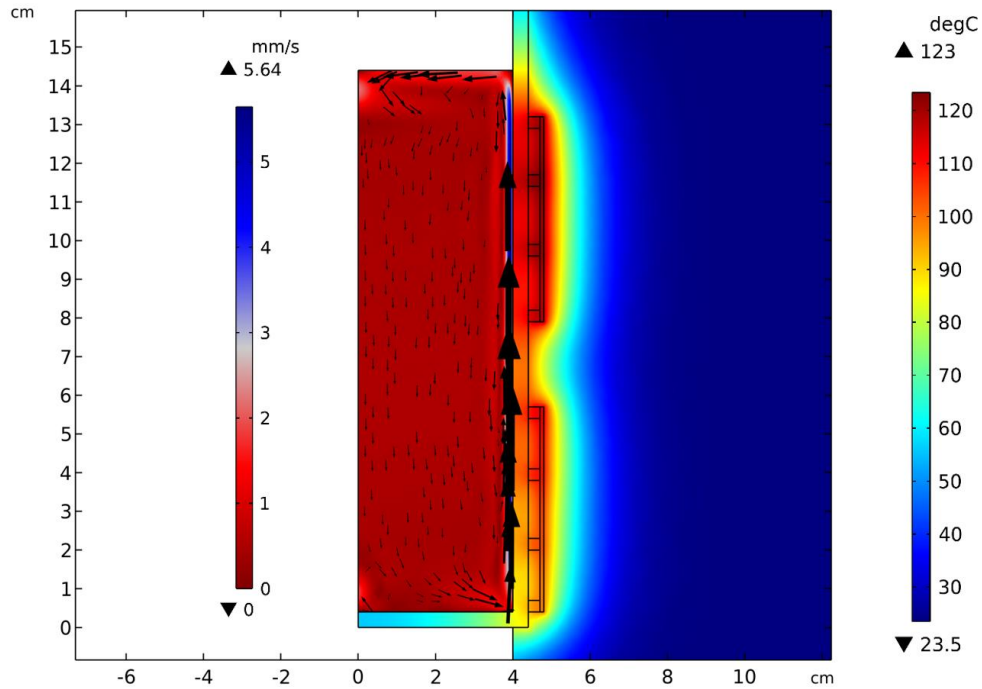


**Figure 3-21** : Surface velocity and temperature profiles for the reactor filled with oil, 450 W, at  $t = 350$  s.

On the other hand, as time and heat convection proceed, the weak fluid flow vortex transforms into multiple vortices due to the high temperature gradient within the fluid itself and near the wall of the reactor, as shown in **Figure 3-22**. In addition, the fluid's viscosity that depends on temperature, plays an important role in the fluid flow as it opposes the fluid motion at the beginning of the heating process due its high viscosity values at lower temperatures, recall **Table 2-5**. Then, as the temperature of the fluid increases with time, the oil viscosity decreases and the fluid flows more easily. Therefore, the velocity profiles increase from  $U_{\max} = 0.005$  m/s (**Figure 3-21**) to  $U_{\max} = 0.02$  m/s (**Figure 3-22**) as the temperature changes from  $60$  °C to  $175$  °C, respectively. Also it is noted that the type of fluid flow in both states is laminar because of the low velocity magnitudes.

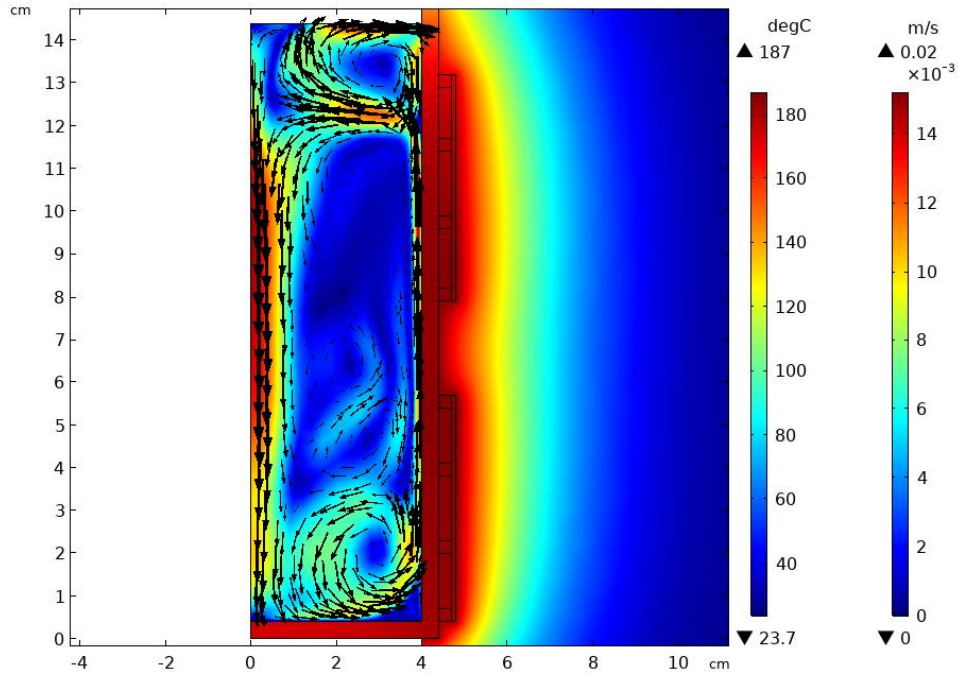


**Figure 3-22** : Surface velocity and temperature profiles for the reactor filled with oil, 450 W, at  $t = 1700$  s.

Furthermore, the simulated results are compared to the experimental ones for further validation, by presenting three main temperature profiles ( $T_1$ ,  $T_2$ , and  $T_4$ ) as shown in **Figure 3-23**, however  $T_3$  is not included since it has almost the same temperature profile of  $T_2$ . The simulated temperature curves fit well the experimental curves with an average error of 5 %. Concerning the energy balance relative error, it has also a low value which is around 5 %.

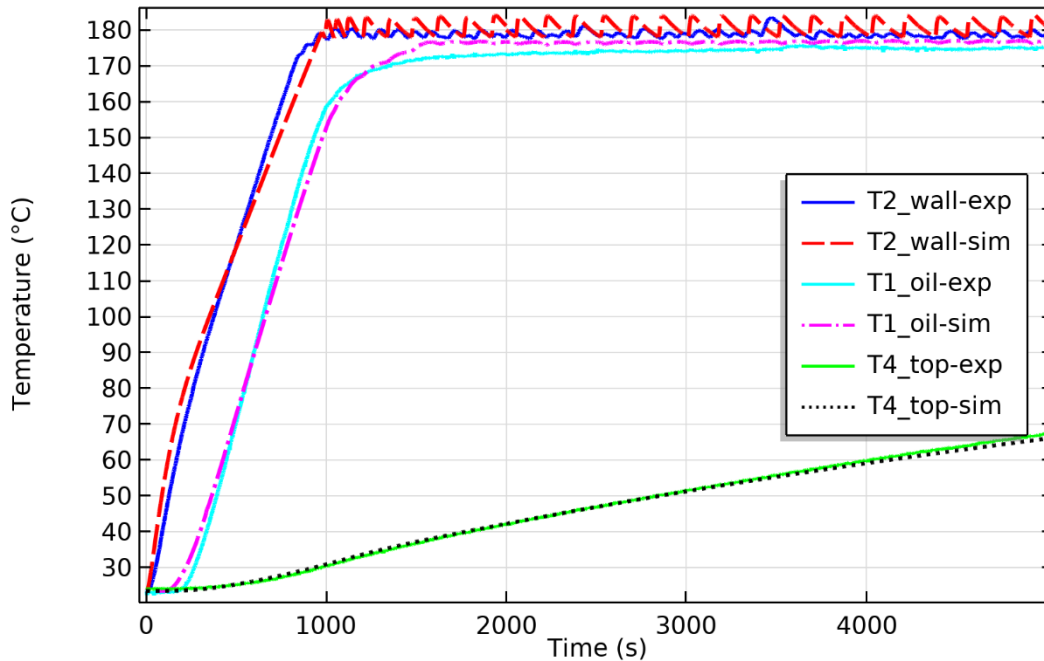


**Figure 3-23 :** Temperature comparison, T1\_oil, T2\_wall, and T4\_top, for reactor filled with oil, heated using 450 W with simulated heat controller.

### b) Heating water

Moreover, similar experiments are also done for low viscous fluid; liquid water. **Figure 3-24** and **Figure 3-25** show the temperature results (T<sub>1</sub> and T<sub>2</sub>) for heating water to 50 °C by 150 W heating power inside the semi-batch reactor. As shown by surface profile temperature, **Figure 3-24**, the upper part of the fluid (water) is hotter (about 42 °C) than the lower one (36 °C), which is due to natural flow of the fluid which carries upwards the heat from the wall of the reactor. In addition, as the temperature of the fluid increases the density decreases, thus, thermal stratification arises in the fluid due to the slight density variance (hotter fluid goes up and colder one rests down). Additionally, the temperature results in **Figure 3-25** are in a good agreement and the relative error among temperature and energy results didn't exceed 3 %, due to the low heating temperature.

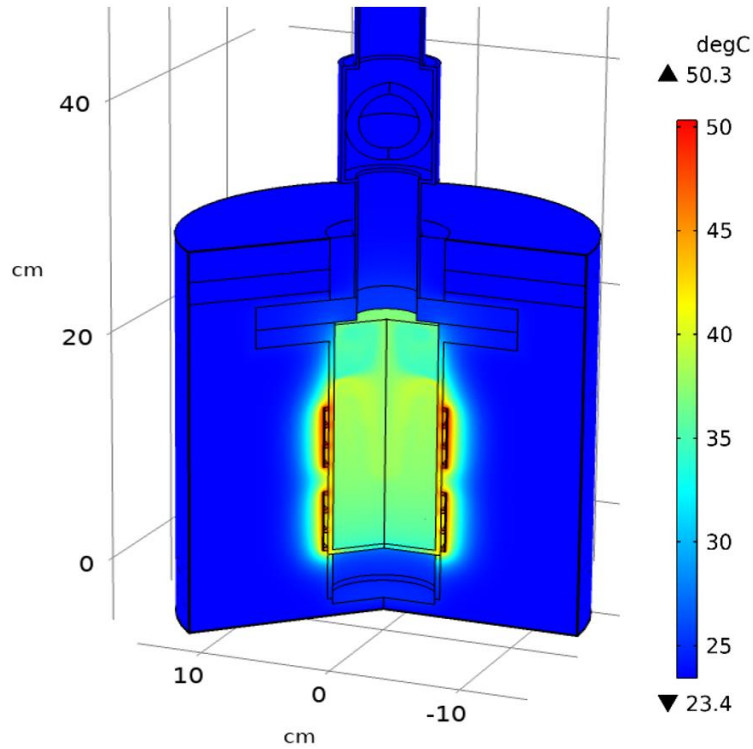


Figure 3-24 : 3-D simulation result for reactor filled with water and heated by 150 W load.

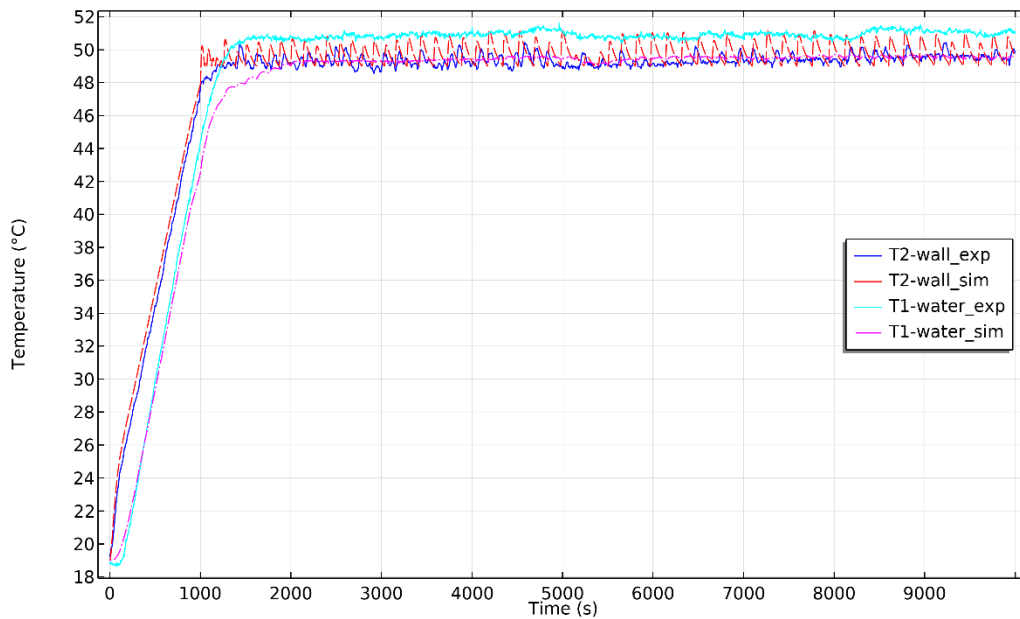


Figure 3-25 : Wall temperature T2 and water temperature T1 for a batch reactor filled with water and heated by 150 W load with simulated heat controller.

Finally, the previous presented results prove that the sensible heat transfer within the semi-batch reactor, empty or loaded (solid: sand or fluid: air, oil, and water), is modelled and validated at

different heating rates with a maximum average relative error of 6 %. Thus the model is ready to be upgraded to model plastic melting process inside the fixed bed semi-batch reactor.

### 3.4 Melting process for PP and HDPE inside the semi-batch reactor

In this section, results of modelling melting process for PP and HDPE inside the semi-batch reactor are presented. But before proceeding to the results, a sub-step is attained to check the validity of the AHCM method by modelling melting inside the semi-batch for a simple and known material such as ice.

#### 3.4.1 Ice melting

Before modelling plastic melting, the AHCM model is checked and validated for natural ice melting process inside the reactor; the ice is chosen for its well-known properties. The reactor is filled and well packed with ice that is left to melt at ambient temperature ( $T_{\text{amb}} = 19 \text{ }^{\circ}\text{C}$ ) without heating. **Figure 3-26** shows a comparison between simulated and measured temperatures of the two thermocouples  $T_1$  and  $T_4$ . For both simulated and experimental results, the ice temperature ( $T_1$ ) clearly remained constant at the freezing temperature (about  $1 \text{ }^{\circ}\text{C}$ ) before it starts to rise up when the melting process ended at the vicinity of the thermocouple  $T_1$ . This shift in the freezing temperature (from  $0$  to  $1 \text{ }^{\circ}\text{C}$ ) can be due to the presence of additives from the ice machine, reading errors by the thermocouple and the thickness of the steel cover protecting the thermocouple. Regarding the top temperature ( $T_4$ ), the simulated and the experimental results are in a good agreement and they are clearly dropping logarithmically through time until the major part of ice is melted (at  $t = 21000 \text{ s}$ ), at which the temperature ( $T_4$ ) starts to rise up from now then. Moreover, the experimental and simulated results show a good agreement with 6 % as an average relative error. Thus, the AHCM revealed a great capability in modelling melting process for ice inside the semi-batch reactor.

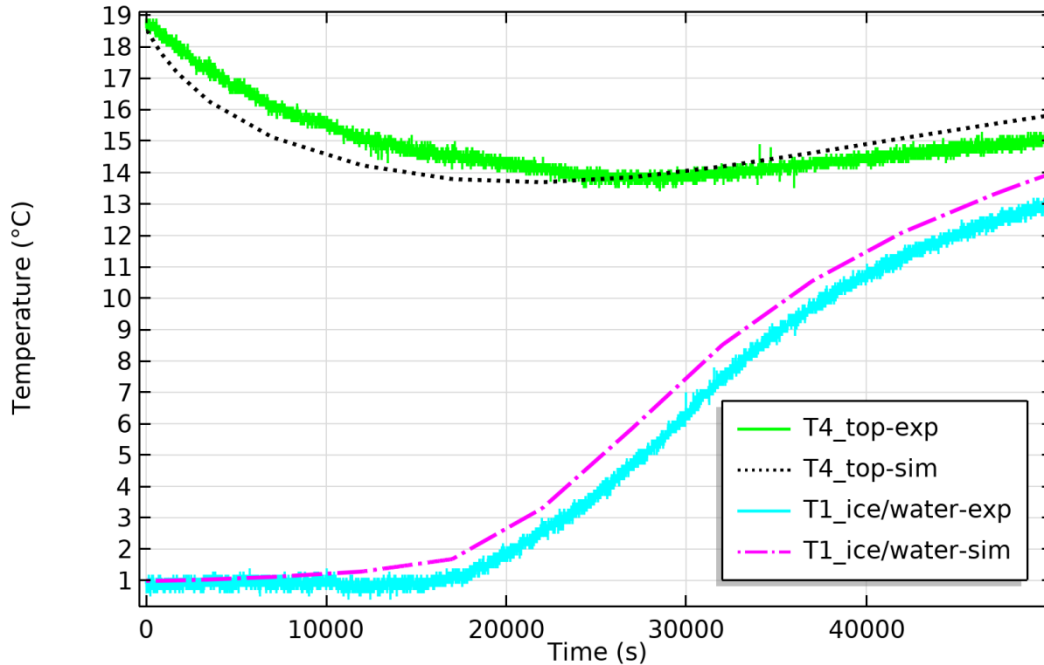


Figure 3-26 : Temperature comparison, T1\_ice/water and T4\_top, ice melting inside the batch reactor without heating.

### 3.4.2 PP melting

After validating the melting process of ice, the AHCM method is used then to simulate plastic melting inside the reactor. PP melting is done in two methods; First approach is considering molten PP as static fluid that doesn't move, however the second approach models the natural fluid flow of molten plastic as it undergoes melting (using the same model and equations used in **section 3.3.2.2**).

#### 3.4.2.1 First approach; Static fluid

According to the first method of simulation, molten plastic is taken as a static fluid because of its high viscosity at very low shearing rate, thus only the energy equation, **Eq. 2-19**, is taken into consideration.

First, the reactor is prepared with 400 g of a bulk solid of PP as mentioned in Chapter Two **section 2.2.2**. Secondly, loaded plastic is heated using 300 W (i.e. 20 % of the maximum power load 1500 W) to reach 190 °C and then cooled down as shown in **Figure 3-27** below. For this simulation, the experimental heating power  $\dot{q}_{exp}(t)$  is directly implemented without modelling a heater and a

controller. The experimental and simulated results show that PP temperature ( $T_1$ ) increases linearly by  $4.5\text{ }^\circ\text{C}/\text{min}$  while plastic is still in the solid state. Then, it starts bending from the beginning of melting (about  $120\text{ }^\circ\text{C}$ ) till the end of melting process (at  $170\text{ }^\circ\text{C}$ ) by a heating rate of  $1.33\text{ }^\circ\text{C}/\text{min}$ . After the melting ends at this vicinity, the heating rate decreases until reaching a constant value of  $0.5\text{ }^\circ\text{C}/\text{min}$ , where  $T_{1\text{-sim}}$  reaches  $185\text{ }^\circ\text{C}$  and  $T_{1\text{-exp}}$  reaches  $180\text{ }^\circ\text{C}$ . In contrast to melting, PP temperature remains constant when solidification occurs due to the slow cooling rate in the cooling process, which is less than  $1\text{ }^\circ\text{C}/\text{min}$ . Nevertheless, simulated and experimental results have the same tendency and behavior during melting and solidification processes. In addition, the average error obtained for all temperature results is less than 7%. Moreover, **Figure 3-28** and **Figure 3-29** show the parity plots for the simulated results and the experimental data for further validation, where the maximum relative error didn't exceed 10 % as shown in **Figure 3-29**.

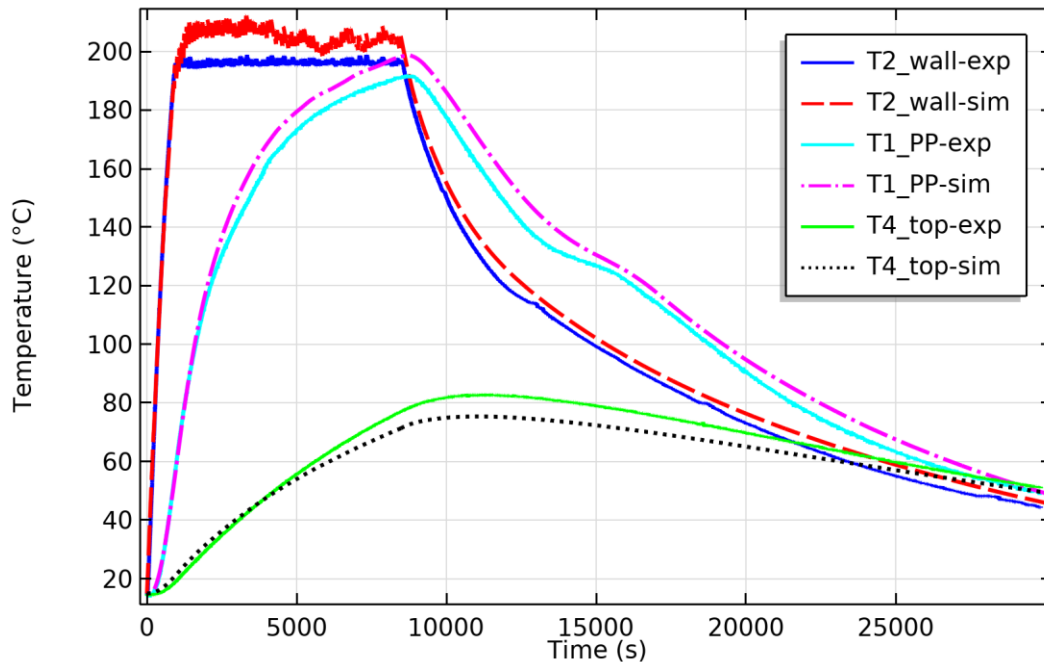


**Figure 3-27** : Temperature comparison,  $T1_{PP}$ ,  $T2_{wall}$ , and  $T4_{top}$ , for melting and cooling PP, heated using 300 W load by direct implementation of  $\dot{q}_{exp}(t)$ , set point  $190^\circ\text{C}$ .

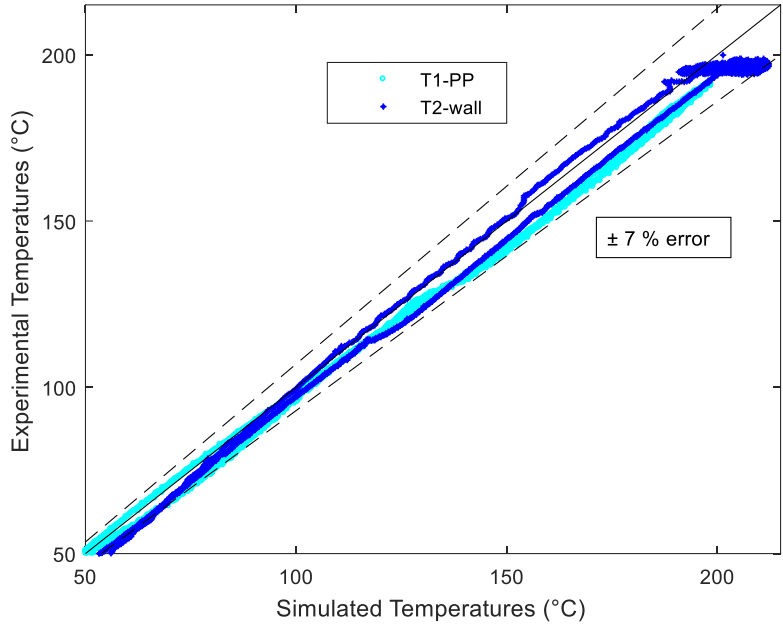


Figure 3-28 : Parity plot for T1\_PP, T2\_wall, for melting and cooling PP, heated using 300 W load by direct implementation of  $\dot{q}_{exp}(t)$ , set point 190°C.

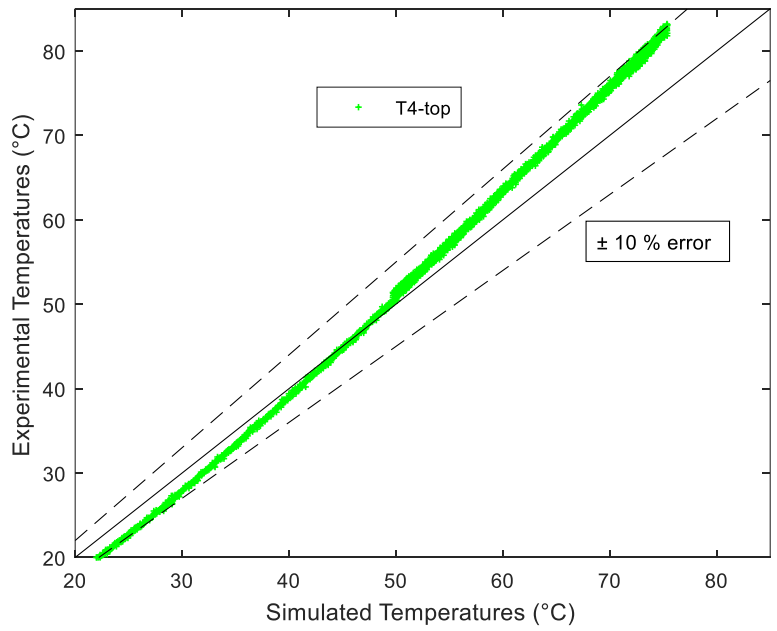


Figure 3-29 : Parity plot for T4\_top, for melting and cooling PP, heated using 300 W load by direct implementation of  $\dot{q}_{exp}(t)$ , set point 190°C.

### 3.4.2.2 Second approach; Moving fluid

In the second approach, the molten plastic is considered in motion, in consequence the fluid flow equation (**Eq. 2-16** and **Eq. 2-17**) is taken into consideration and coupled to the energy equation (**Eq. 2-18**), where the viscosity of molten plastic is fixed to 1000 Pa.s based on Agassant et al.'s work (Agassant *et al.*, 2019).

400 g of PP are melted and heated by 450 W to reach a very high temperature about 340 °C, which is 60 °C lower than the minimum onset temperature of cracking, determined by TGA technique. **Figure 3-30** and **Figure 3-31** show the surface results (conversion, temperature, and velocity) at time = 560 s of melting and heating PP to reach 340 °C according to the second method (i.e. fluid flow is considered). As **Figure 3-30** displays, about 0.5 cm radial thickness of plastic are melted (in the white color) at  $t = 560$  s when the average temperature of the wall is about 170 °C (above the melting temperature of PP). In addition, the blue arrows indicate the direction of the molten plastic flow. However, the magnitude of the velocity of the flow is negligible, about  $6 \times 10^{-7}$  mm/s as **Figure 3-31-(a)** shows. This indicates that there is no fluid motion inside the reactor and the molten plastic is at a static state; the same case if the first approach (molten plastic considered as static fluid) is used. Moreover, **Figure 3-31-(b)** illustrates the temperature distribution within plastic. Whereas, the results indicate that the major part of plastic is still in solid state at  $t = 560$  s; temperature is below 100 °C (domain with the blue color). On the other hand, the temperature of the thin molten layer is above 140 °C, which is higher than the start melting temperature of PP ( $118 \pm 2$  °C).

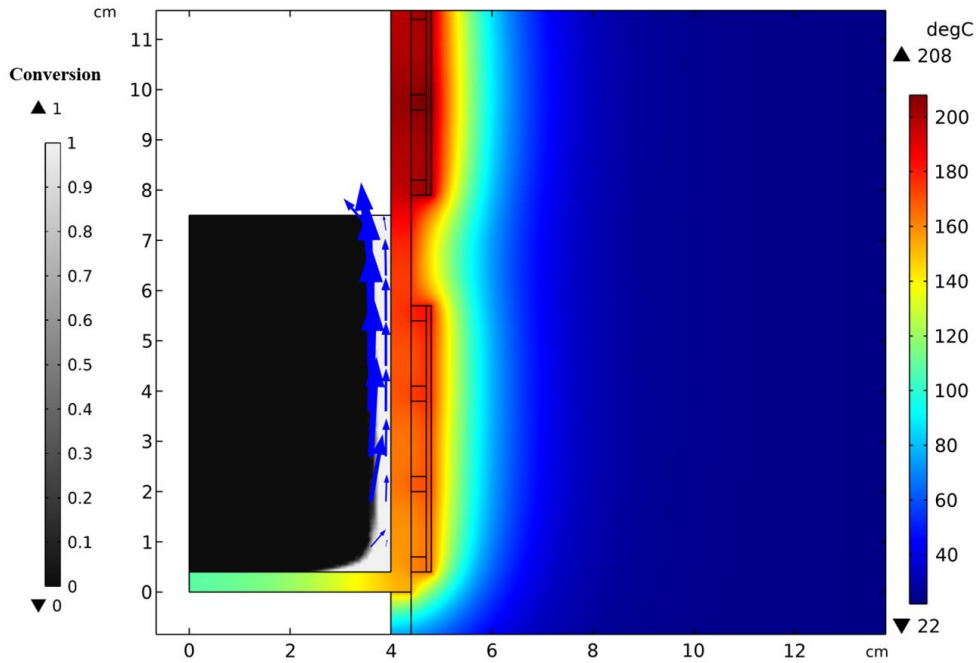


Figure 3-30 : Surface conversion and temperature profiles for melting PP considering the fluid flow approach, 450 W, at t = 560 s.

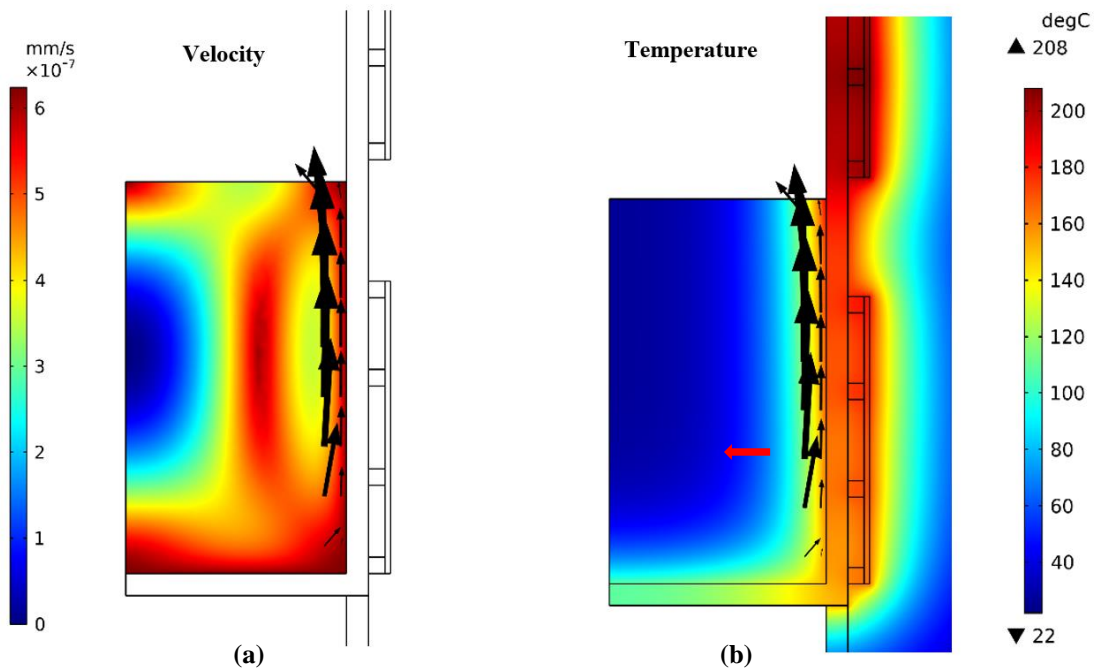
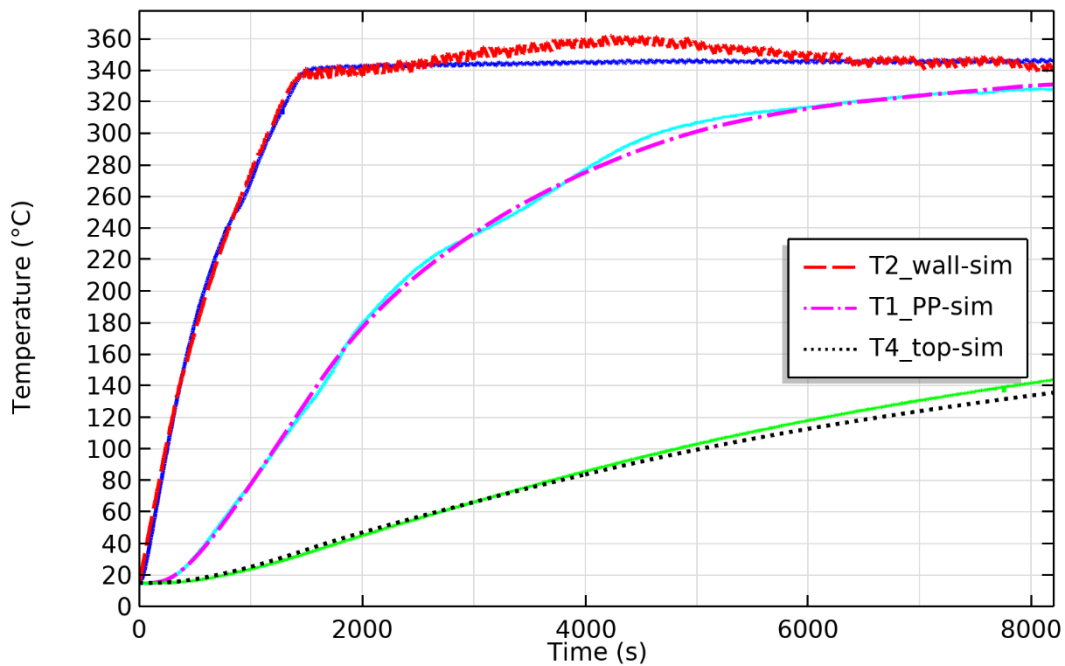


Figure 3-31 : (a) Surface velocity and (b) temperature profiles for melting PP considering the fluid flow approach, 450 W, at t = 560 s.

As well, **Figure 3-32** presents the temperature results of melting and heating PP according to the second approach (i.e. fluid flow is considered). It is noticed that, PP temperature ( $T_1$ ) curve doesn't obviously bend in the melting range 120 – 170 °C as it did in the previous experiment; this is due to the higher heating rate which is about 6.4 °C/min. Recalling **Figure 3-27**, plastic starts melting when the wall temperature ( $T_2$ ) is stabilized at 190 °C. On the other hand, in **Figure 3-32** melting starts when the wall temperature reaches 340 °C. Therefore, the heating rate in the second experiment is much higher than the first, which leads to the low deflection in the curve during melting ( $T_1$  from 120 to 170 °C in **Figure 3-32**). Moreover,  $T_1$  curve is bended again starting from a higher temperature, about 200 °C. The cause of this shift in bending is related to the slow diffusion of heat towards the center (from  $T_1$  position to the left, the red arrow in **Figure 3-31-(b)**).



**Figure 3-32** : Temperature comparison,  $T_1$ ,  $T_2$ , and  $T_4$ , for PP melting and heating by 450 W with direct implementation of  $\dot{q}_{exp}(t)$ .

Furthermore, to emphasize the simulation results another simulation is done for the same experiment (melting and heating PP to 340 °C by 450 W power) but instead of using fluid flow approach, the static fluid method is utilized. The obtained results are exactly the same as the pervious experiment. Therefore, it is deduced that molten plastic can be modelled as a static fluid rather than dynamic one which also favors in reducing the computational time of simulation.

Finally and not over, the pervious experiment (melting and heating PP to 340 °C by 450 W power) is repeated using a modelled heater and controller instead of using  $\dot{q}_{exp}(t)$ . Meanwhile, the deduced results agree with the experimental data, and the average error for temperatures is less than 6 % however for the energy balance it didn't exceed 4 % (further results are found in **Appendix: A, Figure 3-4A**).

### 3.4.3 HDPE melting

As a result from the previous section (**section 3.4.2**) the static fluid approach is used in modelling melting process for HDPE. A 350 g of prepared HDPE is heated by 600 W (i.e. 40 % maximum power load) till  $T_2$  (temperature of the wall of the reactor) reaches 350 °C, just before the cracking onset temperature of HDPE. As **Figure 3-33** illustrates, the plastic temperature  $T_1$  increases with straight line, whereas the wall temperature  $T_2$  starts to bend at  $T = 120$  °C (which is just before the melting peak temperature 135 °C). This is due to the latent heat absorbed by HDPE while undergoing phase change process (melting). However, the average relative error among all of the simulated and experimental temperatures is less than 5 %. Therefore, the showed temperature results and the low error values calculated between the simulated and experimental data validate the model used for plastic melting and heating for PP and HDPE inside the semi-batch reactor.

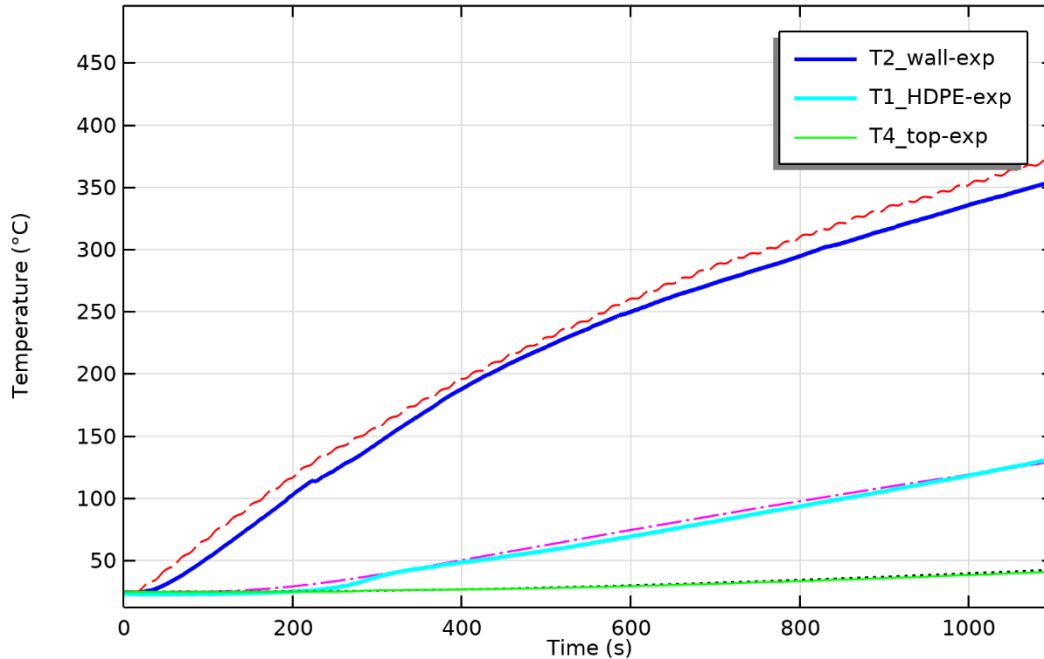


**Figure 3-33 :** Temperature comparison, T1, T2, and T4, for HDPE melting and heating by 600 W, with direct implementation of  $q_{\text{exp}}(t)$ .

### 3.4.4 Numerical results of melting in literature

Regarding the work done before, as mentioned in the state of the art (**section 1.7**), modelling and simulating plastic melting using FEM in a buffer solution is rarely reported in literature. On the other hand, many researchers investigated melting process and heat convection for other relatively similar materials. Madruga et al., for example, made an experimental investigation and a numerical study on melting tetracosane paraffin within a cubic enclosure (Madruga *et al.*, 2018). They used a heat sink term in the energy equation to attain for the absorbed heat during melting. In addition, they used the momentum equation with the buoyancy force term to encounter the flow of the molten material, as done in **section 3.3.2.2**. After they compared the simulation results with the experimental one, they stated that the results are in a good agreement and have the same tendency without mentioning the relative error among the results.

Meanwhile, Murray and Groulx and Samara et al. performed numerical studies for melting phase change materials (PCM) inside an enclosure, RT25 and octadecane respectively, using the AHCM method (Murray and Groulx, 2011; Samara *et al.*, 2012). In addition, they used the buoyancy force in the momentum equation to model the natural convection of the viscous material, as discussed

in **section 1.7**. Moreover, they illustrated that the model is working fine and it well models the melting phenomena of PCM. However, in both studies, the melting temperatures (below 30 °C) are low relatively to our work and the heating mode is done by using a uniform heat flux, which is not the case in this study (non-uniform heat flux due to the heaters).

Furthermore, Salvi et al. also used the AHCM in their work, where they modelled the phase change (evaporation) for carboxymethyl cellulose solution by microwave heating (Salvi *et al.*, 2011). But instead of using a conversion function, they used a predefined Gaussian distribution function ( $\delta$ ) to model the latent heat during phase change. They stated that the average numerical values of temperature were in fairly good agreement with the average experimental temperatures for carboxymethyl cellulose ( $R^2 = 0.91$ ), without mentioning the relative error among the results. However, they affirmed that the relative error between the numerical and experimental heat generation results is below 6 %. Nonetheless, the apparent heat capacity method (AHCM) was also used in other different studies to incorporate the phase change phenomenon (Curet *et al.*, 2006; Pryor, 2007; Vallejos and Duston, 2005), where it showed a good capability to model the phase change phenomena with a maximum average relative error of 20 % among the simulated and experimental results.

On the other hand, modelling and validating plastic heating and melting at high temperatures inside a batch reactor or a fixed enclosure is rarely reported in literature. Consequently, in this study the semi-batch reactor is heated by electrical heating coils with high heating rates (10 – 20 °C/min), and non-uniform temperatures. Also, the reactor is heated from ambient temperature up to relatively high temperatures that could reach 350 °C for a large interval of time, which is not the case found in literature. Thus, the AHCM revealed a high capability in modelling the melting process of plastic even at relatively high temperatures and heating rates. Finally, a summary of the average relative errors corresponding to the preceding experiments done in this study are displayed in **Table 3-2** below; while the maximum average relative error among temperatures in all of the experiments didn't exceed 8 %.

**Table 3-2 :** Temperature and energy relative errors for all of the heating and melting experiments using the batch reactor.

| Reactor status | Controller    | Relative error (%) |                |                |                |                |        |
|----------------|---------------|--------------------|----------------|----------------|----------------|----------------|--------|
|                |               | T <sub>1</sub>     | T <sub>2</sub> | T <sub>3</sub> | T <sub>4</sub> | T <sub>5</sub> | Energy |
| Empty reactor  | without Cont. | -                  | 4              | 4.6            | 5.8            | 5.5            | -      |
|                | with Cont.    | -                  | -              | 3              | 7.8            | 6.5            | 1.5    |
| Sand heating   | without Cont. | 4.2                | 5.5            | 2              | 3              | 5.2            | -      |
|                | with Cont.    | 1                  | -              | 5              | 5              | 5.5            | 4.5    |
| Oil heating    | without Cont. | 4.5                | 3.5            | 5.8            | 4              | 5.5            | -      |
|                | with Cont.    | 3.9                | -              | 4.8            | 3              | 5              | 5      |
| Water heating  | without Cont. | 3                  | 2.9            | 3.5            | 2              | 2              | -      |
|                | with Cont.    | 2.2                | -              | 4.8            | 2.3            | 3              | 2.7    |
| Ice melting    | without Cont. | 6                  | 7              | 5              | 6              | 2              | -      |
|                | with Cont.    | -                  | -              | -              | -              | -              | -      |
| PP melting     | without Cont. | 3                  | 4              | 3              | 7              | 5              | -      |
|                | with Cont.    | 4                  | -              | 2.5            | 8              | 4.5            | 3.8    |
| HDPE melting   | without Cont. | 2.5                | 6              | 3              | 3              | 4              | -      |
|                | with Cont.    | 4                  | -              | 2              | 4              | 5              | 3.5    |

### 3.5 Conclusions

Plastic pyrolysis includes different sub-processes like heating, melting and cracking. Therefore, the objective of this chapter is to illustrate the results for modelling melting process for PP and HDPE at a milli-particle and laboratory fixed bed semi-batch reactor (1 L capacity) scales.

First, a DSC survey is carried out to find the melting characteristics (**Table 3-1**) and heat capacities for PP and HDPE at several heating rates (4 – 10 °C/min).

Then, the melting process at a milli-particle scale for PP and HDPE inside the DSC is modelled by the apparent heat capacity method (AHCM) and the heat conduction equation, using COMSOL-Multiphysics and finite element method. The maximum average relative error among all the results did not exceed 9 %.

On the other hand, modelling plastic melting process inside the semi-batch reactor is divided into two stages: (1) Modelling and validating sensible heat transfer in the semi-batch reactor (blank, loaded with sand, oil and water), (2) Modelling and validating phase change (melting ice and plastic). Sensible heat transfer within the reactor, empty or loaded (solid: sand or fluid: air, oil and water), is modelled and validated (relative errors equal to 6 % for temperatures results and 5 % for the energy balance) with the experimental results in two ways. The first way is by inserting the experimental heater power  $\dot{q}_{exp}(t)$  as a predefined heat source function into the simulation. However, the second way is by modelling the heater and the controller in the simulation to mimic the role of the real heater.

However, regarding modeling phase change process inside the semi-batch reactor, AHCM is also used to model melting process for ice, polypropylene and high density polyethylene. Results revealed the high capability and accuracy of the method in modelling and simulating melting phenomena; 8 % and 4 % as maximum average relative error for temperatures and for the energy balances, respectively (**Table 3-2**).

Thus, the validated models of heating and melting can be set as a prerequisite to simulate the plastic cracking process inside the TGA-DSC apparatus and in the semi-batch reactor; which in the next chapter.

## Chapter 4 Modelling and validating pyrolysis process for PP and HDPE

In the previous chapter, the modeling of melting process for PP and HDPE at the two scales (milli-particle and laboratory semi-batch reactor) was presented. This chapter presents the results of modelling the whole pyrolysis process (including the cracking phase) of PP and HDPE at milli-particle scale inside a TGA-DSC apparatus, and, at a laboratory scale in the semi-batch reactor used in this study.

First, the TGA-DSC pyrolysis results for PP and HDPE at different heating rates (4 – 10 °C/min) are illustrated. Then by validating the theoretical conversion with the experimental one, a kinetic study is employed to deduct the kinetic parameters ( $f(x)$ ,  $E$  (J/mol), and  $A$  (s<sup>-1</sup>)) that describe the best the cracking process for PP and HDPE. Then, the deduced kinetic model is implemented into simulation to model the pyrolysis process for PP and HDPE at a milli-particle scale; hence the simulation results are compared and validated with the experimental one.

Finally, by using COMSOL-Multiphysics, the validated kinetic model (at milli-particle scale) is used along with a two phase flow model to simulate plastic pyrolysis (PP and HDPE) in the semi-batch reactor. Then the speed of the reaction determined from the mass flow rate of the pyrolysis by-products will be compared and validated with the experimental one over time. In addition, different simulation temperatures, such as the plastic temperature  $T_1$  and the reactor's temperature  $T_2$  will be compared with the experimental results for further validation.

### 4.1 TGA-DSC results for PP and HDPE pyrolysis

Four TGA-DSC pyrolysis experiments are realised for PP and HDPE at different heating rates  $\beta$  (4, 6, 8, and 10 °C/min), where each experiment is replicated. First, the pyrolyzed samples (having a mass of  $18 \pm 2$  mg) are sustained at isothermal state (25 °C) for 20 min, then they are heated up to 500 °C at different constant heating rates. Moreover, during the process, the system is purged using nitrogen gas (N<sub>2</sub>) of 20 mL/min to prevent oxidation reaction and to carry on the by-product gases. The sample temperature (°C), the mass (mg), and the heat flow absorbed by the sample material (mW) are recorded for further analysis, as shown in **Figure 4-1** and **Figure 4-2** for the PP and **Figure 4-3** and **Figure 4-4** for HDPE.

**Figure 4-1** and **Figure 4-3** represent respectively the TG curves of PP and HDPE pyrolysis, i.e. variation of sample mass with respect to its temperature during pyrolysis. First thing to notice from the TG data is that the TG curve shifts to the right with the increase of the pyrolysis heating rate, i.e.  $T_{onset,c}$ ,  $T_{offset,c}$ ,  $T_{c,max}$ , and  $T_{end,c}$  increase, because the increase in heating rate of plastic particle becomes higher than the kinetic rate of the pyrolysis reaction which results in the shift of temperatures, where different studies illustrate the same effect (Aboulkas *et al.*, 2010; Das and Tiwari, 2017). In contrast, the start of cracking temperatures ( $T_{start,c}$ ) remains constant for PP (375 °C) and HDPE (425 °C) as the heating rate increases, as illustrated in **Figure 4-1** and **Figure 4-3**. Recalling, the procedure of determining the start ( $T_{start,c}$ ), onset ( $T_{onset,c}$ ), offset ( $T_{offset,c}$ ), maximum ( $T_{c,max}$ ), and end ( $T_{end,c}$ ) temperatures of the cracking phase is illustrated in Chapter Two **section 2.1.2**.

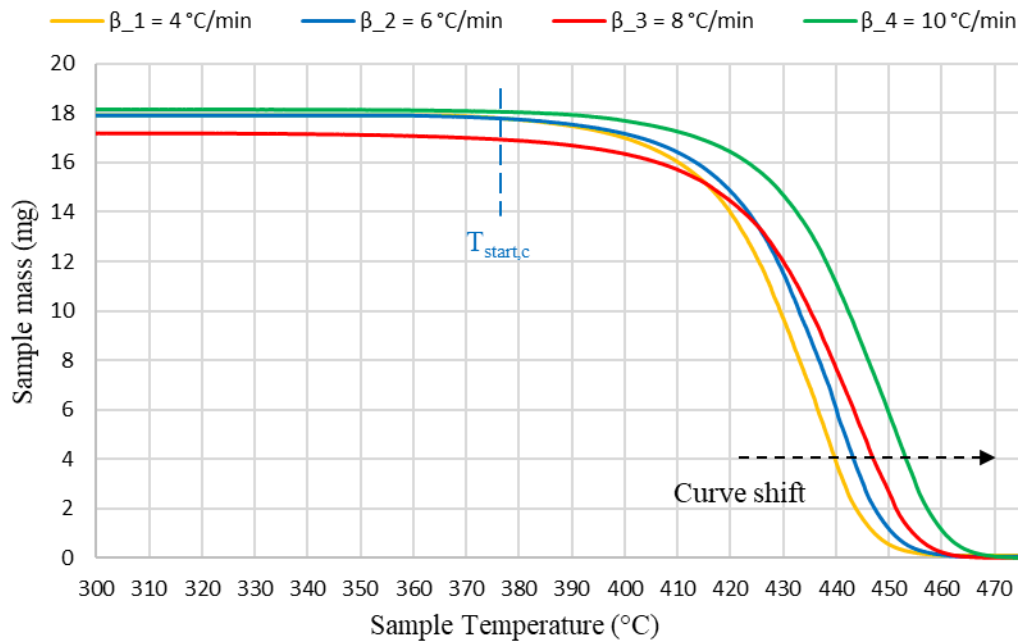


**Figure 4-1** : Mass versus temperature for PP pyrolysis at different heating rates.

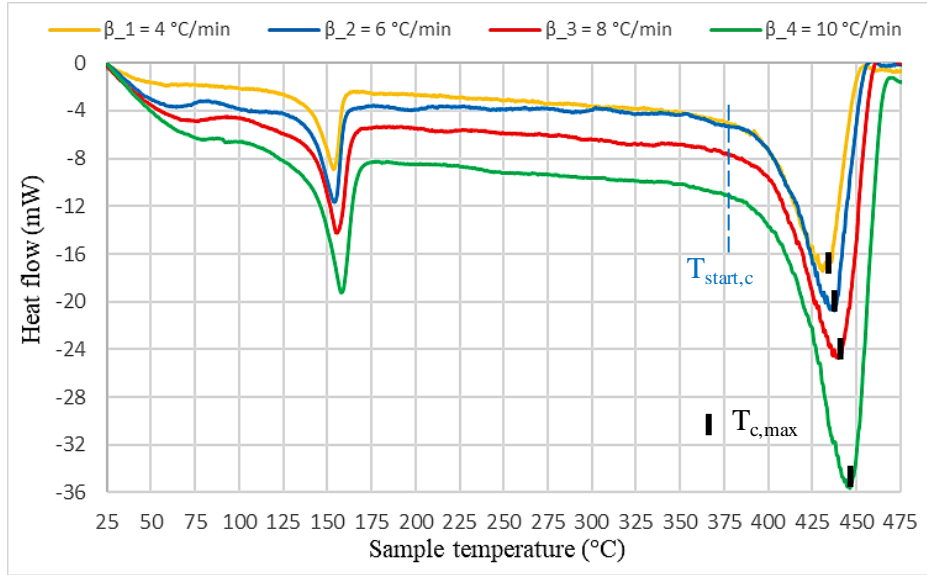


Figure 4-2 : Absorbed heat flow (by the sample) versus temperature for PP pyrolysis (melting and cracking) at different heating rates.

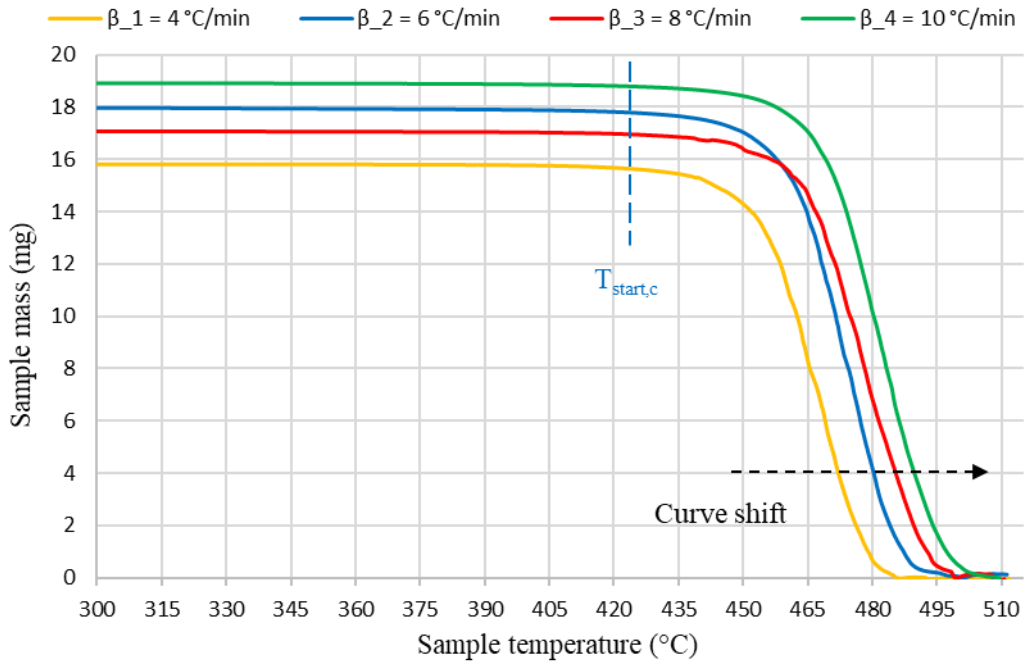
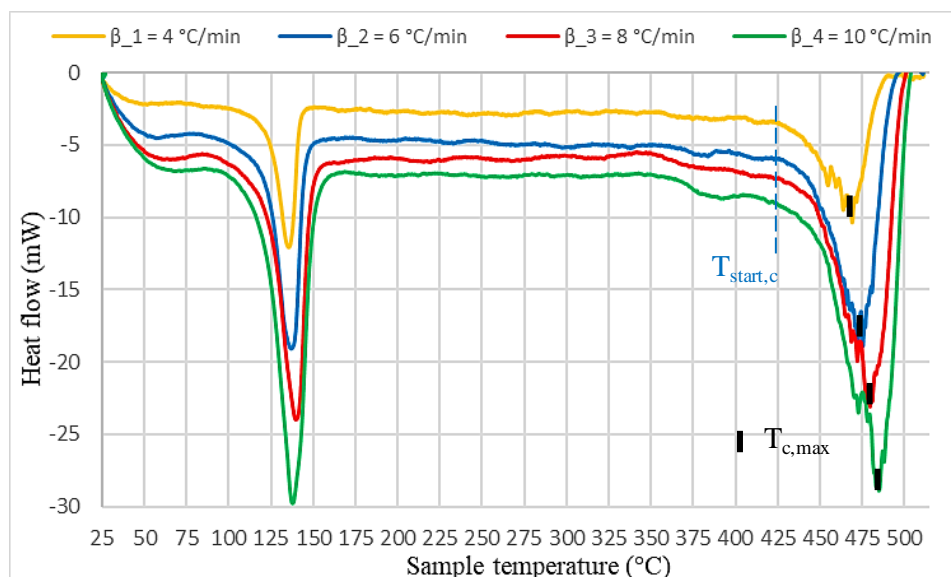


Figure 4-3 : Mass versus temperature for HDPE pyrolysis at different heating rates.



**Figure 4-4 :** Absorbed heat flow (by the sample) versus temperature for HDPE pyrolysis (melting and cracking) at different heating rates.

On the other hand, **Figure 4-2** and **Figure 4-4** show the power  $\dot{Q}_a$  (mW), i.e. heat flow, absorbed by the sample during the whole pyrolysis process for PP and HDPE at different heating rates (4, 6, 8, and 10 °C/min). The heat flow melting curves almost have the same tendency and behavior as the cracking curves, however the melting results are extensively analysed in Chapter Three **section 3.1**. The cracking phase analysis starts at 300 °C and ends at 500 °C for PP and HDPE. In addition, the results show that the maximum cracking temperature ( $T_{c,max}$ ) increases from 437 to 450 °C for PP and from 467 to 483 °C for HDPE as the heating rate varies from 4 to 10 °C/min (**Figure 4-2** and **Figure 4-4**). Nevertheless, if the results are further analysed, an interesting phenomenon appears just before the cracking phase ( $T_{start,c}$ ) of PP and HDPE.

For PP, as shown in **Figure 4-5**, the absorbed heat is almost constant as temperature rises from 300 till 350 °C, then a short rapid increase occurs from 350 till 375 °C, which is just before the start of the cracking phase (i.e. mass loss in TGA). Heat capacity of PP is found to be constant (2500 J/kg/K) between 300 and 350 °C, then it increases to become 3300 J/kg/K at 375 °C (start cracking temperature).

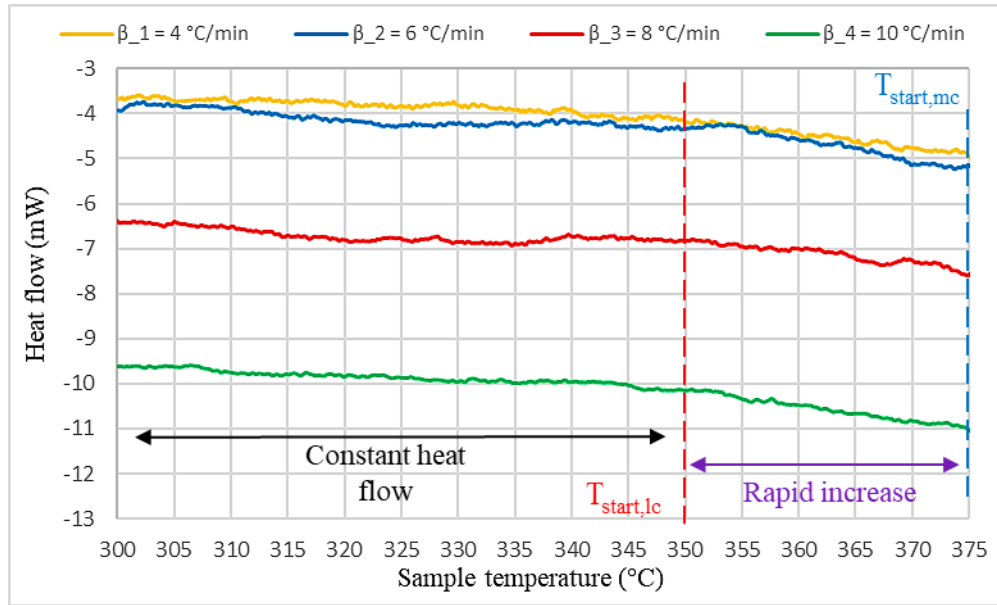


Figure 4-5 : PP pyrolysis heat flow just before the cracking phase starts at different heating rates.

This phenomenon is clearer in HDPE pyrolysis results (Figure 4-6). In Figure 4-6, the heat capacity of HDPE is constant (2500 J/kg/K) between 300 and 360 °C, then, it increases to become 3300 J/kg/K at  $T_{start,mc} = 425$  °C. Thus the absorbed heat remains constant between 300 and 360 °C and starts to increase almost linearly from 360 °C till  $T_{start,c}$  (425 °C). This increase in the absorbed heat is occurring before the mass loss starts to appear, thus, it can be interpreted as a latent cracking, i.e. the cracking process is starting at 350 °C for PP and 360 °C for HDPE, but the pyrolysis by-products are still non-volatile heavy hydrocarbons (oil) that can't escape from the crucible.

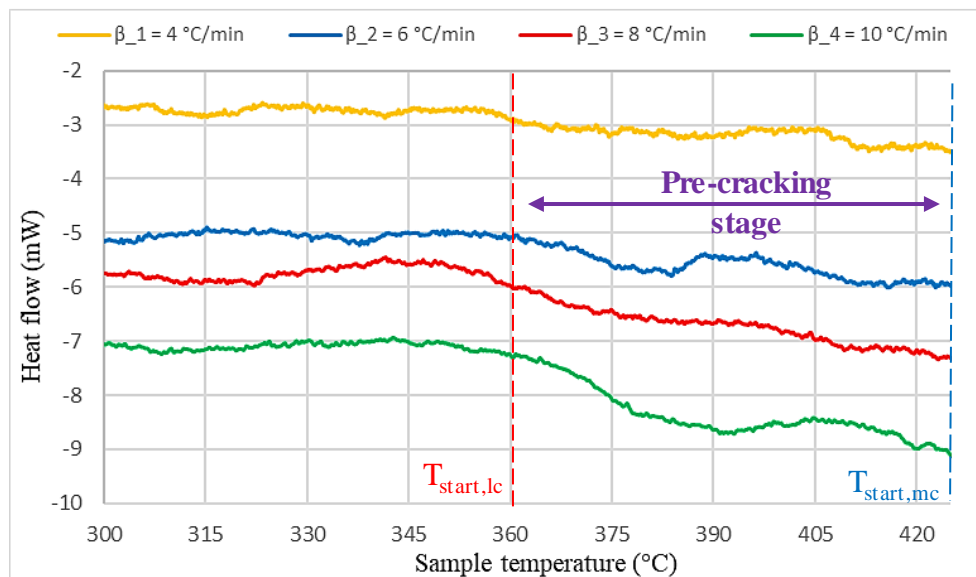


Figure 4-6 : Pre-cracking phase for HDPE pyrolysis at different heating rates.

Thus, the whole cracking process for PP and HDPE, can be divided into two overlapping parts; (1) the latent cracking part that starts at  $T_{start,lc}$  (start latent cracking temperature) and (2) the mass cracking part that starts at  $T_{start,mc}$  (start mass cracking temperature). In the second part, mass loss starts to appear because plastic is decomposing into volatile materials that are leaving the crucible. Moreover, the latent cracking or the pre-cracking phenomenon will be discussed later in this chapter in the modelling of the pyrolysis process for PP and HDPE at milli-particle scale (**section 4.3**).

Furthermore, the specific cracking enthalpies  $\Delta h_c$  (kJ/kg) for PP and HDPE pyrolysis, are determined by integrating the experimental heat flow power  $\dot{Q}_a$  (mW) with respect to time and then subtracting from it the sensible heat thermal energy during cracking, the final result is then divided by the initial mass of plastic ( $m_0$ ) as illustrated in **Eq. 4-1**.

$$\Delta h_c = \left( \int_{t_{start,lc}}^{t_{end,c}} \dot{Q}_a dt - C_p \int_{T_{start,lc}}^{T_{end,c}} m dT \right) / m_0 \quad \text{Eq. 4-1}$$

Where  $t_{start,lc}$  (s) and  $T_{start,lc}$  ( $^{\circ}\text{C}$ ) are the starting time and the starting temperature of the latent cracking phenomena,  $t_{end,c}$  (s) and  $T_{end,c}$  ( $^{\circ}\text{C}$ ) are the end time and the end temperature of the whole cracking process,  $C_p$  is the specific heat capacity for PP and HDPE just before the cracking process starts (2500 J/kg/K for PP and HDPE),  $m$  (kg) is the mass of plastic inside the crucible measured over time, and  $m_0$  (kg) is the initial mass of PP and HDPE before cracking. Finally, the other characteristic temperatures ( $T_{onset,c}$ ,  $T_{c,max}$ ,  $T_{offset,c}$ , and  $T_{end,c}$ ) and the specific cracking enthalpies for PP and HDPE pyrolysis at different heating rates (4, 6, 8, and 10  $^{\circ}\text{C}/\text{min}$ ) are illustrated in **Table 4-1**. These values are also checked using many studies and found to be within the range established in literature (INEOS, 2014a, 2014b; Jin *et al.*, 2019; Yin *et al.*, 2014).

**Table 4-1** : Characteristic temperatures and specific cracking enthalpies of PP and HDPE pyrolysis.

| $\beta$ (°C/min) | Cracking characteristic temperatures (°C) |             |                |             |               |             |                |             | Cracking enthalpy (kJ/kg) |              |
|------------------|---|-------------|----------------|-------------|---------------|-------------|----------------|-------------|---------------------------|--------------|
|                  | PP  |             |                |             | HDPE          |             |                |             | PP                        | HDPE         |
|                  | $T_{onset,c}$                             | $T_{c,max}$ | $T_{offset,c}$ | $T_{end,c}$ | $T_{onset,c}$ | $T_{c,max}$ | $T_{offset,c}$ | $T_{end,c}$ | $\Delta h_c$              | $\Delta h_c$ |
| 4                | 415                                       | 437         | 447            | 455         | 454           | 467         | 479            | 485         | 415                       | 300          |
| 6                | 419                                       | 440         | 451            | 460         | 460           | 473         | 486            | 492         | 423                       | 320          |
| 8                | 422                                       | 444         | 455            | 465         | 463           | 478         | 492            | 498         | 435                       | 334          |
| 10               | 427                                       | 450         | 461            | 470         | 467           | 483         | 495            | 503         | 445                       | 345          |

## 4.2 Pyrolysis kinetic study for PP and HDPE

In order to proceed in modelling plastic pyrolysis at a milli-particle and laboratory fixed bed semi-batch reactor scales, the first step to do is to find the optimum kinetic law (conversion rate **Eq. 2-24**) that describes the pyrolysis process using the previous TGA-DSC results (**section 4.1**). Thus in this section, a vast kinetic study is conducted for PP and HDPE pyrolysis, where the best fitting kinetic parameters ( $f(x)$ ,  $E$  (J/mol), and  $A$  ( $s^{-1}$ )) are determined. Best kinetic models  $f(x)$  are determined using the Criado's method, as a first step. Then, the activation energies  $E$  are computed according to the three isoconversional methods; Friedman (FR), Kissinger-Akahira-Sunose (KAS), and Flynn-Wall-Ozawa (FWO), discussed in Chapter Two **section 2.5.1**. Later, the pre-exponential factor  $A$  is determined using each isoconversional method. Finally, the theoretical conversions are computed according to the several combination results, then, compared to the experimental conversion in order to find the best combination that describes the pyrolysis process.

### 4.2.1 PP kinetic results

In this section, first, the best fitting kinetic models will be found by the Criado's method for PP pyrolysis at different heating rates  $\beta$  (4, 6, 8, and 10 °C/min). Then, the activation energy and the pre-exponential factor will be computed according the three isoconversional methods (FR, KAS, and FWO).

#### 4.2.1.1 Determining the kinetic model $f(x)$

As mentioned in Chapter Two **section 2.5.1**, Criado's method is a curve fitting method that compares the theoretical kinetic models found in literature (**Table 2-6**) with the TGA data of a pyrolysis process. **Figure 4-7** illustrates the results ( $z(x) = f(x)g(x)$ ) of the theoretical curves (A2, R2, R3, D2, F2, and F3) and the experimental ones (exp1 ( $\beta_1$ ), exp2 ( $\beta_2$ ), exp3 ( $\beta_3$ ), and exp4 ( $\beta_4$ )) function of the conversion  $x$ . As shown, almost all of the theoretical kinetic models, except F2 and F3, represent well the experimental data from 0 to 0.5 conversion, however, after  $x = 0.5$ , the best models that fit the experimental results are R3 and A2.

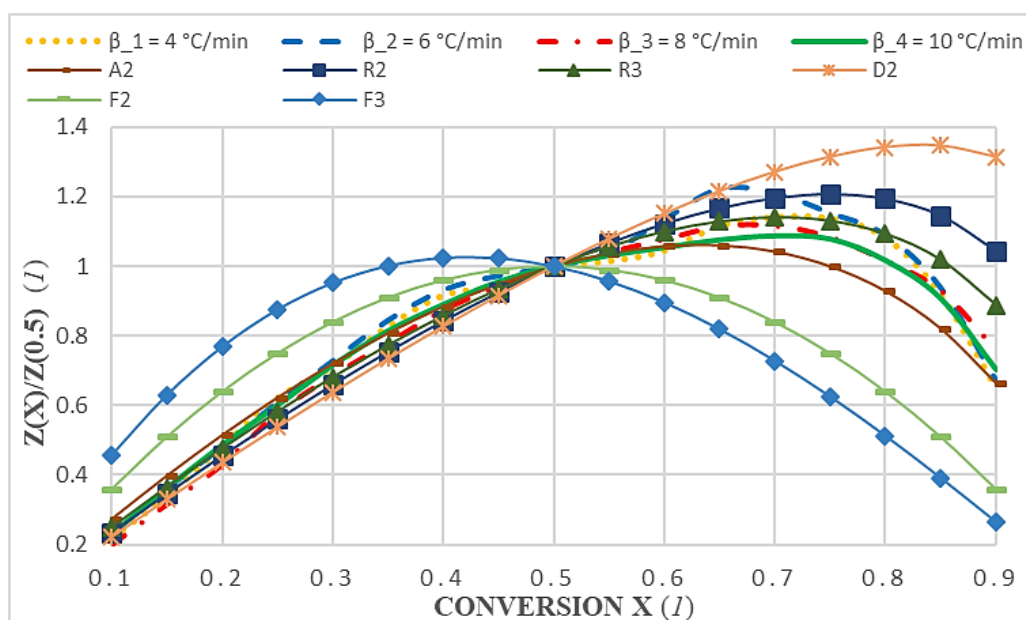


**Figure 4-7 :** Theoretical master plots for different reaction models compared with the experimental data for PP pyrolysis at different heating rates.

Moreover, to emphasize this result, the coefficient of determination  $R^2$  is calculated among the theoretical and the experimental results and shown in **Figure 4-8**. It is deduced that the best models that fits PP pyrolysis with the highest average coefficient of determination are, respectively, A2 with  $R^2 = 0.97$  and R3 with  $R^2 = 0.95$ . Furthermore, it is commonly found in literature that the reaction models for PP is R3 (contracting sphere) at relatively high heating rates, above 10 °C/min (*Aboulkas et al., 2010; Xu et al., 2018*). However, in other studies it is found that the reaction model A2 represents the pyrolysis process for PP at low heating rates, below 10 °C/min (*Kim et al., 2008; Kim and Kim, 2005*). Thus the deduced kinetic model (A2) for PP pyrolysis determined in this study, at heating rate below 10 °C/min, well matches with the results found in literature.

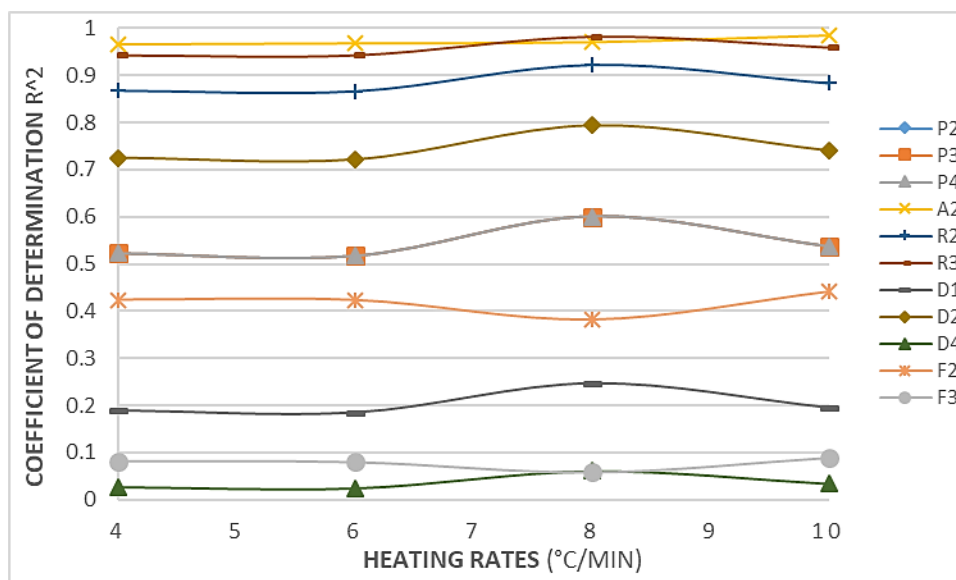


**Figure 4-8 :** Coefficient of determination  $R^2$  versus heating rates, for PP pyrolysis, for different reaction models.

#### 4.2.1.2 Calculating the activation energy and the pre-exponential factor

The second step, after finding the best fitting kinetic models for PP pyrolysis, is to determine the activation energy  $E$  (J/mol), then the pre-exponential factor  $A$  ( $s^{-1}$ ) that represent pyrolysis at low heating rates (below 10 °C/min).

**Figure 4-9 – Figure 4-11** show the experimental data and the fitting curves for PP pyrolysis at different heating rates (4, 6, 8, and 10 °C/min) using the three isoconversional methods (FR, KAS, and FWO). Where, each straight line is fitting four experimental results according to the four heating rates at a constant conversion  $x$ , as explained in Chapter Two **section 2.5.1**. The results show that the fitting lines are likely to be more parallel in **Figure 4-10** and **Figure 4-11**, which indicates that the activation energy results determined by KAS and FWO methods are much uniform over the conversion  $x$  (i.e. over the reaction) in contrast to the results determined by FR method (**Figure 4-9**).

**Figure 4-9** displays the results according to FR method, i.e. evaluating  $\ln(dx/dt)$  with respect to  $1/T$  for the four heating rates at each constant conversion  $x$ . The fitting straight lines seem to fit very well with the experimental data (the four points represents the experiment results at the four heating rates (4, 6, 8, 10 °C/min)) over all the conversion range. On the other hand, in **Figure 4-10**

and Figure 4-11, the experimental data at low conversions ( $x \leq 0.3$ ) are more scattered than that in the FR method (Figure 4-9). This indicates that  $R^2$  value of the activation energy in FR method will be higher than that in KAS and FWO.

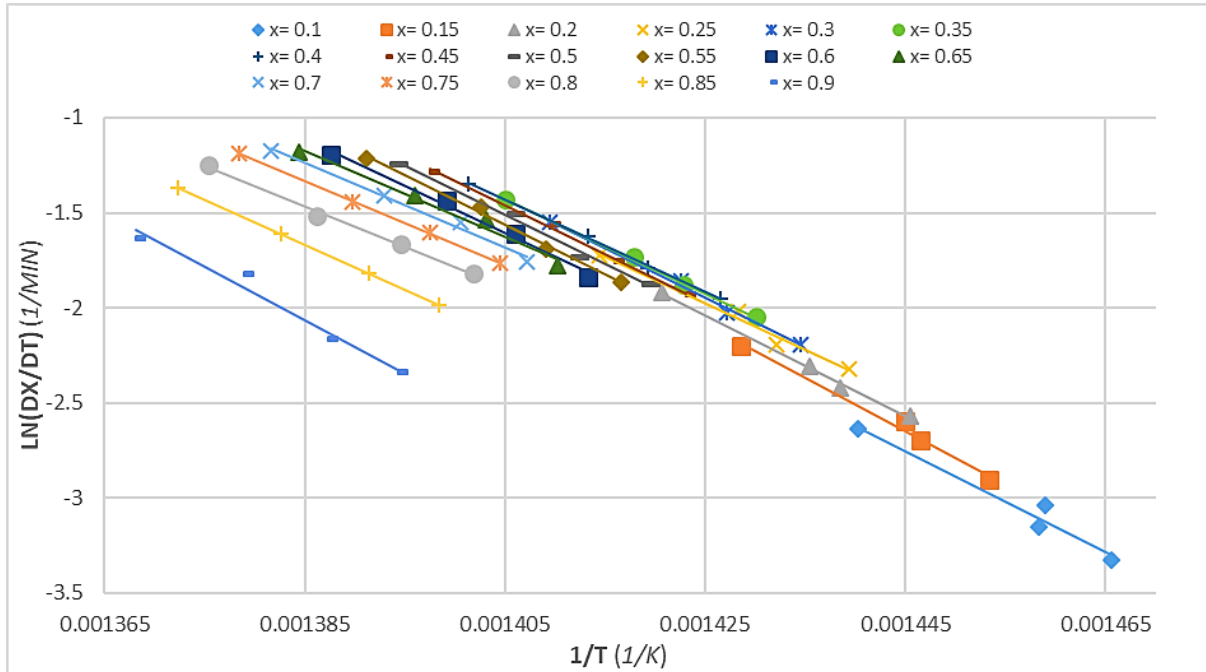
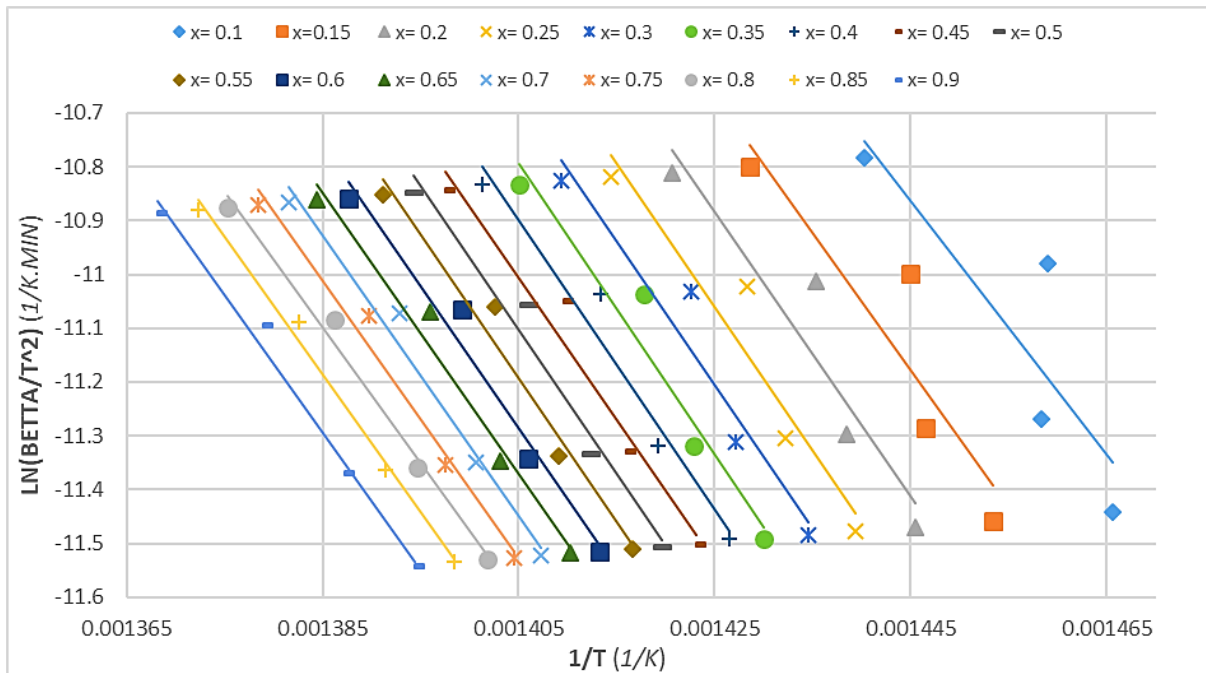
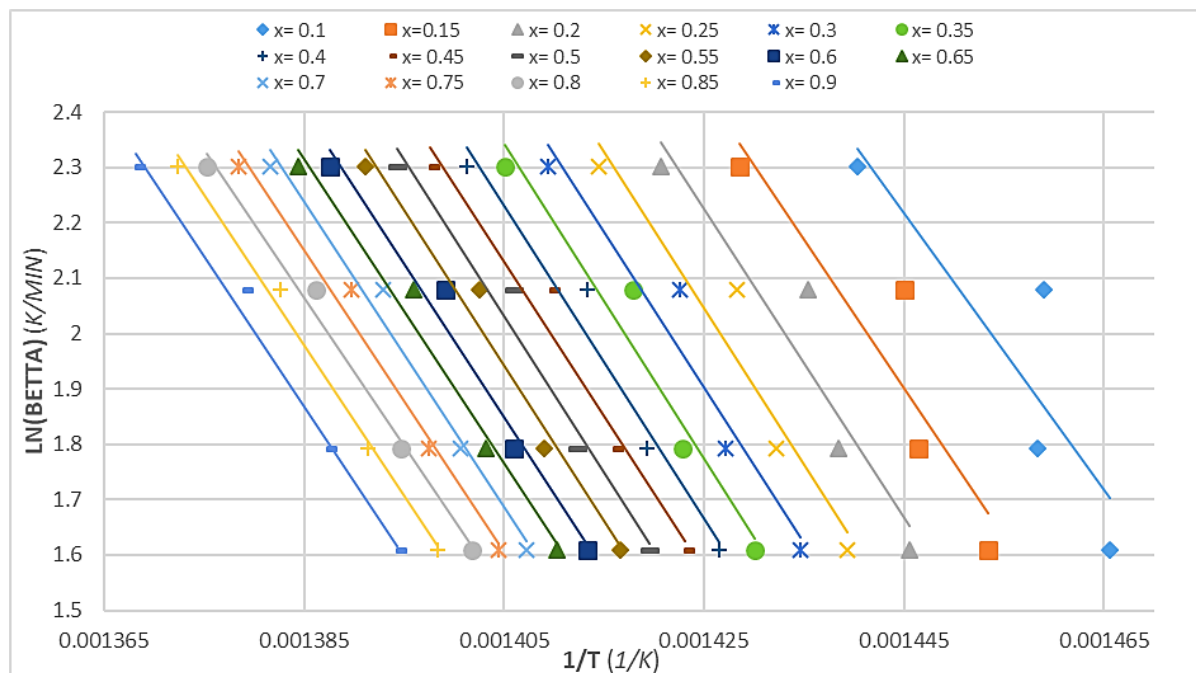


Figure 4-9 : Plotting  $\ln(dx/dt)$  w.r.t.  $1/T$  at each conversion for PP pyrolysis at heating rates (4, 6, 8, 10 °C/min) according to FR method.



**Figure 4-10 :** Plotting  $\ln(\beta T^2)$  w.r.t.  $1/T$  at each conversion for PP pyrolysis at heating rates (4, 6, 8, 10 K/min) according to KAS method.



**Figure 4-11 :** Plotting  $\ln(\beta)$  w.r.t.  $1/T$  at each conversion for PP pyrolysis at heating rates (4, 6, 8, 10 K/min) according to FWO method.

After illustrating the results, the activation energies are calculated at each conversion and according to each isoconversional method. Three tables (**Table 4-1A – Table 4-3A**), mentioned in **Appendix: A**, illustrate the results for PP in details using FR, KAS, and FWO methods. First, the average value of the activation energy (about 220 kJ/mol) is almost the same using KAS and FWO methods with  $R^2 = 0.96$ . On the other hand, the deduced average activation energy according to the FR method is 202 kJ/mol with  $R^2 = 0.99$ .

Moreover, the pre-exponential coefficient  $A$  (1/min) is determined from the intercept values of the fitting lines for each isoconversional method (FR, KAS, and FWO) employing the deduced kinetic models (A2 and R3) from the previous section (**section 4.2.1.1**). Also as the results illustrate, the average values of the pre-exponential coefficient  $A$  are approximately the same for KAS and FWO, about  $4.15 \times 10^{15}$  (1/min) for A2 model and  $1.2 \times 10^{15}$  (1/min) for R3 model. However, the average results according to FR method are lower than that deduced by KAS and FWO;  $8.79 \times 10^{14}$  (1/min) for A2 model and  $3.27 \times 10^{14}$  (1/min) for R3 model.

**Table 4-2** resumes the deduced average kinetic triplet for PP pyrolysis, where the results by KAS and FWO are similar.

**Table 4-2 :** Average deduced kinetic parameters ( $f(x)$ ,  $E$ , and  $A$ ) for PP pyrolysis at heating rates below 10 °C/min.

| <b>Kinetic triplet for PP pyrolysis</b> |              |                       |                       |
|---|--------------|-----------------------|-----------------------|
|   | $E$ (kJ/mol) | $A$ (1/min)           |                       |
|   |              | $f(x) = \mathbf{A2}$  | $f(x) = \mathbf{R3}$  |
| <b>FR</b>                               | 202          | $8.79 \times 10^{15}$ | $3.27 \times 10^{15}$ |
| <b>KAS &amp; FWO</b>                    | 220          | $4.15 \times 10^{15}$ | $1.2 \times 10^{15}$  |

Finally, the average kinetic parameters presented in **Table 4-2**, are implemented in the kinetic equation (**Eq. 2-24**), which is solved by an iterative method, in order to evaluate the theoretical conversion  $x$ . Then, the theoretical conversions, calculated according to the isoconversional methods and the selected kinetic models (A2 and R3), are plotted and compared with experimental conversions to choose the best kinetic parameters that models PP pyrolysis.

**Figure 4-12** illustrates the theoretical and experimental conversions for PP pyrolysis, at a heating rate of 4 °C/min. First, the FR results (FR\_A2 and FR\_R3) are excluded since the theoretical conversion diverges away from the experimental one as shown in the figure. Thus, FR method doesn't describe PP pyrolysis. Furthermore, the results of KAS/ FWO are well promising, especially by using A2 model (KAS/FWO\_A2 curve). The theoretical conversions using KAS/FWO\_A2 fit the experimental conversion with an average relative error between less than 3 % (**Figure 4-12**). Therefore, the best kinetic model that describes the PP pyrolysis at 4 °C/min is the Avrami-Erofe'v (A2) with an activation energy of 220 (kJ/mol) and a pre-exponential coefficient  $A = 4.15 \times 10^{15}$  ( $\text{min}^{-1}$ ) determined both by using either KAS or FWO method.

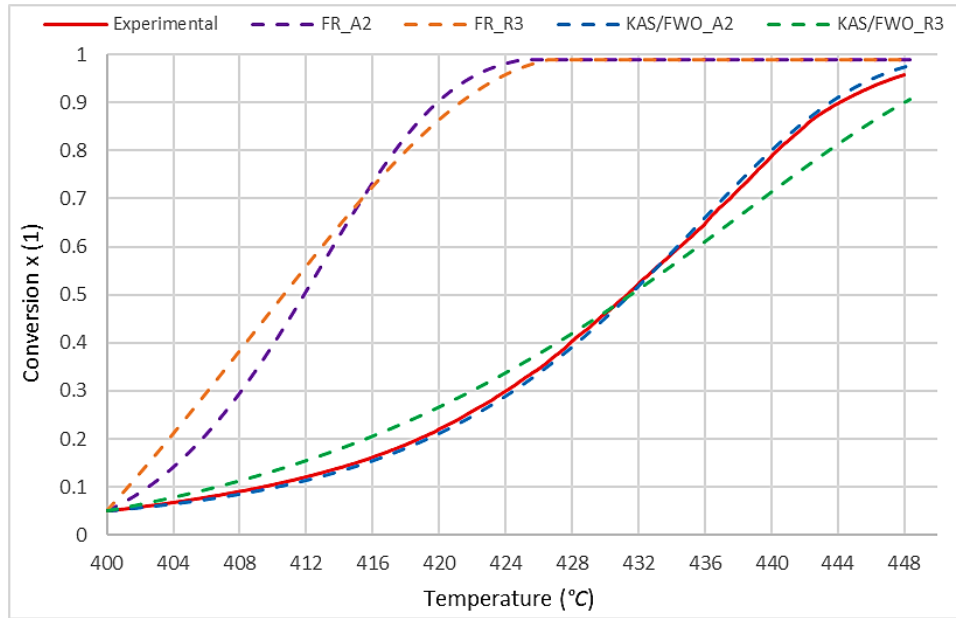


**Figure 4-12 :** Theoretical and experimental conversions for PP pyrolysis, at heating rate 4 °C/min, according to the best chosen kinetic models (R3, and A2).

Moreover, the best deduced kinetic parameter combination for PP pyrolysis at a heating rate of 4 °C/min is also tested for the other heating rates ( 6, 8, and 10 °C/min) for the sake of validation, as shown in **Figure 4-13**. The average relative error between the theoretical and the experimental conversions didn't exceed 5 %. Therefore, the best kinetic model that models PP pyrolysis at low heating rate (below 10 °C/min) is the Avrami-Erofe'Ve model (A2) with an activation energy of 220 (kJ/mol) and pre-exponential coefficient  $A = 4.15 \times 10^{15}$  ( $\text{min}^{-1}$ ) determined by either KAS or FWO methods. Nonetheless, the determined values of the activation energy for PP pyrolysis are within the ranges found in literature, 190 to 230 kJ/mol, however, the determined results for the pre-exponential coefficient are higher than that found literature,  $1 \times 10^{10}$  to  $1 \times 10^{13}$  ( $1/\text{min}$ ) (Ceamanos *et al.*, 2002; Das and Tiwari, 2017; Gao *et al.*, 2003). Whereas, this is could be caused by the difference in the heating rates applied in this study (below 10 °C/min) and the ones found in literature (from 10 to 50 °C/min).

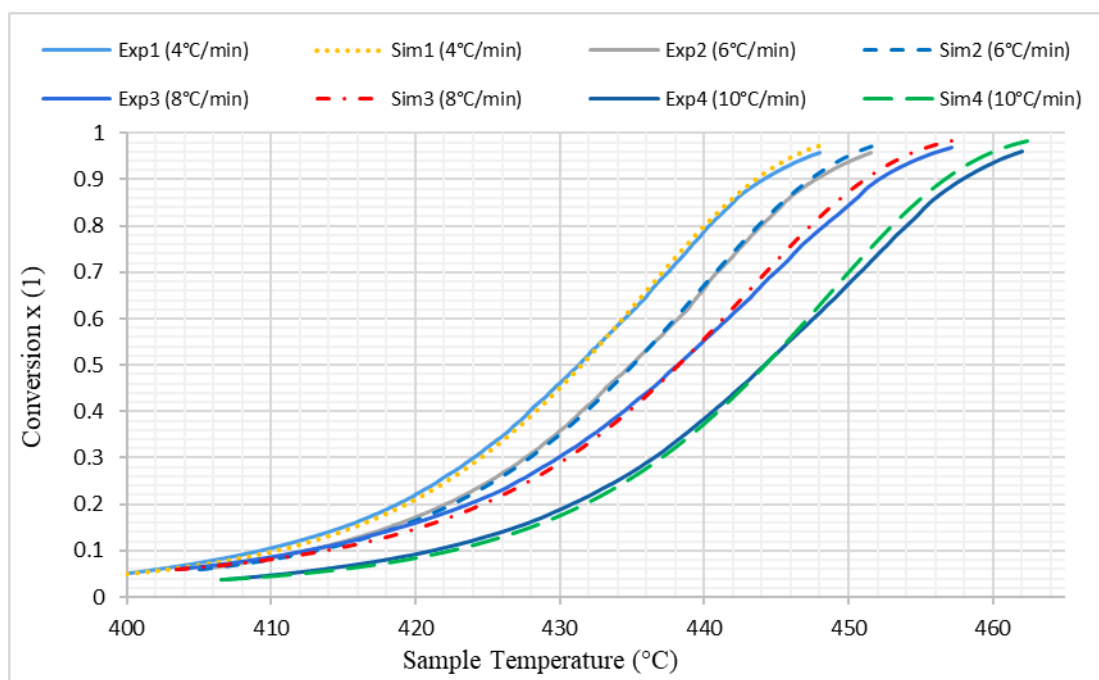


**Figure 4-13 :** Theoretical and experimental conversions for PP pyrolysis for four heating rates (4, 6, 8, and 10 °C/min), according to the best deduced kinetic parameters ( $E = 220$  (kJ/mol),  $f(x)$  is A2, and  $A = 4.15E+15$  (1/min)).

### 4.2.2 HDPE kinetic results

After finding the kinetic parameters for PP pyrolysis, same methodology and procedure are applied for HDPE in order to find the best kinetic parameters. As a result, the kinetic parameters that describes HDPE pyrolysis the best at low heating rates (4, 6, 8, and 10 °C/min) are:  $E = 264$  kJ/mol (according to KAS and FWO methods), kinetic model  $f(x)$  is also Avarami-Erofe'Ve (A2), and the pre-exponential factor is  $A = 8.3 \times 10^{17}$  (1/min). Theoretical conversions calculated using these parameters, in addition, to the experimental conversions at different heating rates are shown in **Figure 4-14**. The average relative error between the theoretical and experimental data is less than 6 %.

Moreover, the determined value of the activation energy of HDPE is within the range (230 to 270 kJ/mol) that is found in literature (Ceamanos *et al.*, 2002; Das and Tiwari, 2017; Gao *et al.*, 2003). But the deduced kinetic model (A2) is different than that found in literature (R2) due to the difference in the heating rates; about 10 to 50 °C/min heating rate found in literature. In addition, the deduced average pre-exponential value,  $8.3 \times 10^{17}$  (1/min), differs from the values that are found

in literature, range between  $10^8$  to  $3 \times 10^{17}$  (1/min), because the deduced kinetic models  $f(x)$  are different (Ceamanos *et al.*, 2002; Das and Tiwari, 2017; Gao *et al.*, 2003).

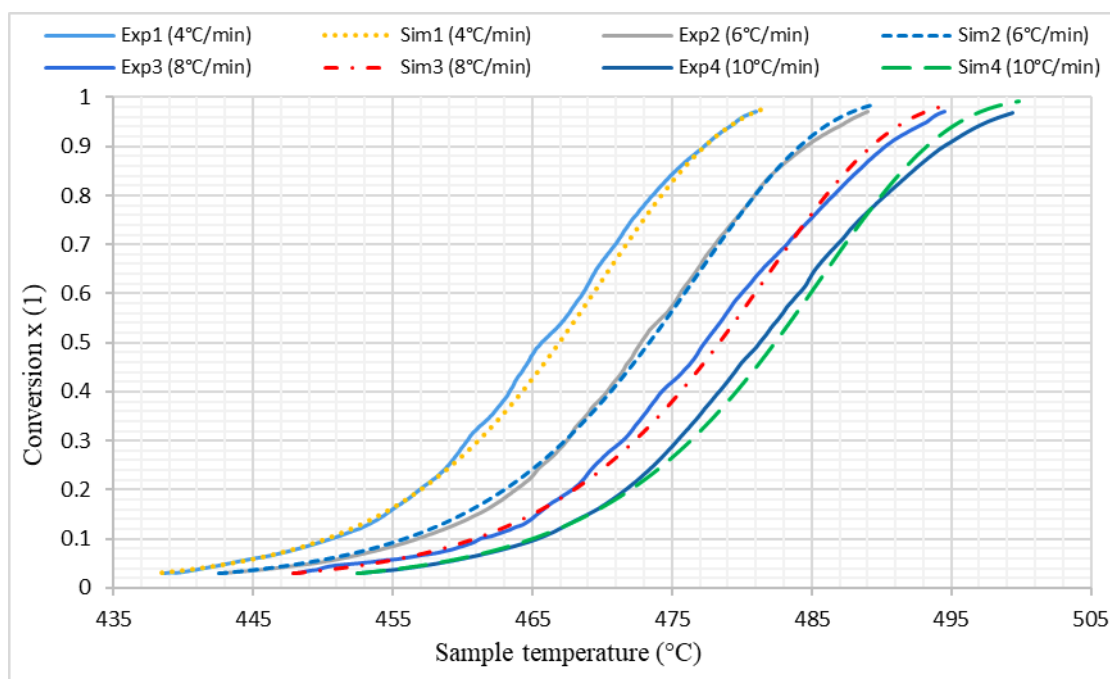


**Figure 4-14** : Theoretical and experimental conversions for HDPE pyrolysis at four heating rates (4, 6, 8, and 10 °C/min), according to best deduced kinetic parameters ( $E = 264$  (kJ/mol),  $f(x)$  is A2, and  $A = 8.3E+17$  (1/min)).

As a conclusion, the best kinetic parameters are determined and the TGA model is checked for PP and HDPE pyrolysis at low heating rates (below 10 °C/min). Therefore, the next step is to simulate and validate these pyrolysis processes at milli-particle scale inside the thermogravimetric analyzer coupled with differential scanning calorimeter (TGA-DSC) before modelling and validating pyrolysis at a larger scale (lab-scale), which is the semi-batch reactor.

### 4.3 Results of modelling plastic pyrolysis for PP and HDPE at milli-particle scale

After the determination of the best kinetic parameters that model the pyrolysis process, the next step is to use these parameters (Eq. 2-24) in modelling and simulating PP and HDPE pyrolysis process inside TGA-DSC as a milli-particle scale. Moreover, the AHCM is used in the simulation to model the melting phase before the pyrolysis process as demonstrated in Chapter Three section 3.2. All the appropriate equations, boundary conditions, and material properties, presented in Chapter Two section 2.5.2 and the cracking characteristics for PP and HDPE pyrolysis (displayed

in **section 4.1**), are applied and implemented in the simulations. In this section, the HDPE results are demonstrated before the PP results because the latent cracking phenomena and results are more clear in the HDPE results.

Regarding results mentioned in literature, Bockhorn et al. and Navarro et al. analytically modelled pyrolysis process of plastic particles inside a thermogravimetric analyzer (Bockhorn *et al.*, 1999; Navarro *et al.*, 2012). Both studies used a one-step kinetic function (from molten plastic to by-products) along with the heat conduction equation (**Eq. 1-29**) to model polymer pyrolysis (ABS (Acrylonitrile Butadiene Styrene) plastic, tyre rubber, and PS). In addition, they compared the simulated conversion and temperature with the experimental ones and the results were in a good agreement, same as done in this work for PP and HDPE pyrolysis. However, in the current research work (PhD), the model is further validated by the energy balance; i.e. by comparing the simulated heat absorption heat over time with the experimental one (recorded by the DSC apparatus).

Also (Ding *et al.*, 2020) modelled pyrolysis process for plastic particles inside a fluidized bed reactor using one-step model; the results were compatible and validated with the experimental data. In addition, there exists in literature several different studies that modelled and simulated pyrolysis process for plastic and other materials at milli-particle scale (Alves and Figueiredo, 1989; Miller and Bellan, 1997; Peters, 2011). These models and equations were coupled with reaction schemes ranging from single one-step reaction, i.e. one rate of reaction equation, to multiple reaction system. However, modelling plastic pyrolysis for PP and HDPE using TGA-DCS is still not found in literature.

### 4.3.1 HDPE simulation results: pyrolysis at milli-particle scale

As a result, **Figure 4-15** and **Figure 4-16** show the experimental and the simulated results, respectively for the conversion and the heat flow, for HDPE pyrolysis inside TGA-DSC, at a heating rate of 8 °C/min.

First of all, it is observed that the mass cracking model (TGA) is working perfectly well as shown in **Figure 4-15**, where the average relative error among the simulated and experimental conversions is below 3 %. However, **Figure 4-16** illustrates the DSC comparison results: the simulated and experimental heat flow results seem to be alike and they have the same response and trend over time. But, the error is relatively high at the cracking phase with an average value of 20 %.

Therefore, the model is compatible to describe the mass cracking process for HDPE that yield volatile products (TGA concept). Whereas, the DSC conception (latent cracking) needs further apprehending and development to enhance the heat flow results at the cracking phase.

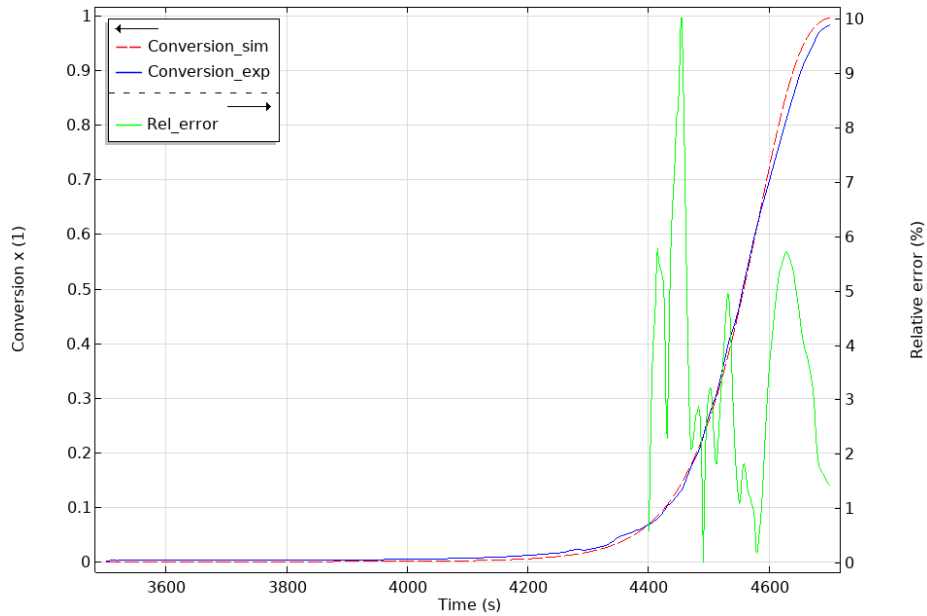


**Figure 4-15** : Simulated and experimental conversion results for HDPE pyrolysis inside TGA-DSC, heating rate  $\beta_3 = 8 \text{ }^\circ\text{C/min}$ .

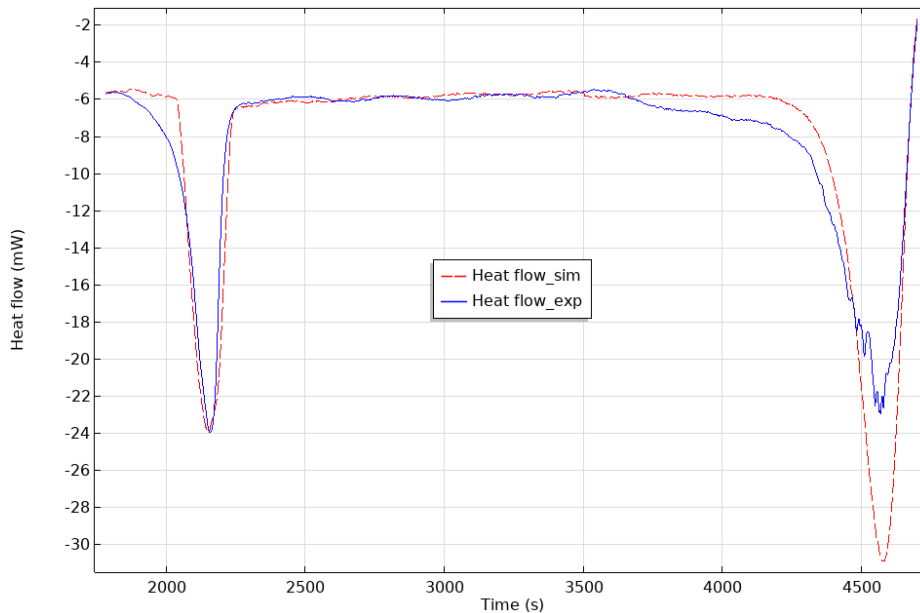


**Figure 4-16** : Simulated and experimental heat flow results for HDPE pyrolysis inside TGA-DSC, heating rate  $\beta_3 = 8 \text{ }^\circ\text{C/min}$ .

Recalling **section 4.1**, it is observed that the cracking phenomenon is divided into two stages; latent and mass cracking, as **Figure 4-17** displays. Whereas, the increase in the absorbed heat that occurs before the mass loss starts at 425 °C is due to the latent cracking (**Figure 4-17**).

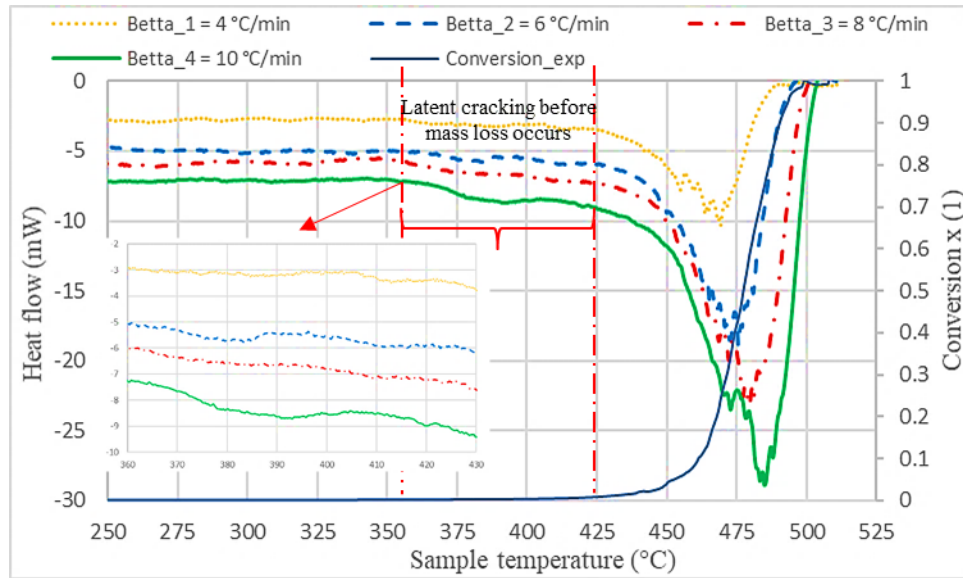


**Figure 4-17** : Heat flow for HDPE pyrolysis, at different heating rates, illustrating the latent cracking phenomena before the mass loss cracking.

In order to model the latent cracking, the heat capacity of plastic should be modified. Therefore, the heat capacity for HDPE is assumed to increase linearly from 2500 J/kg.K (at 360 °C) to 3300 J/kg.K (at 425 °C). Moreover, to model this phenomenon during the second phase of cracking, HDPE heat capacity is assumed to continue increasing linearly as the mass cracking starts, as illustrated in **Figure 4-18**.

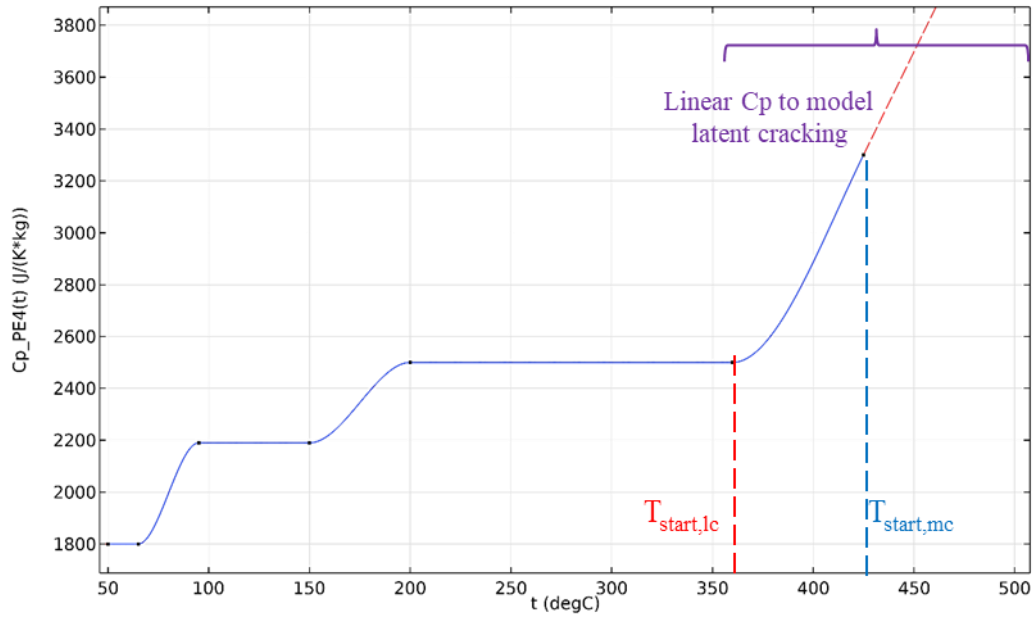


**Figure 4-18** : Heat capacity w.r.t. temperature for HDPE used to model the latent cracking for HDPE pyrolysis at heating rates below 10 °C/min.

After implementing the modified  $C_p$  for HDPE (**Figure 4-18**) into simulation, the results are enhanced for the cracking phase. **Figure 4-19** shows the enhanced results for HDPE pyrolysis at heating rate of 8 °C/min. As the results display, the latent cracking phenomenon starts (at  $T_{start,lc}$ ) before the mass cracking due to the increase in the heat capacity. However, the sensible heat (cyan line) is constant before the start of mass cracking temperature,  $T_{start,mc}$ , due to the constant mass and heat capacity (2500 J/kg/K), then, it starts to increase as the mass loss begins. Furthermore, the mass cracking (green dashed line) starts at the mass cracking temperature ( $T_{start,mc}$ ). Therefore, the sum of the three curves, sensible heat, latent cracking, and mass cracking, constitute the total thermal power (magenta dashed line) absorbed during the cracking phase of HDPE, which is in a very good agreement with the absorbed power (blue solid line), found experimentally; with an average relative error of 4 % (**Figure 4-19**).

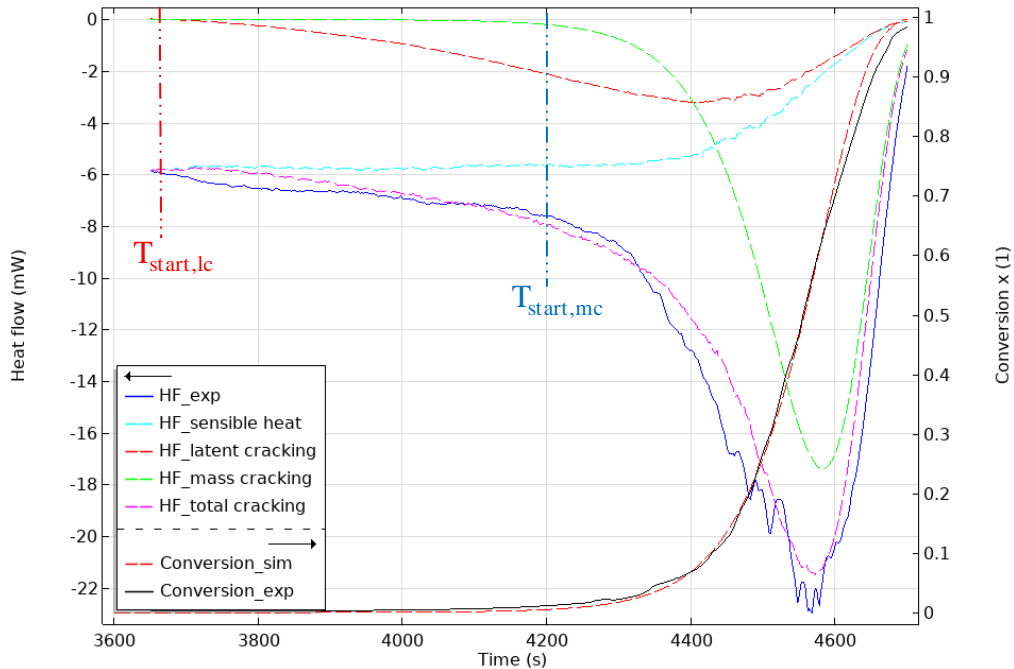


**Figure 4-19 :** Heat flow comparison for HDPE pyrolysis at 8 °C/min inside TGA-DSC according to the new enhanced model, latent cracking modelling.

Moreover and since the total cracking energy ( $\Delta h_c = 325$  kJ/kg for HDPE) is divided into latent and mass cracking enthalpies, the energy required for the mass cracking implemented into simulation is  $\Delta h_{mc} = 215$  kJ/kg (which is determined from simulation by trial and error method), however, the specific latent cracking enthalpy ( $\Delta h_{lc} = 110$  kJ/kg) is evaluated from the simulation results by subtracting the sensible heat and the mass cracking enthalpy from the total heat of cracking. Therefore, the same specific mass enthalpy is utilized for the other experiments at different heating rates (4, 6, and 10 °C/min) for the sake of validation, where the latent cracking enthalpy is determined from the simulation results.

**Figure 4-20** illustrates the other new results for HDPE pyrolysis ( $\beta = 4$  °C/min) after modelling the latent cracking phenomena. It is clearly noticed that the results of the cracking phase are much enhanced, where the average relative error didn't exceed 5 %. Furthermore, two more results ( $\beta = 6$  and 10 °C/min) are presented in **Appendix: A (Figure 4-1A and Figure 4-2A)** for further validation; the maximum average relative error is below 8 %. In addition, the computed latent heat specific enthalpy in all of the HDPE pyrolysis simulations is found to be almost equal to 110 kJ/kg.

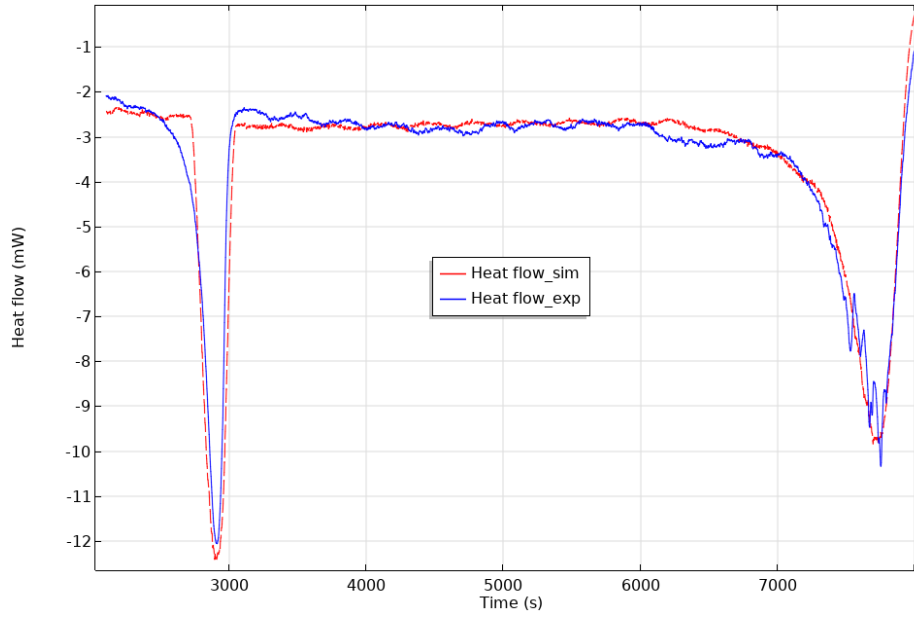


Figure 4-20 : Simulated and experimental results for HDPE pyrolysis at heating rate  $\beta_1 = 4 \text{ }^\circ\text{C/min}$ .

### 4.3.2 PP simulation results: pyrolysis at milli-particle scale

PP pyrolysis simulations are done following the same methodology as HDPE, with the appropriate heat capacity function, illustrated in Figure 4-21.

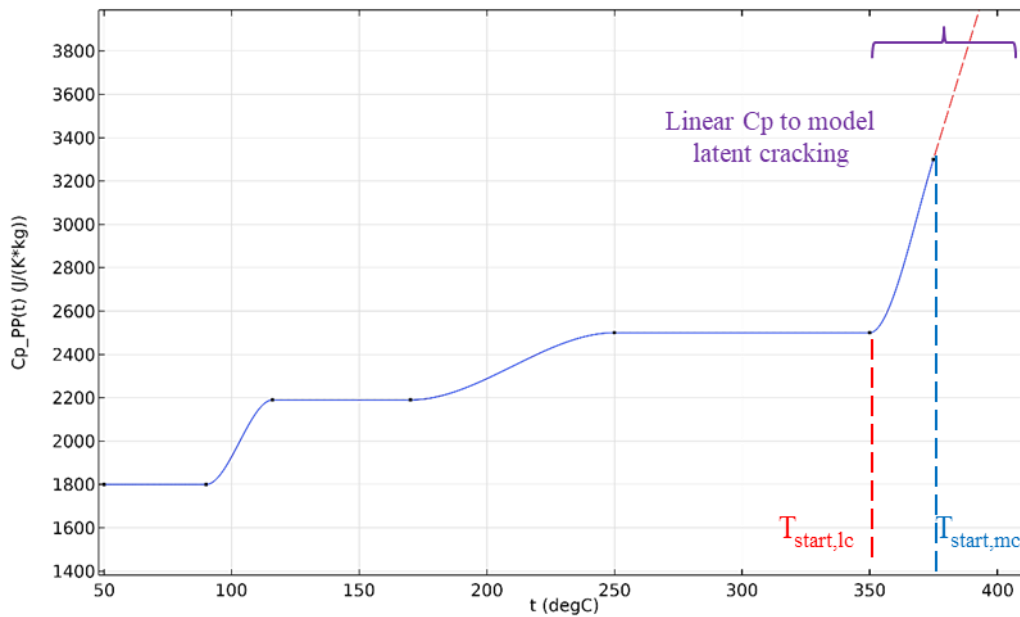
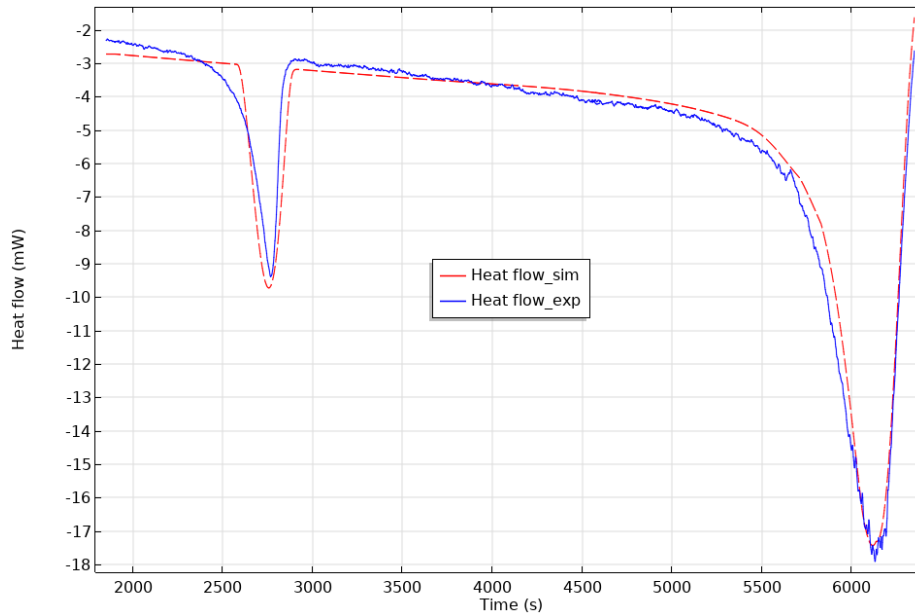


Figure 4-21 : Heat capacity w.r.t. temperature for PP used to model the latent cracking for PP pyrolysis at heating rates below  $10 \text{ }^\circ\text{C/min}$ .

As well as, **Figure 4-22** demonstrates the results for PP pyrolysis, at milli-particle scale, at the heating rates  $4\text{ }^{\circ}\text{C}/\text{min}$ . The simulated results are in a very good agreement with the experimental one where the average relative error didn't exceed 6 %. Additionally, three more results at different heating rates are illustrated in **Appendix: A** for further validation (**Figure 4-3A – Figure 4-5A**); with an average relative error below 6 %. The latent cracking energy is computed in all PP pyrolysis simulations and it is equal to  $135\text{ kJ}/\text{kg}$ . On the other hand,  $\Delta h_{mc} = 290\text{ kJ}/\text{kg}$  is used as a fixed value in all the simulations (PP) to model absorbed energy due to mass cracking phase.



**Figure 4-22** : Simulated and experimental results for PP pyrolysis at heating rate  $\beta_1 = 4\text{ }^{\circ}\text{C}/\text{min}$ .

Further, it is deduced from the results, that the latent cracking enthalpies have almost the half value of the mass cracking enthalpies for all PP and HDPE pyrolysis process simulations (**Table 4-3**). However, the latent cracking phenomenon (pre-cracking) and the obtained results ( $\Delta h_{mc}$  and  $\Delta h_{lc}$ ) are still not mentioned in literature, since modelling plastic particle pyrolysis in a TGA coupled with DSC is still not found in literature. **Table 4-3** shows the constant values of the mass loss cracking enthalpies used in these simulations and the deduced average latent cracking enthalpies from the numerical studies. In addition, it is obvious that the summation of the two preceding enthalpies is equal to the average total cracking enthalpies deduced from the experimental DSC measurements (**Table 4-1**).

**Table 4-3** : Mass loss enthalpies and deduced latent cracking enthalpies.

|      | $\Delta h_{mc}$ | $\Delta h_{lc}$ | $\Delta h_c$ |
|------|-----------------|-----------------|--------------|
|      | <i>kJ/kg</i>    | <i>kJ/kg</i>    | <i>kJ/kg</i> |
| PP   | 290             | 135             | 425          |
| HDPE | 215             | 110             | 325          |

Finally, the whole pyrolysis process for PP and HDPE at milli-particle inside TGA-DSC is modelled and validated. Whereas, the next step is to upgrade the simulation to model and validate pyrolysis process in a semi-batch reactor as a larger scale rather than milli-particle scale.

#### 4.4 Results of modelling PP and HDPE pyrolysis inside a laboratory-scale semi-batch reactor

After modelling pyrolysis process for PP and HDPE at milli-particle scale, the validated kinetic model will be utilized to model the process in a laboratory scale semi-batch reactor (**Figure 2-7**). Modelling pyrolysis in laboratory semi-batch reactor is a necessary step to validate the pyrolysis model at a bulk scale after the milli-particle one to understand more the process and to employ it later on when modelling the continuous reactor.

Regarding similar works done in literature, Jin et al. modelled and simulated plastic pyrolysis process for a thin film flow, about 2 mm thickness, in a vertical falling film reactor (Jin *et al.*, 2019). They used the volume of fraction (VOF) method along with the momentum equation to model the two phases flow (molten plastic and by-products) same as the concept used in this thesis. However, they used the first order model (**Table 2-6**) as a kinetic model to describe the pyrolysis of mixed plastic waste (PE, PP, and PS) and modelled pyrolysis for thin layer of molten plastic (about 2 mm); which differs from modelling pyrolysis of a bulk of plastic inside a semi-batch reactor (as done in the current work). Moreover, they mentioned that the experimental and the simulated results were in a good agreement. In another study, Guo et al. (Guo *et al.*, 2009) modelled gas–liquid two-phase flow in an evaporative condenser using the VOF method; similar to the model used in the current study (PhD thesis) and that will be illustrated in this section. On the other hand, Csukas et al. (Csukas *et al.*, 2013) modelled plastic pyrolysis in a continuous tubular reactor using Direct Computer Mapping (DCM) algorithm i.e. C++ algorithm with a

graphical user interface, but without using FEM or any conventional numerical software, same as done in this current work. Nevertheless, modelling and simulating plastic pyrolysis process using FEM and conventional commercial software at relatively large lab-scale is still rarely found in literature.

In this section, PP and HDPE pyrolysis experimental results inside the semi-batch reactor are demonstrated and discussed. In addition, the simulation results for PP and HDPE pyrolysis will be illustrated and compared with the experimental ones.

### 4.4.1 PP and HDPE experimental results: pyrolysis in semi-batch reactor

A 400 g of PP raw materials are loaded in the semi-batch reactor and heated from ambient temperature (about 20 °C) to 500 °C with different heating powers; 600 W and 750 W, i.e. 40 and 50 % of the maximum heating power. During the pyrolysis experiments, three main temperatures ( $T_1$ ,  $T_2$ , and  $T_4$ ), presented in **Figure 2-7**, are recorded with respect to time, in addition to the volume of the pyrolysis oil at the outlet of the reactor (after the condenser in **Figure 2-7, section 2.2.1**). However, the non-condensable by-products are purged away by a ventilator. Whereas, the total mass and the total volume of the pyrolytic oil are measured at the end of the process.

**Figure 4-23** shows the temperatures results of PP pyrolysis with 600 W as heating power. The wall temperature of the reactor,  $T_2$ , increases from 22 °C till 170 °C during 360 s with a constant heating rate of 27 °C/min. Then, as the main melting process starts (around  $T_m = 155$  °C) the heating rate, for the wall temperature  $T_2$ , decreases to become 12 °C/min. This heating rate remains constant (12 °C/min) until the main pyrolysis process starts at  $T_2 = 430$  °C ( $t = 1573$  s). Then  $T_2$  is stabilized at a temperature around 440 °C due to the endothermal reaction (pyrolysis), as shown in **Figure 4-23**. This matches with the experimental results determined by the TGA method where the average onset temperature for PP was about 420 °C (**Table 4-1**). Moreover,  $T_2$  remains stabilized at 440 °C until  $t = 3300$  s, which then increases (due to the level of the bed of the reactor gets beneath the level of  $T_2$ , which will be illustrated in the simulation results later on) to reach 500 °C (the set temperature). Afterwards,  $T_2$  is stabilized at 500 °C because the controller of the heaters starts to function at  $t = 3870$  s, as illustrated also in **Figure 4-24**. Finally, the pyrolysis process ends at  $t = 4500$  s, where the final mass and volume of the by-product oil are respectively, 351.4 g and 465

mL. Thus, the oil yield represents about 87.8 % of the final products with an average density of 755 kg/m<sup>3</sup> and the non-condensable gas yield represents about 12.2 %.

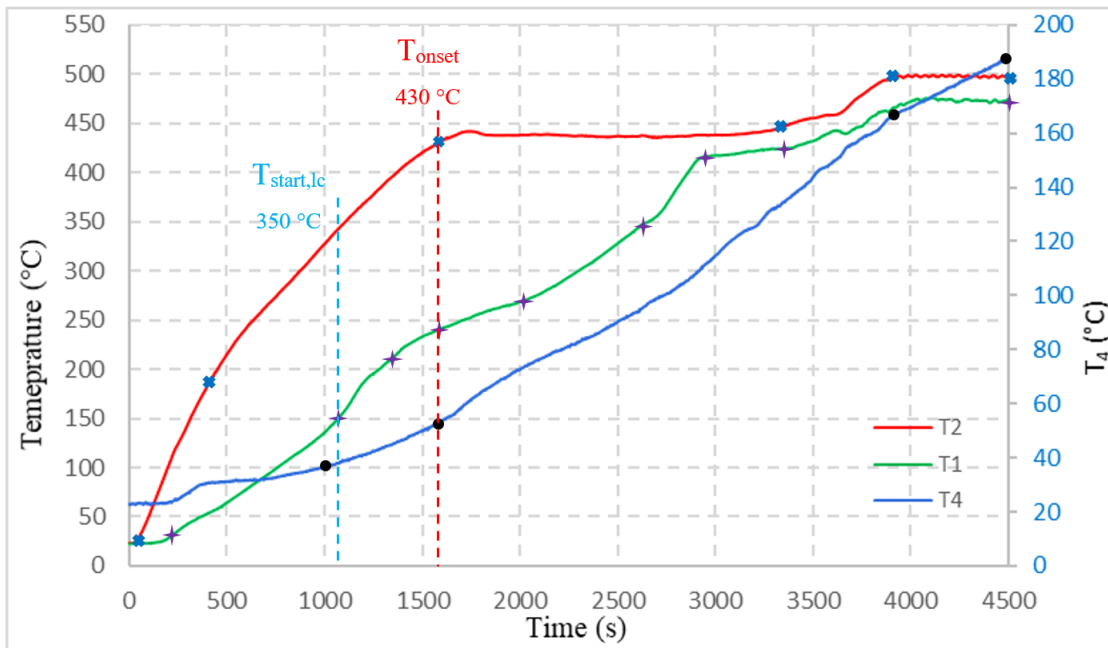
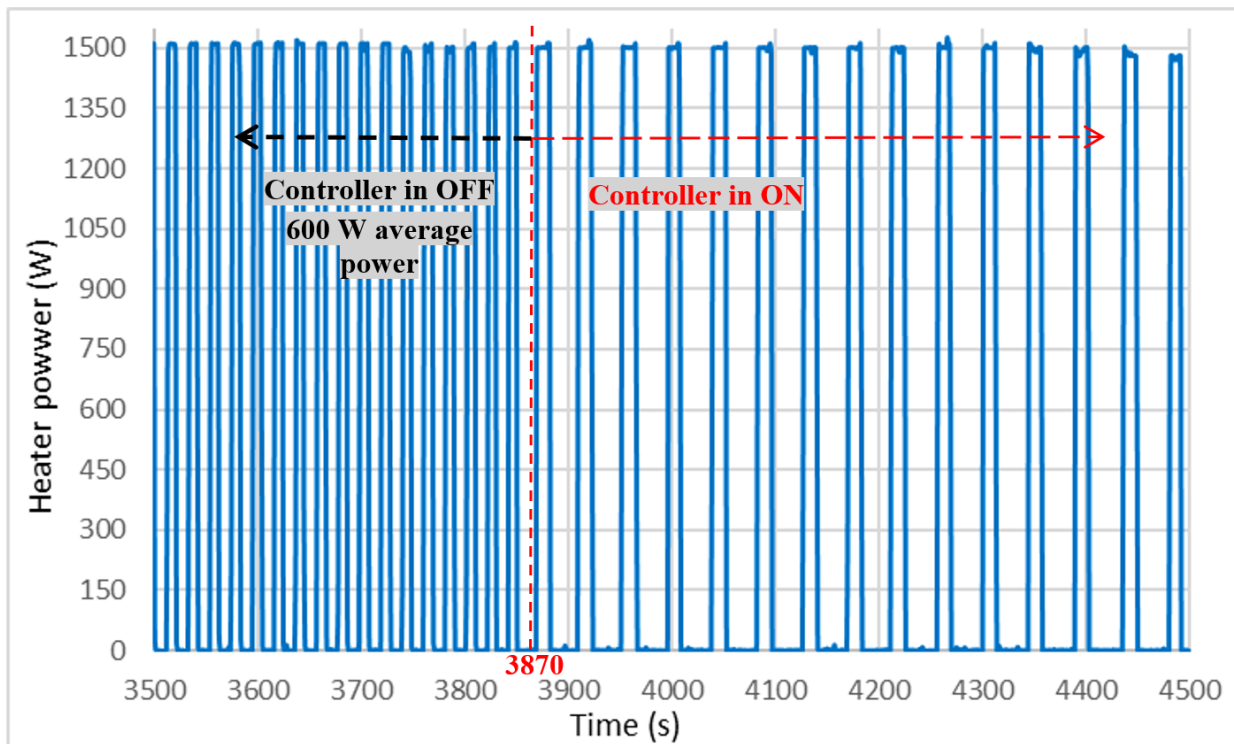


Figure 4-23 : Temperature results of 400 g PP pyrolysis inside the semi-batch reactor of 600 W average heating power.



**Figure 4-24 :** Heater power versus time for PP pyrolysis experiment (400 g) inside the semi-batch reactor heated by 600 W average heating power.

On the other hand, the plastic temperature  $T_1$ , which is 1 cm far away from the wall of the reactor (**Figure 2-7**), increases linearly with respect to time from ambient temperature (22 °C) to 140 °C at  $t = 1000$  s (just before melting starts at  $T_m = 155$  °C) with a constant heating rate of 8 °C/min. However, regarding the convex curve of  $T_1$  between 1050 s and 2000 s, it is due to the pre-cracking phenomenon effect (**section 4.1**) which is converting the molten plastic (at the wall vicinity) into different material with lower heat capacity and higher thermal conductivity. Thus, this phenomenon increases the heat flow from the wall towards  $T_1$  (at  $t = 1050$  s); the wall temperature is equal to 350 °C at which the pre-cracking starts (**Figure 4-5**). Then, as the mass cracking starts at  $T_2 = 380$  °C (1250 s) more energy is consumed. Hence, the curve of  $T_1$  starts to flatten and bend until it reaches a constant heating rate about 6.5 °C/min at  $t = 2000$  s. After that, it continues to rise with constant heating rate (6.5 °C) until it reaches the start latent cracking temperature 350 °C at  $t = 2630$  s, and flattens again for a short period of time (about 40 – 50 s) due to latent cracking at the vicinity of thermocouple  $T_1$ . Afterwards,  $T_1$  starts to rise again to reach 415 °C with a higher heating rate, 16 °C/min, due to the change in the thermal conductivity and heat capacity of the cracked material at the thermocouple vicinity ( $T_1$ ) caused by the latent cracking. At 415 °C (about the onset temperature of PP,  $420 \pm 5$  °C), curve flattens another time due to the high heat absorption as the mass cracking begins. After that,  $T_1$  continues to increase following the same pattern of the wall temperature  $T_2$  (from 3380 to 4500 s) as **Figure 4-23** shows.

Regarding the top temperature of the reactor ( $T_4$ ), it increases from 36 to 52 °C with a constant heating rate, 1.7 °C/min, from  $t = 1000$  s to  $t = 1573$  s. However, at  $t = 1573$  s, the mass cracking just starts (at the wall vicinity) which increases the top temperature,  $T_4$ , to achieve 167 °C at  $t = 3900$  s with an average heating rate of 3 °C/min. This sudden increase in heating rate and temperature is due to the condensation of the oil vapor pyrolysis by-products when hitting the top of the reactor which is relatively cold and has a high mass inertia. Moreover, this phenomenon (condensation) will be clearer and will be discussed notably in the next pyrolysis experiment results (50 % heating power, i.e. 750 W). Then,  $T_4$  continues to increase with a lower constant heating rate, about 1.8 °C/min till the end of the process (**Figure 4-23**).

On the other hand, **Figure 4-25** shows the cumulative mass of the oil versus time, recorded at the outlet of the semi-batch creator (after the condenser). As the results illustrate, the pyrolysis oil starts to appear at  $t = 1570$  s, same as deduced from the temperature results (**Figure 4-23**), i.e.  $T_2 = 430$  °C ( $t = 1573$  s), then it increases linearly and slowly (1.08 g/min) till  $t = 2400$  s; where only 15 g of oil have left the reactor during these 13.8 minutes. After that, the oil flowrate at the outlet increases exponentially till  $t = 3700$  s, where the majority of plastic is pyrolyzed (300 g). Then it starts to bend at  $t = 3870$  s as the heating power starts to decrease due to controller's activation (**Figure 4-24**). Recalling **Figure 4-23**,  $T_2$  was stabilized at 440 °C due to the occurrence of cracking process  $t = 1573$  s. However, only 100 g of oil left the reactor during 27 minutes (from 1573 to 3200 s), followed by 200 g during the following 8.3 minutes, as shown in **Figure 4-25**. This rapid increase in the oil mass flowrate emphasizes the effect of the condensation process affected by the top temperature of the reactor ( $T_4$ ). When the top temperature ( $T_4$ ) becomes hot enough (above 130 °C, which is the condensation temperature of the hydrocarbon byproducts ( $C_7 - C_9$ ) illustrated in **Table 2-7**) the oil condensation-recirculation process inside the reactor decays logarithmically which increases exponentially the mass flowrate leaving the system. On the other hand, at low temperatures of  $T_4$  (below 130 °C) the effect of the condensation process is extremely high and at high temperatures of  $T_4$  (above 130 °C) condensation effect is very weak.

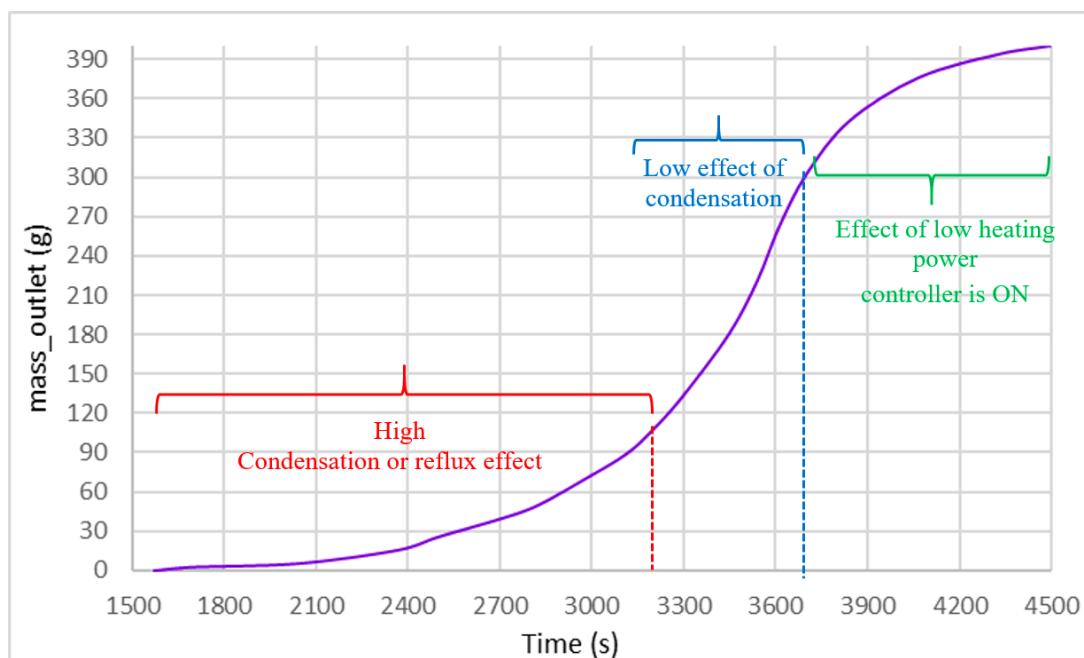


**Figure 4-25** : Mass of the oil by-product (at the outlet) vs time of 400 g PP pyrolysis inside the semi-batch reactor of 600 W average heating power.

Another PP pyrolysis experiment is realized at 50 % heating power (750 W) to emphasis the effect of the condensation process on the results inside the semi-batch reactor; results are illustrated in **Figure 4-26** and **Figure 4-27**.

As **Figure 4-26** shows, the curves tendencies ( $T_1$ ,  $T_2$ , and  $T_4$ ) are the same as displayed in **Figure 4-23**, however, the heating rate for  $T_1$  (plastic temperature) varies between 8 to 10 °C/min as the temperature rises from 270 to 350 °C. Thus, the desired heating rate (below 10 °C/min) is still respected when pyrolyzing PP at 750 W. In addition, the reactor’s wall temperature  $T_2$  is also stabilized at 440 °C, as illustrated in **Figure 4-23**, but a small peak is noticed between 1300 and 1700 s due to the higher heating power (750 W). On the other hand, the reactor’s top temperature  $T_4$  increases from 26 °C ( $t=700$  s) to 48 °C ( $t=1400$  s) with 1.9 °C/min heating rate, then it jumps rapidly to 117 °C (2100 s) by 5.9 °C/min, which means three times higher than using 600 W as power. This is clearly the effect of the condensation process of the pyrolytic vapors at the top of the reactor, which appears more distinctly as the heating power increases from 600 to 750 W.



**Figure 4-26** : Temperature results of 400 g PP pyrolysis inside the semi-batch reactor of 750 W average heating power.

This phenomenon is further validated by the cumulative oil’s mass measured at the outlet of the reactor (**Figure 4-27**). Whereas, in 23 minutes (from 1220 to 2600 s) only 80 g of oil have left the

reactor. However after that, the oil flowrate increases 3 folds (250 g) in only 8.3 minutes before controller's activation reduces heating power resulting in a rapid decrease in oil's flowrate, as shown in **Figure 4-27**.

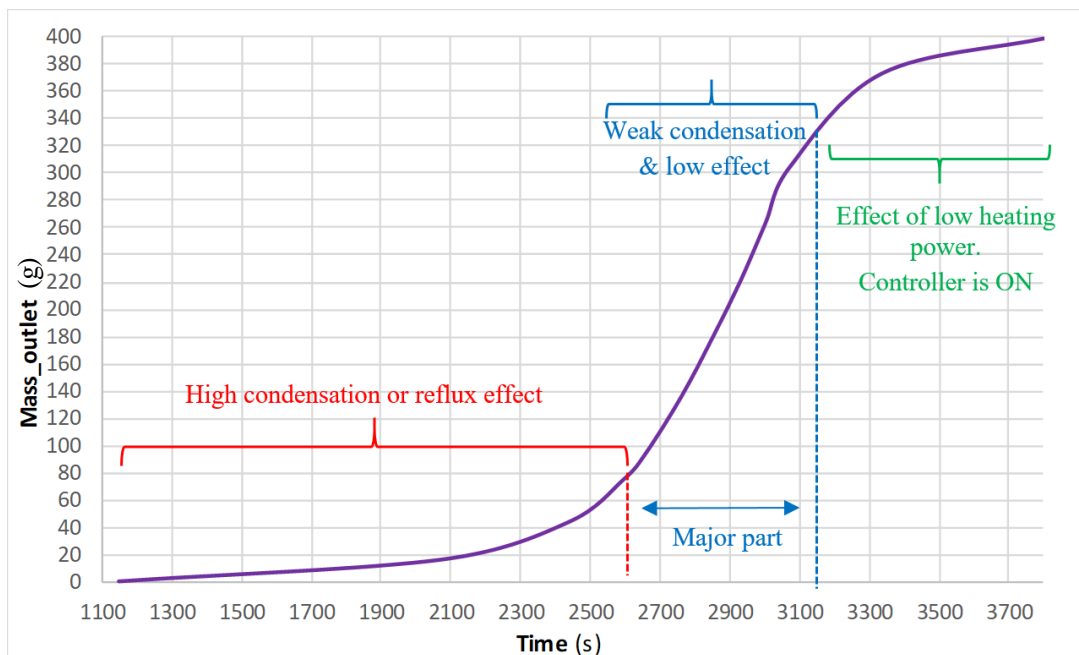


**Figure 4-27** : Mass of the oil by-product (at the outlet) vs time of 400 g PP pyrolysis inside the semi-batch reactor of 750 W average heating power.

Thus, this large and sudden increase in the oil flowrate is occurring when the top temperature ( $T_4$ ) exceeds  $130\text{ }^{\circ}\text{C}$  (at  $t = 3250\text{ s}$  in **Figure 4-23**, and at  $t = 2600\text{ s}$  in **Figure 4-26**); where the condensation-recirculation process decreases (**Figure 4-26** and **Figure 4-27**). Therefore, the condensation-recirculation of the pyrolytic vapors has a large impact on the oil flowrate and on the whole process during reactor's heating phase, i.e. before the top part of the reactor gets above  $130\text{ }^{\circ}\text{C}$ .

On the other hand, regarding the HDPE pyrolysis results, illustrated in **Appendix: A (Figure 4-6A** and **Figure 4-7A)**, they have the same trends as PP. Pyrolysis starts slowly at wall temperature ( $T_2$ ) about  $425\text{ }^{\circ}\text{C}$  ( $T_{\text{start,mc}}$ ), then  $T_2$  continues increasing to reach the onset temperature  $460\text{ }^{\circ}\text{C}$  (**Table 4-1**) at which the main pyrolysis begins. In addition, the condensation reflux increases the top temperature ( $T_4$ ) rapidly from  $60$  to  $130\text{ }^{\circ}\text{C}$  by a high heating rate of  $6\text{ }^{\circ}\text{C}/\text{min}$ , then the heating rate of  $T_4$  starts to decrease gradually to reach a constant value of  $2\text{ }^{\circ}\text{C}/\text{min}$  at temperature of  $190\text{ }^{\circ}\text{C}$ , where the effect of condensation-recirculation is negligible. Nevertheless, about  $220\text{ g}$  (more

than 50 % of the total mass) of pyrolysis by-products are collected at the outlet during only 5 minutes as the top temperature ( $T_4$ ) exceeds 190 °C.

This emphasizes more and more the huge impact of the condensation process at the beginning of the process inside the semi-batch reactor for PP and HDPE pyrolysis. As a conclusion, it could be said that the pyrolysis process inside the semi-batch reactor is composed of two stages; transient and steady state. First stage is considered as the transient phase (warming up the reactor, especially the top part that have a high mass inertia) where the condensation has a high impact. On the other hand, the second stage is termed by the steady state stage, because the pyrolysis process is the dominant and the condensation-recirculation process is very low due to the high temperature of the top of the reactor.

### **4.4.2 PP and HDPE simulation results using COMSOL-Multiphysics: pyrolysis in semi-batch reactor**

After noticing experimentally the occurrence of the condensation process of the vapor by-products inside the semi-batch reactor. The next step is to model and simulate PP and HDPE pyrolysis process inside the reactor. But knowing that the condensation process inside the semi-batch reactor is a complex phenomenon because of the variety of the pyrolytic vapors composition and evaporation/condensation characteristics (enthalpy, density,  $T_{\text{boil}}$ , etc...), as illustrated in Chapter Two **section 2.5.3 (Table 2-7)**. Two approaches of modelling are tested; First, PP and HDPE pyrolysis are modelled without the condensation process to reduce the complexity and to distinguish the effect of the condensation process on the simulation results. However, the second approach is modelling the condensation process, for PP, along with the pyrolysis to mimic more the real experimental process.

#### ***4.4.2.1 Modelling pyrolysis without condensation***

Phase filed equation, described in Chapter Two **section 2.5.3**, is used to model the two phase flow of molten plastic and pyrolysis by-products vapor. Whereas, the pyrolytic vapor is considered as a gas having average thermo-physical properties (**Table 4-4**) of all the hydrocarbon byproducts ( $C_7 - C_{24}$ ) illustrated in **Table 2-7**. Also, the non-condensable pyrolytic gas is assumed to leave the reactor immediately to sustain the atmospheric pressure conduction inside the semi-batch reactor.

Therefore, no building up pressure or gases inside the reactor, however all the products of the plastic pyrolysis leave the reactor directly.

**Table 4-4 :** Average thermo-physical properties of the pyrolytic vapor.

| Average pyrolysis by-products vapor properties |           |          |         |
|--|-----------|----------|---------|
| $\rho$   | $\mu$     | $C_p$    | $k$     |
| $kg/m^3$                                       | $Pa.s$    | $J/kg/K$ | $W/m/K$ |
| 5  | $10^{-5}$ | 2500     | 0.05    |

Regarding the molten plastic viscosity , it is considered constant and having a value of 1000 Pa.s with a surface tension of 0.04 N/m (Agrawal, 2005; Lertwimolnun and Vergnes, 2004). In addition, the kinetic model validated in **section 4.2.1** is used and inserted in the mass source equation (**Eq. 2-43**) to model the mass transfer rate from molten plastic to vapor phase. Moreover, molten plastic density and thermal conductivity are taken as constants and have respectively the values  $900 kg/m^3$  and  $0.17 W/K.m$ . The heat capacity is taken as function of temperature (**Figure 4-21**) to model the latent cracking phenomenon (**section 4.3**).

After setting all the parameters and the equations with the boundary conditions (**section 2.5.3**), the simulation study is launched for PP pyrolysis inside the semi-batch reactor using 40 % of the maximum heating power. The profiles presented in **Figure 4-28** show the temperature profile (for all of the reactor except plastic inside) and conversion (molten plastic and by-product gas) at different specific instants; the empty part of the reactor is assumed to be filled with pyrolysis vapors at the beginning of the process. From the simulation results, pyrolysis process starts at 1520 s almost at the same time as the experimental one (at 1550 s), where the bed of the reactor in simulation (molten plastic) started to decrease. This indicates that the energy diffusion inside the reactor (especially at the wall and in molten plastic) and the implemented kinetic model are validated and describe the experimental process during heating, melting, and start of cracking. Moreover, concerning the amount of pyrolytic oil that left the reactor : in the simulation results (**Figure 4-28**) about 300 g of molten plastic are pyrolyzed during 8.3 minutes (from 1550 to 2050 s). However, recalling the experimental results (**Figure 4-25**), only 10 g of oil have been recovered, which is due to the impact of condensation inside the reactor as has been illustrate previously in **section 4.4.1**. The condensation process circulates the heavy hydrocarbons inside the reactor and

prevents them from leaving directly the reactor; where the secondary cracking is also occurring. However, in this simulation results (Figure 4-28), the condensation process is not modelled. Thus the condensation process affects very well the comparison of the plastic bed reduction speed over time between the simulated and experimental results.

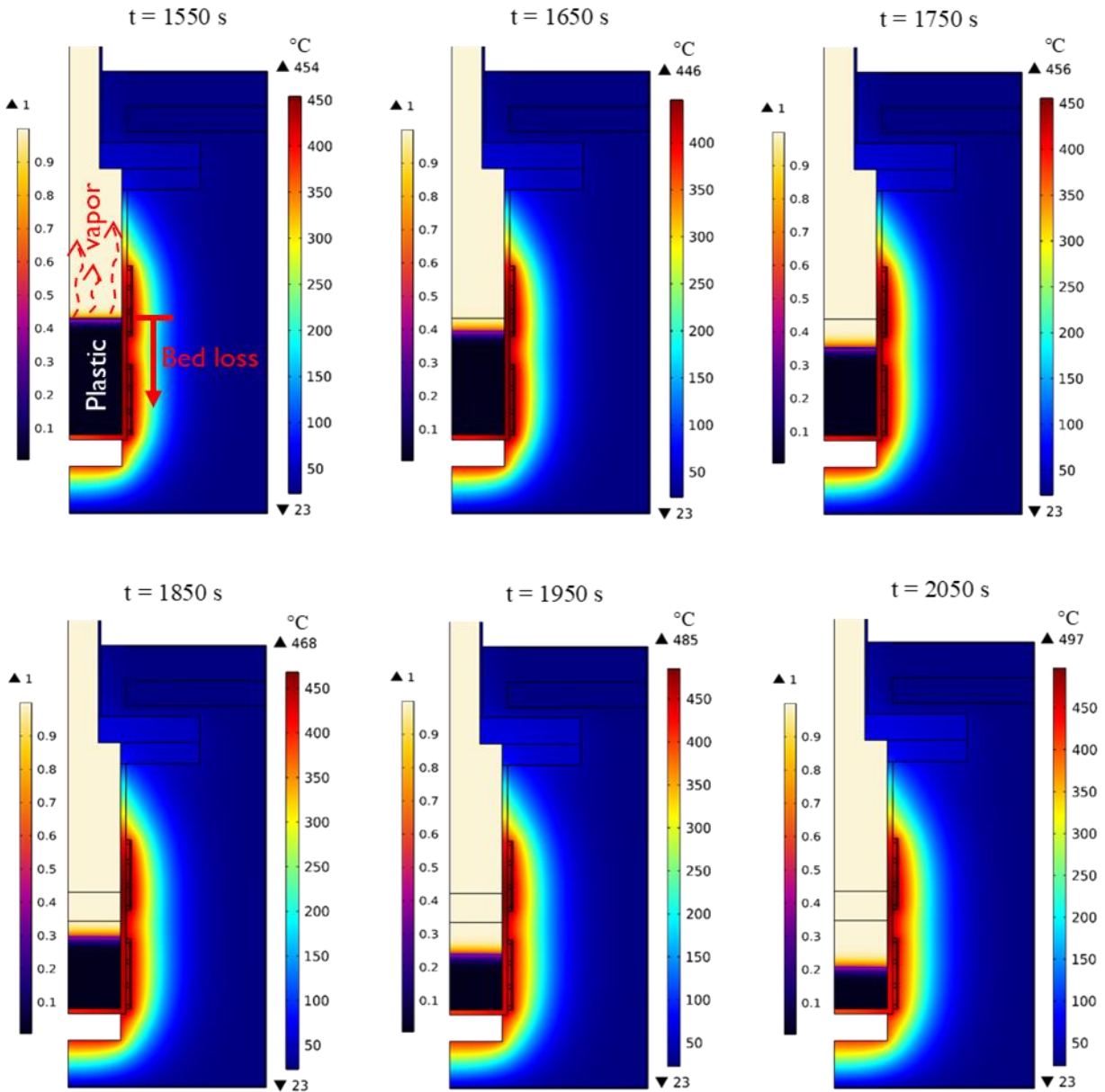
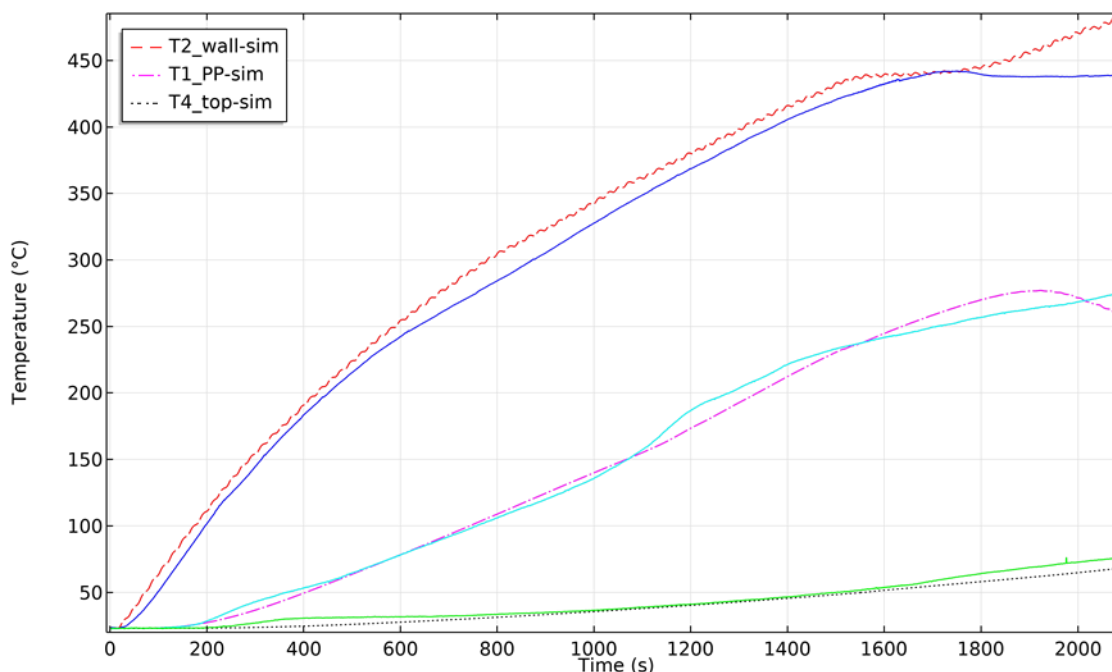


Figure 4-28 : Simulated results, surface temperature and pyrolysis conversion for PP pyrolysis at 600 W heating power, without modelling the condensation process.

Figure 4-29 illustrates the experimental and simulated temperature profiles for T<sub>1</sub>, T<sub>2</sub>, and T<sub>4</sub>. Regarding melting and heating processes (from 0 to 1550 s) the simulated and experimental results

are in a good agreement (about 7 % average relative error), as expected, since heating and melting process for PP and HDPE inside the semi-batch reactor are modelled and validated before in the previous chapter (Chapter Three **section** 3.4.2.2). Then, as the cracking process starts at  $t = 1550$  s, the simulated wall temperature  $T_{2\text{-sim}}$  aligns with the experimental one and stabilizes at  $440$  °C till  $t = 1750$  s, which indicates that the simulated heat absorption due to the pyrolysis process is the same as the experimental one. On the other hand,  $T_2$  simulated starts to increase from  $t = 1750$  s due to the fact that the plastic bed inside the reactor starts to decrease below the wall temperature,  $T_2$ , level (**Figure 4-28**,  $t = 1750$  s), but in reality the bed loss didn't exceeds 10 g of molten plastic as **Figure 4-25** illustrates. In addition, plastic temperature  $T_{1\text{-sim}}$  is in a well agreement with the experimental one with  $\Delta T_{\text{max}} \approx 12$  °C ( $T_{1\text{-sim}} - T_{1\text{-exp}}$ ) between 1550 and 1900 s, then it starts to deviates due to technical disturbance in simulation that will be discussed in the next subsection **4.4.2.2(b)**. Regarding  $T_4$ , the experimental temperature starts to deviate linearly from the simulated one as the cracking process begins (1550 s) to reach  $75$  °C at 2050 s where the  $T_{4\text{-sim}}$  is  $65$  °C, because the condensation process isn't taken into consideration in the model. This difference continues to increase with time even though the heat transfer at the top vicinity (in simulation) is enhanced with the natural convection of the hot arising pyrolysis vapors, with an average convection heat transfer coefficient of  $10$  W/K/m<sup>2</sup>. Moreover, it is difficult to compare the simulated and experimental temperatures unless the condensation process is modelled and the bed drop speed in the simulated and experimental results is the same.



**Figure 4-29** : Simulated results, Temperature profiles ( $T_1$ ,  $T_2$ , and  $T_4$ ), for PP pyrolysis at 600 W heating power, without modelling the condensation process.

Thus, for further interpretation of the results the simulated bed drop of the reactor is compared to the experimental one as **Figure 4-30** shows. **Figure 4-30** illustrates the height of bed drop from the beginning of pyrolysis process till the time at which the controller is activated (almost at  $t = 63$  minutes), because after this time the average heating power decreases due to the controller. The experimental bed drop of the reactor is calculated from the experimental outlet mass of the byproducts (**Figure 4-25**) along with the density and the geometry of the reactor. Whereas, the simulated bed drop is determined graphically from the simulated results (**Figure 4-28**). By calculating the slopes of the curves (**Figure 4-30**), an important result is revealed; the speed of bed loss (equivalent to the speed of the reaction) is almost the same between the simulated (7.1 mm/min) and experimental (6.9 mm/min) results between 57 to 62 minutes where more than 100 g of plastic is pyrolyzed. Knowing that the condensation is very low in this interval of time (57 to 62 minutes where  $T_4$  is higher than  $130^\circ\text{C}$ ) as illustrated in the previous results (**Figure 4-25**) and the pyrolysis process inside the semi-batch reactor is said to be at the steady state stage (review **section 4.4.1**). Therefore, at the steady state stage the speed of reaction is the same between the experimental and simulated results with an average relative error of 3 %. Thus, the kinetic model, all parameters, and whole pyrolysis model is validated and describes well the experimental thermal

pyrolysis of PP inside the semi-batch reactor at the steady state, i.e. when there is no condensation effect.



**Figure 4-30 :** Bed loss comparison between the simulated and experimental results for PP pyrolysis at 600 W heating power, without modelling the condensation process.

For further validation, the second experiment of PP pyrolysis at 750 W heating power is modelled without the effect of condensation where the results are illustrated in **Figure 4-31** below. As displayed by the results (**Figure 4-31**), the steady state phase (i.e. only pyrolysis is occurring) is more extended and about 150 g of PP are cracking and leave the reactor directly without condensation. Thus, the steady state stage (i.e. pyrolysis only) contributes to more than 70 % of the pyrolysis process inside the semi-batch reactor. Moreover, the rate of bed loss determined by simulation, 8.6 mm/min, is almost the same as the experimental bed loss, 7.8 mm/min, at the steady state phase (47 to 52 minutes); with an average relative error of 9 %. Therefore, PP pyrolysis process, at two heating rates (600 and 750 W), is modelled and validated inside the semi-batch reactor at the steady state where the condensation process is negligible.

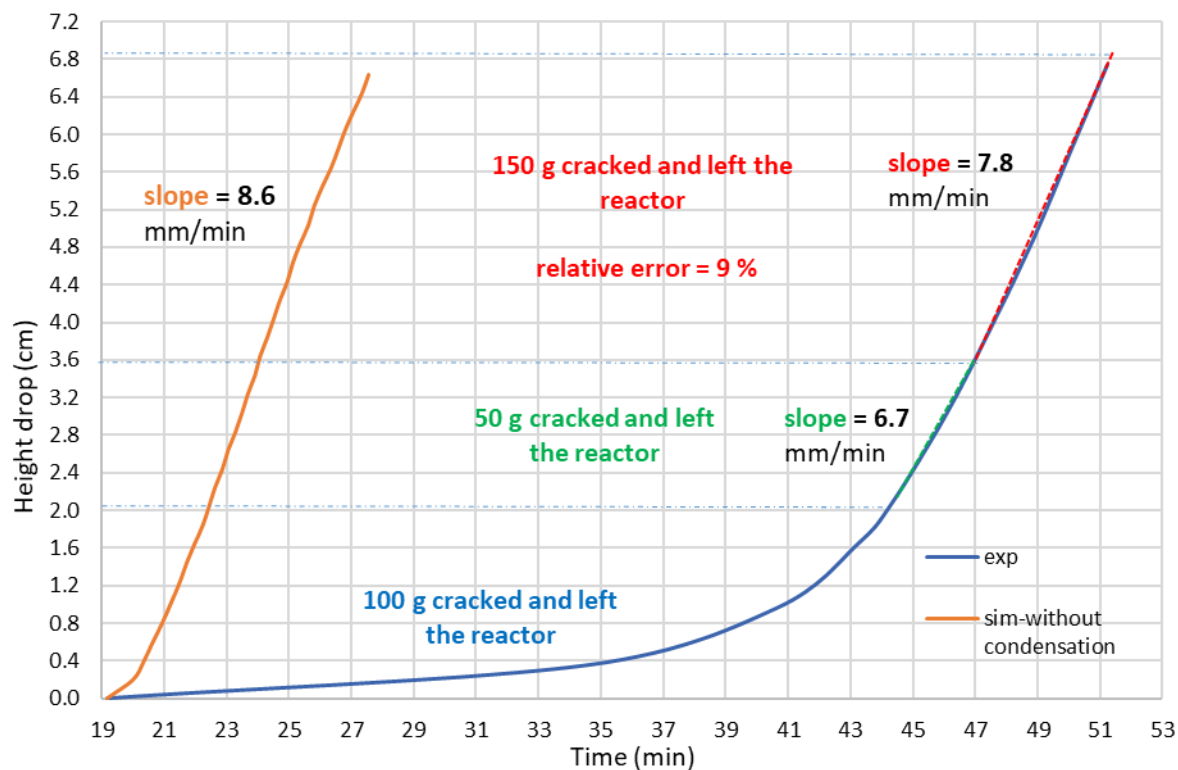


**Figure 4-31** : Bed loss comparison between the simulated and experimental results for PP pyrolysis at 750 W heating power, without modelling the condensation process.

For further validation of the pyrolysis model at the steady state for different type of plastic inside the semi-batch reactor, HDPE pyrolysis experiment (illustrated in **section 4.4.1**) is simulated, where the simulated and experimental results are compared. As a result, the speed of the bed loss in the simulation (9.3 mm/min) is almost the same as that in the experiment (8.9 mm/min) with a relative error of 4 %, (**Figure 4-8A** illustrated in **Appendix: A**). The results are validated for the major and steady state stage of pyrolysis, which contributes to more than 50 % of the process (more than 200 g are pyrolyzed). Therefore, pyrolysis process for PP and HDPE inside the semi-batch reactor are modelled and successfully validated by the experimental results at the steady state stage of the process, i.e. only pyrolysis and without condensation.

#### 4.4.2.2 Modelling condensation process along with the pyrolysis process

After validating the pyrolysis process for PP and HDPE at the steady phase stage (without condensation), the next step is to model the condensation process along with the pyrolysis one and to compare the simulated and experimental results (temperatures and bed loss at the transient state). In this sub-section, the condensation process for PP ( for the first experiment with 600 W heating

power, illustrated in **section 4.4.1**) is modelled in two ways; First method is by modelling the natural reflux of condensation inside the reactor. However, the second way is by implementing a forced reflux into simulation to control the bed loss in the semi-batch reactor.

### a) Modelling natural condensation reflux

Recalling from **Table 2-7**, the latent evaporation enthalpies of the hydrocarbon chains of the pyrolysis products are almost the same with an average value of 350 kJ/kg, however the boiling/condensation temperatures vary from 100 to 390 °C (C<sub>7</sub> to C<sub>24</sub>). Therefore, as a first case study, the pyrolysis vapors in the semi-batch reactor is taken to have  $T_{\text{boil}} = 300$  °C as a condensation temperature and 350 kJ/kg as a condensation enthalpy, considering that the heavy hydrocarbons (C<sub>16</sub> to C<sub>24</sub>) by-products are the main products. Whereas, **Eq. 2-44** is used to model the mass source from vapor to liquid by-product (condensate), with  $f = 0.1$  s as a tuning factor (**ANSYS, 2009**). In addition, **Eq. 2-43** is used as another mass source to model the transformation from liquid hydrocarbon to lighter ones (due to the secondary cracking), assuming that the same kinetic rate is validated for primary and secondary cracking. The results of the first case study (in the violet color, sim-with conden) are demonstrated in **Figure 4-32** below. **Figure 4-32** represents the height drop of the plastic bed (in the semi-batch reactor) according to two simulation results, with and without condensation (two results), in addition to the experimental results of the bed drop. First of all, it is clear that modelling the condensation flattens the rate of bed drop the first 2 minutes (in the transient state), like the experimental results. In addition, the condensation effect in the simulation starts gradually to decrease with time until it becomes negligible. Thus, between 40 and 42 minutes the rate of bed drop (simulation with condensation) restores the same ideal rate 7.1 mm/min (i.e. simulation result without condensation). However, the average rate of bed loss drops from ideal rate (7.1 mm/min) to 4 mm/min in the transient state (from 25 to 40 minutes) due to the effect of modeling condensation in the simulation. Therefore, the simulated results are enhanced at the transient state due to modelling condensation, but still it needs to be more improved.

Therefore, to improve condensation inside the reactor, the condensation model is enhanced by implementing three condensation temperatures;  $T_{\text{cond1}} = 100$  °C,  $T_{\text{cond2}} = 200$  °C, and  $T_{\text{cond3}} = 300$  °C, which represents the average temperatures of the three hydrocarbon groups presented in **Table 2-7**. As **Figure 4-32** illustrates (green line, sim-with conden 2), the rate of bed loss is enhanced

very obviously at the beginning of the transient state (from 25 to 34 minutes), however, the effect of the condensation rapidly diminishes in simulation and the rate of bed loss retains its ideal value 7.1 mm/min rapidly (between 39 and 43 minutes). Thus the condensation in the simulation is working fine so far, but it is rapidly decreasing in contrast to the experimental one, which needs further refinements.

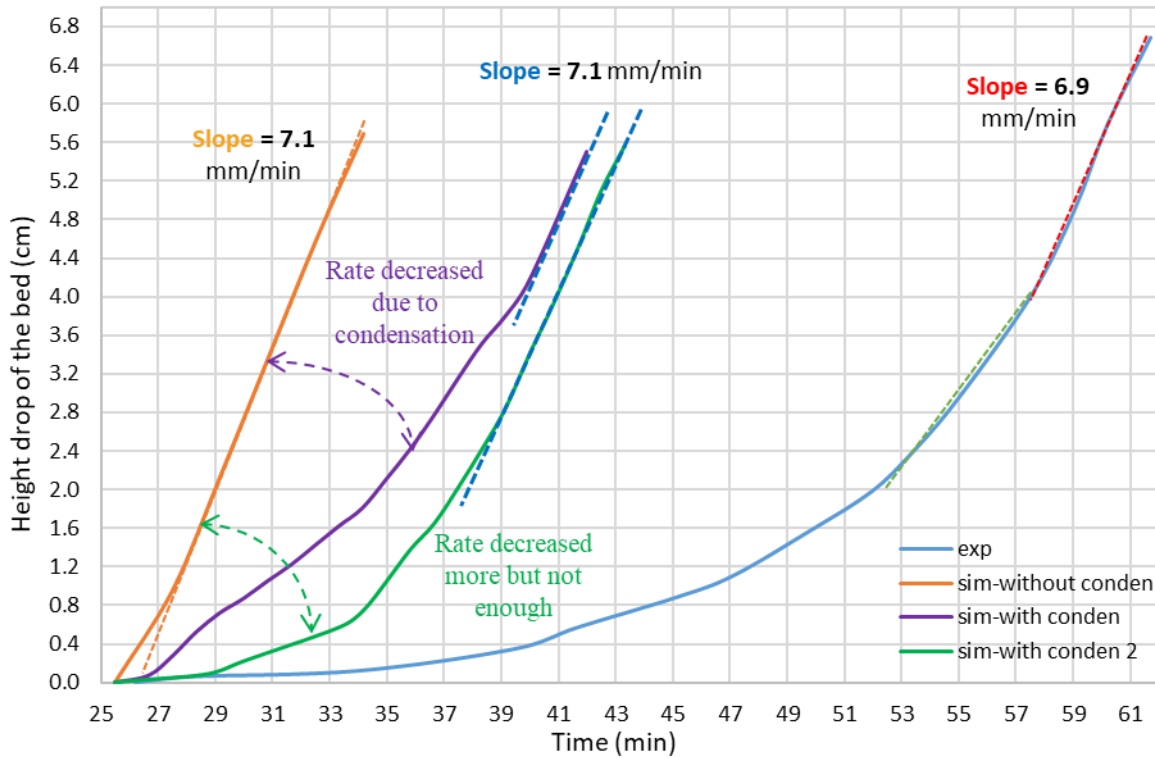


**Figure 4-32 :** Bed loss comparison between the simulated and experimental results for PP pyrolysis at 600 W heating power, without condensation, with modelling the condensation process ( $T_{\text{cond}} = 300\text{ }^{\circ}\text{C}$  and  $\Delta h_{\text{cond}} = 350\text{ kJ/kg}$ ), and with modelling the condensation (2) process ( $T_{\text{cond1}} = 100\text{ }^{\circ}\text{C}$ ,  $T_{\text{cond2}} = 200\text{ }^{\circ}\text{C}$ , and  $T_{\text{cond3}} = 300\text{ }^{\circ}\text{C}$  and  $\Delta h_{\text{cond}} = 350\text{ kJ/kg}$ ).

Further refinement is taken into consideration concerning the condensation temperatures; six equally spaced ( $50\text{ }^{\circ}\text{C}$ ) temperatures from  $100\text{ }^{\circ}\text{C}$  to  $350\text{ }^{\circ}\text{C}$  are set as condensation temperatures. However, the results didn't enhance that much from the previous results (green line, 3 condensation temperatures in **Figure 4-32**), and the condensation effect is again rapidly decreasing with time in simulation study, as shown in **Figure 4-33**. The condensation mass source (**Figure 4-33**) drops slowly and logarithmically at the beginning of the process (from 1550 to 1750 s), then it continues to decrease in a linear pattern to reach  $0.2\text{ g/s}$  at 2400 s; which is much lower than the average cracking mass rate (about  $0.8\text{ g/s}$ ).

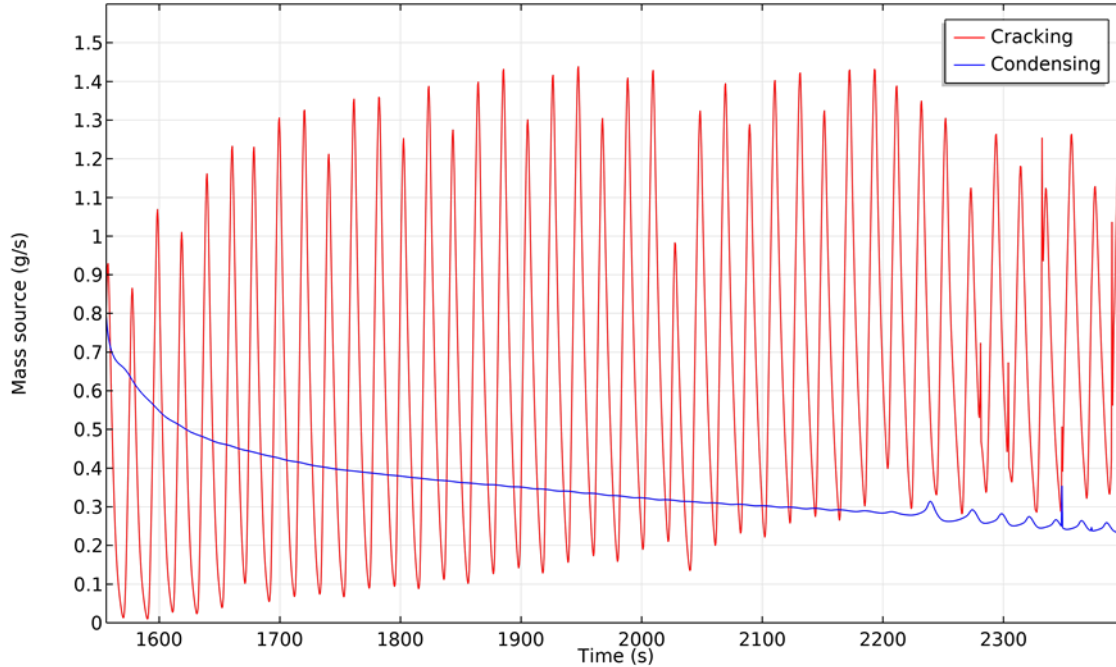


**Figure 4-33 :** Mass source of cracking and condensation for PP pyrolysis at 600 W heating power, with condensation model of six temperatures ((100 °C, 50, 350 °C) and  $\Delta h_{\text{cond}} = 350$  kJ/kg).

This fast drop of condensation process (in simulation) is due to the rise of the vapor temperature inside the reactor and the dominance of the higher condensation temperature 350 °C all over the other condensation temperatures (**Figure 4-34**). In addition, this increase of vapor temperature rises up the wall temperature of the top of the reactor, which affects in decreasing the condensation process as illustrated in previous section **4.4.1**.

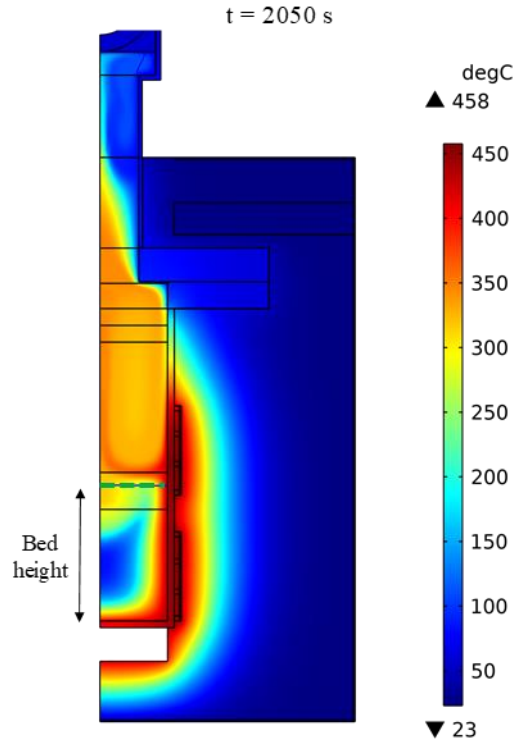


**Figure 4-34 :** Surface temperature result for PP pyrolysis at 600 W heating power, with condensation model of six temperatures ((100 °C, 50, 350 °C) and  $\Delta h_{\text{cond}} = 350 \text{ kJ/kg}$ ).

Moreover, as **Figure 4-34** displays, the higher condensation temperature 350 °C is the dominant over the other five temperatures, where this is due to the fact that the six vapor by-products are taken to have the same density ( $5 \text{ kg/m}^3$ ) and treated as an incompressible fluid with constant density in the simulation. Thus, all the six products are treated as one vapor, which leads to mixing the temperatures and the dominance of the higher one in the simulation. The reason behind that is the limitation in COMSOL software in modelling the condensation phenomenon. Whereas, the densities of the six vapor types, for example, are taken as a constant value equal to  $5 \text{ kg/m}^3$ , because the software only supports two phase flow (incompressible) and not multi-phase flow for each type of by-products vapor.

Nonetheless, experimentally, the case differs; denser hydrocarbon vapor stays down with high temperatures and the lighter one rises up with lower condensation temperatures, which forms a density and temperature stratification in the empty part of the semi-batch reactor (including the top part); which is not the case in the simulation. This stratification inside the reactor permits to decrease the condensation process inside the reactor more slowly and more efficiently than the constrained simulated model. Therefore, as a result, it is impossible to model the total natural

condensation process inside the semi-batch reactor due to the limitation in the incompressible two phase flow model built in COMSOL-Multiphysics.

### b) Implementing forced condensation reflux

Nevertheless, the condensation process can be modelled also as a forced reflux instead of the natural phenomenon model presented before. In this model, a mass source term is added to the simulation to compensate and regulate the bed of the reactor to be almost the same as the experimental one (as shown in **Figure 4-35** and **Figure 4-36**). And, the condensation energy is distributed evenly all over the top part of the reactor to maintain an energy balance in the system. In order to sustain the same bed drop, the mass source (g/s) of condensation (**Figure 4-35**) is set to be 80 % of the mass source of cracking between 1550 to 2400 s (**Figure 4-35**), since 80 % of the pyrolysis by-products are circulating inside the reactor at this period of time (deduced from dividing the ideal bed loss (i.e. simulation without condensation) over the experimental bed loss, **Figure 4-32**). Thus, the simulated and experimental bed loss are similar as shown in **Figure 4-36** with an average error below 3 %.

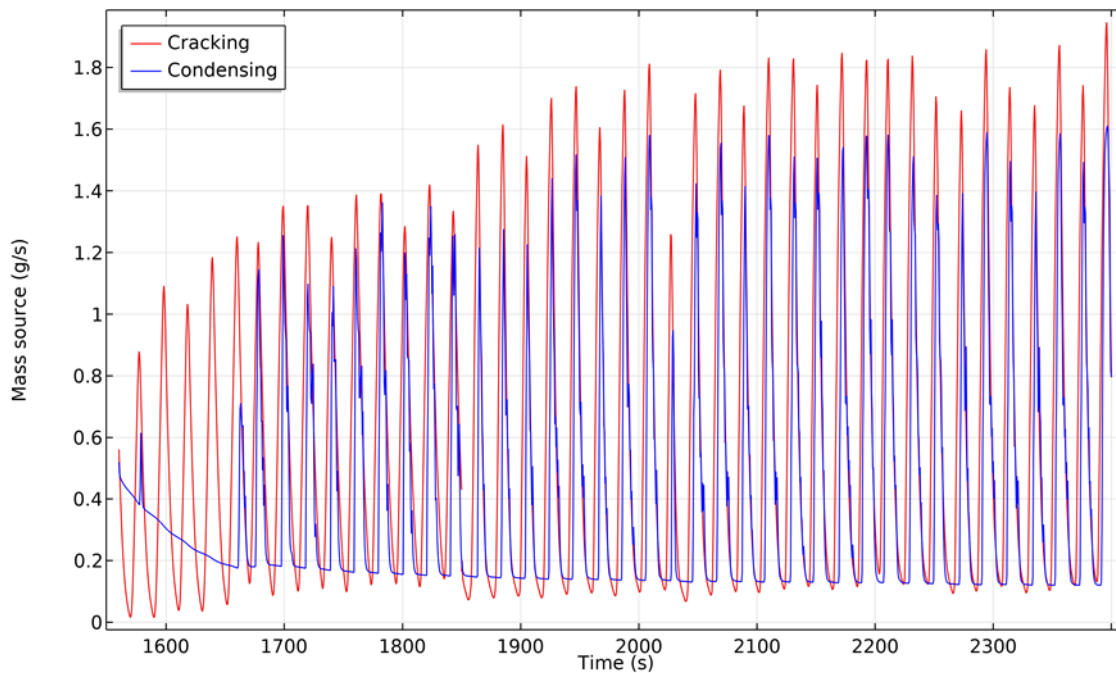


**Figure 4-35** : Mass source of cracking and condensation for PP pyrolysis at 600 W heating power, with a forced condensation reflux.

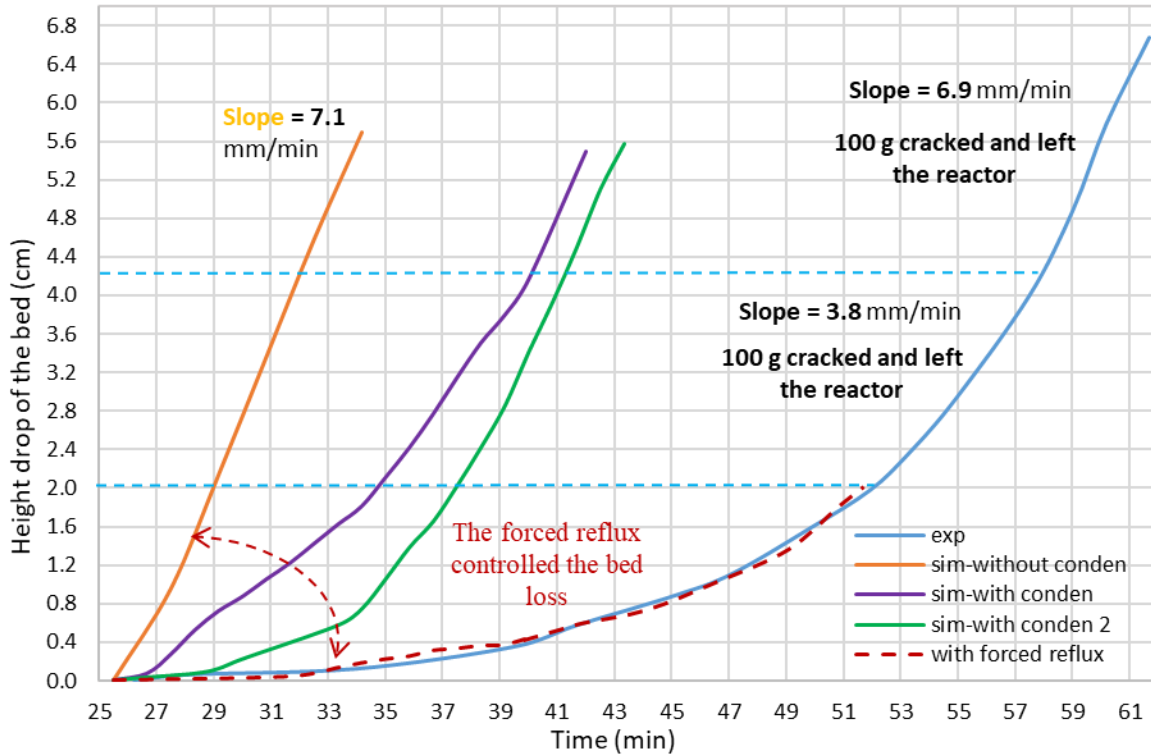


**Figure 4-36 :** Bed loss comparison between the simulated and experimental results for PP pyrolysis at 600 W heating power, with forced condensation reflux.

Therefore, after controlling the simulated bed loss for the transient state (high condensation effect), the simulated and experimental temperatures are compared to validate the heat transfer within the material. **Figure 4-37** shows the PP temperature results with respect to time for the experimental and the simulated ones. First of all,  $T_{2-sim}$  is in a good agreement with the experimental temperature as pyrolysis process proceeds (from 1550 to 2400 s) with an average error below 2 %, which indicates that the energy balance due to the pyrolysis process at the wall vicinity and in the molten plastic is validated. Moreover, the top temperature ( $T_{4-sim}$ ) has the same profile as the experimental one (5 % average relative error), where the condensation energy (given to the top part) increased the top temperature same as the experimental one (**Figure 4-37**). On the other hand, plastic temperature  $T_{1-sim}$  is in a good agreement with the experimental results till 2100 s with an average error below 2 %, whereas after that  $T_{1-sim}$  tends to be steady, in contrast to the experimental data which continue to increase.

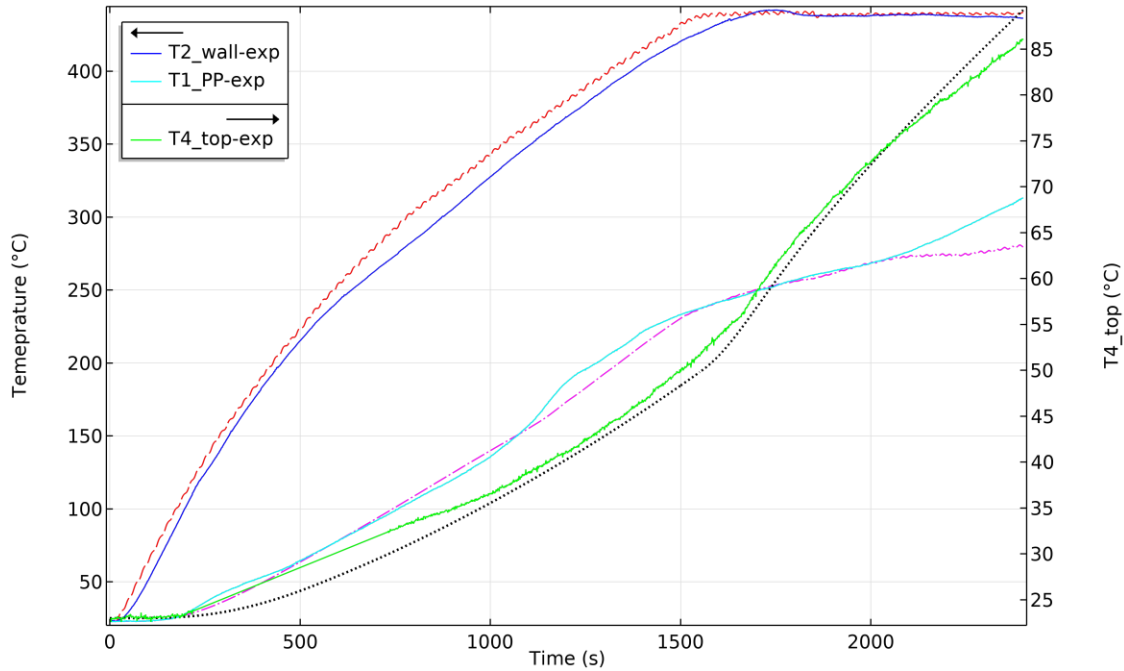


**Figure 4-37 :** Temperature results for PP pyrolysis at 600 W heating power, with forced condensation reflux.

This high error and disturbance in  $T_1$  (more than 10 %), same as happened in **Figure 4-29**, is caused by a light motion of solid plastic in the simulation (about  $10^{-6}$  mm/s average speed) which leads to a slight motion of the temperature profile of molten plastic. Since, molten plastic and solid plastic, in the simulation, are considered as one fluid with different viscosities and having one velocity function, the induced motion of the molten plastic also induces a very weak displacement of the solid plastic; which differs than the real life. This slight displacement holds the temperature profile stand still and shifts it very slightly to the right (**Figure 4-38**), which affects  $T_{1-sim}$  profile. As, illustrated in **Figure 4-38**, the velocity has the same tendency and direction in the solid and molten plastic, however it damps more in the solid phase due to the higher viscosity (more than 10000 Pa.s). The reason behind that, is that in the AHCM method, the two phases (solid and molten) are considered as one fluid instead of two separated phases.

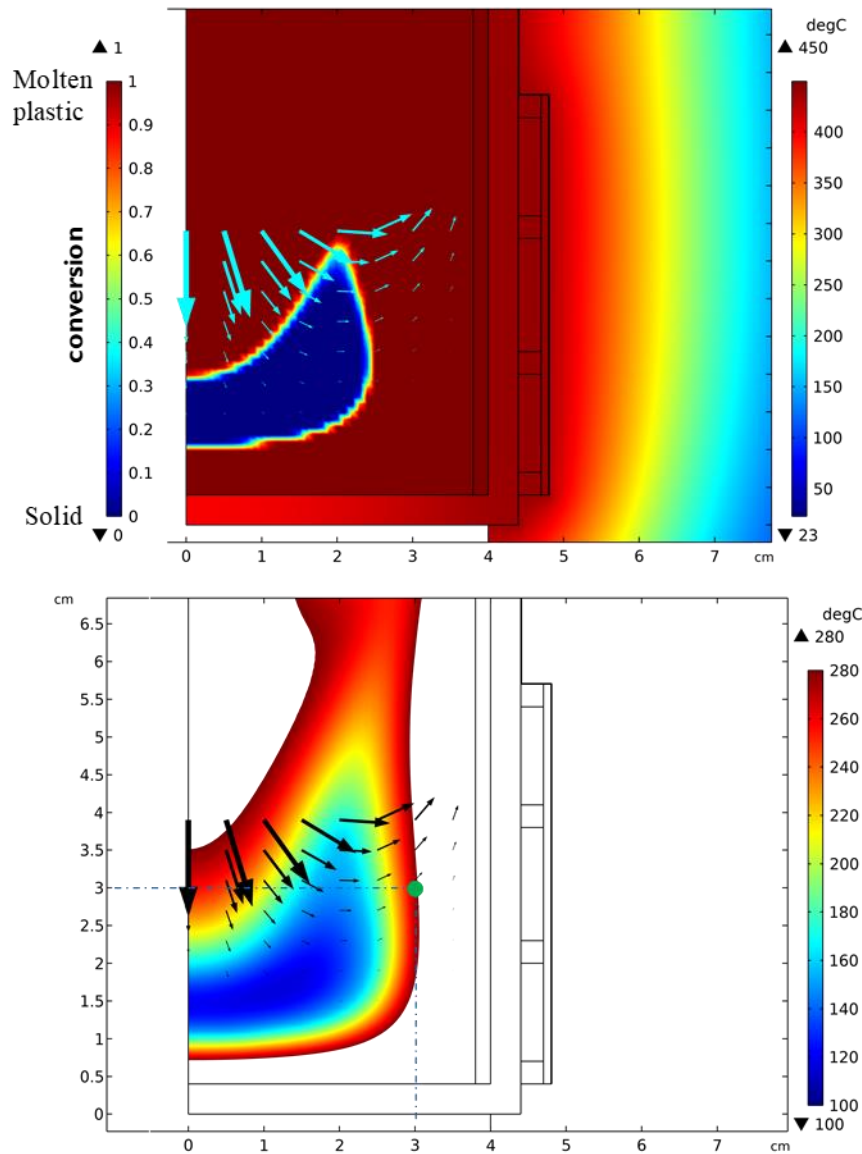


**Figure 4-38 :** Surface profile results (melting conversion and temperature) for PP pyrolysis at 600 W heating power, with forced condensation reflux.

Therefore, even after forcing and regulating the condensation inside the reactor, the plastic temperature ( $T_{1-sim}$ ) can't be further compared to the experimental one due to COMSOL limitation in considering only two phase flow model, which induces technical disturbance in simulation. Therefore, in order to model the condensation process naturally and to eliminate this disturbance in  $T_{1-sim}$ , a multi-phase flow model should be used, i.e. phase for solid, phase for molten plastic, and phase for each pyrolysis vapor group and COMSOL can't be used to model more than two phases flow.

Yet, pyrolysis process is extensively modelled and validated for PP and HDPE inside the semi-batch reactor at the steady state phase (4.4.2.1). But modelling the condensation process along with the pyrolysis one for the transient state needs further enhancement by using another software (like ANSYS) that supports multi-phase flow model. Moreover, the continuous pyrolysis reactor, aimed to be modelled in this research work, will be modelled at the steady state (i.e. condensation doesn't exist). Even though if it is modelled at the transient state, the condensation process is still considered negligible in the continuous reactor because in the counter flow fire tubes reactor, i.e. plastic strictly rises in temperature as it proceeds inside the reactor (**Figure 2-17**). Therefore, the validated steady state model for PP and HDPE is sufficient to model pyrolysis process inside the continuous reactor for low heating rates (below 10 °C/min). And now the model is ready to be upgraded and implemented in the continuous scale to model the continuous reactor, as the next chapter will discuss.

### 4.5 Conclusions

After modelling melting process for PP and HDPE, in the previous chapter, at a milli-particle scale and inside a laboratory scale semi-batch reactor, this chapter continues to illustrate the results of modelling the whole pyrolysis process for PP and HDPE at the two scales.

First, the experimental TGA-DCS results for PP and HDPE pyrolysis at low heating rates (4, 6, 8, and 10 °C/min) are demonstrated and analyzed. In addition, the pyrolysis characteristics (**Table 4-1**) are also determined. Furthermore, a pre-cracking phenomenon is detected, by the TGA-DCS results, to be occurring before the start of mass loss for PP and HDPE pyrolysis.

Furthermore, an extensive kinetic pyrolysis study is performed to determine the best kinetic parameters that model pyrolysis process for PP and HDPE at low heating rates (below 10 °C/min). The results reveal that the best kinetic parameters that model PP pyrolysis at low heating rate are the Avrami-Erofe'Ve kinetic model (A2) with an activation energy of 220 (kJ/mol) and pre-exponential coefficient  $A = 4.15 \times 10^{15} \text{ (min}^{-1}\text{)}$  determined by either KAS or FWO method. Nonetheless, the average relative error between the deduced kinetic model and the experimental TGA results didn't exceed 5 %.

In the same manner, the best deduced kinetic results for HDPE pyrolysis at the heating rates (4, 6, 8, and 10 °C/min) are:  $E = 264 \text{ (kJ/mol)}$  (according to KAS or FWO method), kinetic model  $f(x)$

is also Avrami-Erofe'Ve (A2), and the pre-exponential factor  $A = 8.3 \times 10^{17}$  (1/min). Whereas, the average relative error between the theoretical and experimental conversion is below 6 %.

After that, the deduced kinetic parameters are implemented along with the appropriate equations and boundary conditions into COMSOL-Multiphysics software to model and simulate the whole pyrolysis process for PP and HDPE inside TGA-DSC at milli-particle scale. The cracking model (TGA) is noticed to work very well, as expected, with an average relative error less than 5 %. Moreover, the DSC results are also validated, by modelling the latent cracking phenomenon before and alongside mass cracking; with maximum average relative error below 8 %. Thus, pyrolysis process for PP and HDPE is said to be well modelled at a milli-particle scale.

Finally, the last section (**section 4.4**) discusses the results of modelling pyrolysis for PP and HDPE at a larger scale, in a laboratory-scale semi-batch reactor, at the same heating rate range (below 10 °C/min). First, experimental results, temperatures and mass yield of pyrolytic products at the outlet, for PP and HDPE pyrolysis are displayed and interpreted. As the results show, pyrolysis process inside the semi-batch reactor has two different progressive stages; First stage is the transient state, where there exists condensation process of the vapor by-products inside the semi-batch reactor. In this stage, the condensation process has a great influence on the results (outlet yield and temperatures). On the other hand, the second stage is the steady state where the condensation process is very low and pyrolysis process is dominant inside the reactor.

More, after illustrating and analyzing the experimental results, pyrolysis process for PP and HDPE is modelled inside the semi-batch reactor using the deduced kinetic model validated at particle scale (from **section 4.2**). In addition, a two phase flow model (phase field model imbedded in COMSOL-Multiphysics) is used to simulate the flow of the molten plastic and its pyrolysis by-products vapor inside the reactor.

Two approaches of simulation are performed; First approach is simulating the pyrolysis process without modelling the condensation process inside the reactor, whereas, the second one is modelling the condensation process along with the pyrolysis one. The results of the first approach revealed that the simulated results (the bed height loss inside the reactor) are well validated model by the experimental results at the steady state phase (i.e. without condensation); maximum average relative error below 9 %.

However, modelling the condensation process (i.e. the second approach) is not achieved accurately due to several limitations and difficulties in the two-phase flow model that is used in this study. Thus, different software that supports the multi-phase flow (unrestricted), like ANSYS for instance, can be used instead of COMSOL to overcome these issues.

Yet, to proceed to the next step of modelling the continuous reactor, the validated pyrolysis model at the steady state is sufficient, since condensation process doesn't exist in the continuous reactor (to be designed), due to the counter flow type in the reactor. Where plastic strictly rises in temperature as it proceeds inside the continuous reactor (**Figure 2-17**).

Therefore, pyrolysis process for PP and HDPE inside the semi-batch reactor is modelled and successfully validated by the experimental results for the steady state stage of the process, i.e. without the presence of condensation. And now the model is ready to be upgraded and implemented in the continuous scale as the next chapter will discuss.

## Chapter 5 Modelling continuous plastic pyrolysis reactor

After validating the plastic pyrolysis modelling in laboratory scale semi-batch reactor in Chapter Four, the next step, presented in this chapter, is to utilize all the preceding models and equations to model plastic pyrolysis process (PP and HDPE) in a continuous reactor heated by hot exhaust gases of an 8 kW diesel engine. First the problem statement and the objective will be presented, which is optimizing the geometry (length of the reactor ( $L_r$ ), number of tubes ( $N$ ), and tube diameter ( $d$ )) and the operating conditions (i.e. mass flow rate of plastic ( $\dot{m}_p$ )) of the continuous plastic pyrolysis reactor. Then, the previous established continuous plastic pyrolysis reactor (realized in GEPEA laboratory) will be modelled to check the validity of the simulation. Afterwards, the feasibility of the suggested analytical model of the continuous reactor, by Kassargy (Kassargy, 2018), will be checked by numerical study. Moreover, a large simulation and optimization campaign (at steady and transient states) will be employed to find the best geometry and operating conditions of the modelled reactor.

### 5.1 Description of the reactor and the objectives

The pursued continuous reactor is represented, previously, by **Figure 2-16** and **Figure 2-17**. It is a counter flow concentric multi-tubes reactor; hot gases flow inside the inner tubes (multi-tubes) of diameter  $d$ , whereas plastic flows in the outer tube of a diameter  $D$ . Regarding the initial and boundary conditions, the inlet plastic temperature ( $T_{p,in}$ ) is assumed to be 20 °C, however, the inlet gas temperature ( $T_{g,in}$ ) is 500 °C (measured at the outlet of the diesel engine). In addition, the mass flow of the hot gases is also measured and it is 82 kg/h. On the other hand, there are two other boundary constraints such as the minimum outlet temperature of hot exhaust gas that should be 150 °C to avoid the condensation of water vapor in the gas fluid. Additionally, the second constraint is that the pressure loss inside the inner tubes can't exceed the maximum back pressure sustained at the outlet of the diesel engine, which is  $\Delta p_{max} = 75$  mbar, for good engine performance.

However, some assumptions are taken into consideration, for the sake of simplicity and to prevent confusion in calculation and drawing such as; (1) by applying a very good insulation at the outer tube of the reactor, the reactor can be considered perfectly isolated, and (2) the mentioned diameters ( $d$  and  $D$ ) are actually the inner diameters of the tubes, whereas the thickness (th) of the

tubes is considered to be about 1.7 mm. In addition, the hot exhaust gas can be treated as a hot air since the main composition of the hot gases is air, which contributes to more than 95 % of mass. The constant properties of air determined at the mean temperature (325 °C) are illustrated in **Table 5-1** (Incropera *et al.*, 2007).

**Table 5-1** : Thermo-physical properties of air at average temperature 325 °C.

| $\rho$   | $\mu$              | $C_p$    | $k$     | $\gamma$ | $Pr$ |
|----------|--------------------|----------|---------|----------|------|
| $kg/m^3$ | $Pa.s$             | $J/K/kg$ | $W/K/m$ | -        | -    |
| 0.588    | $3 \times 10^{-5}$ | 1051     | 0.0466  | 1.38     | 0.68 |

where  $\gamma$  is the ratio of specific heats, and  $Pr$  is the Prandtl number of air.

Moreover, the triangular alignment, **Figure 5-1(a)**, is chosen to be the formation of the inner tubes bundle, rather than the rectangular one, because it is more efficient in heat transfer and more compact as geometry, as shown in **Figure 5-1**.

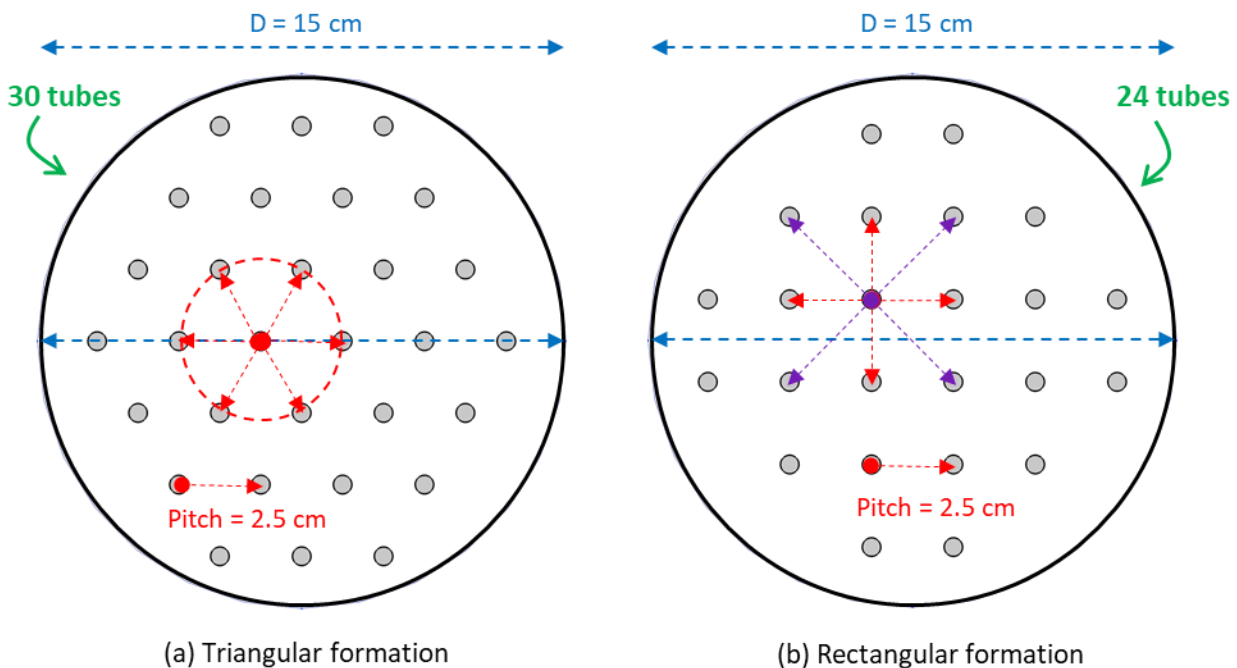


**Figure 5-1** : Triangular (a) and rectangular (b) formations of the inner tubes.

In addition, using same outer diameter ( $D = 15$  cm), 30 tubes fit inside the reactor having the triangular formation **Figure 5-1(a)**, however, 24 tubes for the rectangular formation **Figure 5-1(b)**.

## Modelling continuous plastic pyrolysis reactor

Moreover, in the triangular assembling, each inner tube is surrounded by six tubes separated all by a pitch length, which enhances more the heat transfer in the reactor, Otherwise, in the rectangular formation, each tube is surrounded by four tubes with a pitch length, as shown in **Figure 5-1(b)**.

**Figure 5-2** illustrates a peer view of the three-dimensional plastic pyrolysis reactor according to the triangular formation. Hot air passes inside the inner tubes, however, plastic passes inside the outer tube. The minimum number of elements to discretize such 3D geometry is above 2 or 3 million of a coarse element (mesh), which requires days or even weeks as computational time. However, for the sake of reducing the enormous simulation time of the 3D model, the continuous reactor is represented by a single isolated concentric tube as shown in **Figure 5-3**, which can be also modelled as 2D-axisymetry.

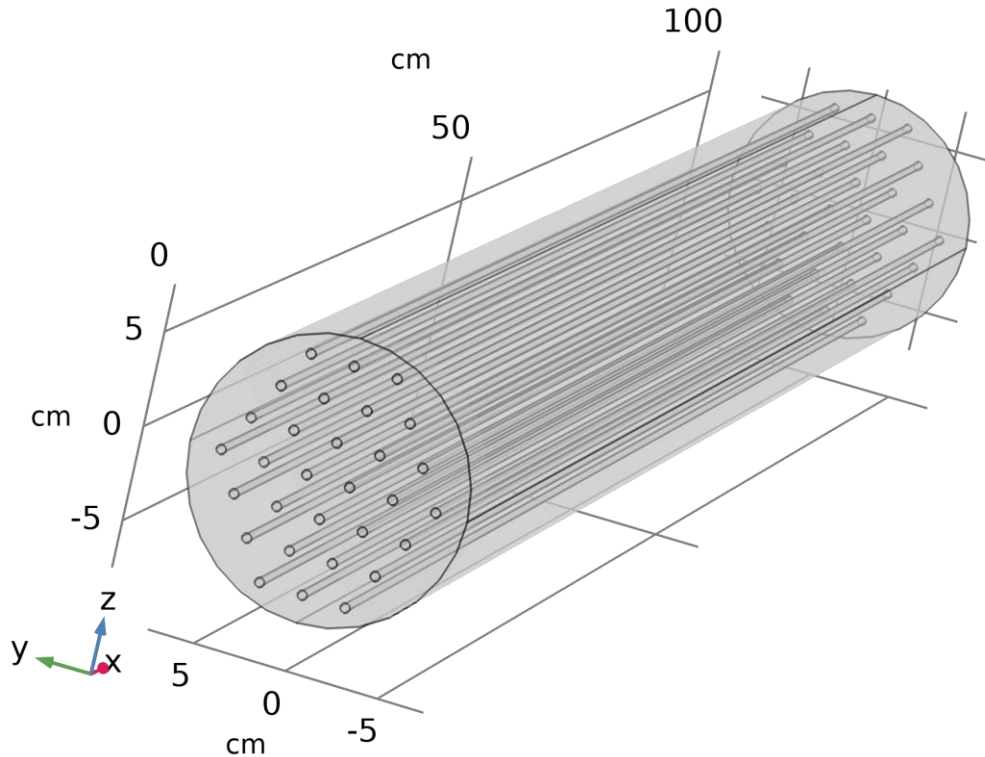


**Figure 5-2** : A 3D preview of the continuous reactor according to the triangular formation.

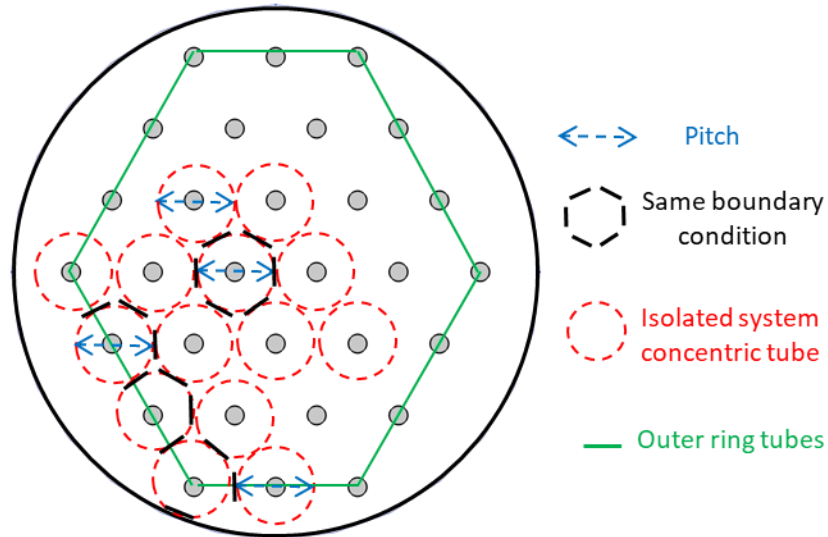


**Figure 5-3 :** Representative system (isolated concentric tube) of the continuous reactor.

This single concentric tube system has an inner diameter  $d$  and an outer diameter equals to the pitch distance  $P$ , as shown **Figure 5-3**. In addition, it is treated as an isolated system because of the uniform boundary conditions at the six surrounding sides, as if each system works alone where each tube is surrounded with another virtual tube of plastic (with pitch diameter). Whereas, the thermal energy diffuses from the inner tube (containing hot gas) to the outer tube that contains plastic material. This, system is repeated for the majority of the tubes, except for the outer ring tubes (marked by the green line) which are surrounded by four equal boundary conditions instead of 6, yet, the summation of the isolated concentric tube system represents more than 80 % of the heat transfer inside the whole reactor, as illustrated by **Figure 5-3**, where the isolated concentric tube system well represents the whole reactor.

Thus, the single concentric tube is an efficient representation of the whole multi-tube continuous reactor, which by modelling it, it provides a very close conception of the whole continuous reactor (geometry and operating conditions) in a relatively short period of time. After that, a 3D model can be constructed and run out, depending on the results of the 2D-axisymetry model, for further refinement and improvement.

The objective of this chapter is to model an efficient and compact continuous plastic pyrolysis using the thermal power that is delivered by the hot exhaust gas from the diesel engine. Compact means that the maximum dimensions of the reactor shouldn't exceed the dimensions of the installed engine (two-cylinder Lister Petter diesel engine of 14.7 kW maximum power) coupled

with a MECCALTE ET20F-200 type electric generator, which are about 1.5 to 2 m length and 60 cm width as shown in **Figure 5-4**.

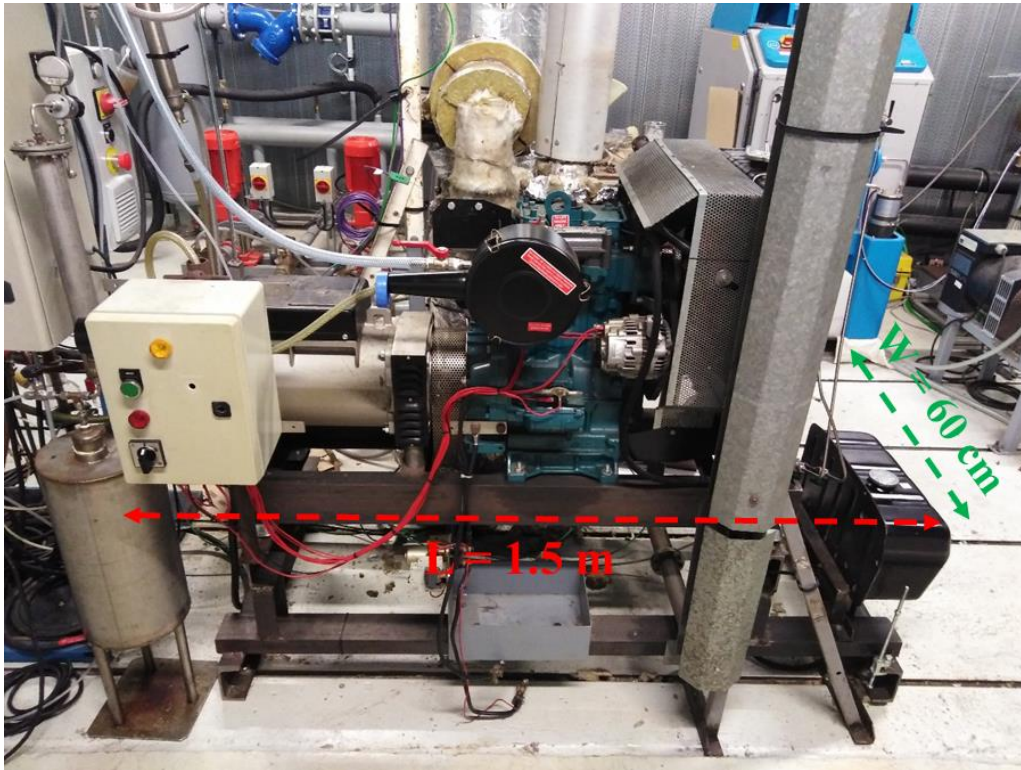


**Figure 5-4** : 14.7 kW two-cylinder Lister Petter diesel engine with an electrical generator MECCALTE ET20F-200 type.

Thus, the continuous reactor, i.e. the concentric tube representative system (illustrated in **Figure 5-3**), will be modelled by utilizing the validated models and equations of the semi-batch reactor (in the previous chapters, **Chapter 3** and **Chapter 4**), as mentioned in **Chapter 2 section 2.6**, to determine the most compatible geometry of the continuous reactor (length of reactor (about 1.5 m), outer tube diameter (maximum of 60 cm), and inner tubes diameter (minimum number of tubes)) at most efficient operating condition (i.e. optimal mass flow rate of plastic  $\dot{m}_p$  and total pyrolysis conversion).

## 5.2 The original continuous reactor installation

The first installation of a plastic continuous reactor coupled with the diesel engine-generator system (established in IMT-Atlantique at GEPEA laboratory) was a counter-flow concentric tube heat exchanger of 34 cm length as shown in **Figure 5-5**, where plastic materials are driven inside

## Modelling continuous plastic pyrolysis reactor

the inner tube, of diameter  $d = 4.6$  cm, by a screw driver. However, the hot exhaust gases enter the outer tube, of diameter  $D = 7.8$  cm, at  $500$  °C and a flow rate of  $82$  kg/h.

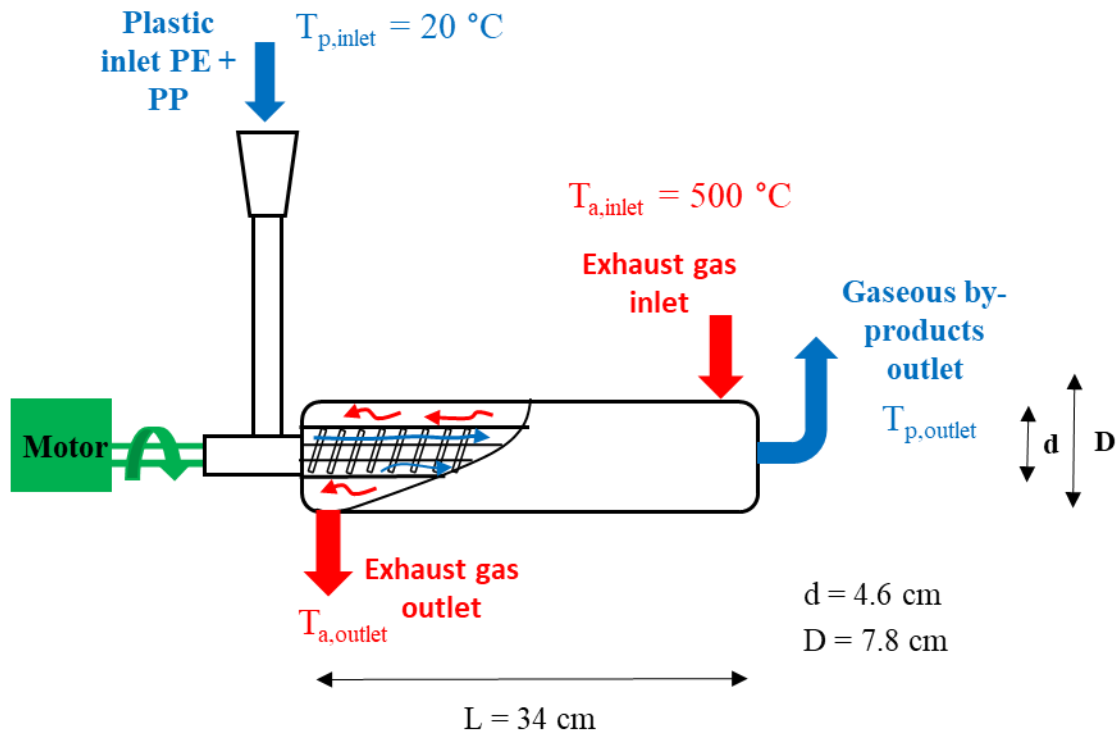


**Figure 5-5 :** Screw kiln counter-flow concentric tube continuous plastic pyrolysis reactor, first installation.

Different experiments are conducted with this configuration at different plastic flow rates ( $0.2$  to  $1$  kg/h) for a mixture of PP and HDPE. But, after experimentation, it revealed that the reactor is inefficient and it needs further enhancement, which will be illustrated later on in this section. Therefore, as a consequence, this thesis study came to fulfill this gap (i.e. the inefficiency of the installed continuous reactor) by conducting a numerical approach, such as plastic pyrolysis modelling and simulation, in order to model and to suggest an efficient and compact continuous plastic pyrolysis reactor for the sake of establishment and experimentation later on. Even more, the maximum experimental heating rate determined from the experimental results of the original installed reactor didn't exceeds  $8$  °C/min, which is the case why this thesis study focuses on slow pyrolysis (below  $10$  °C/min).

In this section, an experiment conducted with the old configuration of the reactor will be modelled and compared with the simulated results for the sake of rough validation and to investigate the feasibility of the numerical model at a first stage (preliminary). During this experiment, the reactor

## Modelling continuous plastic pyrolysis reactor

---

is fed with 200 g of plastic waste mixture (50 % HDPE and 50 % PP) at ambient temperature (20 °C), after heating up the system (empty reactor) for only 5 minutes. Then, after one hour, all the plastic material is pyrolyzed and the process is ended. Whereas during the process, the temperature difference in the hot exhaust gas is about 25 °C (i.e.  $T_{a,outlet} = 475$  °C), however, the temperature of the gaseous by-products ( $T_{p,outlet}$ ) is not measured (plastic outlet are totally pyrolyzed and they are at the gaseous state). Moreover, the maximum potential experimental heating rate (8 °C/min) is computed from the experimental results by **Eq. 5-1** below.

$$\beta = U_p \frac{\Delta T}{\Delta x} \quad \text{Eq. 5-1}$$

where  $\beta$  (°C/min) is the heating rate,  $U_p$  (m/s) is the average inlet velocity of plastic given by **Eq. 5-2**,  $\Delta T$  (°C) is the maximum temperature difference among the plastic side (which is 480 °C), and  $\Delta x$  (m) is the minimum length of which plastic is cracked and heated to 500 °C (which will be taken as  $L/2$ , i.e. 17 cm).

$$U_p = \frac{4\dot{m}_p}{\rho\pi(d^2 - d_s^2)} \quad \text{Eq. 5-2}$$

where  $\dot{m}_p$  is the mass flow rate of plastic equals to 200 g/h,  $\rho$  (925 kg/m<sup>3</sup>) is the average density of the plastic mixture,  $d$  is the diameter of the inner tube (where plastic moves) equals to 4.6 cm, and  $d_s$  (2.3 cm) is the diameter of the shaft of the screw driver.

The reactor is modelled as continuous process and at steady state due to the difficulty of modelling the system with unsteady flow (i.e. the tube is not fully filled or developed with plastic material). This continuous model represents roughly the experimental process, since at steady state, the only power needed to pyrolyze 200 g of plastic mixture is transferred from hot air to the plastic side. Therefore, the validated melting and cracking models illustrated previously in **sections 3.4** and **4.3** are employed, and the continuous reactor is modelled as 2D-axisymerty as shown in **Figure 5-6** below.

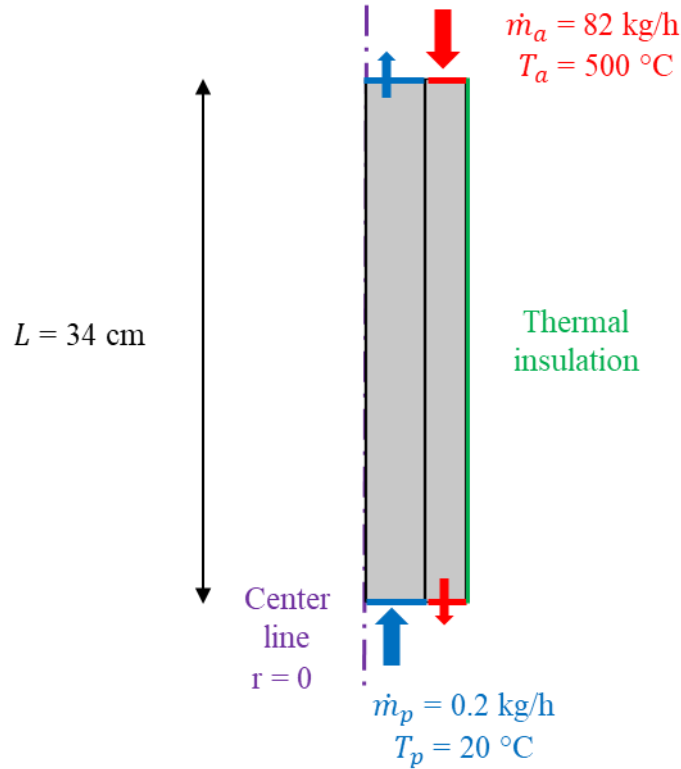


**Figure 5-6** : 2D-axisymmetric scheme model of the original continuous plastic pyrolysis reactor with the boundary conditions.

The mass flow rate of plastic is taken to be 200 g/h, entering at ambient temperature (20 °C), but on the other side, hot gases enter at 500 °C and flow rate of 82 kg/h. The outer surface of the reactor is assumed to be perfectly isolated and the thickness of the tubes is not taken into consideration because of the steady state study, as shown in **Figure 5-6**. Moreover, average thermo-physical properties of plastic mixture are used in the simulation (**Table 2-1**). However, regarding the hot air side, the thermo-physical properties of air are taken to be temperature dependent. In addition, by computing the Reynold's number of the air flow using **Eq. 5-3**, at the average temperature 325 °C (**Table 5-1**), the flow of air is said to be turbulent ( $Re_a = 7800$ ). The turbulent compressible flow of air is modelled with the k- $\epsilon$  model using **Eq. 2-58 – Eq. 2-61** illustrate in **section 2.6**.

$$Re = \frac{\rho U D_h}{\mu} = \frac{\dot{m} D_h}{S \mu} \quad \text{Eq. 5-3}$$

where  $\rho$  (kg/m<sup>3</sup>) is the density,  $U$  (m/s) is the average inlet velocity,  $D_h$  (m) is the hydraulic diameter expressed in **Eq. 5-4**,  $\mu$  (Pa.s) is the dynamic viscosity,  $\dot{m}$  (kg/s) is the mass flow rate, and  $S$  (m<sup>2</sup>) is the cross section surface area of the flow.

$$D_h = 4S/P \quad \text{Eq. 5-4}$$

where  $P$  (m) is the perimeter length, and in case of the annulus tube (outer tube of air)  $D_h = (D - d)$  and for the inner tube  $D_h = d - d_s$  (since there exist a screw shaft inside the tube).

Contrarily, the plastic flow is considered laminar ( $Re_p = 10^{-6}$ , using **Eq. 5-3**) and very slow due to the very low velocity ( $U_p = 4.8 \times 10^{-5}$  m/s) and the high viscosity (about 1000 Pa.s). Therefore, **Eq. 2-27 – Eq. 2-29** are used to model the fluid flow and heat transfer for plastic, however, the three terms ( $Q_{hs}$ ,  $Q_{sink}$ , and  $Q_{cond}$ ) are excluded from **Eq. 2-29**.

Due to the steady state study, the kinetic equation (**Eq. 2-24**) cannot be evaluated because it is time dependent. Thus, the maximum theoretical conversions  $x$  (i.e. at  $\beta = 10$  °C/min) function of temperature for PP and HDPE (**Figure 4-14** and **Figure 4-15**) are implemented into the simulation. In addition, a heat sink term,  $Q_c = \Delta H_c dx/dT$ , is added to the heat capacity of plastic in **Eq. 2-29** (same as the apparent heat capacity method) to account for the cracking phenomenon. Whereas,  $\Delta H_c$  (kJ/kg) is the specific cracking enthalpy at 10 °C/min for PP and HDPE given by **Table 4-1**, and  $dx/dT$  (1/°C) is the variation of the conversion  $x$  with respect to temperature.

**Figure 5-7** illustrates the simulation results; melting, cracking and temperature profiles, at the steady state, according to the first installation of the plastic pyrolysis reactor with a plastic mixture flow rate of 200 g/h. As the results show, the melting process is accomplished after 4 cm of the reactor inlet, however, the cracking process is completed at a length equals to 30 cm, which is higher than the minimum length  $\Delta x$  (17 cm) utilized before to evaluate the maximum potential heating rate. Thus the average heating rate computed from the simulation, according to **Eq. 5-1**, is lower than the maximum one and equal to 3 °C/min.

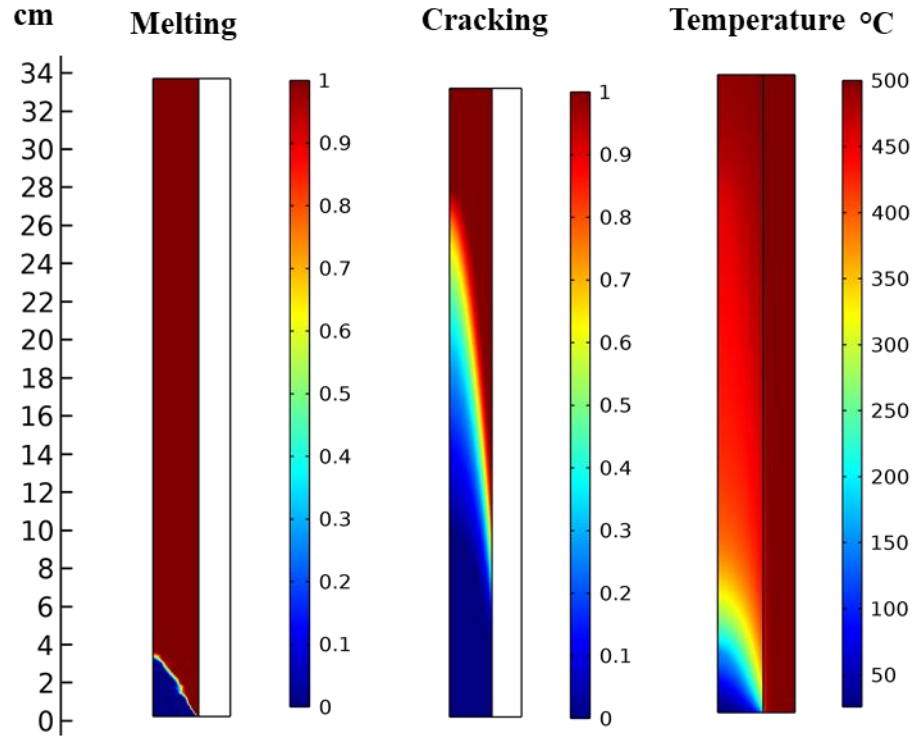


**Figure 5-7 :** Surface simulation results (melting , cracking and temperature) for the original configuration of the continuous reactor at steady state, with plastic mass flow rate of 200 g/h.

Moreover, **Figure 5-7** also illustrates the temperature surface profile, where the outlet average temperatures for plastic and air are 495 and 490 °C, respectively. Air temperature drops 10 °C in the steady state simulation study, which is lower than in the experimental result (which is 25 °C). This difference is logical and expected, since in the steady state process (i.e. in the simulation), different aspects are not taken into consideration such as the transient heating of the screw shaft and the walls of the tubes that totally weighs about 3.5 kg, in addition to the heat loss to the surrounding (due to imperfect insulation) and the effect of mixing plastic due to the screw, which increases the heat transfer. All of these aspects occur in the experiment (because it is transient and not steady) as different heat sinks, which lowers the air temperature further. Yet, the simulation and the experimental results (temperature drop and the completion of cracking) are logical and not too far from each other, thus, the simulation model reveals a good compatibility and feasibility in modeling the experimental process inside the original configuration of the continuous reactor.

Finally, the total heat power transferred ( $Q_t$ ) from the hot air to the plastic at steady state and according to the simulation results is 93 W, on the other hand, the maximum power that could be recovered from the hot exhaust gases is approximately 8.38 kW, given by **Eq. 5-5**.

$$Q_{max} = \dot{m}_a C_p (T_{a,inlet} - T_{a,outlet}) \approx 8.38 \text{ kW} \quad \text{Eq. 5-5}$$

Where  $\dot{m}_a = 82 \text{ kg/h}$  is the mass flow rate of hot exhaust gas,  $C_p$  is the heat capacity of air at average temperature  $325 \text{ }^\circ\text{C}$  from **Table 5-1**,  $T_{a,inlet} = 500 \text{ }^\circ\text{C}$  temperature of gas at the inlet, and  $T_{a,out} = 150 \text{ }^\circ\text{C}$  is the maximum acceptable outlet temperature for the exhaust gas.

Therefore, the thermal effectiveness ( $\zeta$ ) of such installation (original configuration **Figure 5-5**) is very low and have a value of 0.01 given by **Eq. 5-6**. Thus, there still exists a vast margin to benefit from the thermal energy of the hot exhaust gases by enhancing heat transfer and modelling efficient continuous reactor, which will be presented in the proceeding sections.

$$\zeta = Q_t / Q_{max} \quad \text{Eq. 5-6}$$

Where  $Q_t$  (kW) is the total heat power transferred from exhaust gases to pyrolyzed materials, and  $Q_{max}$  (8.38 kW) is the maximum heat power that could be transferred.

### 5.3 Checking the previous suggested geometry of the continuous reactor

After clarifying the need to enhance the first continuous plastic pyrolysis reactor by a new design based on the numerical studies, the first step is to start from the suggested geometry and configuration by a previous work. As mentioned in Chapter 2 **section 2.6**, this work is done (at IMT-Atlantique, GEPEA laboratory) to find the geometry and number of tubes of the continuous reactor using analytical modelling, i.e. using the logarithmic mean temperature difference method (LMTD). The suggested reactor is as follows; 1 m length, 34 inner tubes of diameter  $d = 0.6 \text{ cm}$  (according to the triangular formation), pitch length of 1.8 cm, outer tube diameter  $D = 12.6 \text{ cm}$ , and thermal effectiveness  $\zeta = 1$  (**Kassargy, 2018**).

The maximum plastic mass flow rate ( $\dot{m}_{p,max}$ ) is determined by **Eq. 5-7** at the maximum thermal effectiveness  $\zeta = 1$  (i.e.  $Q_t = Q_{max} = 8.38 \text{ kW}$ ).

$$\dot{m}_{p,max} = \frac{Q_{max}}{\Delta H_p} \quad \text{Eq. 5-7}$$

where  $\Delta H_p$  (J/kg) is the total energy consumed by plastic to undergo total pyrolysis starting from ambient temperature ( $20 \text{ }^\circ\text{C}$ ) till total conversion.  $\Delta H_p$  for PP and HDPE are determined by

integrating the DSC results (i.e. energy absorbed by the plastic particle  $\dot{Q}_a$ , given by **Figure 4-2** and **Figure 4-4**), then by dividing with the initial mass of plastic ( $m_0$ ), as **Eq. 5-8** shows.

$$\Delta H_p = \int_{t_{start}}^{t_{end}} \dot{Q}_a dt / m_0 \quad \text{Eq. 5-8}$$

where  $\dot{Q}_a$  (mW) is the experimental heat flow power given by the DSC results,  $t_{start}$  (s) is the starting time of the pyrolysis process at the ambient temperature (20 °C), and  $t_{end}$  (s) is the end time of the pyrolysis process at the end of the reaction (i.e. at  $T_{end}$ ). The deduced total specific pyrolysis energy values for PP and HDPE are respectively, 1550 and 1500 kJ/kg. Therefore, using **Eq. 5-7**, the maximum mass flow rates for PP and HDPE are approximately 19 and 20 kg/h, respectively. Hence, due to the similarity in the maximum mass flow rate ( $\dot{m}_{p,max}$ ) and the total pyrolysis energy ( $\Delta H_p$ ) for PP and HDPE, one of the two types of plastic will be checked and modelled, which is PP for instance.

Further, as mentioned in **section 5.1**, the 3D reactor is represented by a single concentric tube system inside the reactor (**Figure 5-1**). In addition, the representative single concentric tube is modelled as 2D-axisymmetric with the appropriate geometry, initial conditions, and boundary conditions, as shown in **Figure 5-8**. However, the average inlet velocities for plastic (PP),  $U_p$ , and hot air,  $U_a$ , are evaluated respectively by **Eq. 5-9** and **Eq. 5-10**.

$$U_p = \frac{4\dot{m}_p}{\rho_p \pi (D^2 - Nd^2)} \quad \text{Eq. 5-9}$$

$$U_a = \frac{4\dot{m}_a}{\rho_a \pi N d^2} \quad \text{Eq. 5-10}$$

where  $\dot{m}_p$  (19 kg/h) and  $\dot{m}_a$  (82 kg/h) are the total mass flow rates for plastic and air (hot exhaust gases) inside the global continuous reactor,  $\rho_p$  (900 kg/m<sup>3</sup>) and  $\rho_a$  (0.588 kg/m<sup>3</sup>) are the average densities for plastic and air,  $D$  (12.6 cm) the diameter of the global continuous reactor (**Figure 5-1**),  $N$  (34 tubes) is the number of tubes where hot exhaust gases circulate (fire tubes), and  $d$  (0.6 cm) is their inner diameter of these fire tubes.

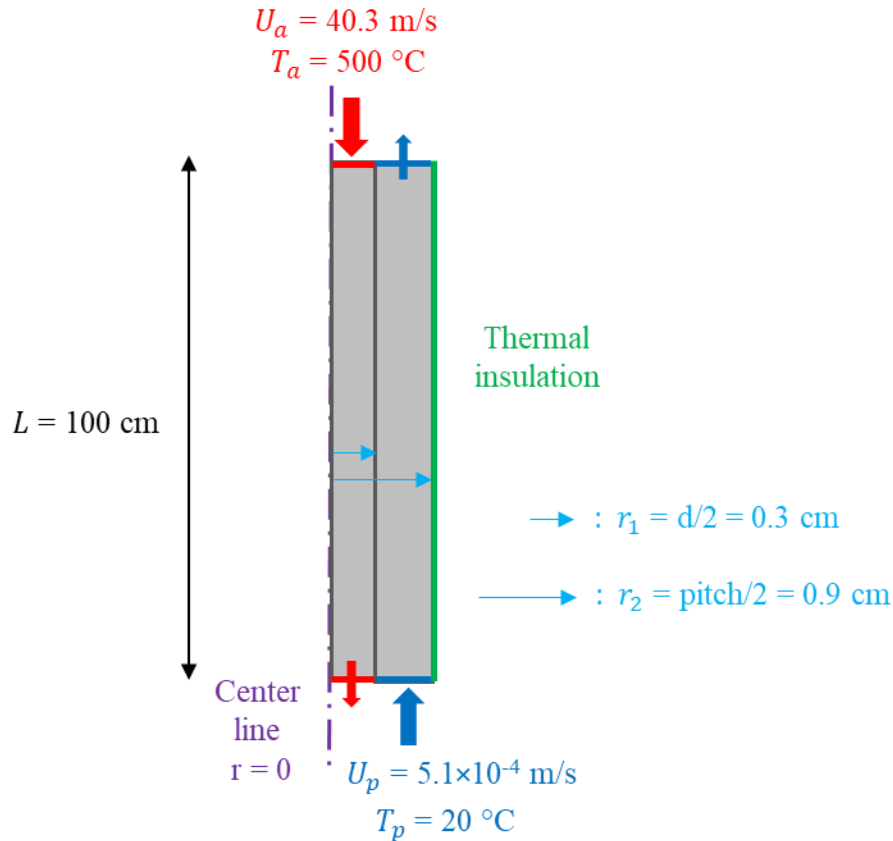


**Figure 5-8** : 2D-axisymmetric scheme of the representative single concentric tube of the continuous plastic pyrolysis reactor, with the proposed geometry and boundary conditions as Kassargy suggested.

Air inside the inner tube (**Figure 5-8**) is modelled as compressible turbulent fluid ( $Re_a = 4739$ , determined by **Eq. 5-3**) using the  $k-\epsilon$  model, same as presented in **section 5.2**. In addition, plastic flow is modelled as a laminar flow ( $Re_p = 5.5 \times 10^{-6}$ , using **Eq. 5-3**) with the same equation mentioned in **section 5.2**. Also, the same heat sink term,  $Q_c = \Delta H_c dx/dT$ , is added to the heat capacity of plastic (PP) in **Eq. 2-29** to model the cracking process, as mentioned in **section 5.2**.

The numerical study is done by COMSOL-Multiphysics software at steady state. And after the solution is converged at minimum element length of 0.02 cm (fine mesh), the simulation results reveal that the average outlet temperature and conversion of plastic reaches 432 °C and 0.22, respectively, as shown in **Figure 5-9**. Moreover, **Figure 5-9** illustrates the simulation results (temperatures and conversions) according to the geometry proposed by Kassargy (1 m length, 34 tubes of diameter 0.6 cm with pitch length of 1.8 cm, and  $\dot{m}_{p,max} = 19 \text{ kg/h}$ ) (**Kassargy, 2018**). First thing to notice from the results (**Figure 5-9**) is that the plastic is not totally pyrolyzed,

however, the results are well promising, knowing that the cracking process is already started at  $L_r = 72$  cm and the average outlet conversion reached 0.22 at  $L_r = 100$  cm, as shown in **Figure 5-9**.

**Figure 5-9** also shows that the melting process is completed at  $L_r = 20$  cm. In addition, the total heat power (determined from the simulation results) transferred from hot exhaust gas to the plastic is  $Q_t = N \times q = 4297$  W (where  $N$  is the number of tubes and  $q = 126.4$  W is the heat power delivered by a single tube) with a thermal effectiveness of  $\zeta = 0.51$ . The thermal effectiveness is much better and enhanced than the first configuration of the continuous reactor ( $Q_t = 93$  W and  $\zeta = 0.01$ , review **section 5.2**). Therefore, further refinement and parametric study can be employed to Kassary's proposition to reach the best compactable and efficient continuous plastic pyrolysis reactor that runs by the 8 kW engine-generator system (discussed in **section 5.1, Figure 5-4**).

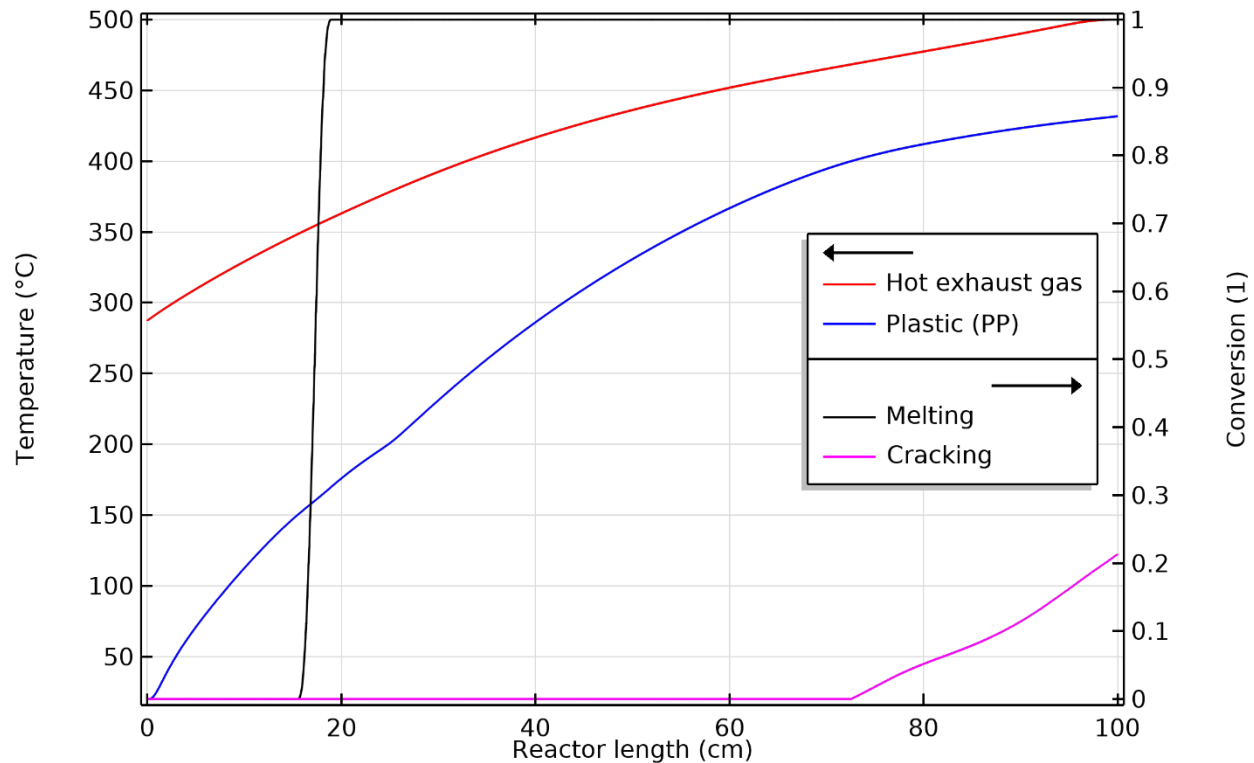


**Figure 5-9** : Simulation results (temperatures and conversions) for the continuous pyrolysis reactor according to Kassary model and geometry (1 m length and 34 tubes of diameter 0.6 cm with pitch length of 1.8 cm, and  $\dot{m}_{p,max} = 19$  kg/h).

Nevertheless, the heat power transferred in a single tube ( $q$ ) can also be approximately evaluated by **Eq. 5-11** and **Eq. 5-12**.

$$q = q_p = \dot{m}_{p,t}(C_p(T_{out} - T_{in}) + \Delta h_m + x_{out}\Delta h_c) \quad \text{Eq. 5-11}$$

$$\dot{m}_{p,t} = \rho_p U_p (\pi/4)(pitch^2 - d^2) \quad \text{Eq. 5-12}$$

where  $q_p$  (W) and  $\dot{m}_{p,t}$  (kg/s) are respectively the energy gained by plastic and the mass flow rate of plastic in a single representative system (one concentric tube),  $C_p$  (2500 J/K/kg) and  $\rho_p$  (900 kg/m<sup>3</sup>) are, respectively, the average heat capacity and density of PP,  $T_{in}$  (20 °C) and  $T_{out}$  (432 °C) are, respectively, the average inlet and outlet temperatures of plastic domain,  $\Delta h_m$  (65 kJ/kg) and  $\Delta h_c$  (420 kJ/kg) are, respectively, the specific melting and cracking enthalpies of PP, and  $x_{out}$  is the average outlet conversion of plastic.

Regarding the heating rate inside the continuous reactor, the maximum heating rate is evaluated at the interface (wall) between air and plastic domains using **Eq. 5-1** from the simulated results, as shown in **Figure 5-10**.

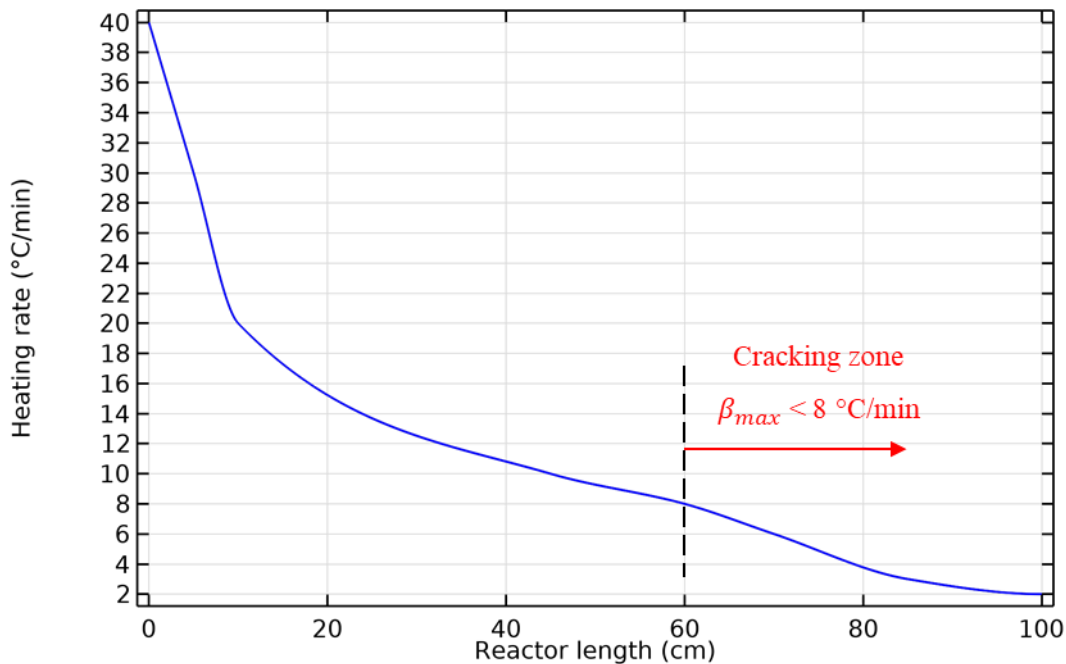


**Figure 5-10** : Maximum heating rate of plastic evaluated at the interface wall between hot exhaust gas and plastic, for PP continuous pyrolysis according to Kassary suggested dimensions.

As shown by **Figure 5-10**, the maximum heating rate of plastic is below 8 °C/min as plastic begins cracking at  $L_r = 60$  cm. On the other hand, for the first 20 cm of the reactor the heating rate is high and drops from 40 to 15 °C/min due to the high temperature difference (between hot air and plastic) at the inlet, which drops from 250 (at  $L_r = 0$ ) to 100 °C (at  $L_r = 20$ ). All in all, the maximum heating

rate of plastic at the cracking process is still within the range that is conducted in this study, which is below 10 °C/min. Therefore, after modelling and checking the feasibility of the counter-flow multi-tubes continuous reactor, the next step is to optimize the reactor by performing a steady state parametric study on the geometry of the reactor (number of tubes  $N$  and tube diameter  $d$ ) and mass flow rate of plastic ( $\dot{m}_p$ ) in order to select the best results for the continuous reactor.

### 5.4 Optimization of the continuous plastic pyrolysis reactor

In this section, a large parametric study for the diameter ( $d$ ) of the inner tubes, the number of tubes ( $N$ ), and the total mass flow rate of plastic ( $\dot{m}_p$ ) will be conducted at steady state in order to select the best efficient continuous plastic pyrolysis reactor. First a steady state parametric study will be conducted for a 2 m length reactor with maximum plastic flow rate  $\dot{m}_{p,max}$  (19 kg/h) by varying the number of tubes ( $N$ ) and the inner tubes diameter ( $d$ ), taking into consideration the laminar and turbulent flows. The length (2 m) is selected based on the preceding results in **section 5.3**, where the length is taken to be two times the length proposed by Kassargy's for the sake of accomplishing total pyrolysis conversion of plastic. Moreover, the 2 m length is still close to the desired length of the reactor which is 1.5 m.

Then, after selecting the best efficient laminar and turbulent models depending on the maximum conversion at the outlet, compactness of the reactor (i.e. number of tubes), and the total heat power transfer  $Q_t$ , another parametric study will be performed for the selected models (laminar and turbulent) with a reactor length of 1.5 m (designed length) by reducing the total mass flow rate of plastic ( $\dot{m}_p$ ) to achieve a total conversion of plastic inside the reactor.

#### 5.4.1 Parametric study for 2 m long reactor with maximum plastic flow rate

This parametric study will focus on varying the number of tubes ( $N$ ) from the  $N_{min} = 4$  (at the maximum acceptable velocity of hot air) to  $N_{max} = 200$  ( $D < 60$  cm) with respect to three selected inner tubes diameters (0.7, 1, and 1.4 cm) for 2 m long continuous reactor and maximum plastic mass flow rate of 19 kg/h. First of all, some basic parameters are redefined as prerequisites to the next coming sub-sections (5.4.1.2 and 5.4.1.3). Then, the steady state parametric study results will be presented; (1) results when the flow of air inside the tubes is said to be laminar, and (2) when the air flow is turbulent.

### 5.4.1.1 Redefining basic model parameters

At the beginning, several parameters will be redefined according to this study such as: (1) the spacing length ( $sp$ ) between the inner tubes is taken to be almost twice the maximum length of the plastic flakes that are fed to the reactor (0.7 cm) and has a value of 1.5 cm, (2) the inner diameter ( $d$ ) of the inner tubes are taken to be the first three Nominal Pipe Sizes (NPS), 1/8, 1/4, and 3/8 (i.e.  $d = 0.7, 1, \text{ and } 1.4$  cm) according to the steel pipes manufactures (Atlas, 2012), (3) the thickness of the tubes is considered constant and taken to be minimum ( $th = 1.7$  mm) found in the stainless steel pipes industry (Atlas, 2012), (4) the pitch length between the inner tubes is redefined using the previous parameters such as,  $pitch = d + 2 \times th + sp$ , and (5) the plastic mass flow rate in a single tube is  $\dot{m}_{p,t} = \dot{m}_p / N$  to assure mass conservation as the  $N$  varies.

Regarding the outer diameter ( $D$ ) of the reactor, for the sake of facilitation and time reduction in fitting the tubes properly every time in a suitable diameter ( $D$ ), an analytical correlation is derived mathematically to estimate the outer diameter ( $D$ ) that fits any number of tubes ( $N$ ) according to the triangular formation (Figure 5-1(a)). The correlation is given by Eq. 5-13 and Eq. 5-14 below.

$$D = pitch (2n + 1) \quad \text{Eq. 5-13}$$

$$nc = \frac{-3 + \sqrt{12N - 3}}{6} \quad \text{Eq. 5-14}$$

where  $nc$  is a positive integer and greater than zero (i.e. rounded up or down),  $N$  is the number of tubes, and  $pitch$  is the pitch length.

Knowing that the designed reactor should be suitable for PP and HDPE pyrolysis, the continuous reactor will be designed according to the limiting type of plastic, which needs more length to crack. Due to the higher total pyrolysis energy (1550 kJ/kg for PP and 1500 kJ/kg) and the lower thermal diffusivity of PP ( $7.55 \times 10^{-8}$  m<sup>2</sup>/s for PP and  $1.68 \times 10^{-7}$  m<sup>2</sup>/s for HDPE, evaluated by Eq. 5-15), PP is said to be the limiting type of plastic. Thus, all the coming numerical studies and modelling will proceed in modelling PP pyrolysis, however, the final designed model of the continuous reactor will be also checked for HDPE pyrolysis for further validation.

$$\phi = k / \rho C_p \quad \text{Eq. 5-15}$$

where  $\phi$  (m<sup>2</sup>/s) is the thermal diffusivity,  $k$  (W/K/m) is the thermal conductivity,  $\rho$  (kg/m<sup>3</sup>) is the density, and  $C_p$  (J/K/kg) is the heat capacity.

### 5.4.1.2 Results for laminar flow

The parametric study is performed at steady state for PP pyrolysis with a 2 m long continuous pyrolysis reactor (counter-flow multi-tubes, **Figure 5-1**) and  $\dot{m}_p = 19$  kg/h. The hot exhaust gas flow ( $Re_a < 2300$ ) and plastic flow ( $Re_p < 10^{-6}$ ) are modelled with **Eq. 2-56** and **Eq. 2-57** due to the laminar flow ( $Re < 2300$ ). Further, the hot exhaust gas is considered as compressible flow in the simulation, whereas, the plastic flow is considered as incompressible fluid having a constant viscosity of 1000 Pa.s. The number of tubes ( $N$ ) will varies from  $N_{L,min}$  (at  $Re_a = 2300$  for air) to  $N_{L,max}$ , where  $N_{L,max}$  is taken to be 200 tubes in this study in order to respect the maximum acceptable outer diameter ( $D_{max} < 60$  cm). Moreover, the diameter of the inner tubes ( $d$ ) will sweeps among three values; 0.7, 1, and 1.4 cm. Regarding the energy equation (**Eq. 2-29**) and the cracking sink term ( $Q_c = \Delta H_c dx/dT$ ), they are also considered in this study to model heat transfer, the same as in the two previous sections (**5.2** and **5.3**). The conversion results  $x$  function of temperature at  $\beta = 10$  °C/min (**Figure 4-13**) that have the highest shift of temperatures (onset, offset, and maximum temperatures) are used in the steady state studies (**sections 5.4.1.2** and **5.4.1.3**) as a safety factor in modelling and designing the continuous reactor (i.e. designing at maximum conditions).

The minimum number of tubes ( $N_{L,min}$  at  $Re_a = 2300$ ) having a laminar flow is determined by **Eq. 5-16** for the three diameters ( $N_{L,min} = 60$  at  $d = 0.7$  cm,  $N_{L,min} = 42$  at  $d = 1$  cm, and  $N_{L,min} = 30$  at  $d = 1.4$  cm).

$$N_{L,min} = \frac{4 \dot{m}_a}{\pi d Re_L \mu} \quad \text{Eq. 5-16}$$

where  $\dot{m}_a$  (82 kg/h) is the total mass flow rate of hot exhaust gas,  $d$  (0.7, 1, 1.4 cm) is the diameter of the inner tubes,  $Re_L = 2300$  is the maximum laminar Reynold's number constant, and  $\mu$  ( $3 \times 10^{-5}$  Pa.s) is the viscosity of air at average temperature 325 °C.

In addition, the pressure drop due to friction inside the fire tubes (hot exhaust gases pipes) is evaluated by **Eq. 5-17** and **Eq. 5-18**. Whereas, the maximum pressure drop ( $\Delta p_f = 675$  Pa) is

## Modelling continuous plastic pyrolysis reactor

determined to be at  $Re_a = 2300$  and  $d = 0.7$  cm, which is still lower than the maximum acceptable back pressure ( $\Delta p_{max} = 7500$  Pa) of the engine.

$$\Delta p_f = \frac{f_t L_r \rho_a U_a^2}{2 d} \quad \text{Eq. 5-17}$$

$$f_t = 64/Re_a \quad \text{Eq. 5-18}$$

where  $\Delta p_f$  (Pa) is the pressure drop in the tubes due to friction,  $f_t$  is the friction coefficient inside the tube,  $L_r = 2$  m is the length of the reactor,  $\rho_a = 0.588$  kg/m<sup>3</sup> is the density of air at average temperature 325 °C,  $U_a$  is the average inlet velocity of air in the tube evaluated by **Eq. 5-10**, and  $d$  (m) is the diameter of the inner tubes.

Hence, after establishing the mesh convergence at a minimum element length of 0.05 cm, the results of the parametric study for varying  $N$  from 30 to 200 tubes and  $d$  from 0.7 to 1.4 cm are presented in **Table 5-2 – Table 5-4**.

**Table 5-2 :** Steady state parametric study for the counter-flow multi-tubes continuous plastic pyrolysis reactor, having 2 m length, inner tube diameter  $d$  of 0.7 cm, and 19 kg/h mass flow rate of PP.

| <b>Laminar flow parametric study, 2 m length, 19 kg/h of PP, and <math>d = 0.7</math> cm</b> |       |        |           |             |             |                       |                 |                 |             |
|--|-------|--------|-----------|-------------|-------------|-----------------------|-----------------|-----------------|-------------|
| $N$  | $q$   | $Q_t$  | $x_{out}$ | $T_{p,out}$ | $T_{a,out}$ | $U_t$                 | $\dot{m}_{p,t}$ | $\dot{m}_{a,t}$ | $D$         |
| (-)  | (W)   | (W)    | (-)       | (°C)        | (°C)        | (W/K/m <sup>2</sup> ) | (kg/h)          | (kg/h)          | (cm)        |
| <b>60</b>  | 100.9 | 6051.2 | 0.17      | 424.6       | 147.3       | 23.2                  | 0.32            | 1.37            | <b>22.9</b> |
| <b>70</b>  | 88.8  | 6215.4 | 0.21      | 429.4       | 139.3       | 21.8                  | 0.27            | 1.17            | <b>22.9</b> |
| <b>80</b>  | 79.4  | 6353.7 | 0.26      | 432.6       | 132.6       | 20.5                  | 0.24            | 1.03            | <b>27.9</b> |
| <b>90</b>  | 71.9  | 6469.5 | 0.29      | 435.1       | 126.9       | 19.4                  | 0.21            | 0.91            | <b>27.9</b> |
| <b>100</b>   | 65.7  | 6566.1 | 0.33      | 437.0       | 122.3       | 18.5                  | 0.19            | 0.82            | <b>27.9</b> |
| <b>110</b>   | 60.4  | 6646.7 | 0.35      | 438.5       | 118.4       | 17.5                  | 0.17            | 0.75            | <b>33.0</b> |
| <b>120</b>   | 56.0  | 6717.1 | 0.38      | 439.7       | 115.1       | 16.7                  | 0.16            | 0.68            | <b>33.0</b> |
| <b>130</b>   | 52.1  | 6777.7 | 0.40      | 440.7       | 112.2       | 15.9                  | 0.15            | 0.63            | <b>33.0</b> |
| <b>140</b>   | 48.8  | 6829.6 | 0.42      | 441.5       | 109.8       | 15.2                  | 0.14            | 0.59            | <b>33.0</b> |
| <b>150</b>   | 45.8  | 6874.5 | 0.43      | 442.2       | 107.6       | 14.6                  | 0.13            | 0.55            | <b>38.1</b> |
| <b>160</b>   | 43.2  | 6914.4 | 0.45      | 442.7       | 105.8       | 14.0                  | 0.12            | 0.51            | <b>38.1</b> |

## Modelling continuous plastic pyrolysis reactor

|            |      |        |      |       |       |      |      |      |             |
|------------|------|--------|------|-------|-------|------|------|------|-------------|
| <b>170</b> | 40.9 | 6949.5 | 0.46 | 443.2 | 104.2 | 13.4 | 0.11 | 0.48 | <b>38.1</b> |
| <b>180</b> | 38.8 | 6978.6 | 0.47 | 443.6 | 102.7 | 12.9 | 0.11 | 0.46 | <b>38.1</b> |
| <b>190</b> | 36.9 | 7006.0 | 0.48 | 444.0 | 101.5 | 12.4 | 0.10 | 0.43 | <b>38.1</b> |
| <b>200</b> | 35.2 | 7030.5 | 0.49 | 444.4 | 100.4 | 12.0 | 0.10 | 0.41 | <b>43.2</b> |

**Table 5-3 :** Steady state parametric study for the counter-flow multi-tubes continuous plastic pyrolysis reactor, having 2 m length, inner tube diameter  $d$  of 1 cm, and 19 kg/h mass flow rate of PP.

| <b>Laminar flow parametric study, 2 m length, 19 kg/h of PP, and <math>d = 1</math> cm</b> |       |        |           |             |             |                       |                 |                 |             |
|--|-------|--------|-----------|-------------|-------------|-----------------------|-----------------|-----------------|-------------|
| $N$  | $q$   | $Q_t$  | $x_{out}$ | $T_{p,out}$ | $T_{a,out}$ | $U_t$                 | $\dot{m}_{p,t}$ | $\dot{m}_{a,t}$ | $D$         |
| (-)  | (W)   | (W)    | (-)       | (°C)        | (°C)        | (W/K/m <sup>2</sup> ) | (kg/h)          | (kg/h)          | (cm)        |
| <b>42</b>  | 136.1 | 5717.1 | 0.09      | 412.7       | 161.6       | 19.31                 | 0.45            | 1.95            | <b>19.9</b> |
| <b>50</b>  | 118.5 | 5924.6 | 0.13      | 420.4       | 151.9       | 18.23                 | 0.38            | 1.64            | <b>25.6</b> |
| <b>60</b>  | 102.2 | 6133.1 | 0.19      | 427.2       | 141.9       | 17.09                 | 0.32            | 1.37            | <b>25.6</b> |
| <b>70</b>  | 89.9  | 6294.9 | 0.24      | 431.3       | 134.1       | 16.02                 | 0.27            | 1.17            | <b>25.6</b> |
| <b>80</b>  | 80.4  | 6430.6 | 0.28      | 434.2       | 127.8       | 15.07                 | 0.24            | 1.03            | <b>31.2</b> |
| <b>90</b>  | 72.7  | 6539.5 | 0.32      | 436.4       | 122.5       | 14.22                 | 0.21            | 0.91            | <b>31.2</b> |
| <b>100</b>   | 66.3  | 6630.6 | 0.35      | 438.2       | 118.2       | 13.46                 | 0.19            | 0.82            | <b>31.2</b> |
| <b>110</b>   | 61.0  | 6708.8 | 0.38      | 439.5       | 114.5       | 12.76                 | 0.17            | 0.75            | <b>36.9</b> |
| <b>120</b>   | 56.5  | 6774.1 | 0.40      | 440.6       | 111.5       | 12.13                 | 0.16            | 0.68            | <b>36.9</b> |
| <b>130</b>   | 52.5  | 6831.2 | 0.42      | 441.4       | 108.9       | 11.54                 | 0.15            | 0.63            | <b>36.9</b> |
| <b>140</b>   | 49.1  | 6879.0 | 0.44      | 442.1       | 106.6       | 11.01                 | 0.14            | 0.59            | <b>36.9</b> |
| <b>150</b>   | 46.1  | 6921.3 | 0.45      | 442.7       | 104.7       | 10.52                 | 0.13            | 0.55            | <b>42.6</b> |
| <b>160</b>   | 43.5  | 6957.6 | 0.47      | 443.3       | 103.1       | 10.07                 | 0.12            | 0.51            | <b>42.6</b> |
| <b>170</b>   | 41.1  | 6989.1 | 0.48      | 443.7       | 101.6       | 9.65                  | 0.11            | 0.48            | <b>42.6</b> |
| <b>180</b>   | 39.0  | 7017.3 | 0.49      | 444.1       | 100.4       | 9.26                  | 0.11            | 0.46            | <b>42.6</b> |
| <b>190</b>   | 37.1  | 7040.2 | 0.50      | 444.4       | 99.2        | 8.90                  | 0.10            | 0.43            | <b>42.6</b> |
| <b>200</b>   | 35.3  | 7062.4 | 0.50      | 444.7       | 98.3        | 8.56                  | 0.10            | 0.41            | <b>48.3</b> |

## Modelling continuous plastic pyrolysis reactor

**Table 5-4 :** Steady state parametric study for the counter-flow multi-tubes continuous plastic pyrolysis reactor, having 2 m length, inner tube diameter  $d$  of 1.4 cm, and 19 kg/h mass flow rate of PP.

| <b>Laminar flow parametric study, 2 m length, 19 kg/h of PP, and <math>d = 1.4</math> cm</b> |       |        |           |             |             |                       |                 |                 |             |
|--|-------|--------|-----------|-------------|-------------|-----------------------|-----------------|-----------------|-------------|
| $N$  | $q$   | $Q_t$  | $x_{out}$ | $T_{p,out}$ | $T_{a,out}$ | $U_t$                 | $\dot{m}_{p,t}$ | $\dot{m}_{a,t}$ | $D$         |
| (-)  | (W)   | (W)    | (-)       | (°C)        | (°C)        | (W/K/m <sup>2</sup> ) | (kg/h)          | (kg/h)          | (cm)        |
| <b>30</b>  | 177.8 | 5335.2 | 0.04      | 392.5       | 177.3       | 15.5                  | 0.63            | 2.73            | <b>22.7</b> |
| <b>40</b>  | 142.9 | 5717.0 | 0.09      | 412.9       | 159.8       | 14.6                  | 0.48            | 2.05            | <b>22.7</b> |
| <b>50</b>  | 119.8 | 5989.2 | 0.15      | 422.9       | 147.2       | 13.6                  | 0.38            | 1.64            | <b>29.2</b> |
| <b>60</b>  | 103.3 | 6196.6 | 0.21      | 429.0       | 137.7       | 12.7                  | 0.32            | 1.37            | <b>29.2</b> |
| <b>70</b>  | 90.8  | 6358.4 | 0.26      | 432.7       | 130.2       | 11.9                  | 0.27            | 1.17            | <b>29.2</b> |
| <b>80</b>  | 81.1  | 6487.1 | 0.30      | 435.4       | 124.1       | 11.2                  | 0.24            | 1.03            | <b>35.6</b> |
| <b>90</b>  | 73.3  | 6594.0 | 0.34      | 437.5       | 119.2       | 10.5                  | 0.21            | 0.91            | <b>35.6</b> |
| <b>100</b>   | 66.8  | 6682.5 | 0.37      | 439.0       | 115.1       | 9.9                   | 0.19            | 0.82            | <b>35.6</b> |
| <b>110</b>   | 61.4  | 6754.5 | 0.39      | 440.2       | 111.7       | 9.4                   | 0.17            | 0.75            | <b>42.1</b> |
| <b>120</b>   | 56.8  | 6818.3 | 0.42      | 441.2       | 108.9       | 8.9                   | 0.16            | 0.68            | <b>42.1</b> |
| <b>130</b>   | 52.9  | 6872.4 | 0.43      | 441.9       | 106.4       | 8.5                   | 0.15            | 0.63            | <b>42.1</b> |
| <b>140</b>   | 49.4  | 6917.9 | 0.45      | 442.6       | 104.3       | 8.1                   | 0.14            | 0.59            | <b>42.1</b> |
| <b>150</b>   | 46.4  | 6956.9 | 0.47      | 443.1       | 102.6       | 7.7                   | 0.13            | 0.55            | <b>48.6</b> |
| <b>160</b>   | 43.7  | 6988.9 | 0.48      | 443.6       | 101.1       | 7.3                   | 0.12            | 0.51            | <b>48.6</b> |
| <b>170</b>   | 41.3  | 7019.9 | 0.49      | 444.0       | 99.8        | 7.0                   | 0.11            | 0.48            | <b>48.6</b> |
| <b>180</b>   | 39.1  | 7045.9 | 0.50      | 444.4       | 98.6        | 6.7                   | 0.11            | 0.46            | <b>48.6</b> |
| <b>190</b>   | 37.2  | 7067.5 | 0.51      | 444.7       | 97.6        | 6.5                   | 0.10            | 0.43            | <b>48.6</b> |
| <b>200</b>   | 35.4  | 7086.3 | 0.51      | 444.9       | 96.8        | 6.2                   | 0.10            | 0.41            | <b>55.1</b> |

Moreover, **Figure 5-11** illustrates the graphical representation of the results, where the total heat transfer  $Q_t$  and the outlet conversion  $x$  are plotted with respect to the number of tubes  $N$  and tube diameter  $d$ .

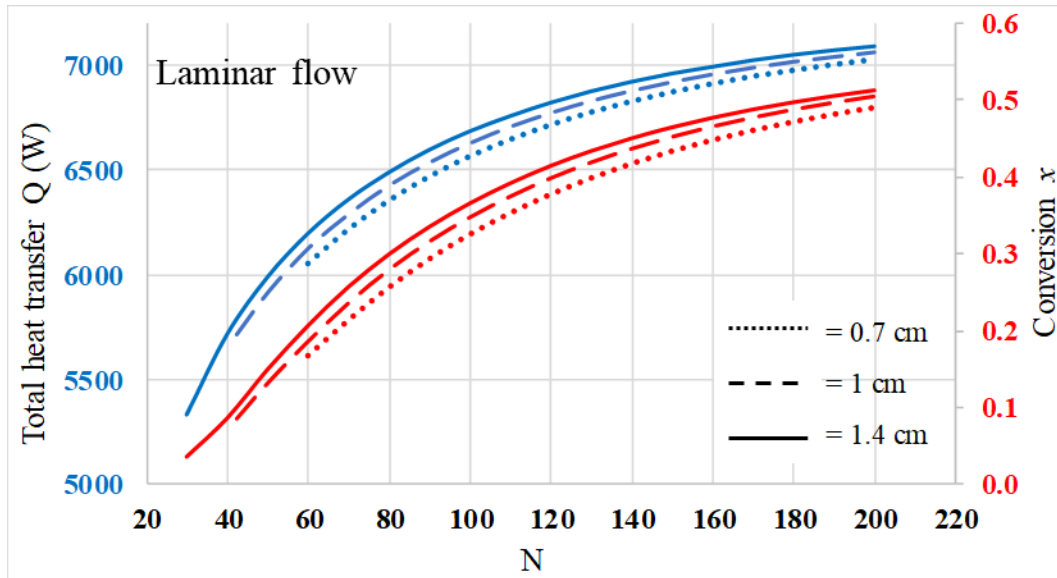


**Figure 5-11** : Steady state parametric study results (total heat transfer and outlet conversion), varying  $N$  from 30 to 200 tubes and  $d$  from 0.7 to 1.4 cm.

First thing to notice from the results is that all the results didn't reach the total pyrolysis conversion inside the reactor ( $x_{out} < 1$ ), even at a high number of tubes such as  $N = 200$ . Moreover, as the tube diameter  $d$  and number of tubes  $N$  increase, the total heat power transferred  $Q_t$  and the average outlet conversion  $x_{out}$  also increases. Thus,  $d = 1.4$  cm is chosen to be the bet diameter, which is also very suitable to prevent fouling issues inside the tubes.

However, for number of tubes higher than 140, the total heat power transferred  $Q_t$  (**Figure 5-11**), starts to increases slowly due to the decrease in the overall heat transfer coefficient, at which the increase in the surface area (i.e. increase of  $N$ ) is no longer beneficial in term of increasing the total heat power transferred. In the same manner, the average outlet conversion,  $x_{out}$ , starts to increase slowly as  $N$  exceeds 160 tubes. Therefore, the best range of the number of tubes is between 80 and 140 tubes, however,  $N = 100$  tubes is selected to be the best choice due to its compactness (fully compact with  $D = 35.6$  cm) and minimum number of tube (easier flow of plastic inside the reactor). Finally, the best deduced geometry for the laminar flow, which has an efficient heat transfer between hot exhaust gas and plastic, is a reactor with 100 tubes and 1.4 cm as a tube diameter.

5.4.1.3 Results for turbulent flow

Regarding the steady state turbulent flow parametric study, the same sweep of tube diameters ( $d$ ) is implemented (from 0.7 to 1.4 cm) for 2 m length and  $\dot{m}_p = 19$  kg/h, however, the maximum turbulent number of tubes  $N_{T,max}$  are evaluated at  $Re_a = 3000$  by **Eq. 5-16**, since between 2300 and 3000 the flow is transient (**Incropera et al., 2007**). The coefficient of friction ( $f_t$ ) in **Eq. 5-17** is determined from the Moody chart given by **Figure 5-12** from the Reynold's number ( $Re_a$ ) and from the relative pipe roughness  $\xi_r = \xi/d$ , where the standard surface roughness ( $\xi$ ) for the structural stainless steel is 0.025 mm (**Incropera et al., 2007**). Therefore, the maximum turbulent number of tubes  $N_{T,max}$  are as follow; 45 tubes for  $d = 0.7$  cm, 32 tubes for  $d = 1$  cm, and 23 tubes for  $d = 1.4$  cm. Moreover, the pressure drop due to the friction,  $\Delta p_f$ , is evaluated by **Eq. 5-17** at  $N_{T,max}$ , where the maximum value is 2100 Pa for  $N_{T,max} = 45$  tubes and  $d = 0.7$  cm, on the other hand, the minimum value is 226 Pa for  $N_{T,max} = 23$  tubes and  $d = 1.4$  cm.

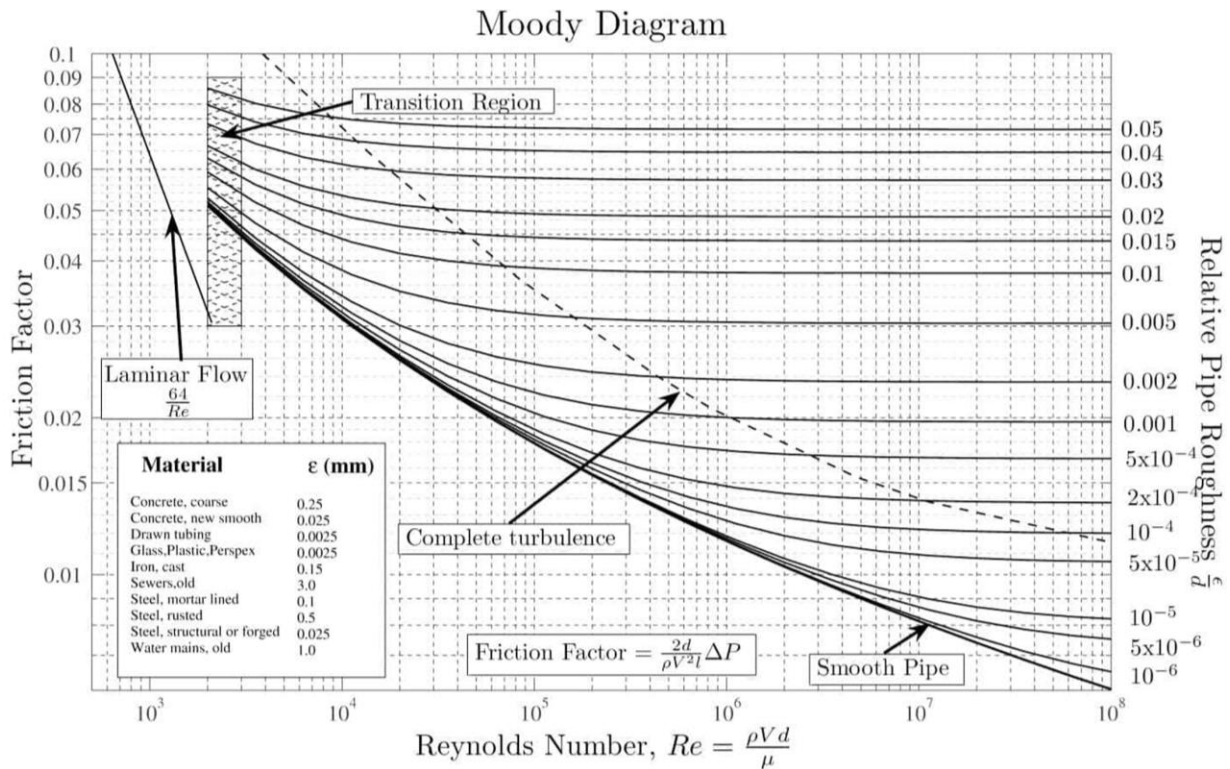


**Figure 5-12** : Moody chart, friction coefficient in pipes versus the Reynold's number and the relative pipe roughness.

Nonetheless, due to the proportionality between the pressure drop and velocity in **Eq. 5-17** and due to the inversely proportional relation between the velocity of air ( $U_a$ ) and the number of tubes

$N$ , there exists a limit for the minimum number of tubes  $N_{T,\min}$  (for the turbulent flow) to avoid exceeding the maximum back pressure ( $\Delta p_{max} = 7500$  Pa) at the outlet of the diesel engine. For that, a safety factor ( $sf = \Delta p_{f,max} / \Delta p_{max}$ ) of 1.5 is taken in this study, at which  $N_{T,\min}$  (at  $\Delta p_{f,max} = 5000$  Pa) is evaluated for the three diameters; the results are 28 tubes for  $d = 0.7$  cm, 10 tubes for  $d = 1$  cm, and 4 tubes for  $d = 1.4$  cm.

Now after specifying the sweep parameters ( $N_{T,\min}$ ,  $N_{T,\max}$ , and  $d$ ), the steady state parametric study is launched for the turbulent flow of hot gases inside the tubes. The plastic flow, the viscosity, and the cracking sink term are the same as in the laminar study discussed in **section 5.4.1.2**. However, the turbulent flow of hot exhaust gases is modelled by the  $k-\varepsilon$  model (**Eq. 2-58 – Eq. 2-61**, illustrated in **section 2.6**). Hence, after conducting the mesh convergence at a minimum element size of 0.02 cm, the steady state results of the turbulent parametric study are illustrated in **Figure 5-13** and **Table 5-5**.

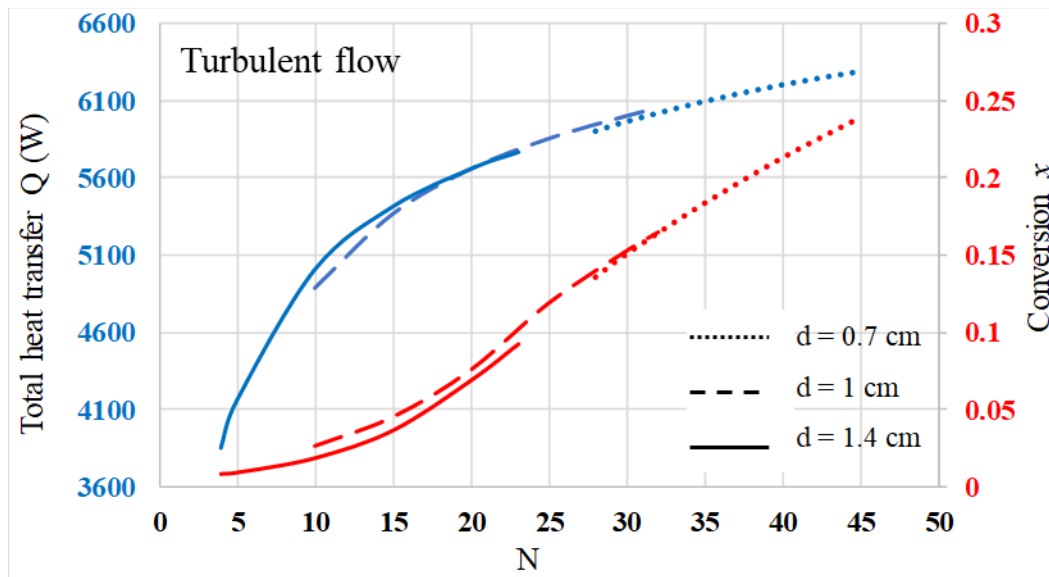


**Figure 5-13** : Steady state parametric study results (total heat transfer and outlet conversion), varying  $N$  from 4 to 45 tubes and  $d$  from 0.7 to 1.4 cm.

The analysis of the results is almost the same as discussed in **section 5.4.1.2** concerning the relation between  $N$  and the other parameters (**Figure 5-13**). However, by comparing the turbulent flow results (**Table 5-5**) with the laminar flow results in **Table 5-2 – Table 5-4**, it is clearly shown that the laminar flow results are much better and more efficient than the turbulent one, where the total

## Modelling continuous plastic pyrolysis reactor

power transferred  $Q_t$  and the average outlet conversion  $x_{out}$  are can reach higher values when the flow of the hot exhaust gas is laminar.

**Table 5-5 :** Steady state turbulent parametric study for the counter-flow multi-tubes continuous plastic pyrolysis reactor, having 2 m length, inner tube diameter d, and 19 kg/h mass flow rate of PP.

| <b>Turbulent flow parametric study, 2 m length, 19 kg/h of PP</b> |                 |                             |                               |                                 |                                 |                             |                               |                               |                 |
|---|-----------------|-----------------------------|-------------------------------|---------------------------------|---------------------------------|-----------------------------|-------------------------------|-------------------------------|-----------------|
| <b><i>N</i></b>   | <b><i>q</i></b> | <b><i>Q<sub>t</sub></i></b> | <b><i>x<sub>out</sub></i></b> | <b><i>T<sub>p,out</sub></i></b> | <b><i>T<sub>a,out</sub></i></b> | <b><i>U<sub>t</sub></i></b> | <b><i>m<sub>p,t</sub></i></b> | <b><i>m<sub>a,t</sub></i></b> | <b><i>D</i></b> |
| (-)   | (W)             | (W)                         | (-)                           | (°C)                            | (°C)                            | (W/K/m <sup>2</sup> )       | (kg/h)                        | (kg/h)                        | (cm)            |
| <b>d = 0.7 cm</b>   |                 |                             |                               |                                 |                                 |                             |                               |                               |                 |
| <b>28</b>   | 211.0           | 5906.5                      | 0.14                          | 418.8                           | 183.1                           | 40.9                        | 0.68                          | 2.93                          | <b>17.8</b>     |
| <b>30</b>   | 199.0           | 5968.7                      | 0.15                          | 421.1                           | 179.9                           | 39.5                        | 0.63                          | 2.73                          | <b>17.8</b>     |
| <b>35</b>   | 174.3           | 6100.1                      | 0.18                          | 425.6                           | 172.5                           | 36.4                        | 0.54                          | 2.34                          | <b>17.8</b>     |
| <b>40</b>   | 155.2           | 6208.2                      | 0.21                          | 428.7                           | 166.8                           | 33.8                        | 0.48                          | 2.05                          | <b>17.8</b>     |
| <b>45</b>   | 139.9           | 6295.7                      | 0.24                          | 430.9                           | 161.8                           | 31.5                        | 0.42                          | 1.82                          | <b>17.8</b>     |
| <b>d = 1 cm</b>   |                 |                             |                               |                                 |                                 |                             |                               |                               |                 |
| <b>10</b>   | 488.6           | 4886.2                      | 0.03                          | 360.1                           | 239.3                           | 44.0                        | 1.90                          | 8.20                          | <b>8.5</b>      |
| <b>15</b>   | 357.7           | 5364.9                      | 0.04                          | 393.1                           | 212.9                           | 39.1                        | 1.27                          | 5.47                          | <b>14.2</b>     |
| <b>20</b>   | 282.7           | 5654.8                      | 0.08                          | 410.0                           | 196.7                           | 35.0                        | 0.95                          | 4.10                          | <b>14.2</b>     |
| <b>25</b>   | 234.0           | 5850.7                      | 0.12                          | 417.6                           | 185.8                           | 31.2                        | 0.76                          | 3.28                          | <b>14.2</b>     |
| <b>30</b>   | 199.9           | 5997.2                      | 0.15                          | 422.9                           | 177.7                           | 28.3                        | 0.63                          | 2.73                          | <b>19.9</b>     |
| <b>32</b>   | 189.0           | 6046.4                      | 0.17                          | 424.5                           | 175.0                           | 27.2                        | 0.59                          | 2.56                          | <b>19.9</b>     |
| <b>d = 1.4 cm</b>   |                 |                             |                               |                                 |                                 |                             |                               |                               |                 |
| <b>4</b>  | 963.5           | 3853.8                      | 0.01                          | 284.7                           | 295.6                           | 44.9                        | 4.75                          | 20.50                         | <b>9.7</b>      |
| <b>5</b>  | 831.3           | 4156.6                      | 0.01                          | 307.5                           | 279.0                           | 42.2                        | 3.80                          | 16.40                         | <b>9.7</b>      |
| <b>10</b>   | 500.8           | 5007.5                      | 0.02                          | 370.4                           | 231.8                           | 34.0                        | 1.90                          | 8.20                          | <b>9.7</b>      |
| <b>15</b>   | 361.0           | 5414.9                      | 0.04                          | 398.2                           | 209.6                           | 29.1                        | 1.27                          | 5.47                          | <b>16.2</b>     |
| <b>20</b>   | 283.0           | 5659.3                      | 0.07                          | 411.4                           | 196.3                           | 25.2                        | 0.95                          | 4.10                          | <b>16.2</b>     |
| <b>23</b>   | 250.7           | 5765.6                      | 0.09                          | 415.6                           | 190.4                           | 23.3                        | 0.83                          | 3.57                          | <b>16.2</b>     |

Therefore, after finding the best geometry ( $N_L = 100$  and  $d = 1.4$  cm), another steady state parametric study will be conducted for the deduced geometry by varying (reducing) the total plastic

## Modelling continuous plastic pyrolysis reactor

mass flow rate ( $\dot{m}_p$ ) to achieve a total conversion at the outlet of the reactor. However, it will be conducted on the most desired reactor length  $L_r = 1.5$  m presented in **section 5.1 (Figure 5-4)**.

### 5.4.2 Parametric study for the best selected models at 1.5 m length reactor

In this sub-section, a steady state parametric study is conducted for the best geometry ( $N = 100$ , and  $d = 1.4$  cm), selected previously in the **sections 5.4.1.2 and 5.4.1.3**, at 1.5 m long reactor by reducing the total plastic mass flow rate ( $\dot{m}_p$ ) of 5 % to reach the total pyrolysis conversion at the outlet of the reactor. The results are shown in **Table 5-6**, where the total conversion is achieved for a mass flow below 8.55 kg/h.

**Table 5-6 :** Steady state parametric study for the counter-flow multi-tubes continuous plastic pyrolysis reactor, having 1.5 m length, tube diameter  $d = 1.4$  cm, and  $\dot{m}_{p,max}$  decreasing with 5 % increment for PP pyrolysis.

| N = 100, d = 1.4 cm, and L = 1.5 m |                             |      |        |             |             |             |                       |                 |                 |
|------------------------------------|-----------------------------|------|--------|-------------|-------------|-------------|-----------------------|-----------------|-----------------|
| $np$                               | $np \times \dot{m}_{p,max}$ | $q$  | $Q_t$  | $x_{out}$   | $T_{p,out}$ | $T_{a,out}$ | $U_t$                 | $\dot{m}_{p,t}$ | $\dot{m}_{a,t}$ |
| (-)                                | (kg/h)                      | (W)  | (W)    | (-)         | (°C)        | (°C)        | (W/K/m <sup>2</sup> ) | (kg/h)          | (kg/h)          |
| <b>1</b>                           | <b>19</b>                   | 64.2 | 6420.8 | <b>0.28</b> | 434.1       | 126.9       | 11.5                  | 0.19            | 0.82            |
| <b>0.95</b>                        | <b>18.05</b>                | 62.4 | 6244.4 | <b>0.33</b> | 437.0       | 135.0       | 11.0                  | 0.18            | 0.82            |
| <b>0.9</b>                         | <b>17.1</b>                 | 60.5 | 6052.1 | <b>0.38</b> | 439.7       | 144.0       | 10.4                  | 0.17            | 0.82            |
| <b>0.85</b>                        | <b>16.15</b>                | 58.5 | 5849.4 | <b>0.44</b> | 442.1       | 153.7       | 9.8                   | 0.16            | 0.82            |
| <b>0.8</b>                         | <b>15.2</b>                 | 56.3 | 5631.4 | <b>0.50</b> | 444.4       | 163.9       | 9.2                   | 0.15            | 0.82            |
| <b>0.75</b>                        | <b>14.25</b>                | 54.0 | 5404.3 | <b>0.56</b> | 446.8       | 174.6       | 8.7                   | 0.14            | 0.82            |
| <b>0.7</b>                         | <b>13.3</b>                 | 51.7 | 5166.4 | <b>0.62</b> | 449.3       | 186.0       | 8.1                   | 0.13            | 0.82            |
| <b>0.65</b>                        | <b>12.35</b>                | 49.2 | 4918.6 | <b>0.69</b> | 452.0       | 197.8       | 7.6                   | 0.12            | 0.82            |
| <b>0.6</b>                         | <b>11.4</b>                 | 46.6 | 4662.8 | <b>0.76</b> | 455.0       | 210.1       | 7.1                   | 0.11            | 0.82            |
| <b>0.55</b>                        | <b>10.45</b>                | 44.0 | 4397.8 | <b>0.84</b> | 458.4       | 223.0       | 6.6                   | 0.10            | 0.82            |
| <b>0.5</b>                         | <b>9.5</b>                  | 41.2 | 4122.7 | <b>0.93</b> | 462.9       | 236.3       | 6.2                   | 0.10            | 0.82            |
| <b>0.45</b>                        | <b>8.55</b>                 | 38.4 | 3837.2 | <b>1.00</b> | 472.2       | 250.3       | 6.2                   | 0.09            | 0.82            |
| <b>0.4</b>                         | <b>7.6</b>                  | 35.2 | 3517.8 | <b>1.00</b> | 492.7       | 265.6       | 8.1                   | 0.08            | 0.82            |
| <b>0.35</b>                        | <b>6.65</b>                 | 31.1 | 3110.2 | <b>1.00</b> | 499.9       | 284.7       | 14.0                  | 0.07            | 0.82            |

## Modelling continuous plastic pyrolysis reactor

Therefore, by taking a margin of safety factor (so that the total pyrolysis conversion is assured to be completed before the outlet of plastic), the best models that fulfill the demand of this thesis study are as follow:  $N = 100$  tubes,  $d = 1.4$  cm,  $\dot{m}_p = 7$  kg/h,  $D = 35.6$  cm, and length 1.5 m with thermal efficiency  $\zeta = 0.4$ .

Moreover, **Figure 5-14** and **Figure 5-15** illustrate the simulation results for the best and efficient continuous plastic pyrolysis model. Plastic pyrolysis conversion starts at  $L_r = 35$  cm and ends at  $L_r = 135$  cm, as **Figure 5-14** shows, whereas the melting process is completed within the first 10 cm of the reactor. Additionally, the heating rate inside the reactor (**Figure 5-15**), for the cracking part, is below  $1$  °C/min; which is in the range that is displayed in this thesis, i.e. less than  $10$  °C/min.

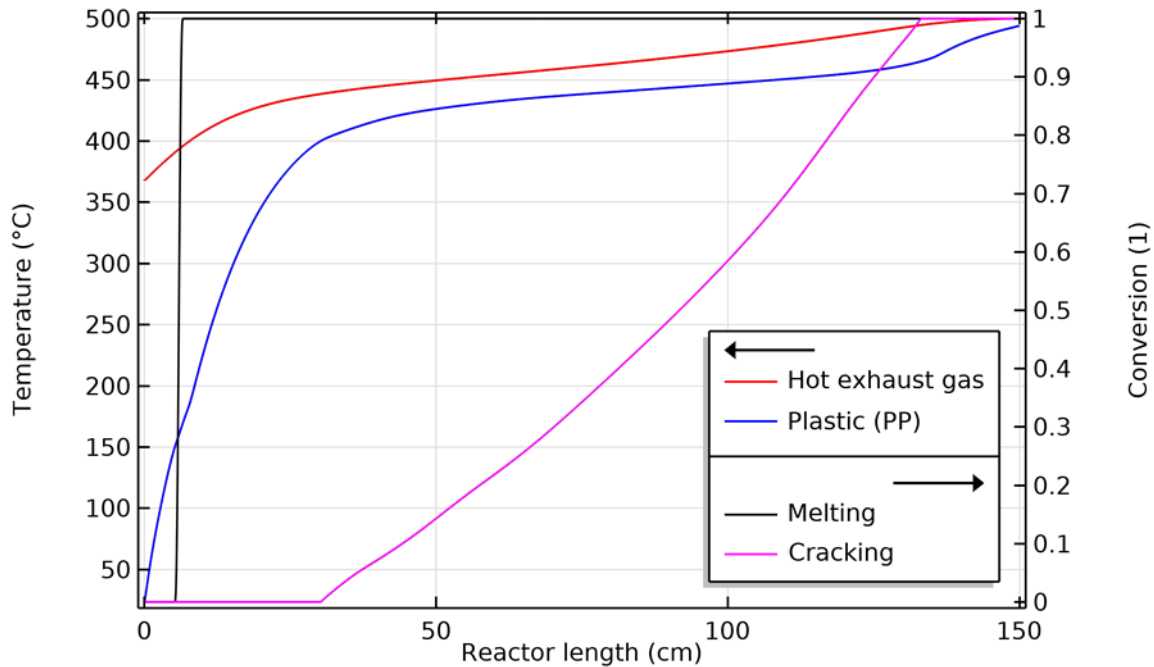


**Figure 5-14** : Average simulation results (temperatures and conversions) for the best model of the continuous pyrolysis reactor (1.5 m length and 100 tubes,  $d = 1.4$  cm, plastic (PP) mass flow rate 7 kg/h).

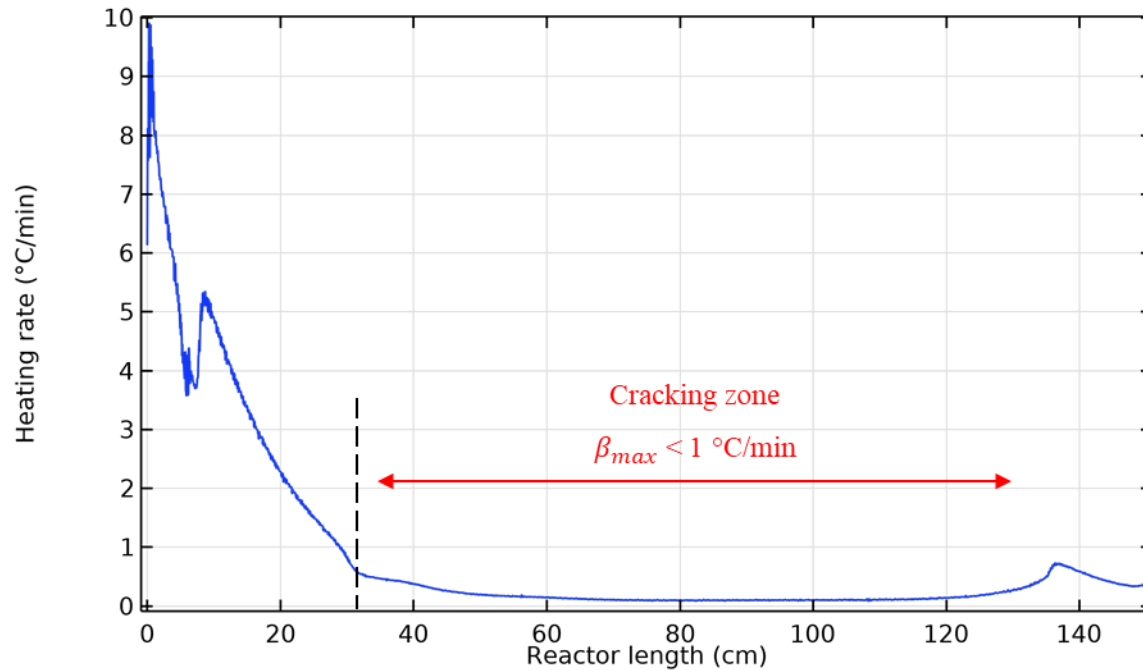


**Figure 5-15** : Average heating rate of plastic with respect to the length of the reactor, for the best model of the continuous pyrolysis reactor (1.5 m length and 100 tubes,  $d = 1.4$  cm, plastic (PP) mass flow rate 7 kg/h).

After finding the best design of the continuous reactor for PP, the same design is checked for the HDPE pyrolysis (1.5 m long, 100 tubes, and  $d = 1.4$  cm) and operation condition ( $\dot{m}_p = 7$  kg/h). Hereby, the results are validated for HDPE pyrolysis and the total pyrolysis conversion is accomplished at  $L_r = 130$  cm with a maximum heating rate 1 °C/min (as illustrated by **Figure 5-1A** and **Figure 5-2A** in **Appendix: A**).

Last and not least, the best selected design of continuous plastic pyrolysis reactor is well modelled for PP and HDPE pyrolysis at steady state, whereas the next step is to simulate the transient phase of this deduced model in order to evaluate the feasibility at starting up of the process.

## 5.5 Transient simulation results of the best models

In this part, a transient study will be conducted for the best deduced model of the continuous reactor (1.5 m long, 100 tubes, and  $d = 1.4$  cm). In addition, the Carreau viscosity model (represented by **Eq. 1-11**, discussed in **section 1.8**) will be used to model the viscosity of molten plastic taking into consideration the following parameters;  $\eta_0 = 1000$  Pa.s,  $\eta_\infty = 1$  Pa.s,  $\lambda = 0.019$  s, and  $n = 0.42$  (Bress and Dowling, 2011). Moreover, the kinetic equation, **Eq. 2-24**, with the deduced kinetic parameters (**section 4.2.1.2**, **Figure 4-13**) are implemented into simulation and solved using

ordinary differential equation solver, which is coupled to the energy equation, **Eq. 2-29** (but without  $Q_{hs}$  and  $Q_{conda}$ ) by the heat sink  $Q_{sink} = \rho_p \Delta h_c dx/dt$ ;  $\rho_p = 900 \text{ kg/m}^3$  and  $\Delta h_c = 420 \text{ kJ/kg}$  from **Table 4-1**.

The transient simulation is done with a full plastic mass flow rate of 7 kg/h. In addition, the reactor (i.e. the representative concentric tube system) is fully loaded with plastic (PP) and is heated from ambient temperature (20 °C). The mesh convergence is stabilized at minimum element length of 0.05 cm. The results reveal that after 2.25 hours (having full load and filled reactor) the total pyrolysis conversion inside the reactor is completed (at  $t = 8100 \text{ s}$ ), as shown in **Figure 5-16**. Moreover, **Figure 5-16** illustrates the average conversion results and heating rate at 2 cm before the outlet of plastic (plastic outlet is at  $L_r = 150 \text{ cm}$ ), i.e. at  $L_r = 148 \text{ cm}$ . As the results show, the heating rate inside the reactor is below 2 °C/min, at the transient state, as the cracking proceeds with respect to time (cracking starts at  $t = 4000 \text{ s}$ ). Even more, the cracking is completed at this position (i.e. at  $L_r = 148 \text{ cm}$ ) at  $t = 8100 \text{ s}$  and the total mass flow rate of plastic (7 kg/h) is said to be totally converted and cracked starting from this instant. Thus, the maximum transient time for the extreme case (i.e. the reactor is fully loaded and operating at the full load of 7 kg/h, and heated from ambient temperature 20 °C) took only 2.25 hours to launch the process successfully at a full load, which is a good and practical time. Therefore, it is recommended to increase linearly the plastic mass flow rate from 1 to 7 kg/h for the first 2 hours only, whereas after that the reactor operates normally at the full load (7 kg/h).

It is worthy to note that, regarding the viscosity of molten plastic inside the reactor, the value of the viscosity didn't change from 1000 Pa.s even by implementing the viscosity model (Carreau model), because the velocity of plastic inside the reactor is very low (below  $10^{-4} \text{ m/s}$ ). Therefore, the shear rate is very weak, and at this case the viscosity of plastic is equal to the viscosity at zero shear rate which is  $\eta_0 = 1000 \text{ Pa.s}$  according to the model. Thus, at higher velocities of plastic flow or injection, it is recommended to use the viscosity models such as Carreau model or Power model (illustrated in **section 1.8**), but for the instance in this study, it is sufficient to use the zero shear rate viscosity  $\eta_0 = 1000 \text{ Pa.s}$ , because of the low velocities of plastic flow.

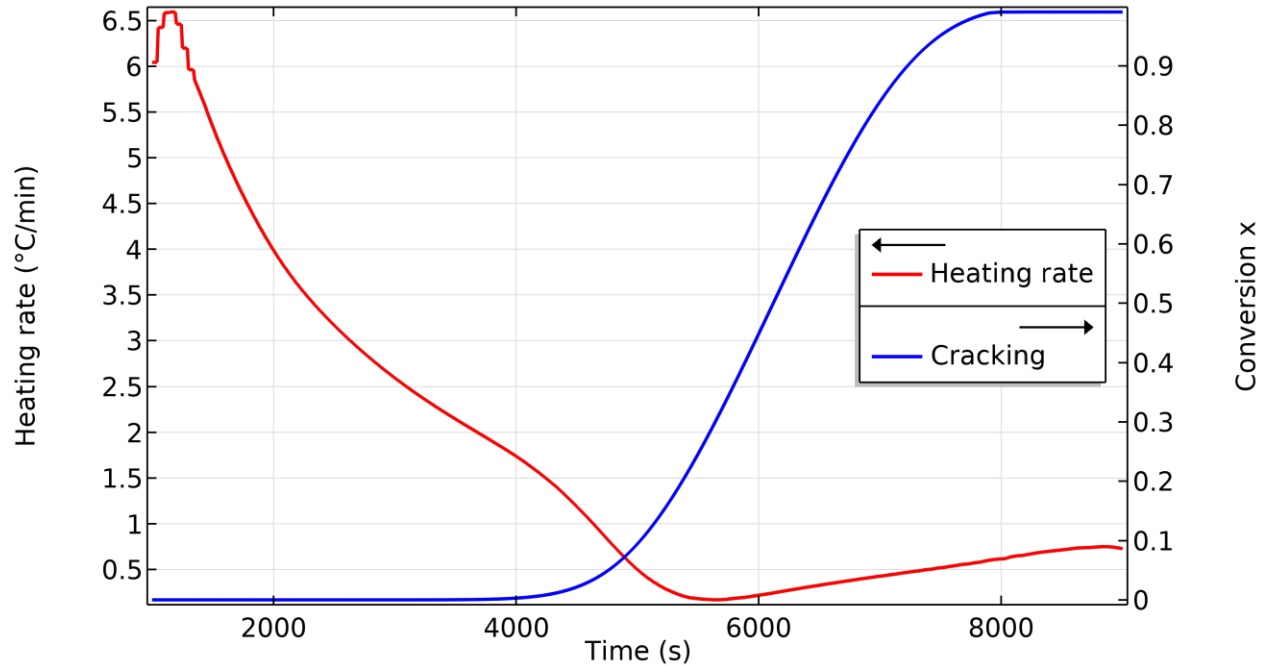


**Figure 5-16 :** Average Transient simulation results (plastic cracking and heating rate) over time at  $L = 148$  cm, for the best deduced model ( $N = 100$ ,  $d = 1.4$  cm, and  $L = 1.5$  m), simulation for fully loaded reactor (with plastic) with total mass flow rate of plastic (7 kg/h) and heated from ambient temperature ( $20$  °C).

Nevertheless, **Figure 5-17** illustrates the conversion evaluated from simulation (i.e. the simulated conversion) and the designing conversion with respect to temperature. The designing conversion is the conversion results at maximum heating rate  $10$  °C/min used in designing the reactor in the previous **sections 5.2 – 5.4**. It is clear from the results (**Figure 5-17**), that the pyrolysis in simulation is occurring at lower temperatures ( $T_{\text{end}} = 415$  °C) than the maximum conversion (design conversion,  $T_{\text{end}} = 460$  °C) due to the low heating rate (below  $2$  °C/min) inside the reactor illustrated in **Figure 5-16** before. This is due to that in the transient study the deduced kinetic rate equation and parameters (**Eq. 2-24** and **Figure 4-13**) are employed into simulation and are solved rather than implementing the conversion results function of temperature at  $\beta = 10$  °C/min evaluated by the kinetic model (**Figure 4-13**).

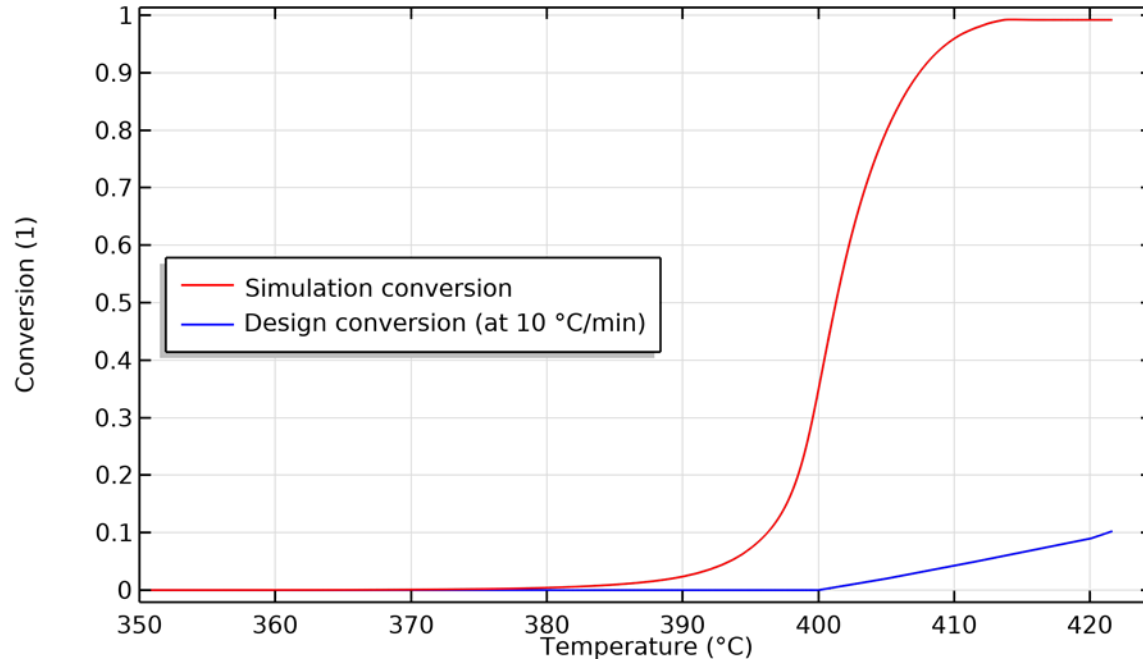


**Figure 5-17** : Simulated conversion and designing conversion comparison at  $L = 148$  cm of the transient study for the best deduced model, fully loaded reactor (with plastic) with 7 kg/h mass flow rate and heated from ambient temperature (20 °C).

Furthermore, **Figure 5-18** displays the plastic and the exhaust gas temperature results and the melting and cracking conversions all along the length of the reactor at  $t = 2$  hours. As shown in the figure (**Figure 5-18**), plastic is totally pyrolyzed at  $L_r = 145$  cm and totally melted at  $L_r = 60$  cm. Moreover, the outlet temperature of plastic reached 430 °C, however, for hot exhaust gas it reached about 150 °C, whereas the heat power transferred within a single tube is  $q = 68$  W. On the other hand, by comparing these results (**Figure 5-18**) to the steady state results (**Figure 5-14**) several facts are acknowledged; (1) cracking process ends at the same vicinity, i.e. length of 140 to 145 cm, but in the steady state cracking starts much earlier in the reactor (at  $L_r = 35$  cm, review **Figure 5-14**), (2) the outlet temperatures (for plastic and hot exhaust gas) are higher in the steady state study, which is normal and expected, and (3) the heat power transferred within a single tube also decreases as the process continue to reach steady state ( $q$  at steady state is almost 35 W, given by **Table 5-6**). Thus, all the results of the transient state are logical and within expectation, however and since the transient study (**Figure 5-18**) needs further time to reach the steady state, the total pyrolysis conversion is achieved at  $t = 2.25$  hours which is a reasonable time. Therefore, the best designed model is also feasible at the transient phase, thus, the reactor is well modelled and designed at both the transient and the steady state. Even more, a further graph shows how the

results (temperatures and conversions) vary after a one hour (i.e. at  $t = 3$  hours) and it is listed in **Appendix: A (Figure 5-3A)**, where  $q$  is decreased to 59.7 W and outlet plastic and hot gas temperatures are increased respectively to 460 and 250 °C.

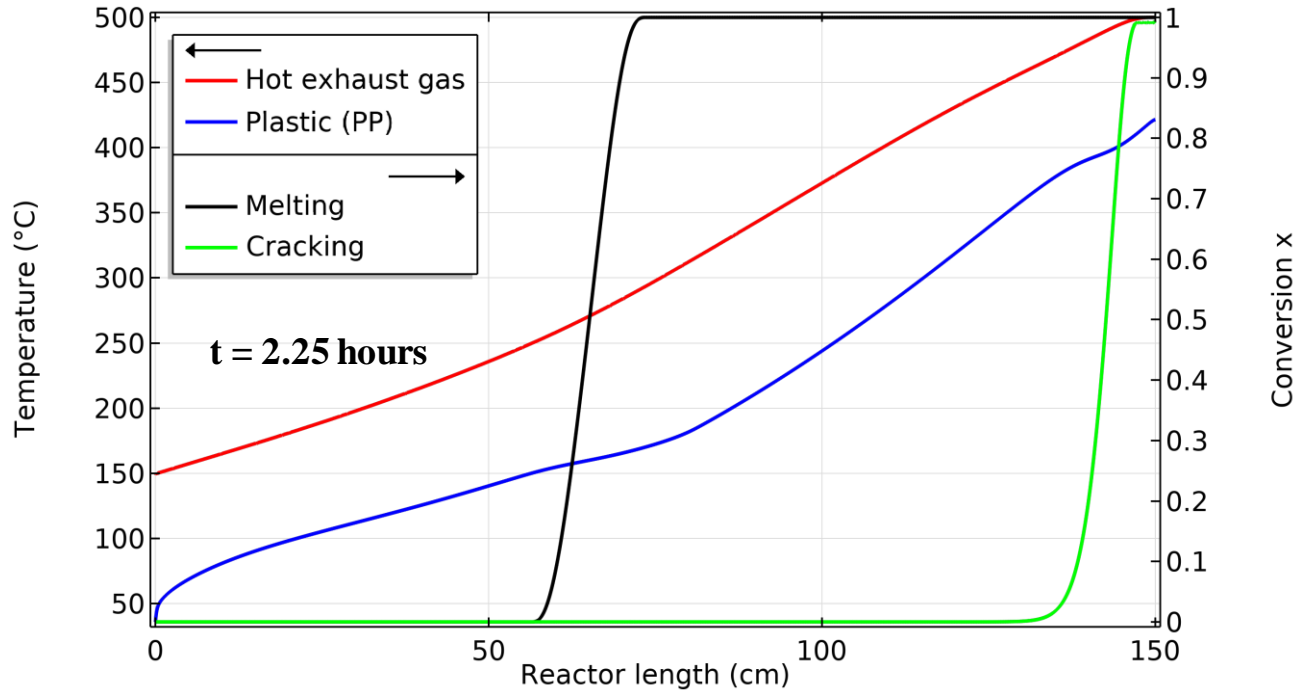


**Figure 5-18 :** Average transient simulation results (temperatures, and plastic conversions) with respect to length of the reactor at  $t = 8100$  s (i.e. at  $t = 2.25$  hours), for the best deduced model ( $N = 100$ ,  $d = 1.4$  cm, and  $L = 1.5$  m) with fully loaded reactor and total plastic flow rate 7 kg/h, heated from ambient temperature 20 °C.

The last transient study is done using the two-phase flow (discussed in **section 2.6, Eq. 2-49 – Eq. 2-53**) to illustrate the effect of the by-products gas flow inside the reactor on the simulation results. **Figure 5-19**, demonstrates the results of the two-phase flow at the same time (2.25 hours) and same simulation conditions of the previous simulation (results without two-phase flow model, **Figure 5-18**). In addition, the temperature and the conversion results are almost the same as in the previous model **Figure 5-18** (i.e. without two-phase flow), and the heat power transferred is almost the same ( $q$  is 65.3 W for the two-phase flow model, whereas it is 68 W for the previous one). Moreover, the overall heat transfer coefficient ( $U_t$ ) is also the same with and without two-phase flow model, having a value of 15 W/K/m<sup>2</sup>. Therefore, the gas flow of the pyrolysis gases inside the reactor has a weak effect in the continuous process due to the forced flow applied to the continuous reactor.

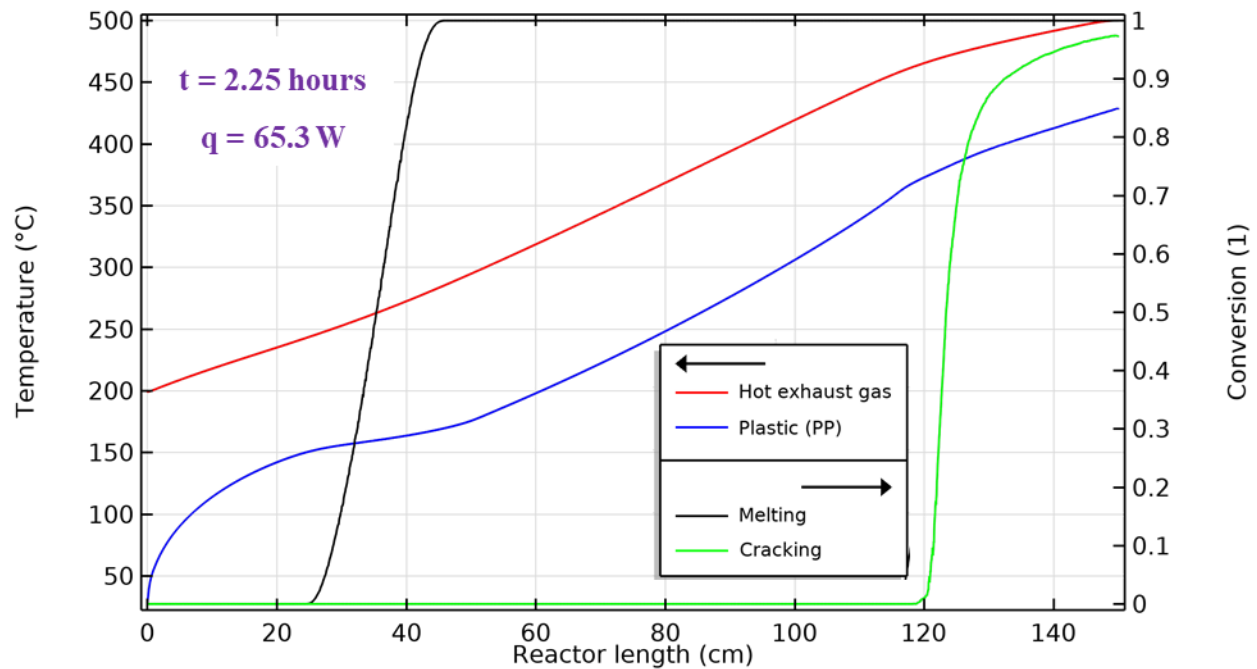


**Figure 5-19 :** Average transient simulation (using the two phase flow model) results, temperatures, and plastic conversions, with respect to length of the reactor at  $t = 8100$  s (i.e. at  $t = 2.25$  hours), for the best deduced model ( $N = 100$ ,  $d = 1.4$  cm, and  $L = 1.5$  m) with fully loaded reactor (with plastic) and total plastic flow rate 7 kg/h, heated from ambient temperature 20 °C.

Finally, the continuous plastic pyrolysis reactor, heated by the exhaust gas of 8 kW diesel engine, is efficiently designed and modelled for PP and HDPE pyrolysis using the representative system of the whole reactor (single concentric tube, discussed in **section 5.1, Figure 5-3**). However, the 3D-model is built but no yet simulated because the time of this study didn't permit to do so, knowing the high computational time that is required for the 3D model simulation (each simulation in terms of days). Nonetheless, modelling the whole reactor with the representative system is efficient and represents more than 80 % of the heat transfer inside the reactor. Moreover, the reactor is designed at the maximum conversion rate and different safety factors are taken into consideration in modelling which assures more and more the feasibility of the reactor and good operation.

### 5.6 Conclusions

The main objective of the thesis was to design and model an efficient continuous plastic pyrolysis reactor heated by the exhaust gas of 8 kW diesel engine. Therefore, Chapter Five came to be the last step in this thesis after modelling plastic pyrolysis in a semi-batch reactor (Chapter Four), profiting from all the previous validated models in the preceded chapters.

First, a rough modelling and validation was done to the first configuration or installation of the continuous pyrolysis reactor (single counter-flow concentric tube reactor with 34 cm length). The results revealed that this configuration is not optimal (thermal efficiency of 0.01 and total heat power transferred of 93 W) and the reactor needs further study and enhancement to operate efficiently.

Therefore, the first design step started based on a previous work done in IMT-Atlantique and GEPEA laboratory. Kassargy (Kassargy, 2018) suggested a multi-tube (hot gases pass inside these tubes) counter-flow continuous pyrolysis reactor with 34 tubes and 1 m length using LMTD method. Thus, this geometry is simulated at steady state and checked at the maximum load of plastic (19 kg/h), where the results are very promising; average outlet pyrolysis conversion reached 0.22 with 0.51 thermal effectiveness. The multi-tube continuous reactor is modelled with a representative system consisting of one tube and circulated with amount of plastic having a diameter of a pitch length (i.e. same as a single concentric tube system).

Therefore, after showing the results of simulation Kassargy's proposed reactor geometry, the model (i.e. geometry, number of tubes and tube diameter  $d$ ) is further studied by a parametric study varying the number of tubes ( $N$ ) from 4 to 200 tubes and the tube diameter  $d$  (from 0.7 to 1.4 cm), taking into consideration the two types of flow; laminar and turbulent flow. The parametric study is held at steady state and maximum flow rate of plastic (19 kg/h) for a reactor of 2 m length. The results revealed that the best model or geometry according to the highest outlet conversion, compactness, and higher total power transferred is the reactor having 100 tubes and  $d = 1.4$  cm. However, this deduced geometry didn't reach complete pyrolysis conversion of plastic at the simulated mass flow rate and length. Thus the length of the reactor is fixed at the desired length (1.5 m) and another steady state parametric study is launched by reducing the total mass flow rate

## Modelling continuous plastic pyrolysis reactor

---

of plastic to reach the total pyrolysis conversion. As a result, the appropriate plastic mass flow rate is conceived; 7 kg/h.

Afterwards, a transient study is performed for the best deduced model ( $N = 100$  tubes,  $d = 1.4$  cm,  $\dot{m}_p = 7$  kg/h,  $L = 1.5$  m, and  $D = 35.6$  cm) to illustrate the feasibility of the model at the starting up phase. The reactor is simulated as it is fully loaded with plastic and with the full plastic flow rate (7 kg/h). The results revealed that it needs only 2.25 hours to achieve total conversion at the outlet of the reactor, hence, the transient phase of the reactor operation is logical and feasible also. Thus it is recommended to increase the mass flow rate from 1 to 7 kg/h during the first two hours of operating.

Thus, an efficient continuous plastic pyrolysis reactor heated by the exhaust gas of 8 kW diesel engine is well designed and modelled at the transient and steady state phases, where the suggested model is suitable for installation and building.

### General conclusions

Nowadays plastic pyrolysis process has a great importance facing the crisis of plastic pollution and the depletion of fossil fuels. In this thesis plastic pyrolysis was defined and the influence parameters were discussed extensively. On the other hand, plastic pyrolysis technology over the past 40 years is found to be based on experimental up-scaling, where unfortunately pyrolysis process is still inefficient and needs more improvements (Huisman, 2001; IEA Bioenergy, 2020). Consequently, the importance of performing numerical modelling and simulation for plastic pyrolysis using finite element method for the sake of developing efficient process was explored and emphasized.

As a result, modelling plastic pyrolysis of a bulk of plastic is still rarely mentioned in the literature. Furthermore, modelling and optimizing efficient plastic pyrolysis reactors that would be applied and invested at the industrial scale is not done yet. Even more, the experimental installation of a continuous plastic pyrolysis reactor heated by 8 kW diesel engine by a previous work done in IMT-Atlantique (GEPEA laboratory) was not that efficient. Therefore, the objective of this thesis was to model and design an efficient continuous plastic pyrolysis reactor heated by the exhaust gas of 8 kW diesel engine for the most abundant plastic materials; PP and HDPE.

However, in order to achieve an overall design and conception of the continuous pyrolysis reactor, plastic pyrolysis process is recommended to be modelled and validated at a particle scale using TGA-DCS, and then, in a laboratory scale semi-batch reactor (Chapter Three and Chapter Four). After that, the validated models, equations, and knowledge are used to model the continuous reactor (Chapter Five).

Therefore, first, a DSC survey is carried out to find the melting characteristics (range of melting, peak temperature, and the fusion enthalpy) and heat capacities for PP and HDPE at several heating rates (4 – 10 °C/min). Then, the melting process at a milli-particle scale for PP and HDPE inside the DSC is modelled by the apparent heat capacity method (AHCM) and the heat conduction equation, using COMSOL-Multiphysics and finite element method. The simulated heat flow absorbed by the plastic samples are compared and validated with the experimental ones; the maximum average relative error among all the results did not exceed 9 %.

## General conclusions

---

Afterwards, the AHCM is also used to model melting process for polypropylene and high density polyethylene inside a semi-batch reactor. Results revealed the high capability and accuracy of the AHCM method in modelling and simulating melting phenomena. In addition, molten plastic is modelled as a bulk of fluid at rest and also as a dynamic fluid, where both methods (stationary and dynamic fluid) show the same results because of the high viscosity of molten plastic at very low shearing rates. Furthermore, PP and HDPE melting/solidification and heating/cooling processes are modelled and validated at different heating rates with 8 % and 4 % as maximum average relative error for temperatures and energy balances, respectively.

Thus, after validating the models of heating and melting of PP and HDPE at milli-particle scale and laboratory scale semi-batch reactor, the models are used as a prerequisite to simulate plastic cracking process at these scales. However, in order to proceed in modelling the pyrolysis process, a kinetic study is mandatory and comes at the first stage.

Therefore, experimental TGA-DCS results for PP and HDPE pyrolysis at low heating rates (4, 6, 8, and 10 °C/min) are performed and demonstrated. In addition, the pyrolysis characteristics such as onset temperatures, maximum temperatures, and enthalpies of cracking are also determined. Furthermore, a pre-cracking phenomenon is detected, by the TGA-DCS results, to have place before the start of mass loss for PP and HDPE pyrolysis.

Then, an extensive kinetic pyrolysis study is performed to determine the best kinetic parameters that model pyrolysis process for PP and HDPE at low heating rates (below 10 °C/min). The results reveal that the best kinetic parameters that model PP pyrolysis are the Avrami-Erofe'v kinetic model (A2) with an activation energy of 220 (kJ/mol) and pre-exponential coefficient  $A = 4.15 \times 10^{15} \text{ (min}^{-1}\text{)}$  determined by either KAS or FWO method. Nonetheless, the average relative error between the deduced kinetic model and the experimental TGA results didn't exceed 5 %.

In the same manner, the best deduced kinetic results for HDPE pyrolysis at low heating rates (4, 6, 8, and 10 °C/min) are:  $E = 264 \text{ (kJ/mol)}$  (according to KAS or FWO method), kinetic model  $f(x)$  is also Avrami-Erofe'v (A2), and the pre-exponential factor  $A = 8.3 \times 10^{17} \text{ (1/min)}$ . Whereas, the average relative error between the theoretical and experimental conversion curves is below 6 %.

After that, the deduced kinetic parameters are implemented along with the appropriate equations and boundary conditions into COMSOL-Multiphysics software to model and simulate the whole pyrolysis process for PP and HDPE inside TGA-DSC at milli-particle scale. The cracking model (TGA) is noticed to work very well, as expected, with an average relative error among all the simulated and experimental conversions for PP and HDPE pyrolysis less than 5 %. On the other hand, the DSC comparison results, i.e. comparing the simulated heat flow results with the experimental ones, are enhanced by modelling the latent cracking phenomenon (pre-cracking), which is occurring before and alongside mass cracking. Thus, the average relative error decreases from 20 % to less than 8 % by modifying the heat capacity for PP and HDPE. Finally, simulated results are in a very good agreement with the experimental ones for modelling PP and HDPE at a milli-particle scale inside a TGA-DSC; maximum average relative error didn't exceed 8 %.

Last but not least, after modelling pyrolysis process at milli-particle scale, the pyrolysis process for PP and HDPE is modelled at laboratory scale semi-batch reactor at the same heating rate range (below 10 °C/min). As the results show, pyrolysis process inside the semi-batch reactor has two different progressive stages; First stage is the transient state, where there exists condensation process of the vapor by-products inside the semi-batch reactor because the top part of the reactor is still cold and in progress of warming up. In this stage, the condensation of the by-products vapor inside the reactor (especially on the top part) plays a great role in recirculating and re-cracking (secondary cracking) the by-products and preventing it from leaving the reactor. On the other hand, the second stage is the steady state where the condensation process inside the reactor is very low due to the rise in the temperature of the upper part of the reactor (more than 130 °C).

After illustrating and analyzing briefly the experimental results, pyrolysis process for PP and HDPE is modelled inside the semi-batch reactor using the deduced kinetic model (from **section 4.2**) and a two-phase flow model (phase field model imbedded in COMSOL-Multiphysics) to simulate the fluid flow of the molten plastic and its pyrolysis by-products vapor. For the sake of simplicity and to notify the influence of the condensation process on the simulation results, two approaches of simulation are performed. First approach is simulating the pyrolysis process without taking into consideration the condensation phenomenon, whereas, the second one is modelling the condensation process along with the pyrolysis one. The results reveal that the model is validated by the experimental results (the bed height loss inside the reactor) for the first approach of

## General conclusions

---

simulation at the steady state phase (i.e. without condensation). Whereas, the ideal (without condensation) speed of the reactor's bed loss determined from simulation is almost the same as the experimental one at the steady state phase for PP and HDPE. In addition, the maximum average relative error among the results didn't exceeds 9 %. Therefore, pyrolysis process for PP and HDPE inside the semi-batch reactor is modelled and successfully validated by the experimental results for the steady state stage of the process, i.e. without the presence of condensation.

On the other side, the results of bed loss at transient state period need to be further enhanced by modelling the condensation process of the pyrolytic vapors inside the reactor. Therefore, condensation inside the reactor is modelled by two means; First one is the natural way, by assigning several condensation temperatures for the by-product vapor to model the condensation at different temperature levels. On the other hand, the second method is by imposing a forced condensation reflux into simulation to control the simulated bed drop at the transient state to be the same as the experimental one. However, several difficulties prevent the total success for neither one of the methods. But knowing the fact that, when modelling the final continuous reactor the condensation process is considered negligible due to the type of the reactor, counter flow fire tubes reactor, i.e. plastic strictly rises in temperature as it proceeds inside the reactor (**Figure 2-17**). Thus, the validated pyrolysis model for PP and HDPE in laboratory scale semi-batch reactor at the steady state phase is sufficient and very good prerequisite for modelling the continuous reactor.

Finally, all the preceding validated models and knowledge are employed to design the continuous pyrolysis reactor having 1.5 to 2 m maximum length and outer diameter ( $D$ ) below 60 cm. First, the suggested model from previous work ([Kassargy, 2018](#)) which is a multi-tube counter-flow continuous pyrolysis reactor (hot gases passes inside these tubes), is utilized to launch the steady state parametric studies for different number of tubes varying from 4 till 200 tube, tube diameter  $d$  changing from 0.7 to 1.4 cm, and the mass flow rate of plastic decreasing from the maximum value (19 kg/h). Therefore, after analyzing the results and taking into consideration the general desired designing criteria (1.5 m length and minimum outer  $D$  or in other words minimum number of tubes ( $N$ )), in addition to the highest outlet pyrolysis conversion  $x_{out}$ , and to the highest total power transferred  $Q_t$ , the best model is deduced ( $N = 100$  tubes,  $d = 1.4$  cm,  $\dot{m}_p = 7$  kg/h,  $L = 1.5$  m, and  $D = 35.6$  cm).

## General conclusions

---

Moreover, a transient study was performed on the best deduced model to check the feasibility of the reactor at the starting up phase. As a result, it is recommended to increase the plastic mass flow rate from 1 to 7 kg/h in two hours for the suggested model, which is a practical and reasonable time.

Finally, and all in all, the optimal goal of this thesis is achieved successfully by designing and modelling an efficient continuous plastic pyrolysis reactor (for PP and HDPE) heated by the exhaust gas of 8 kW diesel. Where this reactor can be further studied and modelled as 3D model. In addition, this reactor can be built for the sake of experimentation (validation) and further enhancement. Even more, the model can be used for different types of plastic like PS and PVC, after establishing the kinetic studies of such types of plastics. Nevertheless, the feeding and the injection procedure of plastic should be well conceived in the future, in addition of the study of its effect on the convection heat transfer coefficient. Furthermore, the convection heat transfer coefficient at the cracking phase needs to be further investigated. Finally, this model is a first step in modelling plastic pyrolysis in continuous reactor for the sake of industrial conception and application, which needs further upgrading and enhancement.

## Perspectives

After achieving the goal of this thesis, further perspectives and future work are suggested below:

1. Further enhancement for modelling whole melting process; that's by using a suitable exponential conversion function according to Arrhenius law instead of the using linear conversion symmetrical function, determined from a kinetic melting study.
2. To validate the simulated heater and controller of the semi-batch reactor; the model can be used to conduct different simulation study analysis for heating/melting different solid or fluid materials with acceptable results without the need to conduct any relative experiments. In addition, the model can be further extended to model different energy engineering applications in the fields of waste/biomass to energy, heat storage, building heating and cooling, thermoplastics processing and equipment design and other unsteady heat flux/temperature problems applications.
3. To Model well the natural condensation process inside the semi-batch reactor by using multi-phase flow model, i.e. one phase for solid, one phase for molten plastic, and one phase for each pyrolysis vapor group (identified by their condensation temperatures). Thus, different software that support the multi-phase flow (unrestricted) are recommended to be used, like ANSYS for instance.
4. To investigate the convection heat transfer coefficient due to pyrolysis or possible bubble formation in the semi-batch reactor during plastic pyrolysis.
5. Further 3D numerical simulation is recommended to be done for best deduced model of the continuous plastic pyrolysis reactor.
6. To build the suggested counter-flow multi-concentric tube continuous plastic pyrolysis reactor ( $N = 100$  tubes,  $d = 1.4$  cm,  $\dot{m}_p = 7$  kg/h,  $L = 1.5$  m, and  $D = 35.6$  cm) for the sake of experimental validation.
7. To use the proposed condensation reflux model in **section** 4.4.2.2 to model the condensation reflux of the pyrolysis by-products after the exit (plastic outlet) of the continuous reactor.

8. To implement the kinetic model (**Eq. 2-24**) in the steady state simulation studies to be solved as length-dependent rather than time-dependent.

### References

- Abbas-Abadi, M.S., Haghghi, M.N. and Yeganeh, H. (2013), “Evaluation of pyrolysis product of virgin high density polyethylene degradation using different process parameters in a stirred reactor”, *Fuel Processing Technology*, Elsevier, Vol. 109, pp. 90–95.
- Aboulkas, A., El Bouadili, A. and EL harfi, K. (2010), “Thermal degradation behaviors of polyethylene and polypropylene. Part I: Pyrolysis kinetics and mechanisms”, *Energy Conversion and Management*, Elsevier, Vol. 51 No. 7, pp. 1363–1369.
- Agassant, J.-F., Pigeonneau, F., Sardo, L. and Vincent, M. (2019), “Flow analysis of the polymer spreading during extrusion additive manufacturing”, *Additive Manufacturing*, Elsevier, Vol. 29, p. 100794.
- Agrawal, A. (2005), “Surface Tension of Polymers”, p. 29.
- Aguado, R., Prieto, R., San José, M.J., Alvarez, S., Olazar, M. and Bilbao, J. (2005), “Defluidization modelling of pyrolysis of plastics in a conical spouted bed reactor”, *Chemical Engineering and Processing: Process Intensification*, Elsevier, Vol. 44 No. 2, pp. 231–235.
- Aho, J. (2011), *Rheological Characterization of Polymer Melts in Shear and Extension: Measurement Reliability and Data for Practical Processing*, Tampere University of Technology, available at: <https://trepo.tuni.fi/handle/10024/114192> (accessed 12 May 2021).
- Aida, I.M.I., Salmiaton, A., the Department of Chemical and Environmental Engineering, Faculty of Engineering, Universiti Putra Malaysia, Serdang 43400 Selangor DarulEhsan, Malaysia, Nur, D.K.B., and Universiti Putra Malaysia, Serdang 43400 Selangor DarulEhsan, Malaysia. (2015), “Mixed Plastic Wastes Pyrolysis in a Fluidized Bed Reactor for Potential

## References

---

- Diesel Production”, *International Journal of Environmental Science and Development*, Vol. 6 No. 8, pp. 606–609.
- Akahira, T. and Sunose, T. (1971), “Method of determining activation deterioration constant of electrical insulating materials”, *Res Rep Chiba Inst Technol (Sci Technol)*, Vol. 16 No. 1971, pp. 22–31.
- Alves, S.S. and Figueiredo, J.L. (1989), “A model for pyrolysis of wet wood”, *Chemical Engineering Science*, Elsevier, Vol. 44 No. 12, pp. 2861–2869.
- ANSYS. (2009), “ANSYS FLUENT 12.0/12.1 Documentation”, available at: <https://www.afs.enea.it/project/neptunius/docs/fluent/> (accessed 12 May 2021).
- Antelava, A., Damilos, S., Hafeez, S., Manos, G., Al-Salem, S.M., Sharma, B.K., Kohli, K., *et al.* (2019), “Plastic Solid Waste (PSW) in the Context of Life Cycle Assessment (LCA) and Sustainable Management”, *Environmental Management*, Vol. 64 No. 2, pp. 230–244.
- Anuar Sharuddin, S.D., Abnisa, F., Wan Daud, W.M.A. and Aroua, M.K. (2016), “A review on pyrolysis of plastic wastes”, *Energy Conversion and Management*, Vol. 115, pp. 308–326.
- Atlas. (2012), “Atlas Pipe\_Dimensions\_chart”.
- Babu, S.P. (2005), “Observations on the current status of biomass gasification”, *Observations on the Current Status of Biomass Gasification*, Elsevier, Oxford, Vol. 29 No. 4, p. I–XII.
- Barnes, H.A., Hutton, J.F. and Walters, K. (1989), *An Introduction to Rheology*, Vol. 3, Elsevier.
- Basu, P. (2013), *Biomass Gasification, Pyrolysis, and Torrefaction: Practical Design and Theory*, Second edition., Academic Press is and imprint of Elsevier, Amsterdam ; Boston.
- Bockhorn, H., Hornung, A., Hornung, U. and Jakobströer, P. (1999), “Modelling of isothermal and dynamic pyrolysis of plastics considering non-homogeneous temperature distribution

## References

---

- and detailed degradation mechanism”, *Journal of Analytical and Applied Pyrolysis*, Elsevier, Vol. 49 No. 1–2, pp. 53–74.
- Bress, T.J. and Dowling, D.R. (2011), “Particle image velocimetry in molten plastic”, *Polymer Engineering & Science*, Vol. 51 No. 4, pp. 730–745.
- Burden, R.L. and Faires, J.D. (2011), *Numerical Analysis*, 9th ed., Brooks/Cole, Cengage Learning, Boston, MA.
- Ceamanos, J., Mastral, J.F., Millera, A. and Aldea, M.E. (2002), “Kinetics of pyrolysis of high density polyethylene. Comparison of isothermal and dynamic experiments”, *Journal of Analytical and Applied Pyrolysis*, Elsevier, Vol. 65 No. 2, pp. 93–110.
- Cheméo. (2021), “Cheméo - Chemical & Physical Properties by Cheméo”, 9 May, available at: <https://www.chemeo.com/> (accessed 9 May 2021).
- Chen, D., Yin, L., Wang, H. and He, P. (2014), “Pyrolysis technologies for municipal solid waste: a review”, *Waste Management*, Elsevier, Vol. 34 No. 12, pp. 2466–2486.
- Chin, B.L.F., Yusup, S., Al Shoaibi, A., Kannan, P., Srinivasakannan, C. and Sulaiman, S.A. (2014), “Kinetic studies of co-pyrolysis of rubber seed shell with high density polyethylene”, *Energy Conversion and Management*, Elsevier, Vol. 87, pp. 746–753.
- Coats, A.W. and Redfern, J.P. (1963), “Thermogravimetric analysis. A review”, *Analyst*, The Royal Society of Chemistry, Vol. 88 No. 1053, pp. 906–924.
- COMSOL. (2017), “COMSOL Multiphysics Reference Manual”, p. 1480.
- Criado, J.M. (1978), “Kinetic analysis of DTG data from master curves”, *Thermochimica Acta*, Elsevier, Vol. 24 No. 1, pp. 186–189.

## References

---

- Csukas, B., Varga, M., Miskolczi, N., Balogh, S., Angyal, A. and Bartha, L. (2013), “Simplified dynamic simulation model of plastic waste pyrolysis in laboratory and pilot scale tubular reactor”, *Fuel Processing Technology*, Elsevier, Vol. 106, pp. 186–200.
- Curet, S., Rouaud, O. and Boillereaux, L. (2006), “Heat transfer models for microwave thawing applications”, *Excerpt from the Proceedings of the COMSOL Users Conference, Paris*.
- Czajczyńska, D., Anguilano, L., Ghazal, H., Krzyżyńska, R., Reynolds, A.J., Spencer, N. and Jouhara, H. (2017), “Potential of pyrolysis processes in the waste management sector”, *Thermal Science and Engineering Progress*, Elsevier, Vol. 3, pp. 171–197.
- Dabiri Atashbeyk, M., Shahbazi, K. and Fattahi, M. (2018), “Pressure profile estimation through CFD in UBD operation considering with influx to wellbore”, *Iranian Journal of Chemistry and Chemical Engineering (IJCCE)*, Iranian Institute of Research and Development in Chemical Industries (IRDCI ...), Vol. 37 No. 6, pp. 271–283.
- Das, P. and Tiwari, P. (2017), “Thermal degradation kinetics of plastics and model selection”, *Thermochimica Acta*, Vol. 654, pp. 191–202.
- Del Remedio Hernández, M., García, Á.N. and Marcilla, A. (2007), “Catalytic flash pyrolysis of HDPE in a fluidized bed reactor for recovery of fuel-like hydrocarbons”, *Journal of Analytical and Applied Pyrolysis*, Vol. 78 No. 2, pp. 272–281.
- Ding, K., Xiong, Q., Zhong, Z., Zhong, D. and Zhang, Y. (2020), “CFD simulation of combustible solid waste pyrolysis in a fluidized bed reactor”, *Powder Technology*, Elsevier, Vol. 362, pp. 177–187.
- Elordi, G., Olazar, M., Lopez, G., Amutio, M., Artetxe, M., Aguado, R. and Bilbao, J. (2009), “Catalytic pyrolysis of HDPE in continuous mode over zeolite catalysts in a conical

## References

---

- spouted bed reactor”, *Journal of Analytical and Applied Pyrolysis*, Elsevier, Vol. 85 No. 1–2, pp. 345–351.
- Elordi, G., Olazar, M., Lopez, G., Artetxe, M. and Bilbao, J. (2011), “Continuous polyolefin cracking on an HZSM-5 zeolite catalyst in a conical spouted bed reactor”, *Industrial & Engineering Chemistry Research*, ACS Publications, Vol. 50 No. 10, pp. 6061–6070.
- Encinar, J.M. and González, J.F. (2008), “Pyrolysis of synthetic polymers and plastic wastes. Kinetic study”, *Fuel Processing Technology*, Elsevier, Vol. 89 No. 7, pp. 678–686.
- ETIA. (2019), “Spirajoule: Electrically heated screw conveyor – Spirajoule”, *ETIA Group*, available at: <https://etia-group.com/our-products/spirajoule/> (accessed 12 May 2021).
- Flynn, J.H. (1983), “The isoconversional method for determination of energy of activation at constant heating rates”, *Journal of Thermal Analysis*, Springer, Vol. 27 No. 1, pp. 95–102.
- Flynn, J.H. and Wall, L.A. (1966), “General treatment of the thermogravimetry of polymers”, *Journal of Research of the National Bureau of Standards. Section A, Physics and Chemistry*, National Institute of Standards and Technology, Vol. 70 No. 6, p. 487.
- Friedman, H.L. (1964), “Kinetics of thermal degradation of char-forming plastics from thermogravimetry. Application to a phenolic plastic”, *Journal of Polymer Science Part C: Polymer Symposia*, Vol. 6, Wiley Online Library, pp. 183–195.
- Gan, Y. (2012), *Continuum Mechanics: Progress in Fundamentals and Engineering Applications*, BoD – Books on Demand.
- Gao, Z., Amasaki, I. and Nakada, M. (2003), “A thermogravimetric study on thermal degradation of polyethylene”, *Journal of Analytical and Applied Pyrolysis*, Elsevier, Vol. 67 No. 1, pp. 1–9.

## References

---

- Geyer, R., Jambeck, J.R. and Law, K.L. (2017), “Production, use, and fate of all plastics ever made”, *Science Advances*, American Association for the Advancement of Science, Vol. 3 No. 7, p. e1700782.
- Gilbert, M. (2017), “Plastics materials: Introduction and historical development”, *Brydson’s Plastics Materials*, Elsevier, pp. 1–18.
- Goswami, D.Y. (2004), *The CRC Handbook of Mechanical Engineering*, CRC Press.
- Greenwood, A. (2018), “INSIGHT: US Agilyx takes big step in producing naphtha, propylene from waste plastics”, *ICIS Explore*, available at: <https://www.icis.com/explore/resources/news/2018/09/27/10262364/insight-us-agilyx-takes-big-step-in-producing-naphtha-propylene-from-waste-plastics> (accessed 12 May 2021).
- Guo, C.-Q., Zhu, D.-S., Jiang, X., Wu, Z.-J. and Zhang, J.-W. (2009), “Numerical simulation of heat and mass transfer in plate-type evaporative condenser”, *Huanan Ligong Daxue Xuebao/Journal of South China University of Technology (Natural Science)*, Vol. 37 No. 3, pp. 53–57.
- Hall, M.R. (2010), *Materials for Energy Efficiency and Thermal Comfort in Buildings*, Elsevier.
- Hamdhan, I.N. and Clarke, B.G. (2010), “Determination of thermal conductivity of coarse and fine sand soils”, *Proceedings of World Geothermal Congress*, pp. 1–7.
- Harvey, P.D. (1982), “American Society for Metals”, *Engineering Properties of Steel*.
- Hernández, M. del R., García, Á.N., Gómez, A., Agulló, J. and Marcilla, A. (2006), “Effect of Residence Time on Volatile Products Obtained in the HDPE Pyrolysis in the Presence and Absence of HZSM-5”, *Industrial & Engineering Chemistry Research*, American Chemical Society, Vol. 45 No. 26, pp. 8770–8778.

## References

---

- Huisman. (2001), “Acceptance Test for Large Biomass Gasifiers”.
- ICChemE. (2019), “Plastics: Towards a Circular Economy”, available at: <https://www.thechemicalengineer.com/features/plastics-towards-a-circular-economy/> (accessed 12 May 2021).
- IEA Bioenergy. (2020), “Bioenergy | International Collaboration in Bioenergy”, available at: <https://www.ieabioenergy.com/> (accessed 12 May 2021).
- IEEE. (2019), “The Advantages of the Finite Element Method”, *IEEE Innovation at Work*, 28 May, available at: <https://innovationatwork.ieee.org/the-advantages-of-fem/> (accessed 12 May 2021).
- Incropera, F.P., Lavine, A.S., Bergman, T.L. and DeWitt, D.P. (2007), *Fundamentals of Heat and Mass Transfer*, Wiley.
- INEOS. (2014a), “Typical Engineering Properties of Polypropylene”.
- INEOS. (2014b), “Typical Engineering Properties of High Density Polyethylene”, p. 3.
- Ionescu, C.M., Birs, I.R., Copot, D., Muresan, C.I. and Caponetto, R. (2020), “Mathematical modelling with experimental validation of viscoelastic properties in non-Newtonian fluids”, *Philosophical Transactions of the Royal Society A: Mathematical, Physical and Engineering Sciences*, Royal Society, Vol. 378 No. 2172, p. 20190284.
- Jafri, Y. (2020), “Emerging Gasification Technologies for Waste & Biomass”, p. 83.
- Jin, Z., Yin, L., Chen, D., Jia, Y., Yuan, J. and Yu, B. (2019), “Heat transfer characteristics of molten plastics in a vertical falling film reactor”, *Chinese Journal of Chemical Engineering*, Vol. 27 No. 5, pp. 1015–1020.
- Kassargy, C. (2018), *Contribution à l'étude de la valorisation énergétique des résidus de plastique par craquage catalytique*, PhD Thesis, Ecole nationale supérieure Mines-Télécom

## References

---

- Atlantique ; École Doctorale des Sciences et de Technologie (Beyrouth), 22 May, available at: <https://tel.archives-ouvertes.fr/tel-01883636> (accessed 12 May 2021).
- Kim, S., Kavitha, D., Tae, U.Y., Jung, J.-S., Song, J.-H., Lee, S.-W. and Kong, S.-H. (2008), “Using isothermal kinetic results to estimate kinetic triplet of pyrolysis reaction of polypropylene”, *Journal of Analytical and Applied Pyrolysis*, Elsevier, Vol. 81 No. 1, pp. 100–105.
- Kim, S. and Kim, Y.-C. (2005), “Using isothermal kinetic results to estimate the kinetic triplet of the pyrolysis of high density polyethylene”, *Journal of Analytical and Applied Pyrolysis*, Elsevier, Vol. 73 No. 1, pp. 117–121.
- Klean Industries. (2020), “Large Scale Plastics Pyrolysis System to Diesel Fuel | Cogeneration & Recycling Technology | Klean Industries”, available at: <https://kleanindustries.com/waste-challenges-innovations/plastic-pyrolysis-recycling/spr-japan/> (accessed 12 May 2021).
- Lee, K.-H. (2008), “Composition of aromatic products in the catalytic degradation of the mixture of waste polystyrene and high-density polyethylene using spent FCC catalyst”, *Polymer Degradation and Stability*, Vol. 93 No. 7, pp. 1284–1289.
- Lertwimolnun, W. and Vergnes, B. (2004), “Influence de la dispersion sur le comportement rhéologique de nanocomposites polypropylène/argile”, p. 10.
- Li, D., Zhou, L., Wang, X., He, L. and Yang, X. (2019), “Effect of crystallinity of polyethylene with different densities on breakdown strength and conductance property”, *Materials*, Multidisciplinary Digital Publishing Institute, Vol. 12 No. 11, p. 1746.
- Madruga, S., Haruki, N. and Horibe, A. (2018), “Experimental and numerical study of melting of the phase change material tetracosane”, *International Communications in Heat and Mass Transfer*, Vol. 98, pp. 163–170.

## References

---

- Marcilla, A., Beltrán, M.I. and Navarro, R. (2009), “Thermal and catalytic pyrolysis of polyethylene over HZSM5 and HUSY zeolites in a batch reactor under dynamic conditions”, *Applied Catalysis B: Environmental*, Vol. 86 No. 1, pp. 78–86.
- Marcilla, A., García-Quesada, J.C., Sánchez, S. and Ruiz, R. (2005), “Study of the catalytic pyrolysis behaviour of polyethylene–polypropylene mixtures”, *Journal of Analytical and Applied Pyrolysis*, Vol. 74 No. 1, pp. 387–392.
- Mastral, F.J., Esperanza, E., García, P. and Juste, M. (2002), “Pyrolysis of high-density polyethylene in a fluidised bed reactor. Influence of the temperature and residence time”, *Journal of Analytical and Applied Pyrolysis*, Vol. 63 No. 1, pp. 1–15.
- Miandad, R., Barakat, M.A., Aburizaiza, A.S., Rehan, M. and Nizami, A.S. (2016), “Catalytic pyrolysis of plastic waste: A review”, *Process Safety and Environmental Protection*, Vol. 102, pp. 822–838.
- Miller, R.S. and Bellan, J. (1997), “A Generalized Biomass Pyrolysis Model Based on Superimposed Cellulose, Hemicellulose and Lignin Kinetics”, *Combustion Science and Technology*, Taylor & Francis, Vol. 126 No. 1–6, pp. 97–137.
- Miskolczi, N., Angyal, A., Bartha, L. and Valkai, I. (2009), “Fuels by pyrolysis of waste plastics from agricultural and packaging sectors in a pilot scale reactor”, *Fuel Processing Technology*, Vol. 90 No. 7, pp. 1032–1040.
- Moradi, F., Kazemeini, M. and Fattahi, M. (2014), “A three dimensional CFD simulation and optimization of direct DME synthesis in a fixed bed reactor”, *Petroleum Science*, Vol. 11 No. 2, pp. 323–330.
- Mostafa, S.M. and Farhoud, M.W. (2013), “Ansys Workbench Basics Guide”, p. 75.

## References

---

- Murray, R.E. and Groulx, D. (2011), “Modeling Convection during Melting of a Phase Change Material”, p. 8.
- Navarro, M.V., Martínez, J.D., Murillo, R., García, T., López, J.M., Callén, M.S. and Mastral, A.M. (2012), “Application of a particle model to pyrolysis. Comparison of different feedstock: Plastic, tyre, coal and biomass”, *Fuel Processing Technology*, Vol. 103, pp. 1–8.
- Peters, B. (2011), “Validation of a numerical approach to model pyrolysis of biomass and assessment of kinetic data”, *Fuel*, Vol. 90 No. 6, pp. 2301–2314.
- Plastic Energy. (2021), “Plastic Energy Collaborates with ExxonMobil on Advanced Recycling Project in France”, *Plastic Energy*, 25 March, available at: [https://plasticenergy.com/plastic\\_energy\\_collaborates\\_with\\_exxonmobil\\_on\\_advanced\\_recycling\\_project\\_in\\_france/](https://plasticenergy.com/plastic_energy_collaborates_with_exxonmobil_on_advanced_recycling_project_in_france/) (accessed 12 May 2021).
- PlasticEurope. (2019), “Plastics\_the\_facts2019”.
- Predel, M. and Kaminsky, W. (2000), “Pyrolysis of mixed polyolefins in a fluidised-bed reactor and on a pyro-GC/MS to yield aliphatic waxes”, *Polymer Degradation and Stability*, Vol. 70 No. 3, pp. 373–385.
- Press, W.H., Press, W.H., Flannery, B.P., Teukolsky, S.A., Vetterling, W.T., Flannery, B.P. and Vetterling, W.T. (1989), *Numerical Recipes in Pascal (First Edition): The Art of Scientific Computing*, Cambridge University Press.
- Pryor, R.W. (2007), “Modeling Materials through a Phase Transition: Using COMSOL Multiphysics and Applying Physics First Principles Techniques”, p. 7.
- PubChem. (2021), “PubChem, National Center for Biotechnology Information.”, 9 May, available at: (accessed 9 May 2021).

## References

---

- Qureshi, M.S., Oasmaa, A., Pihkola, H., Deviatkin, I., Tenhunen, A., Mannila, J., Minkkinen, H., *et al.* (2020), “Pyrolysis of plastic waste: Opportunities and challenges”, *Journal of Analytical and Applied Pyrolysis*, Vol. 152, p. 104804.
- Rao, S.S. (2017), *The Finite Element Method in Engineering*, Butterworth-Heinemann.
- Ratnasari, D.K., Nahil, M.A. and Williams, P.T. (2017), “Catalytic pyrolysis of waste plastics using staged catalysis for production of gasoline range hydrocarbon oils”, *Journal of Analytical and Applied Pyrolysis*, Vol. 124, pp. 631–637.
- Recycling Technologies. (2018), “Chemical recycling of plastic waste back into monomers and feedstock”, *Recycling Technologies*, available at: <https://recyclingtechnologies.co.uk/technology/> (accessed 12 May 2021).
- Rojas, E.E.G., Coimbra, J.S. and Telis-Romero, J. (2013), “Thermophysical properties of cotton, canola, sunflower and soybean oils as a function of temperature”, *International Journal of Food Properties*, Taylor & Francis, Vol. 16 No. 7, pp. 1620–1629.
- Salvi, D., Boldor, D., Aita, G.M. and Sabliov, C.M. (2011), “COMSOL Multiphysics model for continuous flow microwave heating of liquids”, *Journal of Food Engineering*, Vol. 104 No. 3, pp. 422–429.
- Samara, F., Groulx, D. and Biwole, P.H. (2012), “Natural Convection Driven Melting of Phase Change Material: Comparison of Two Methods”, p. 8.
- Scheirs, J. and Kaminsky, W. (Eds.). (2006), *Feedstock Recycling and Pyrolysis of Waste Plastics: Converting Waste Plastics into Diesel and Other Fuels*, J. Wiley & Sons, Chichester, UK ; Hoboken, NJ.

## References

---

- Seo, Y.-H., Lee, K.-H. and Shin, D.-H. (2003), “Investigation of catalytic degradation of high-density polyethylene by hydrocarbon group type analysis”, *Journal of Analytical and Applied Pyrolysis*, Vol. 70 No. 2, pp. 383–398.
- Shafigullin, L.N., Romanova, N.V., Gumerov, I.F., Gabrakhmanov, A.T. and Sarimov, D.R. (2018), “Thermal properties of polypropylene and polyethylene blends (PP/LDPE)”, *IOP Conference Series: Materials Science and Engineering*, pp. 012070–012070.
- Snegirev, A.Yu., Talalov, V.A., Stepanov, V.V. and Harris, J.N. (2013), “A new model to predict pyrolysis, ignition and burning of flammable materials in fire tests”, *Fire Safety Journal*, Vol. 59, pp. 132–150.
- Sobko, A.A. (2008), “Generalized van der Waals-Berthelot equation of state”, *Doklady Physics*, Vol. 53 No. 8, pp. 416–419.
- Starink, M.J. (2003), “The determination of activation energy from linear heating rate experiments: a comparison of the accuracy of isoconversion methods”, *Thermochimica Acta*, Vol. 404 No. 1, pp. 163–176.
- Stelmachowski, M. (2010), “Thermal conversion of waste polyolefins to the mixture of hydrocarbons in the reactor with molten metal bed”, *Energy Conversion and Management*, Vol. 51 No. 10, pp. 2016–2024.
- Swallowe, G.M. (1999), *Mechanical Properties and Testing of Polymers: An A–Z Reference*, Springer Science & Business Media.
- Vadxx energy. (2016), “Vadxx Energy Establishes Waste Plastic to EcoFuel™ Facility in Akron | Ohio’s Polymer Industry Resource”, *PolymerOhio*, 12 August, available at: <https://polymerohio.org/vadxx-energy-establishes-waste-plastic-ecofuel-facility-akron/> (accessed 12 May 2021).

## References

---

- Vallejos, P. and Duston, C. (2005), “Carbon Foam Filled with Phase Change Materials ... - COMSOL.com”, *Yumpu.Com*, available at: <https://www.yumpu.com/en/document/read/4591761/carbon-foam-filled-with-phase-change-materials-comsolcom> (accessed 12 May 2021).
- Van Grieken, R., Serrano, D.P., Aguado, J., García, R. and Rojo, C. (2001), “Thermal and catalytic cracking of polyethylene under mild conditions”, *Journal of Analytical and Applied Pyrolysis*, Vol. 58–59, pp. 127–142.
- Vargaftik, N.B. (1975), “Handbook of physical properties of liquids and gases-pure substances and mixtures”, Hemisphere Publishing Corporation, New York, NY.
- Vasile, C., Pakdel, H., Mihai, B., Onu, P., Darie, H. and Ciocâlțeu, S. (2001), “Thermal and catalytic decomposition of mixed plastics”, *Journal of Analytical and Applied Pyrolysis*, Vol. 57 No. 2, pp. 287–303.
- Vos et al. (2017), “gasification\_guide\_final\_guideline\_for\_safe\_and\_eco\_friendly\_biomass-3.pdf”, IEA Bioenergy.
- Vyazovkin, S., Burnham, A.K., Criado, J.M., Pérez-Maqueda, L.A., Popescu, C. and Sbirrazzuoli, N. (2011), “ICTAC Kinetics Committee recommendations for performing kinetic computations on thermal analysis data”, *Thermochimica Acta*, Vol. 520 No. 1, pp. 1–19.
- Vyazovkin, S. and Wight, C.A. (1997), “Kinetics in Solids”, *Annual Review of Physical Chemistry*, Vol. 48 No. 1, pp. 125–149.
- Vyazovkin, S. and Wight, C.A. (1998), “Isothermal and non-isothermal kinetics of thermally stimulated reactions of solids”, *International Reviews in Physical Chemistry*, Taylor & Francis, Vol. 17 No. 3, pp. 407–433.

## References

---

- Wallis, M.D., Sarathy, S., Bhatia, S.K., Massarotto, P., Kosior, E. and Mercier, A. (2008), “Catalytic Degradation of High-Density Polyethylene in a Reactive Extruder”, *Industrial & Engineering Chemistry Research*, Vol. 47 No. 15, pp. 5175–5181.
- White, F.M. (2007), *Viscous Fluid Flow*, 3. ed., internat. ed., [Nachdr.], McGraw-Hill, Boston.
- Wong, S.L., Ngadi, N., Abdullah, T.A.T. and Inuwa, I.M. (2015), “Current state and future prospects of plastic waste as source of fuel: A review”, *Renewable and Sustainable Energy Reviews*, Vol. 50, pp. 1167–1180.
- Xu, F., Wang, B., Yang, D., Hao, J., Qiao, Y. and Tian, Y. (2018), “Thermal degradation of typical plastics under high heating rate conditions by TG-FTIR: Pyrolysis behaviors and kinetic analysis”, *Energy Conversion and Management*, Elsevier, Vol. 171, pp. 1106–1115.
- Xu, Q., Pang, S. and Levi, T. (2011), “Reaction kinetics and producer gas compositions of steam gasification of coal and biomass blend chars, part 1: Experimental investigation”, *Chemical Engineering Science*, Vol. 66 No. 10, pp. 2141–2148.
- Yan, K. and Che, D. (2010), “A coupled model for simulation of the gas–liquid two-phase flow with complex flow patterns”, *International Journal of Multiphase Flow*, Vol. 36 No. 4, pp. 333–348.
- Yin, L.J., Chen, D.Z., Wang, H., Ma, X.B. and Zhou, G.M. (2014), “Simulation of an innovative reactor for waste plastics pyrolysis”, *Chemical Engineering Journal*, Elsevier, Vol. 237, pp. 229–235.

# Appendix: A

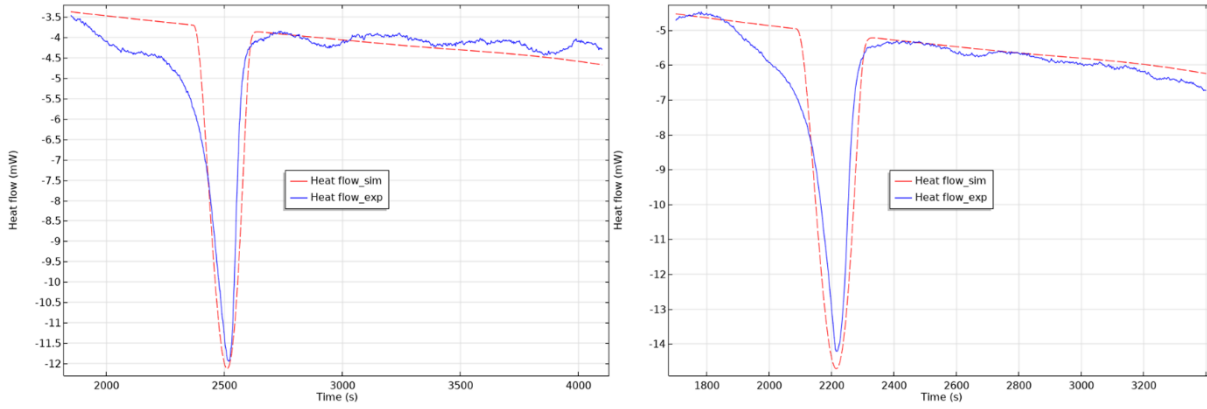


**Figure 3-1A:** Experimental and simulated results for PP melting at 6 and 8 °C/min, respectively.

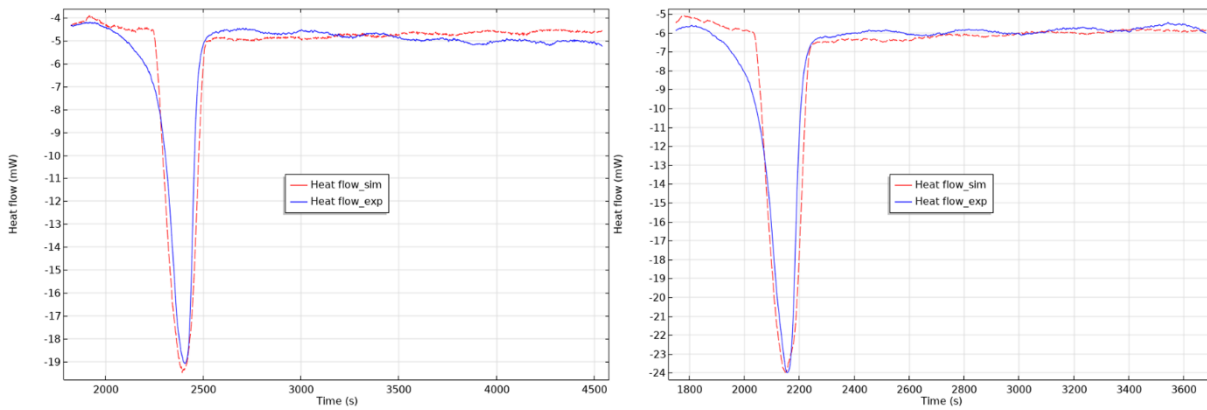


**Figure 3-2A:** Experimental and simulated results for PP melting at 6 and 8 °C/min, respectively.

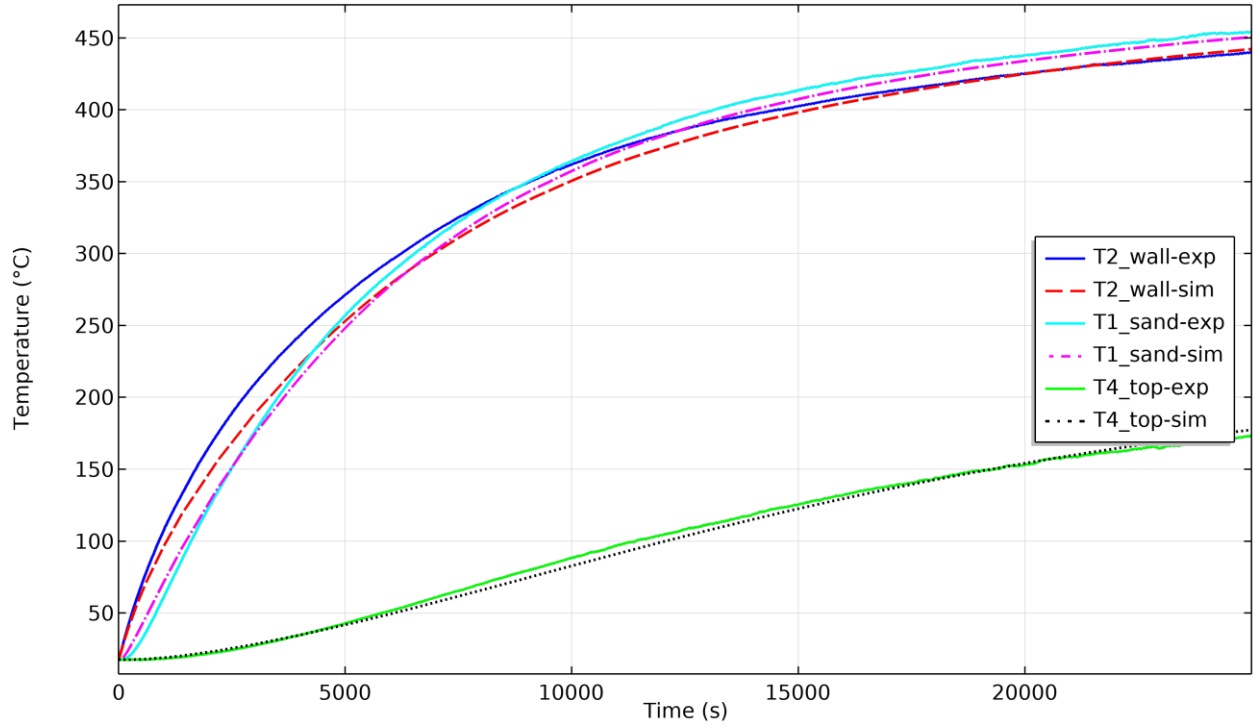


**Figure 3-3A:** Temperature comparison, T1, T2, and T4, for sand heating inside the semi-batch reactor, by 150 W heating power.

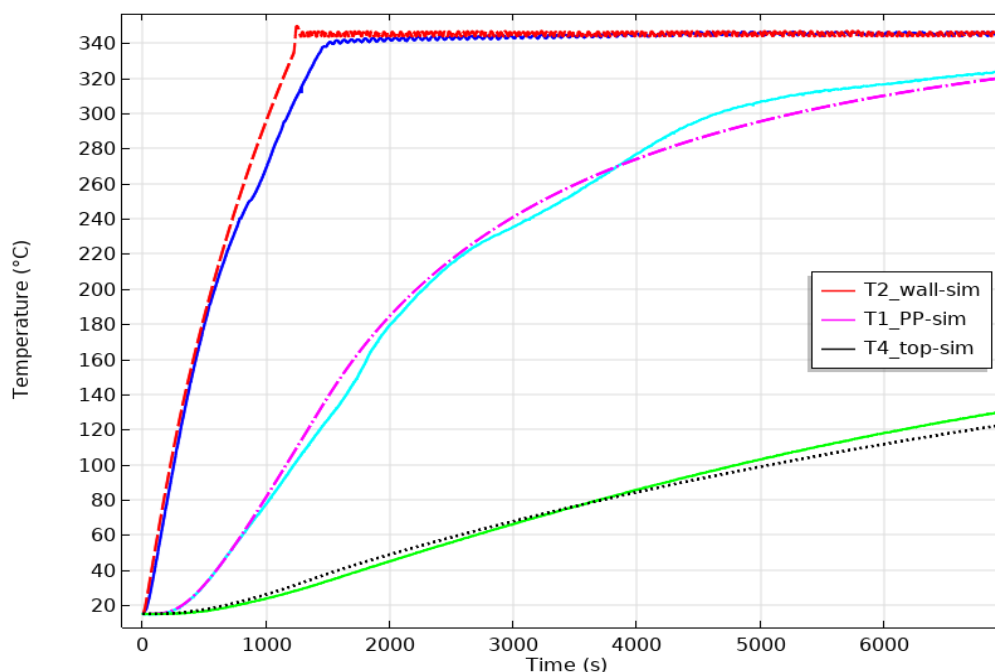


**Figure 3-4A:** Temperature comparison, T1, T2, and T4, for PP melting and heating by 500 W, modelled heater and controller.

**Table 4-1A :** Activation energy and coefficient of determination  $R^2$  for PP pyrolysis w.r.t. conversion according to FR method.

| Friedman Equation (FR) |           |              |                |        |           |           |
|------------------------|-----------|--------------|----------------|--------|-----------|-----------|
|                        | (-E/R)    | (Ln[A*f(x)]) |                |        | f(x) = A2 | f(x) = R3 |
| Conversion x           | Slope     | Intercept    | R <sup>2</sup> | E      | A         | A         |
| mg/mg                  | 1/k       | 1/min        | 1              | kJ/mol | (1/min)   | (1/min)   |
| <b>0.1</b>             | -26504.68 | 35.55        | 0.96           | 220.36 | 4.69E+15  | 9.80E+14  |
| <b>0.15</b>            | -27846.60 | 37.59        | 0.99           | 231.52 | 3.09E+16  | 7.87E+15  |
| <b>0.2</b>             | -26442.72 | 35.64        | 0.99           | 219.84 | 3.98E+15  | 1.16E+15  |
| <b>0.25</b>            | -24598.01 | 33.08        | 0.98           | 204.51 | 2.88E+14  | 9.35E+13  |
| <b>0.3</b>             | -25825.10 | 34.85        | 0.99           | 214.71 | 1.64E+15  | 5.79E+14  |
| <b>0.35</b>            | -24939.34 | 33.61        | 1.00           | 207.35 | 4.65E+14  | 1.76E+14  |
| <b>0.4</b>             | -24190.95 | 32.55        | 1.00           | 201.12 | 1.60E+14  | 6.44E+13  |
| <b>0.45</b>            | -25559.43 | 34.45        | 1.00           | 212.50 | 1.08E+15  | 4.55E+14  |
| <b>0.5</b>             | -25768.98 | 34.70        | 0.99           | 214.24 | 1.41E+15  | 6.21E+14  |
| <b>0.55</b>            | -26047.28 | 35.03        | 0.99           | 216.56 | 2.04E+15  | 9.30E+14  |
| <b>0.6</b>             | -24737.70 | 33.15        | 0.99           | 205.67 | 3.25E+14  | 1.53E+14  |

## Appendix: A

|                       |           |       |             |               |                             |                             |
|-----------------------|-----------|-------|-------------|---------------|-----------------------------|-----------------------------|
| <b>0.65</b>           | -22454.84 | 29.93 | 0.98        | 186.69        | 1.38E+13                    | 6.66E+12                    |
| <b>0.7</b>            | -22211.42 | 29.52 | 0.99        | 184.67        | 1.01E+13                    | 4.93E+12                    |
| <b>0.75</b>           | -22169.88 | 29.37 | 1.00        | 184.32        | 9.68E+12                    | 4.79E+12                    |
| <b>0.8</b>            | -21273.70 | 28.00 | 1.00        | 176.87        | 2.84E+12                    | 1.41E+12                    |
| <b>0.85</b>           | -23803.07 | 31.30 | 1.00        | 197.90        | 9.48E+13                    | 4.63E+13                    |
| <b>0.9</b>            | -28112.55 | 36.87 | 0.97        | 233.73        | 3.40E+16                    | 1.60E+16                    |
| <b>Average values</b> |           |       | <b>0.99</b> | <b>202.23</b> | <b>8.79×10<sup>14</sup></b> | <b>3.27×10<sup>14</sup></b> |

**Table 4-2A** : Activation energy and coefficient of determination  $R^2$  for PP pyrolysis w.r.t. conversion according to KAS method.

| <b>Kissinger-Akahira-Sunose Equation (KAS)</b> |               |                           |                      |               |                             |                             |
|--|---------------|---------------------------|----------------------|---------------|-----------------------------|-----------------------------|
|  | <b>(-E/R)</b> | <b>(Ln[A*R/(E*g(x))])</b> |                      |               | <b>f(x) = A2</b>            | <b>f(x) = R3</b>            |
| <b>Conversion x</b>                            | <b>slope</b>  | <b>Intercept</b>          | <b>R<sup>2</sup></b> | <b>E</b>      | <b>A</b>                    | <b>A</b>                    |
| <i>mg/mg</i>                                   | <i>1/K</i>    | <i>1/(K.min)</i>          | <i>1</i>             | <i>kJ/mol</i> | <i>(1/min)</i>              | <i>(1/min)</i>              |
| <b>0.1</b>                                     | -23600.38     | 23.24                     | 0.76                 | 196.21        | 9.48E+13                    | 1.01E+13                    |
| <b>0.15</b>                                    | -25410.55     | 25.54                     | 0.83                 | 211.26        | 1.27E+15                    | 1.66E+14                    |
| <b>0.2</b>                                     | -26489.14     | 26.86                     | 0.89                 | 220.23        | 5.81E+15                    | 8.82E+14                    |
| <b>0.25</b>                                    | -26675.77     | 26.95                     | 0.92                 | 221.78        | 7.26E+15                    | 1.24E+15                    |
| <b>0.3</b>                                     | -26724.56     | 26.88                     | 0.93                 | 222.19        | 7.51E+15                    | 1.41E+15                    |
| <b>0.35</b>                                    | -26949.67     | 27.07                     | 0.94                 | 224.06        | 1.01E+16                    | 2.06E+15                    |
| <b>0.4</b>                                     | -26810.90     | 26.77                     | 0.96                 | 222.91        | 8.06E+15                    | 1.77E+15                    |
| <b>0.45</b>                                    | -26431.34     | 26.13                     | 0.97                 | 219.75        | 4.55E+15                    | 1.06E+15                    |
| <b>0.5</b>                                     | -26798.59     | 26.55                     | 0.97                 | 222.80        | 7.56E+15                    | 1.87E+15                    |
| <b>0.55</b>                                    | -26621.57     | 26.21                     | 0.97                 | 221.33        | 5.74E+15                    | 1.50E+15                    |
| <b>0.6</b>                                     | -26298.86     | 25.66                     | 0.97                 | 218.65        | 3.52E+15                    | 9.68E+14                    |
| <b>0.65</b>                                    | -26144.23     | 25.36                     | 0.98                 | 217.36        | 2.77E+15                    | 7.99E+14                    |
| <b>0.7</b>                                     | -26156.71     | 25.30                     | 0.98                 | 217.47        | 2.79E+15                    | 8.41E+14                    |
| <b>0.75</b>                                    | -25834.39     | 24.77                     | 0.98                 | 214.79        | 1.74E+15                    | 5.46E+14                    |
| <b>0.8</b>                                     | -25345.02     | 24.01                     | 0.99                 | 210.72        | 8.56E+14                    | 2.80E+14                    |
| <b>0.85</b>                                    | -25672.84     | 24.37                     | 0.99                 | 213.44        | 1.36E+15                    | 4.62E+14                    |
| <b>0.9</b>                                     | -25615.42     | 24.18                     | 0.99                 | 212.97        | 1.24E+15                    | 4.37E+14                    |
| <b>Average values</b>                          |               |                           | <b>0.96</b>          | <b>219.54</b> | <b>4.10×10<sup>15</sup></b> | <b>1.17×10<sup>15</sup></b> |

## Appendix: A

**Table 4-3A :** Activation energy and coefficient of determination  $R^2$  for PP pyrolysis w.r.t. conversion according to FWO method.

| Flynn-Wall-Ozawa Equation (FWO) |                      |   |             |               |                             |                             |
|---------------------------------|----------------------|---|-------------|---------------|-----------------------------|-----------------------------|
|                                 | $(-1.052 \cdot E/R)$ | $(\ln[A \cdot E/(R \cdot g(x))]) - 5.331$ |             |               | $f(x) = A2$                 | $f(x) = R3$                 |
| Conversion x                    | slope                | Intercept                                 | $R^2$       | E             | A                           | A                           |
| mg/mg                           | 1/K                  | K/min                                     | 1           | kJ/mol        | (1/min)                     | (1/min)                     |
| 0.1                             | -24977.90            | 38.31                                     | 0.78        | 197.40        | 1.23E+14                    | 1.30E+13                    |
| 0.15                            | -26799.41            | 40.63                                     | 0.85        | 211.80        | 1.44E+15                    | 1.89E+14                    |
| 0.2                             | -27885.48            | 41.96                                     | 0.90        | 220.38        | 6.16E+15                    | 9.35E+14                    |
| 0.25                            | -28078.05            | 42.06                                     | 0.92        | 221.90        | 7.65E+15                    | 1.30E+15                    |
| 0.3                             | -28131.58            | 41.99                                     | 0.94        | 222.33        | 7.94E+15                    | 1.49E+15                    |
| 0.35                            | -28361.05            | 42.19                                     | 0.95        | 224.14        | 1.06E+16                    | 2.15E+15                    |
| 0.4                             | -28225.82            | 41.89                                     | 0.97        | 223.07        | 8.57E+15                    | 1.88E+15                    |
| 0.45                            | -27849.86            | 41.26                                     | 0.97        | 220.10        | 5.00E+15                    | 1.17E+15                    |
| 0.5                             | -28220.47            | 41.68                                     | 0.97        | 223.03        | 8.12E+15                    | 2.01E+15                    |
| 0.55                            | -28046.54            | 41.35                                     | 0.97        | 221.65        | 6.27E+15                    | 1.64E+15                    |
| 0.6                             | -27727.32            | 40.81                                     | 0.98        | 219.13        | 3.96E+15                    | 1.09E+15                    |
| 0.65                            | -27575.83            | 40.51                                     | 0.98        | 217.93        | 3.17E+15                    | 9.12E+14                    |
| 0.7                             | -27591.31            | 40.45                                     | 0.98        | 218.06        | 3.20E+15                    | 9.63E+14                    |
| 0.75                            | -27272.01            | 39.92                                     | 0.98        | 215.53        | 2.05E+15                    | 6.43E+14                    |
| 0.8                             | -26785.59            | 39.16                                     | 0.99        | 211.69        | 1.05E+15                    | 3.44E+14                    |
| 0.85                            | -27116.72            | 39.53                                     | 0.99        | 214.30        | 1.63E+15                    | 5.55E+14                    |
| 0.9                             | -27063.61            | 39.35                                     | 0.99        | 213.88        | 1.50E+15                    | 5.31E+14                    |
| <b>Average values</b>           |                      |   | <b>0.96</b> | <b>219.92</b> | <b>4.25×10<sup>15</sup></b> | <b>1.27×10<sup>15</sup></b> |

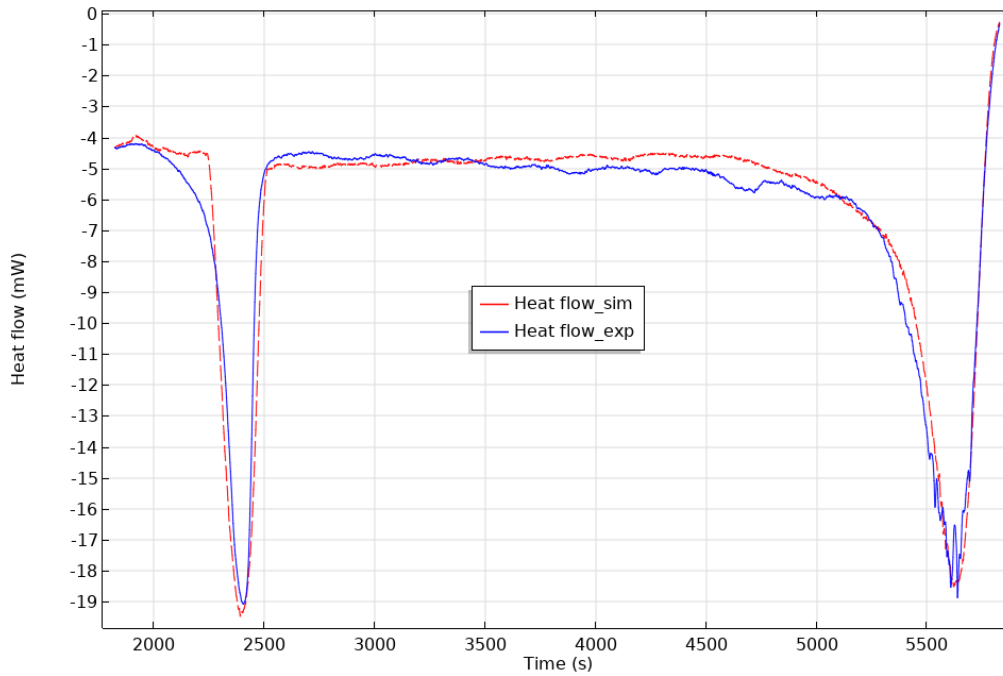


Figure 4-1A : Simulated and experimental results for HDPE pyrolysis at heating rate  $\beta_2= 6 \text{ }^\circ\text{C/min}$ .

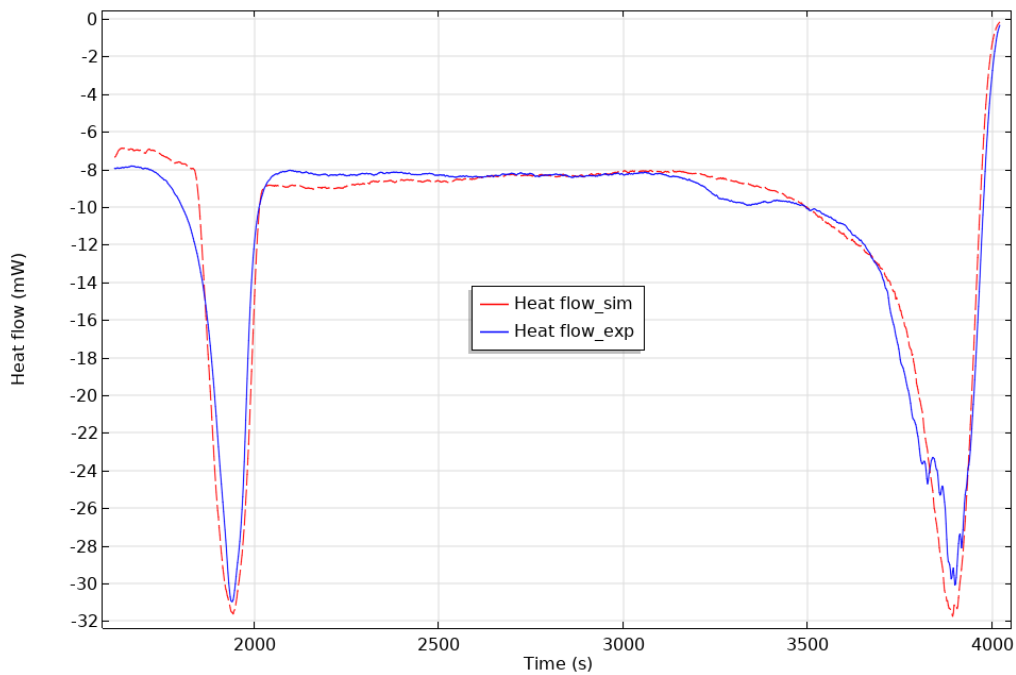


Figure 4-2A : Simulated and experimental results for HDPE pyrolysis at heating rate  $\beta_4= 10 \text{ }^\circ\text{C/min}$ .

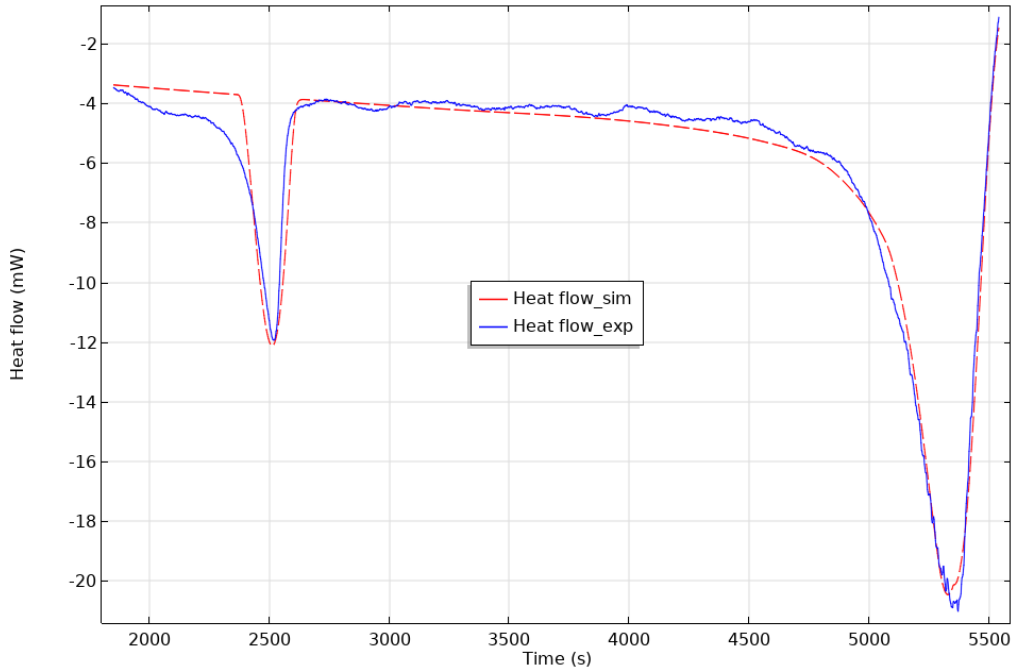


Figure 4-3A : Simulated and experimental results for PP pyrolysis at heating rate  $\beta_2= 6 \text{ }^\circ\text{C}/\text{min}$ .

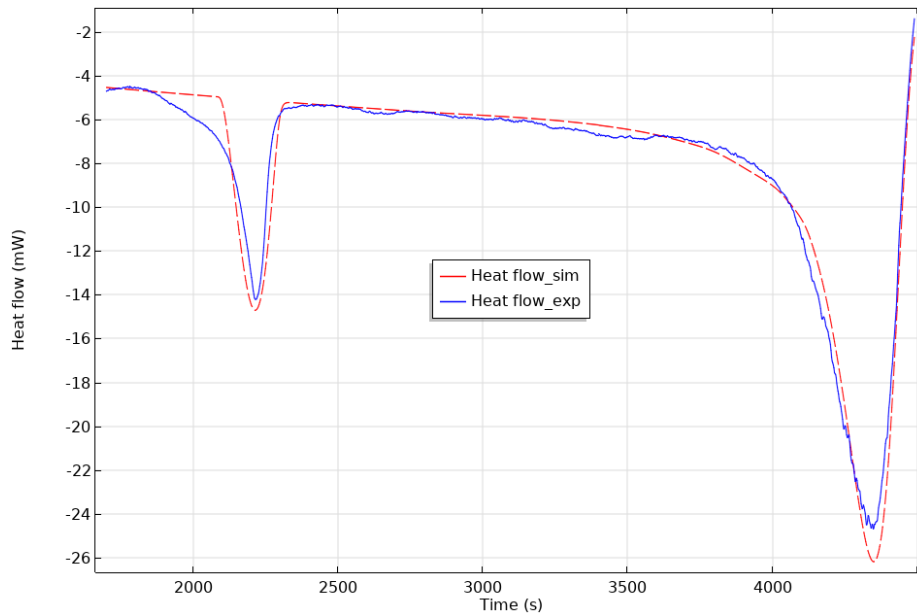


Figure 4-4A : Simulated and experimental results for PP pyrolysis at heating rate  $\beta_3= 8 \text{ }^\circ\text{C}/\text{min}$ .

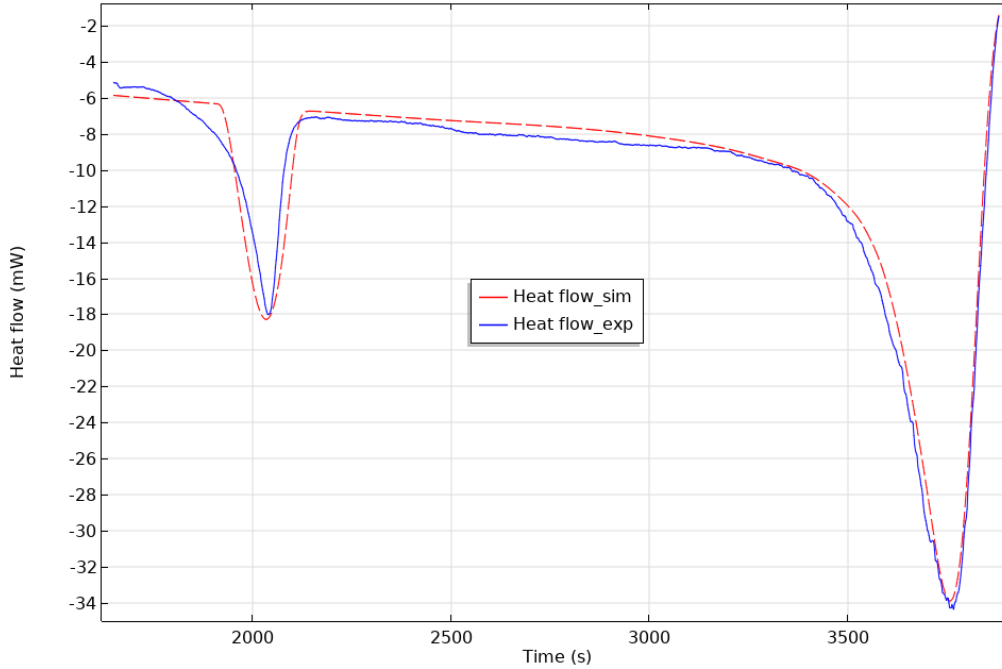


Figure 4-5A : Simulated and experimental results for PP pyrolysis at heating rate  $\beta_4 = 10 \text{ }^\circ\text{C/min}$ .

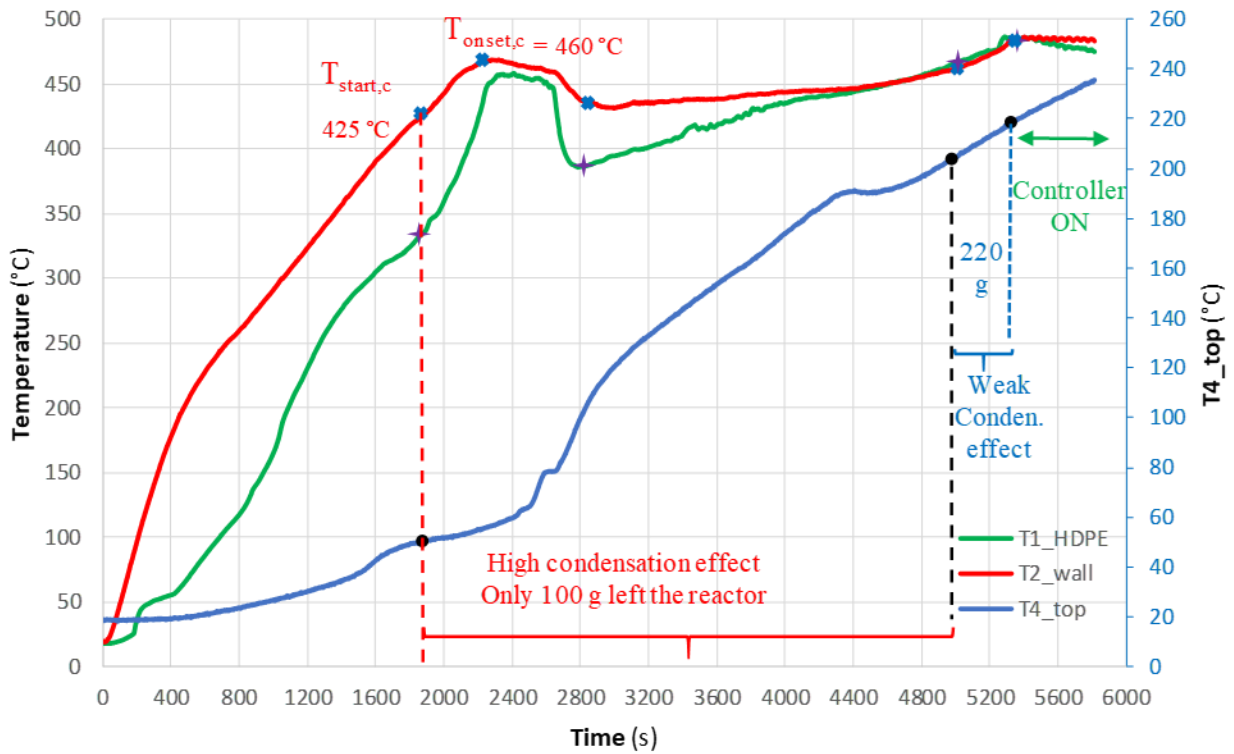
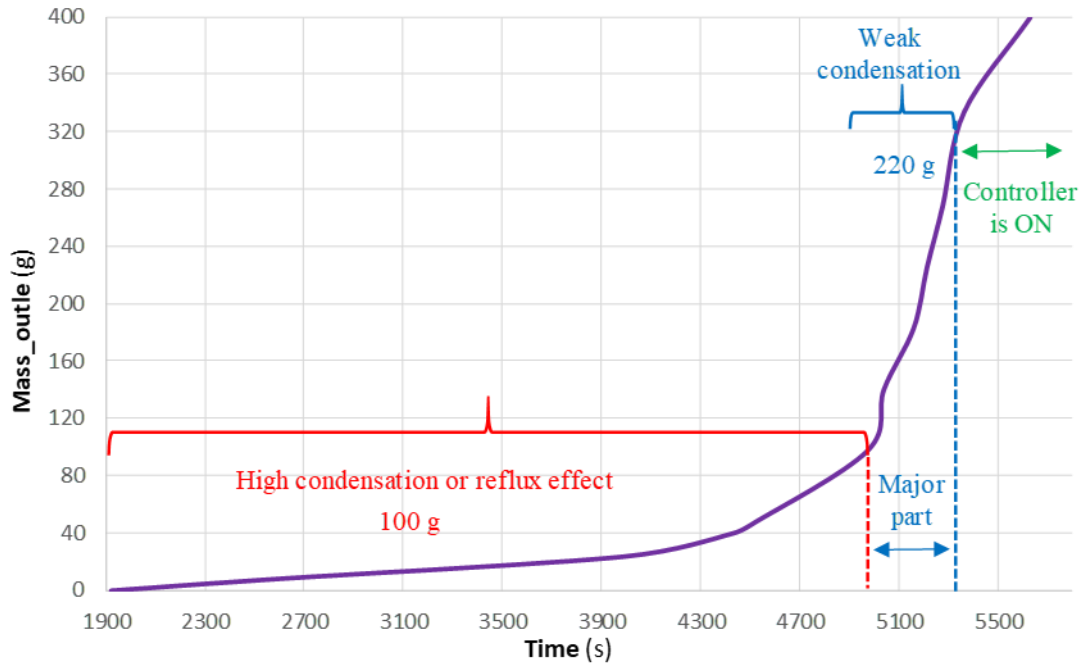
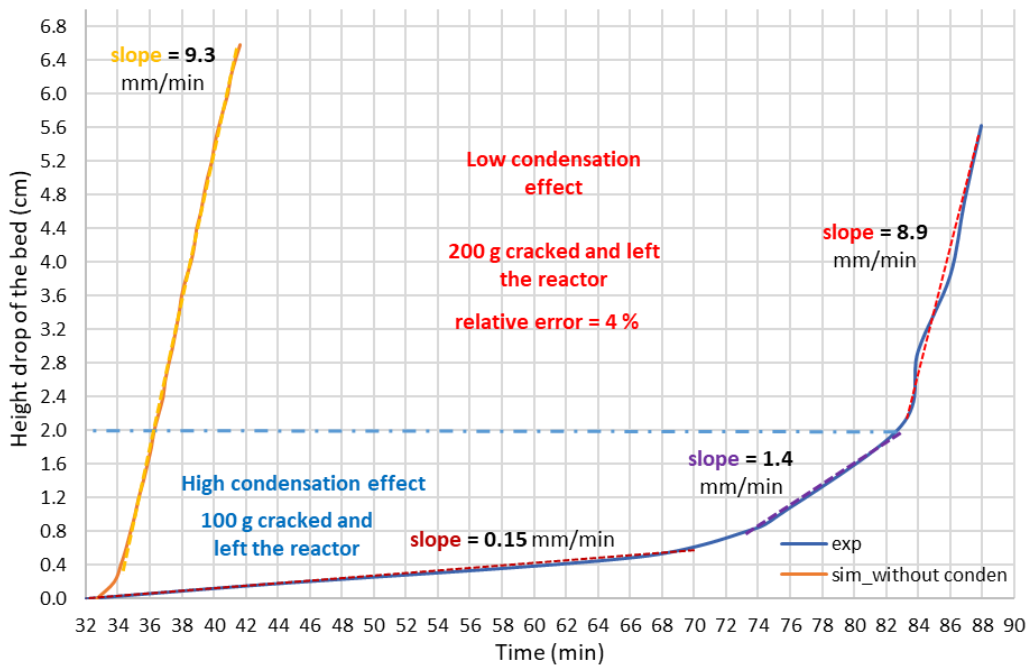


Figure 4-6A : Temperature results of 400 g HDPE pyrolysis inside the semi-batch reactor of 6000 W average heating power.



**Figure 4-7A :** Mass of the oil and wax by-product (at the outlet) vs time of 400 g HDPE pyrolysis inside the semi-batch reactor of 600 W average heating power.



**Figure 4-8A :** Bed loss comparison between the simulated and experimental results for HDPE pyrolysis at 600 W heating power, without modelling the condensation process.

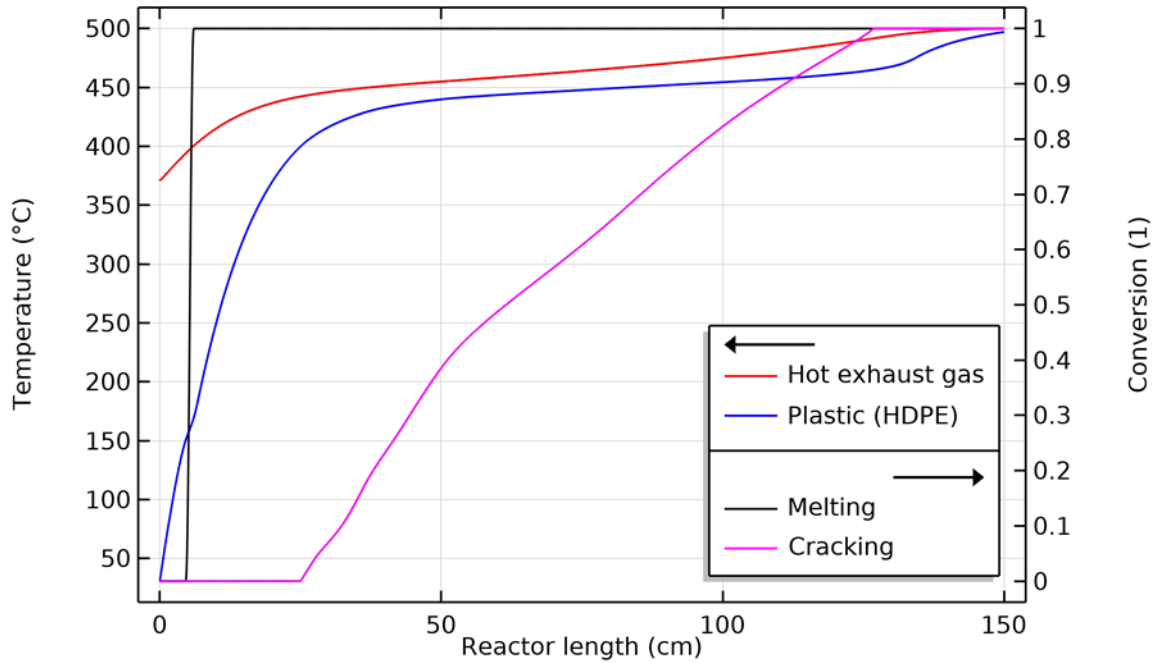


**Figure 5-1A:** Average simulation results (temperatures and conversions) for the best deduced model of the continuous pyrolysis reactor (1.5 m length and 100 tubes,  $d = 1.4$  cm, plastic (HDPE) mass flow rate 7 kg/h).

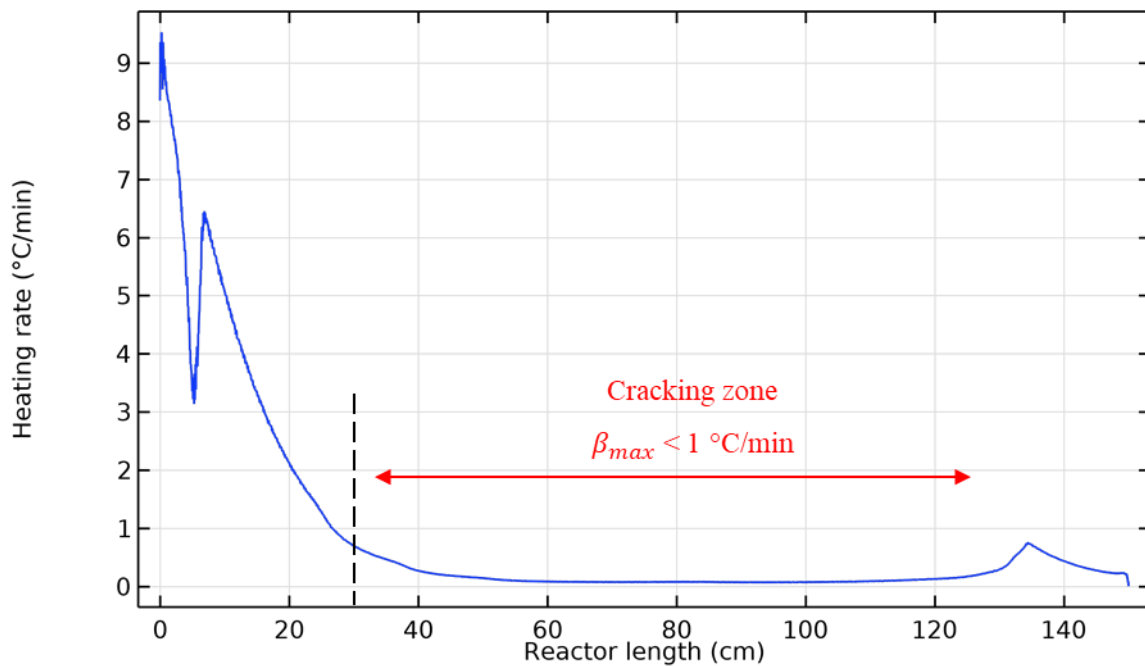


**Figure 5-2A:** Average heating rate of plastic with respect to the length of the reactor, for the best deduced model of the continuous pyrolysis reactor (1.5 m length and 100 tubes,  $d = 1.4$  cm, plastic (HDPE) mass flow rate 7 kg/h).

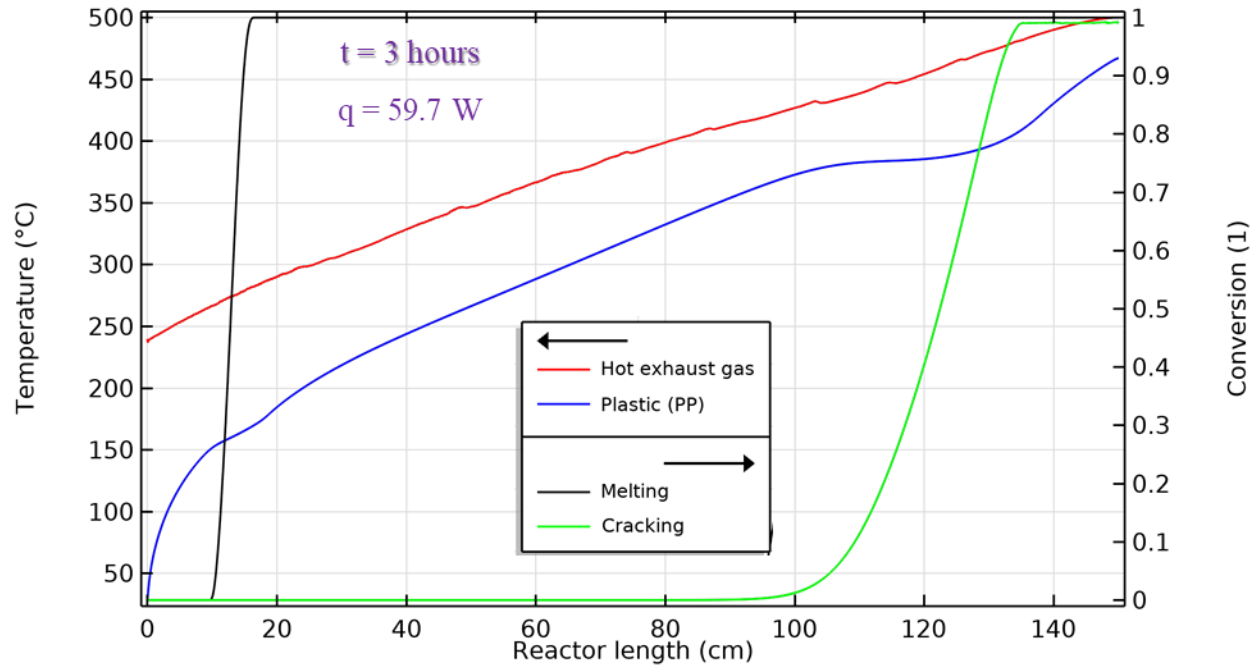


**Figure 5-3A:** Average Transient simulation results (Temperatures, and plastic conversions) with respect to length of the reactor at  $t = 10800$  s (i.e. at  $t = 3$  hours), for the best deduced model ( $N = 100$ ,  $d = 1.4$  cm, and  $L = 1.5$  m) with fully reactor (with plastic) 7 kg/h mass flow rate heated from ambient temperature.

**Titre : Extension et mise à niveau d'un pilote de production de carburants alternatifs à partir de déchets plastiques.**

**Mots clés :** Pyrolyse ; Déchets plastiques ; Transfert de chaleur ; Méthode des Eléments Finis ; Modélisation mécanistique.

**Résumé :** De nos jours, après l'épuisement des réserves mondiales d'énergie fossile, l'implémentation des énergies renouvelables est devenue un enjeu crucial. Alors que l'humanité est confrontée à l'énorme croissance des déchets plastiques accumulés chaque année, en raison de la limitation des décharges et des processus de recyclage. Par conséquent, une solution pour l'accumulation de déchets plastiques est le processus de pyrolyse, qui convertit les déchets plastiques en une large gamme de carburants et de produits chimiques. La pyrolyse consiste en une décomposition thermique de polymères à longues chaînes en l'absence d'oxygène. Différents paramètres affectent ce processus comme la température, la vitesse de chauffage, la matière première, le catalyseur, le type de réacteur et la pression. Cependant, de nombreuses études expérimentales sont réalisées à ce jour concernant l'influence de ces paramètres sur le processus de pyrolyse et ses sous-produits. D'autre part, la modélisation et la simulation du processus de pyrolyse plastique, à l'échelle

du laboratoire ou à l'échelle industrielle, sont rarement trouvées dans la littérature. Ainsi, l'objectif de ce projet de thèse est de modéliser et de mettre à niveau un réacteur de pyrolyse continue réalisable à l'échelle industrielle, chauffé par des gaz d'échappement chauds provenant d'un moteur diesel de 8 kW, pour convertir les déchets plastiques en carburants. Mais avant de franchir cette étape, le procédé de pyrolyse plastique pour le PP et le HDPE est modélisé et validé, à l'échelle milli-particulaire, dans un analyseur thermogravimétrique couplé à un calorimètre différentiel à balayage (TGA- DSC), puis dans un réacteur semi-batch à l'échelle du laboratoire en utilisant la méthode des éléments finis et le logiciel COMSOL-Multiphysics. Finalement, les modèles mécanistiques élaborés et validés à l'échelle de milli-particule et du réacteur semi-continu sont utilisés pour concevoir un réacteur continu et étudier son comportement numériquement.

**Title : Up-scaling of a pilot plant for the production of alternative fuels from waste plastics.**

**Keywords :** Pyrolysis ; Plastic wastes ; Heat transfer ; Finite Element Method ; Mechanistic modelling.

**Abstract :** Nowadays, after the depletion of fossil energy reserves worldwide, the pursue for renewable energy became a crucial issue and subject for many researchers and academic institutions. Whereas, humanity is facing serious dilemma: the enormous growth of accumulated plastic wastes every year, due to the limitation of landfills and recycling processes. Therefore, a solution for plastic wastes accumulation and an alternative source of energy is pyrolysis process, which converts plastic wastes into a wide range of fuels and chemicals. Plastic pyrolysis consists of a thermal decomposition of large chain polymers in absence of oxygen. Different parameters affect this process like; Temperature, heating rate, feedstock material, catalyst, type of the reactor and pressure. However, many experimental studies are made so far regarding the influence of these parameters on the

pyrolysis process and its by-products. On the other hand, modelling and simulating plastic pyrolysis process, at a lab-scale or industrial-scale, are rarely found in literature. Thus, the aim of this thesis is to model and upgrade a continuous pyrolysis reactor feasible at the industrial scale, heated by hot exhaust gases coming from 8 kW diesel engine, to convert plastic waste into heat and transportation fuels. But before crossing this step, plastic pyrolysis process for PP and HDPE is modelled and validated, as milli-particle scale, in a thermogravimetric analyzer coupled with differential scanning calorimeter (TGA-DSC), then in a laboratory scale semi-batch reactor (1 liter capacity) using Finite Element method and COMSOL-Multiphysics software. Finally, the calibrated models are used to conceive a continuous reactor and to study its behavior numerically.